Electrochemical Studies of Interfacial Polymerisation Processes

By Elizabeth Ellen Oseland

A thesis submitted for the degree of Doctor of Philosophy

Department of Chemistry

University of Warwick

August 2016

For my loving parents and brother Andrew

“We shall not cease from exploration. And the end of all our exploring will be to arrive where we started and know the place for the first time.”

-T. S. Eliot

Contents

List of Figures

Chapter 1 – Introduction

Chapter 2 -Experimental

Chapter 3 - Using Electrochemical and Optical Technqiues to Understand the Formation of Polymeric Microparticles

Chapter 4 - Investigating Poly(Urea) Film Formation at a Micro-Liquid/Liquid Interface

Chapter 5 - Surface Patterning of Polyacrylamide Gel on Gold Surfaces Using Scanning Electrochemical Cell Microscopy (SECCM)

List of Tables

Acknowledgements

Firstly, I would like to thank my supervisor Prof. Patrick Unwin for all his help, advice and enthusiastic encouragement throughout the course of my PhD. I would also like to thank Prof. Julie Macpherson for her support, Dr Paul Wilson and Dr Andrew Basile for guidance during the polymer patterning work, Dr Joshua Byers for advice during the impedance work, and Dr Max Joseph for being an all-round fountain of knowledge. Thanks must also go to my industrial collaborators at Syngenta, Anita Rea, Martine de Heer and Jeffrey Fowler for their invaluable guidance, support and enthusiasm during the course of this project.

I would also like to thank all of the past and present members of the Warwick Electrochemistry & Interfaces Group (WEIG) for random help and advice over the years. In particular, massive thanks must go to all the members of office A105 for all their support over the past few years (Tania “I love cats” Read, Zoë “Don’t you know who I am” Ayres, Jenny “Two drinks” Webb, Jon Newland, Rob Channon, Sam Cobb, Haytham Hussein and Lingcong Meng). I would also like to thank Sophie Kinnear, Ashley Page and Minkyung Kang for all their support and advice over the past few years. Thanks also to Bryn Jones, Lee Simcox, Rob Johnson, Harriet Pearce and Mareike Herrmann for providing much needed tea breaks during the writing of this thesis. Without you all I may not have reached this far (and definitely would have had a lot less laughs)!

Finally, I would like to give thanks to my family for all their love and support, especially my parents who have supported and inspired me the most.

Declaration

The work contained within this thesis is entirely original and carried out by myself apart from where stated. I confirm that this thesis has not been submitted for a degree at another university.

MEMED experiments carried out in Chapter 3 were performed using a LabVIEW program written by Dr Kim McKelvey. SEM images of poly(urea) films shown in Chapter 4 were collected with the help of Minkyung Kang. Gold substrates used for polymer patterning in Chapter 5 were synthesised by Dr Lingcong Meng and Emma Ravenhill. XPS data shown in Chapter 5 was collected and analysed in collaboration with Zoë Ayres.

Parts of this thesis have been submitted for publication as detailed below:

E. E. Oseland, Z. J. Ayres, A. Basile, D. M. Haddleton, P. Wilson and P. R. Unwin, Surface patterning of polyacrylamide gel using scanning electrochemical cell microscopy (SECCM), *Chem. Commun.*, 2016, **52**, 9929-9932

E. E. Oseland, A. Rea, M. I. de Heer, J. D. Fowler and P. R. Unwin, Interfacial kinetics in a model emulsion polymerisation system using microelectrochemical measurements at expanding droplets (MEMED) and time lapse microscopy, *J. Colloid Interface Sci.*, 2017, **490**, 703-709

Abstract

This thesis describes how electrochemical analytical techniques have been used to understand some of the physicochemical processes that underpin interfacial polymerisation reactions. A few of the reaction systems studied are currently used in the agrichemical industry for the formation of microcapsules for active ingredient encapsulation. Interfacial processes that take place at the oil-water interface of an epoxy-amine emulsion polymerisation system have been studied. Time-lapse microscopy of epoxide droplets in water or aqueous amine solutions has shown the effect of temperature on droplet dissolution and interfacial polymerisation. Quantitative kinetic data were extracted. A combination of microelectrochemical measurements at expanding droplets and finite element modelling has been used to measure the fast transfer of amine out of an organic phase comprised of epoxide and amine into the aqueous phase. Electrochemical impedance spectroscopy was used to monitor a growing poly(urea) film formed at a model liquid/liquid interface at the tip of a micropipette. A simple circuit diagram was used to model the liquid/liquid interface before and after film formation, highlighting how the presence of the film will increase interfacial resistance and decrease interfacial capacitance. Poly(urea) formation under a range of different reaction conditions was investigated using a combination of impedance versus time measurements and scanning electron microscopy. Finally, the polymerisation of acrylamide monomers at a solid/liquid interface for discrete surface functionalisation was examined using a combination of scanning electron microscopy and atomic force microscopy.

Abbreviations

Abbreviation	Description
ACN	Acetonitrile
AFM	Atomic force microscopy
AI	Active ingredient
ATRP	Atom transfer radical polymerisation
BTBACl	Benzyltributylammonium chloride
CPE	Constant-phase element
CV	Cyclic voltammetry
DCE	1,2-dichloroethane
DPV	Differential pulse voltammetry
eATRP	Electrochemical ATRP
EIS	Electrochemical impedance spectroscopy
$FcTMA^+$	Ferrocenylmethyltrimethylammonium hexafluorophosphate
FEM	Finite element modelling
FE-SEM	Field-emission scanning electron microscopy
HEAA	N-hydroxyethyl acrylamide
HMDA	Hexamethylene-1,6-diamine
IP	Interfacial polymerisation
IPA	Propan-2-ol
ITIES	Interface between two immiscible electrolyte solutions
MCEM	Micro-capillary electrochemical method
MEMED	Microelectrochemical measurements at expanding droplets
Me_6TREN	Tris[2-(dimethylamino)ethyl]amine
pBDD	Polycrystalline boron doped diamond
PEI	Polyethylenimine

PMP	Polymeric microparticle
PMPPI	Polymethylenepolyphenylisocyanate
QRCE	Quasi-reference counter electrode
RDGE	Resorcinol diglycidyl ether
SAM	Self-assembled monolayer
SCE	Saturated calomel electrode
SECCM	Scanning electrochemical cell microscopy
SECM	Scanning electrochemical microscopy
SEM	Scanning electron microscopy
SI-eATRP	Surface-initiated eATRP
SPM	Scanning probe microscopy
TBATPBCl	Tetrabutylammonium tetrakis (4-chlorophenyl) borate
TDI	Toluene-2,4-diisocyanate
UME	Ultramicroelectrode
XPS	X-ray photoelectron spectroscopy

Glossary of Symbols

Symbol	Description
A	Electrode area
AC	Alternating current
C	Concentration
D	Diffusion coefficient
DC	Direct current
E	Potential
eV	Electronvolt
F	Faraday's Constant
i_{barrel}	Barrel ion-conductance current
$i_{barrel\ AC}$	AC barrel current magnitude
i_{lim}	Steady state current
i_p	Peak current
$i_{surface}$	Surface current
j	Flux
j	$\sqrt{-1}$
n	Number of moles of electrons transferred
R	Resistance
T	Temperature
$V_{surface}$	Surface potential
Z	Impedance
α	CPE exponent
Ω	Ohms
ω	Frequency

Chapter 1

Introduction

This thesis is concerned with understanding the dynamics of polymerisation reactions that take place at the liquid/liquid and solid/liquid interface. Initially, this chapter outlines the polymer synthesis methods studied within this thesis. These can be broadly split into two categories: polymerisation at liquid/liquid interfaces for microcapsule synthesis and polymerisation at solid/liquid interfaces for the deposition of biofunctional polymer films. The principles behind the electroanalytical techniques used to study these polymerisation reactions is discussed, followed by a review on the structure of the liquid/liquid interface and its use in electrochemical studies. Finally, the scanning probe techniques used for the synthesis (scanning electrochemical cell microscopy) and analysis (atomic force microscopy) of biofunctional polymer films are explained.

1.1 Polymer Synthesis

Polymers are large macromolecules comprised of many recurring subunits.[1] They are formed by the polymerisation of smaller molecules, otherwise known as monomers, into a covalently bonded chain or network. The high molecular mass of polymers provides them with a number of unique features, such as tuneable robustness and viscoelasticity. As the properties of polymers can be readily modified depending on the method of

polymerisation and monomer used, they are widely utilised in both the natural world (e.g. DNA, proteins) and in synthetic chemistry (e.g. polystyrene, nylon).

Broadly speaking, there are two polymerisation reaction mechanisms (Figure 1.1). Step-growth polymerisation is a process in which bi-functional or multi-functional monomers react together to make many oligomers (small chains of monomer), which eventually link together to form long chain polymers.[2] Conversely, chain-growth polymerisation involves the addition of unsaturated monomers onto the active site(s) at the end of a growing polymer chain.

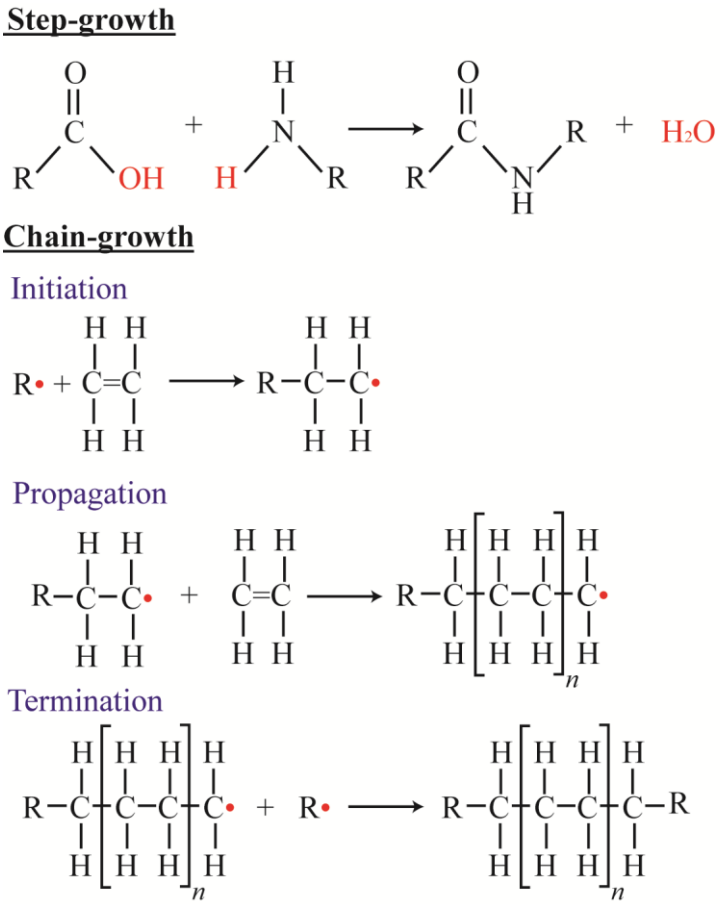

Figure 1.1 *Schematic of the two main polymerisation reaction mechanisms.*

The active sites which monomers link onto (•) can be a free radical (radical polymerisation)[3], carbocation (cationic polymerisation)[4], carbanion (anionic polymerisation)[5] or an organometallic complex (coordination polymerisation).[6]

Biopolymers tend to be formed via the step-growth mechanism, whereas synthetic polymers can be formulated using both reaction mechanisms to create a wide range of useful products.

1.1.1 Polymeric Microparticles

Polymeric microparticles (PMPs) are spherical polymer structures with dimensions between 1 and 1000 μm (Figure 1.2). There is currently interest in both developing synthetic routes to novel PMP systems and exploiting the morphology of PMPs for useful applications such as the delivery of toxic or therapeutic molecules to a target site in a controlled manner.[7]

The release of an active ingredient (AI) from within a PMP can be achieved either by diffusion of the AI through the PMP wall[8] or by breakdown of the PMP wall, with the latter providing a higher level of control if the PMP has been designed to degrade when it comes into contact with certain stimuli such as a change in pH[9] or temperature.[10]

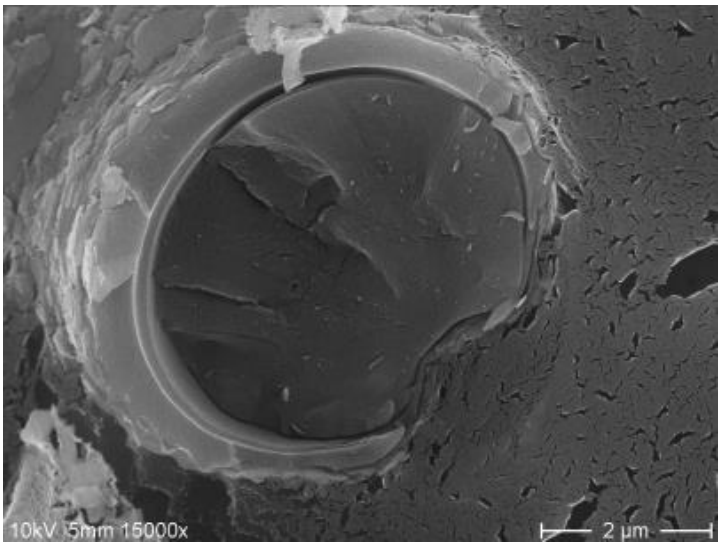

Figure 1.2 *Cryo-SEM of a polymeric microparticle (Ref: collected at Syngenta Jealott's Hill International Research Centre, Bracknell).*

PMPs can be formed using a variety of synthesis methods, with the type of method used depending on the application of the microcapsule. Generally speaking, these methods can be split into either chemical[11-13] or physical techniques.[14-16] The PMP synthesis methods studied in this project are both examples of emulsion polymerisation, a chemical synthesis technique.

1.1.1.1 Emulsion Polymerisation

Polymeric particles on the micro/nano scale are often synthesised using emulsion polymerisation processes (the most common type being oil-in-water emulsions). Initially, the monomer of choice is mixed with surfactant(s) and then dispersed via ultrasonication as an emulsion in an immiscible solvent.[17] The surfactant is added to ensure that droplets of monomers remain stable and do not coalesce. Depending on the nature of the emulsion, initiation of the polymerisation reaction will take place through either the addition of a radical initiator[18], photoinitiation[19], an increase in temperature[20] or a reaction between monomers and/or the solvent in which they are dispersed.[21] The overall outcome of the emulsion polymerisation reaction will be to form solid particles of a defined size, which can be used not only for AI encapsulation (if included in the monomer/surfactant mix before dispersion) but for other application such as in paints [22], coatings [23] and adhesives.[24]

1.1.1.2 Application of Microparticles for Controlled Release

There is currently a great deal of interest in utilising microparticles for the controlled release of active ingredients to specific locations. Microcapsules are already a well-established technology in the food[25] and cosmetic industries.[26] In the industrial coatings

sector, so called "smart" coatings capable of self-cleaning[27], self-healing[28] or antifouling[29] are currently in development that rely on microcapsule release technology.

Microcapsule systems are also being explored as a route towards the controlled *in vivo* release of drugs[30], hormones[31] and vaccines.[32] Containing these kinds of agents in bio-degradable microparticles should provide a number of advantageous properties. For example, microcapsules could protect these agents from degradation until they reach the desired point of action. This would have a number of benefits, such as allowing previously injection-based formulations to be converted to orally administered formulations (which can be stored and administered more easily).[33] Microcapsules could be designed to trigger the release of the agent following the application of a stimulus, not only ensuring that the agent is protected until it reaches the point of action but also potentially reducing drug load required and associated side-effects to the patient.[34]

The controlled release of AI from microcapsules is also of interest within the agrochemical sector. By encapsulating pesticides or herbicides in microcapsules, not only can the shelf-life of these AIs be extended but they can also be protected from external factors (e.g. UV light) which may degrade them prior to reaching their point of action.[35] Microcapsules could also be designed to release AI in a controlled manner following triggers in agrochemistry such as rain, UV light or the pH of an insect's digestive tract. However, the majority of microencapsulated agrochemicals on the market currently are slow release formulations designed to release AI over a sustained period of time.[36]

1.1.1.3 Microparticle Synthesis Pathways Studied In This Project

Both of the microparticle systems studied during this project were based upon step-growth emulsion polymerisation reactions currently used in the agrochemical industry to encapsulate pesticides.[37, 38] The first emulsion polymerisation system studied (see Chapter 3) was a temperature-dependent addition reaction between the epoxide resorcinol diglycidyl ether (RDGE) and amine Jeffamine D230. The structures of these two monomers are shown in Figure 1.3.

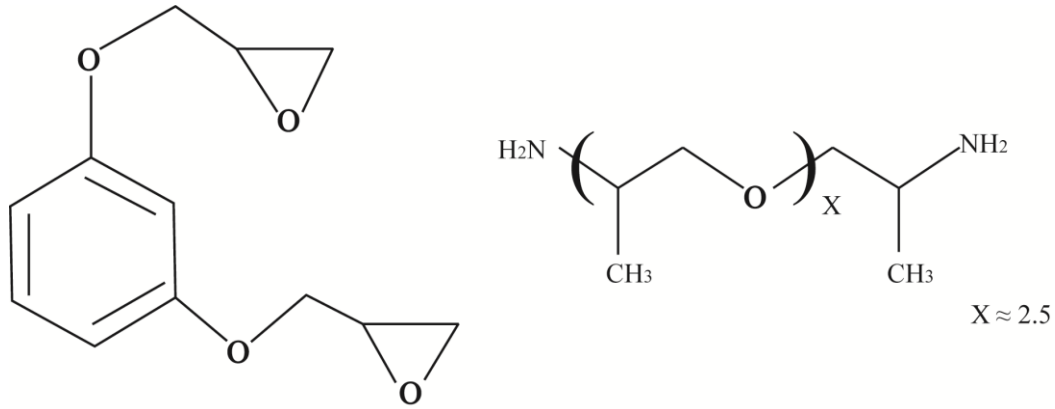

Figure 1.3 *Structures of RDGE (left) and Jeffamine D230 (right).*

AI is typically distributed in the organic phase containing both epoxide and amine monomers. This is then dispersed via sonication in an aqueous continuous phase containing kaolin clay and surfactants to stop droplets from coalescing (known as a Pickering emulsion).[39] The solution is then heated to around 70 °C to initiate the epoxy-amine polymerisation reaction, with the interface between the organic dispersed phase and the aqueous continuous phase ensuring that the curing process forms spherical PMPs embedded with AI.

Figure 1.4 shows a general schematic of the reaction that takes place between the epoxy and amine monomers during the emulsion polymerisation reaction. The amine groups within the jeffamine D230 monomers undergo an addition reaction with the epoxide

groups within the RDGE monomers, leading to epoxide ring-opening and thus step-growth polymerisation.

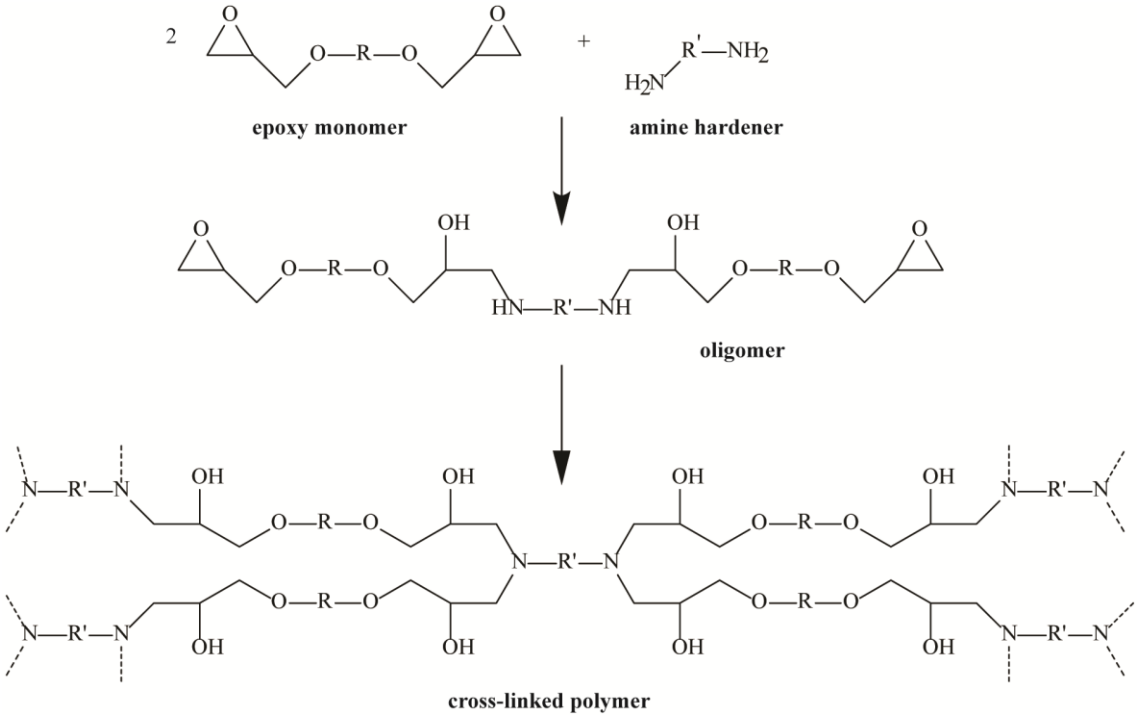

Figure 1.4 *Schematic of the reaction between epoxide and amine monomers to form a cross-linked polymer.*

The second emulsion polymerisation reaction studied (see Chapter 4) is based upon an interfacial polymerisation reaction involving isocyanate monomers toluene-2,4-diisocyanate (TDI) and polymethylenepolyphenylisocyanate (PMPPI), which are shown in Figure 1.5.

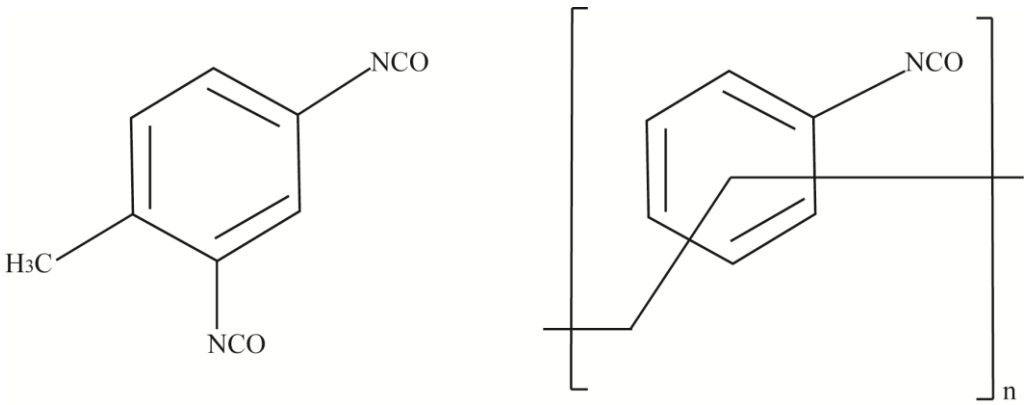

Figure 1.5 *Structures of the isocyanates TDI (left) and PMPPI (right) used to form poly(urea) microparticles via interfacial polymerisation.*

Similar to the epoxy-amine system, the AI is would typically be distributed within an organic phase containing the isocyanate monomers. This organic phase is dispersed as an emulsion in an aqueous phase, with the isocyanate monomers reacting with water at the liquid-liquid interface to form an amine and carbon dioxide. This amine then reacts with another isocyanate monomer to form poly(urea). The overall pathway to poly(urea) synthesis is shown in Figure 1.6.

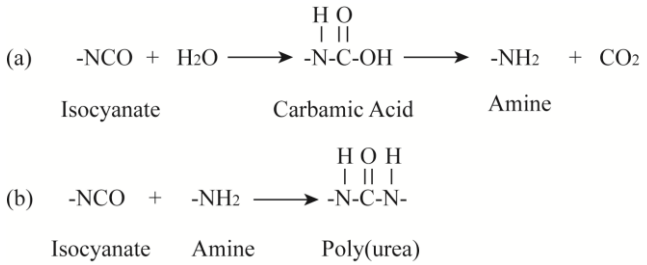

Figure 1.6 *Schematic showing the reaction of isocyanate groups with (a) water and (b) amine.*

Poly(urea) oligomers formed during this reaction will eventually combine to form microparticles containing AI. Although poly(urea) can be produced using only isocyanate monomers, it is sometimes desirable to add amine monomers to the aqueous phase to accelerate the reaction or to modify the properties of the polymeric microparticle wall. As such, some of the studies carried out in Chapter 4 included additional amine monomers, polyethylenimine (PEI) or hexamethylenediamine (HMDA), in the aqueous phase. The structures of these amine monomers are shown in Figure 1.7.

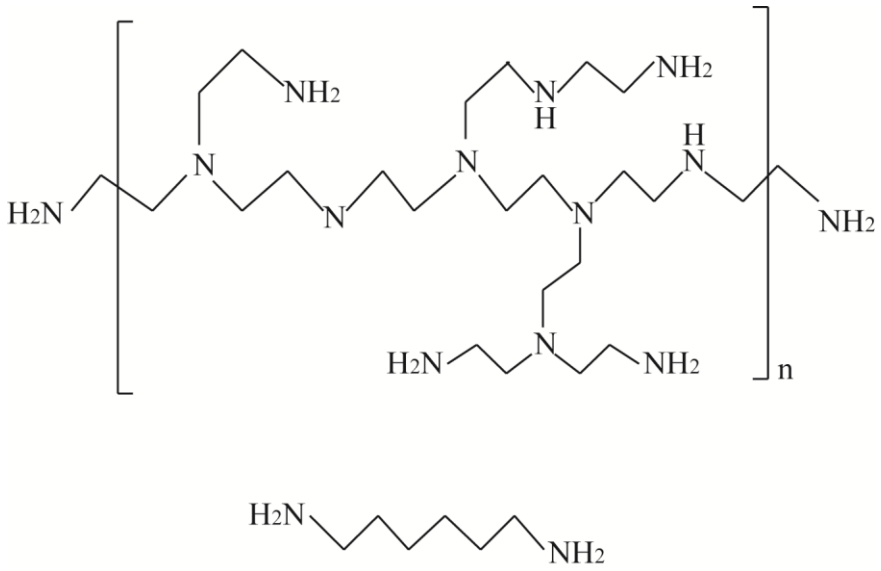

Figure 1.7 *Structures of the amine monomers PEI (top) and HMDA (bottom) added to the aqueous phase to react with isocyanate monomers to form poly(urea).*

1.1.2 Atom Transfer Radical Polymerisation

Atom transfer radical polymerisation (ATRP) is a form of reversible-deactivation radical polymerisation, which unlike the more conventional radical polymerisation techniques currently used allows for the production of polymer morphology that can be more closely controlled. ATRP employs a dynamic equilibrium constant (K_{ATRP}) between dormant species and activated propagating radicals to produce polymers with well-defined molecular weights, controllable architectures (in terms of topology, composition, and functionality) and low dispersities.[40]

There is increasing commercial interest in ATRP due to the ease of use, mild conditions (it can be performed at room temperature in either aqueous or organic solvents) and relatively inexpensive nature of its reagents. Since its invention, ATRP has been used to successfully formulate better pigment dispersants for inkjet printing, cosmetics adhesives and sealants for self-cleaning windows.[40]

Figure 1.8 shows a general mechanism for ATRP. The equilibrium between dormant species and propagating polymer chains controls the polymerisation mechanism. The lower oxidation state transition metal in the metal-ligand complex intermittently activates dormant polymer chains by alkyl halogen (R-X) homolytic bond cleavage to form alkyl radical chains which grow periodically.

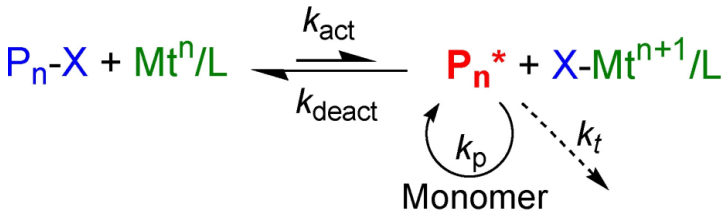

Figure 1.8 *General mechanism for ATRP. Mt^n is usually Cu^I (from halide salts) and L can be any amine, pyridine or pyridine-imine based chelating ligand. The dynamic equilibrium favours the dormant state, which decreases the concentration of propagating polymer chains and thus leads to their simultaneous growth when active.*[40]

The activation reaction (k_{act}) forms deactivating metal-ligand species with a higher oxidation state that coordinate to halide ligands. These deactivators subsequently react with the propagating polymer chain (k_{deact}) to revert back to the activator species and a dormant polymer chain. The redox active transition metal catalyst is usually a Cu-ligand complex; however ATRP using other transition metal catalysts has also been studied.[17]

1.1.2.1 Activator Regenerated by Electron Transfer (ARGET) ATRP

Although conventional ATRP has been shown to be capable of producing well defined polymer morphologies, the technique has a number of flaws. Metal complex catalysts that are in the lower oxidation state are more capable of dimerizing or strongly binding to the halide initiators. Therefore, it is more likely that the activity of the Cu^I catalyst will be reduced due to these side reactions taking place.[40] To avoid these unwanted side reactions, methods of ATRP that begin with the addition of the less reactive Cu^{II}

complex were developed. These "reverse" ATRP reactions involve the activation of the deactivator Cu^{II} complex to the active Cu^{I} form using reducing agents such as ascorbic acid[41], hydrazine[42], excess ligands[43] or Mt^0 species[44] (the most common being Cu^0) instead of a radical initiator.

The reducing/reactivating cycle employed during ARGET ATRP not only reduces catalytic side reactions but can also act to reduce unwanted reactions with O_2 or radical traps present in the system. The cyclic regeneration of the catalyst will also make the reaction "greener" as only a small amount of initial deactivator catalyst will be required.[40]

1.1.2.2 Electrochemically Mediated ATRP (eATRP)

Although the formation of side products is reduced by using methods such as ARGET ATRP, some will still form via the oxidisation of the reducing agents (e.g. to form copper halides when using Cu^0).[40] This oxidation will reduce the activity of these reducing agents and thus the efficiency of the ATRP reaction. Therefore, it is desirable to carry out ATRP in a manner that does not require any chemical reducing agents.

Electrochemically mediated ATRP (eATRP) (mechanism shown in Figure 1.9) replaces the action of chemical reducing agents with electrons generated by the application of a voltage, current or charge. By using electrochemistry to control the ratio of the concentrations of the activator and deactivator form of the redox-active catalyst, it is possible to achieve high levels of control over the rate of polymerisation.[45]

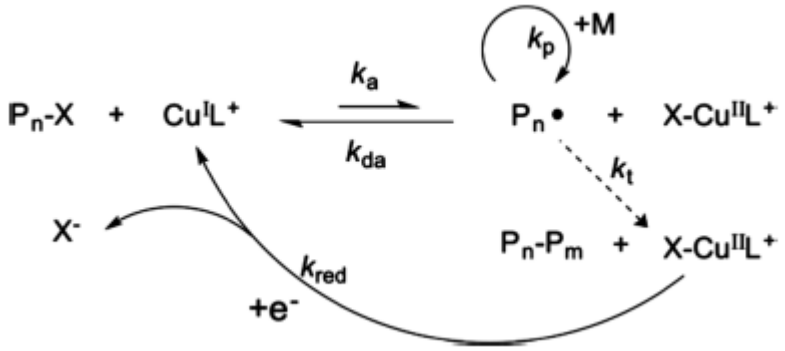

Figure 1.9 *Mechanism for Electrochemically Mediated ATRP (eATRP).* [46]

The high level of control achieved during eATRP can mainly be attributed to the level of voltage, current or charge applied during the process. For example, applying an increasingly negative over-potential to the system will lead to a higher concentration of the activator form of the transition metal catalyst (Cu^IL^+) and therefore a faster rate of polymerisation. Higher levels of catalyst present during eATRP have also shown faster rates of polymerisation.[47] However, the rate of polymerisation during eATRP will also depend on the choice of ligand and concentration of catalyst. More active ligands have been shown to give faster rates of polymerisation and higher levels of conversion due to larger K_{ATRP} values.[48]

1.2 Electroanalytical Methods

In analytical chemistry, electrochemical methods can be used to study an analyte by measuring the potential and/or current generated whilst it is within an electrochemical cell containing electrolyte(s) and electrode(s). The electrochemical cell setup will depend on the nature of the experiment being performed, as explained in the following sections.

1.2.1 Potentiometry

Potentiometry is a passive electroanalytical method capable of quantifying the concentration of an analyte in a solution by the measurement of a potential difference (in volts) between a reference and indicator electrode. The system is said to be in equilibrium as there is no net electrochemical reaction and thus no flowing current. For an overall electrochemical cell reaction:

$$bW + cX \rightleftharpoons dY + eZ \tag{1.1}$$

The potential, *E*, measured will be representative of the redox reactions occurring at the two electrodes in accordance with the Nernst-equation:[49]

$$E = E_0 - \frac{RT}{nF} \ln \frac{a_Y{}^d a_Z{}^e}{a_W{}^b a_X{}^c} \tag{1.2}$$

where E_0 is the standard rate constant, R (J K^{-1} mol^{-1}) is the molar gas constant, T (K) is the temperature, n is the number of moles of electrons transferred, F is Faraday's constant (96485 C mol^{-1}) and a is the activity of the chemical species involved, given by:

$$a = \gamma C \tag{1.3}$$

where γ is the activity coefficient and C is the concentration. Activity is a measure of the "effective concentration" of a species in solution, with the activity coefficient used to account for deviations from thermodynamic ideal behaviour (i.e. non-zero enthalpy change and volume variation with solution mixing). However, low concentrations of solute will behave ideally as the concentration of the solvent tends toward purity. Henceforth, under these circumstances the Nernst-equation can be used in terms of concentration alone as the activity coefficient tends towards 1.[50]

Reference electrodes employed in electrochemical cells have their own inherent stable potential which remains constant regardless of solution conditions. Henceforth, in potentiometry they are used to verify the potential of the other half cell and thus determine the concentration of the ion of interest.[51]

The ability of potentiometry to simply determine ion concentration has been utilised in the fabrication of a number of ion-sensitive electrodes (ISEs).[52] Figure 1.10 shows a typical structure of the widely-used pH glass electrode, which is made of a doped glass membrane sensitive to hydrogen ions. pH is defined in accordance to the equation:

$$pH = -\log\left(a_{H^+}\right) \tag{1.4}$$

Henceforth, the potential difference produced across this glass membrane in the presence of hydrogen ions can be related to their concentration, thus allowing pH to be measured.[53]

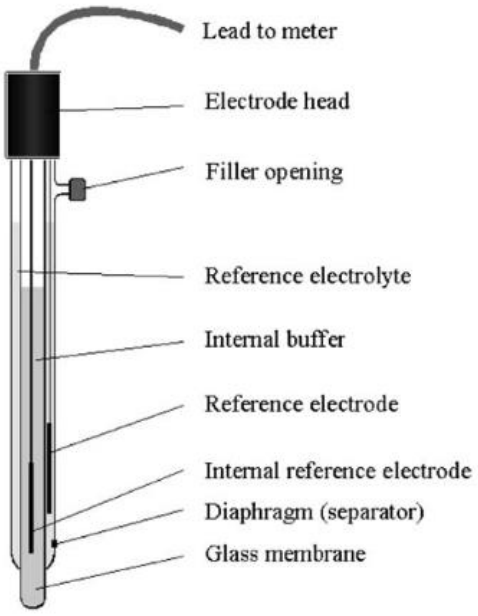

Figure 1.10 *Schematic of a standard pH glass electrode.*[53]

1.2.2 Dynamic Electrochemistry

In dynamic electrochemistry, the usual equilibrium of a redox couple or ion partioning or adsorbing at an electrode-solution interface is disturbed by the application of overpotential. This applied potential will drive the reaction towards either net oxidation or net reduction, resulting in net electron transfer and thus generating a measureable faradaic current. Figure 1.11 shows a general three electrode electrolytic cell which would typically be employed during dynamic electrochemistry.[49]

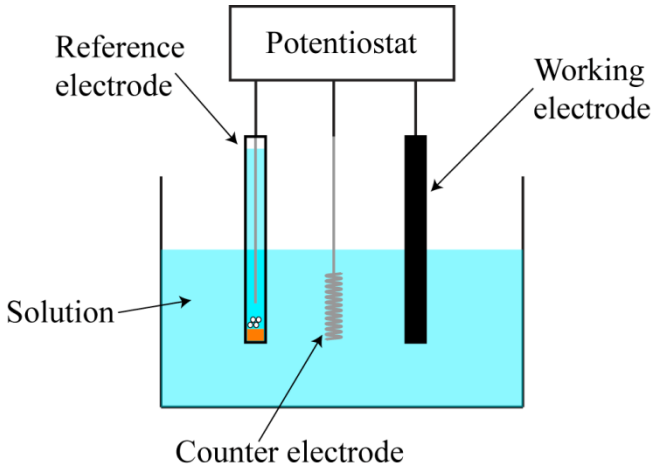

Figure 1.11 *Diagram of a typical three electrode electrolytic cell.*

Potential is applied between the working and reference electrode via the potentiostat. The resulting transfer of electrons at the surface of the working electrode thus generates a measurable current (*i*). If the current measured is sufficiently large (i.e. µA and above), a counter electrode is required to stop the polarisation of the reference and to counteract the effect of ohmic drop (*i*R). This occurs when the resistance, R, associated with passing current through the electrodes, solution, wiring and electrode-solution interface within the electrochemical cell becomes too great. High resistance leads to some of the applied potential being used to pass current through the reference electrode instead of the working electrode. This in turn causes the applied potential and the potential experienced at the working electrode to become unequal, leading to reduced

current flow. The potentiostat therefore acts to apply an equal opposing current (-*i*) to the counter electrode, ensuring that current flows efficiently between the working and reference electrode.[49] Ohmic drop effects can also be counteracted by adding a high concentration of inert salt (background electrolyte) to ensure that solution resistances remain low.[54]

1.2.2.1 Mass Transport- Diffusion, Convection and Migration

The faradaic current that arises from electron transfer at the electrode-solution interface is governed by equation 1.5:[49]

$$i = nAFj \tag{1.5}$$

where n is the number of electron transferred in the faradaic process, A is the surface area of the working electrode (cm^{-2}), F is Faraday's constant (96485 C mol^{-1}) and j is the flux (mol cm^{-2} s^{-1}). Flux of a chemical species to the surface of an electrode is directly proportional to the rate of reaction at the electrode surface, with the process illustrated in Figure 1.12.

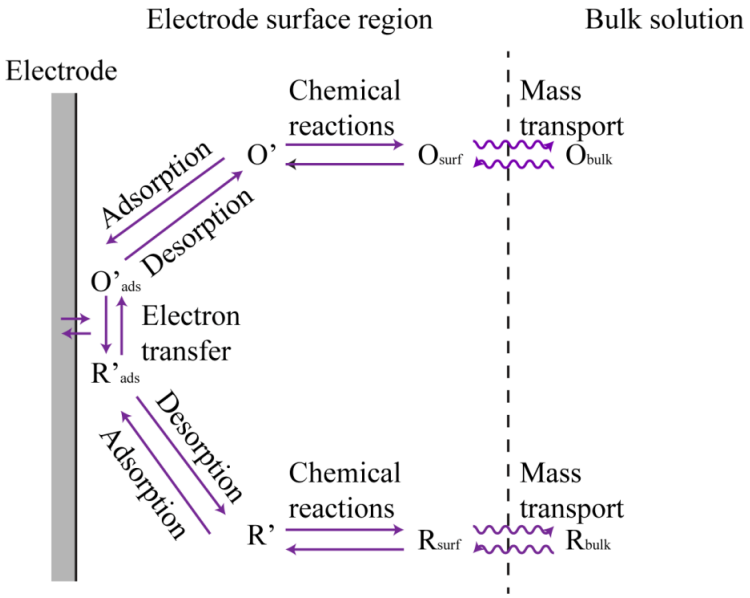

Figure 1.12 *Illustration of heterogeneous electron transfer and mass transport at the surface of an electrode.*[49]

The rate of electron transfer k_r (cm s^{-1}) will become the rate limiting step so long as the rate of mass transport k_t (cm s^{-1}) is sufficiently higher.

There are three means of mass transport of a chemical species to an electrode-solution interface prior to faradaic electron transfer: diffusion, convection and migration. The combined influence of these processes determines k_t, with each process discussed as follows:

Diffusion. This is the net movement of a chemical species down a concentration gradient. When a species is oxidised or reduced at the surface of a working electrode, the surface concentration of the original species C_s is depleted in comparison with the bulk concentration C^*. Material then moves down the resulting concentration gradient from bulk solution to the surface of the working electrode to counteract the imbalance in concentration. Figure 1.13 illustrates this process, with δ representing the length of the diffusion layer that develops as a reducing or oxidising potential is applied at the working electrode.

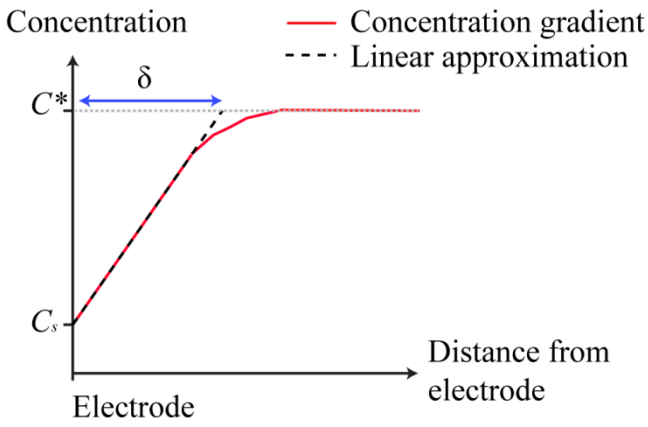

Figure 1.13 *Diffusion layer at an electrode in 1D.*[49]

The geometry of the working electrode will determine the characteristics of the diffusion field that develops. Macroelectrodes will have linear diffusion profiles

whereas microelectrodes and nanoelectrodes will have radial diffusion profiles, as shown in Figure 1.14.

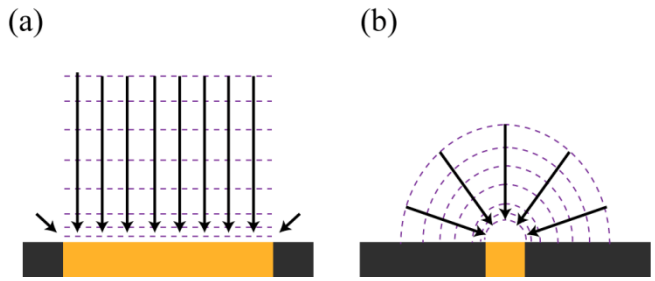

Figure 1.14 *Radial diffusion profiles for (a) a macroelectrode and (b) a micro/nano electrode.*

The radial diffusion profiles experienced at micro/nano electrodes significantly augments the diffusional flux of species arriving at the surface of the electrode per unit area per unit time, enhancing k_t and thus increasing the chance that k_r will control the rate of reaction at the electrode surface. In comparison, the linear diffusion profiles of macroelectrodes entail a reduced diffusional flux of species. Henceforth, k_t will be lower than k_r and thus the reaction at the electrode surface will be diffusion-controlled.[49]

Convection. This is the movement of a chemical species in response to a temperature, pressure or mechanical gradient. In solution, convection is generally induced by heating, flow or stirring.

Migration. This is the movement of charged chemical species due to the influence of a nearby electric field.

To simply quantify mass transport, it is often desirable to minimise the effects of both convection and migration by experimental design. Convection can be minimised by ensuring that the electrochemical experiments are maintained at room temperature (298 K) and pressure (1 atm) whilst ensuring that the solution remains static. To nullify migration effects, an excess of inert salt (background electrolyte, usually KNO_3 or KCl)

can be added to solution. This shrinks the diffuse layer at the electrode-solution interface (see section 1.2.2.2), reducing the change in potential to within the electron tunnelling distance and thus screening the faradaic species from the electric field until it has diffused to the electrode surface.[49]

1.2.2.2 The Electrode-Solution Interface

When a solid object (such as an electrode) is placed into an electrolyte solution, a structure called an electrical double layer will form whereby counter ions assemble at the surface to balance its charge. Figure 1.15 illustrates the two parallel layers which comprise the double layer: the Inner Helmholtz Plane (IHP) and Outer Helmholtz Plane (OHP).

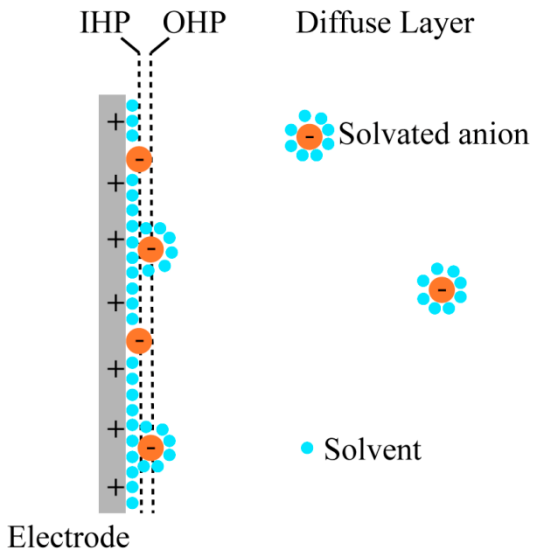

Figure 1.15 *Diagram of the electronic double layer at an electrode-solution interface for a positively charged electrode.*[49]

The IHP is designated by the distance of closest approach of a surface-adsorbed ion, whereas the OHP is designated by the distance of the closest approach of a solvated ion. Unlike the adsorbed ions of the IHP, the movement of solvated ions at the OHP is less restricted, hence the "diffuse" nature of the double layer.

The structure of the double layer is fundamentally a molecular dielectric, allowing it to store charge electrostatically. Therefore, when the potential at the electrode is altered the charge on the electrode surface also changes, causing the double layer to rearrange and thus inducing a capacitive current. These capacitive currents contribute to the overall faradaic current recorded, with larger electrodes and faster potential scanning rates inducing larger background capacitive currents.[49]

1.2.2.3 Linear and Cyclic Voltammetry

Voltammetry is one of the simplest electroanalytical methods used and involves the measurement of current as the potential at a working electrode is changed with time.[49] Typically, the potential is swept linearly (using a designated scan speed in V s^{-1}) from the point at where there is no electron transfer to a point past E_0. Oxidation or reduction of the analyte at a particular potential will be recorded as either a positive anodic peak (oxidation) or negative cathodic peak (reduction). In the case of linear sweep voltammetry (LSV) only a forward sweep is carried out, whereas in cyclic voltammetry (CV) both forward and reverse sweeps in potential are applied. Figure 1.16 illustrates how potential is varied with time and a typical current response for a disk macroelectrode during a cyclic voltammetry experiment.

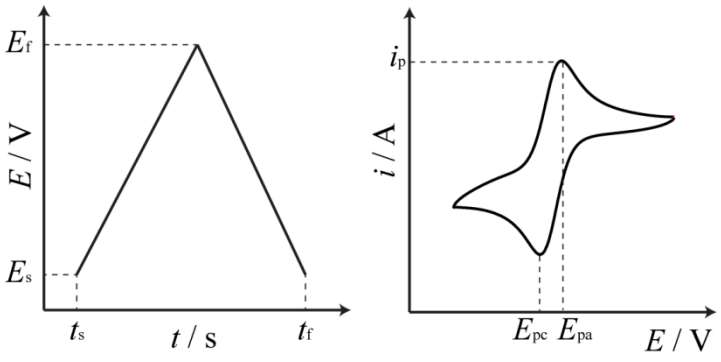

Figure 1.16 *Voltage versus time applied (left) and current versus voltage measured (right) during a typical cyclic voltammetry experiment.*

The application of increasing potential at the working electrode during the forward sweep causes oxidation of the analyte and thus rising current as electrons are transferred to the electrode at an increasing rate. Chemical species diffuse down the concentration gradient as material is oxidised (see Figure 1.12) until a point is reached where diffusion can no longer keep up with rate of electron transfer. This causes current to peak (i_p) at E_{pa} and then decay. When the direction of the potential sweep is subsequently reversed, species that were previously oxidised are reduced in a similar manner (for a reversible reaction). This gives rise to a reduction peak at E_{pc}.

Cyclic voltammograms recorded using ultramicroelectrodes (UMEs) (diameter ≤ 25 μm) will differ in appearance from those recorded using macroelectrodes due to enhanced diffusional flux (see section 1.2.2.1). Instead of reaching a peak current and then decaying, the current will rise and reach a steady state before retracing the curve on the reverse potential sweep as shown in Figure 1.17.

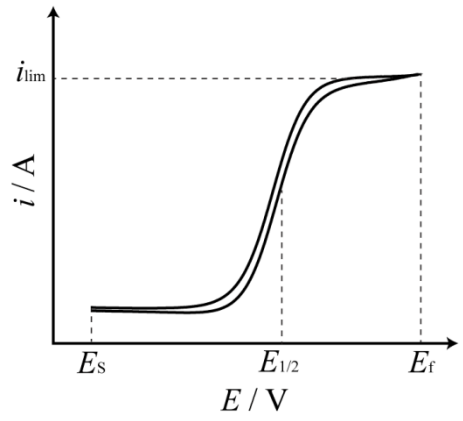

Figure 1.17 *Cyclic voltammogram recorded for an oxidative process using a disk microelectrode, where i_{lim} is the steady state current.*

Equation 1.6 relates the electrode radii and species concentration to the steady state current (or limiting current, i_{lim}):[49]

$$i_{lim} = 4nFDC^{*}a \tag{1.6}$$

where n is the number of moles of electrons transferred, F is Faraday's constant (96485 C mol^{-1}) D is the diffusion coefficient (cm^2 s^{-1}), C^* is the bulk concentration (mol cm^{-3}) and a is the radius of the micro/nano electrode (cm).

1.2.2.4 Differential Pulse Voltammetry

Another voltammetric method often used in electroanalysis is differential pulse voltammetry (DPV). Unlike linear and cyclic voltammetry, potential is applied as a series of regular pulses as illustrated in Figure 1.18.[49]

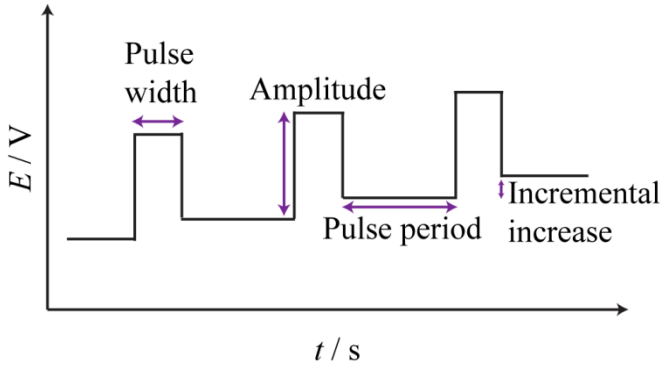

Figure 1.18 *Illustration of the staircase voltage pulses that take place during differential pulse voltammetry of an oxidative process.*

During DPV current is sampled before and after each potential step, unlike LSV where current sampling is constant. This decreases the contribution of charging current, minimising the background capacitive current from the overall current recorded. Therefore the differential current will peak at the point where an LSV would experience its greatest gradient change, as illustrated in Figure 1.19.

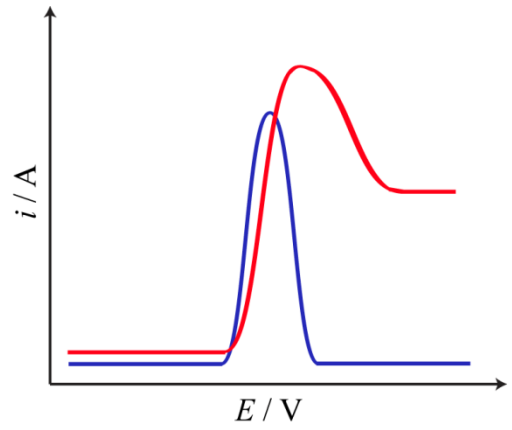

Figure 1.19 *Comparison between a typical differential pulse voltammogram (-) and a linear sweep voltammogram (-) for an oxidative process.*

1.2.3 Electrochemical Impedance Spectroscopy

The application of potential and resulting flow of current passed through an electrical circuit will result in an electrical resistance *R*, which is the ability of the circuit to resist current flow. Ideal resistance is a ratio between voltage *E* and current *I* and is defined by Ohm's Law:[55]

$$R = \frac{E}{I} \tag{1.7}$$

Although Ohm's Law is useful, it is limited to simple electronic systems (i.e. an ideal resistor) where resistance is independent of frequency and AC current/voltage signals are in phase with each other. For multifaceted electronic systems, the presence of other circuit elements (e.g. capacitors) and their associated behaviours must be taken into account.

We can characterise more complex electrochemical systems using electrochemical impedance spectroscopy (EIS). In EIS, a small AC voltage signal (typically 5-10 mV to ensure that the cell's response will be pseudo-linear) is applied. This produces a current signal that will be either in or out of phase with the potential depending on which

frequencies the circuit acts as either an ideal resistor (in phase, 0°), an ideal capacitor (out of phase, 90°), or somewhere in-between, as shown in Figure 1.20.[49]

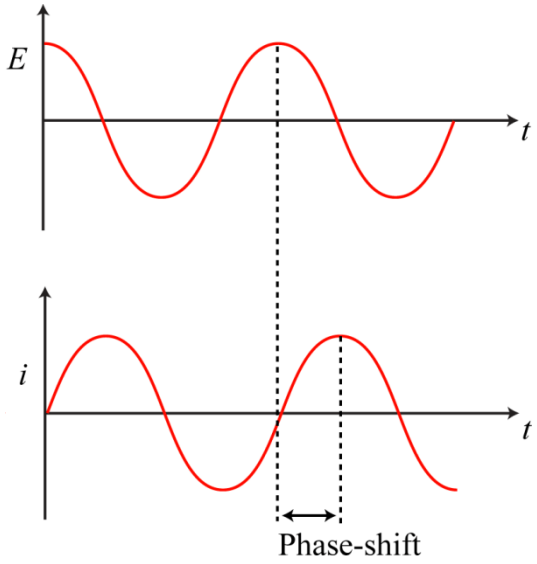

Figure 1.20 *Illustration showing the phase shift between voltage and current which takes place when an AC potential is applied to a system.*

The time-dependent excitation signal can be expressed as:

$$E_t = E_0 \sin(\omega t) \tag{1.8}$$

where E_t is the potential at time t, E_0 is the signal amplitude and ω is the radial frequency. The radial frequency ω (rad.s^{-1}) is related to frequency f (Hz) by:

$$\omega = 2\pi f \tag{1.9}$$

Therefore, we can assume that the frequency applied during the EIS will affect the excitation signal. So long as the system remains pseudo-linear, the time-dependent response signal will be shifted in phase (ϕ) and amplitude compared to I_0:

$$I_t = I_0 \sin(\omega t + \phi) \tag{1.10}$$

The excitation and response signals can be combined in a form analogous to Ohm's Law to calculate the impedance Z in ohms (Ω):

$$Z = \frac{E_t}{I_t} = \frac{E_0 \sin(\omega t)}{I_0 \sin(\omega t + \phi)} = Z_0 \frac{\sin(\omega t)}{\sin(\omega t + \phi)} \tag{1.11}$$

Impedance is therefore the frequency-dependent ability of an electronic system to oppose the flow of electrical current.[56]

As mentioned previously, electronic systems will contain circuit elements other than ideal resistors. Capacitors in an electronic circuit will charge and discharge with the application of an AC voltage signal, with the capacitance varying with the frequency of the AC signal. Like resistors, capacitors will also have some opposition to current flow in an AC circuit. This is known as capacitive reactance, X_C (Ω):[49]

$$X_C = \frac{1}{2\pi fC} = \frac{1}{\omega C} \tag{1.12}$$

where f is the frequency (Hz) and C is the capacitance (Farads). The capacitive reactance of a capacitor is for any given capacitance is therefore inversely proportional to the frequency. At high frequencies the rapid voltage change across the capacitor leads to fast charging rates, allowing current to flow more easily. At low frequencies, capacitors will become fully charged and block current flow, hence their high reactance.

For a resistor and capacitor in series we can combine the resistance and capacitive reactance to calculate impedance Z:[55]

$$Z = R + \frac{1}{j\omega C} \tag{1.13}$$

where complex number $j = \sqrt{-1}$ and represents the imaginary part of impedance which contains both phase and magnitude information.

1.2.3.1 Bode and Nyquist Plots

There are two approaches which can be used to present impedance data: the Bode plot and the Nyquist plot. The Bode plot, which is arguably the simpler of the two, plots log Z against both ϕ and log ω whereas the Nyquist plot displays imaginary impedance against real impedance. Both types of plot are illustrated in Figure 1.21, which shows typical plots for a Randles circuit (which describes the double layer at an electrode experiencing linear diffusion; see section 1.2.3.2 for more detail).

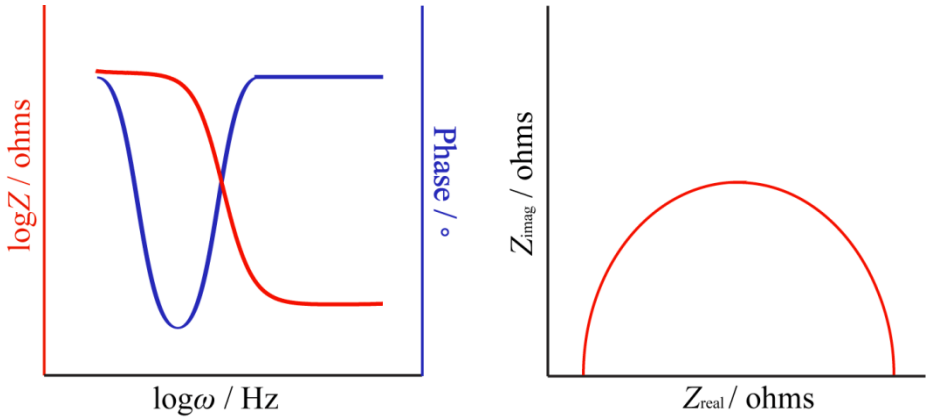

Figure 1.21 *Examples for a Randles circuit of a Bode plot (left) and Nyquist plot (right).*

The shapes of both plots can provide information on the magnitude of the solution resistance and charge-transfer resistance. The magnitude of log Z at high frequencies on the Bode plot specifies the solution resistance, whereas the magnitude of log Z at low frequencies is a combination of solution and charge-transfer resistance.[57] Magnitude of log Z where the gradient is -1/2 indicates the frequencies where Z is the capacitive reactance. As mentioned previously, the phase on the Bode plot indicates at which frequencies the circuit behaves more like a resistor (0°) or a capacitor (90°).

The shape of the Nyquist plot denotes the assorted components of which the impedance of the system is comprised and can be used to deduce both phase angle α and magnitude of total impedance. Figure 1.22 illuminates how different components of a Nyquist plot

can be used to characterise the assorted rate determining steps for a redox process at an electrode.

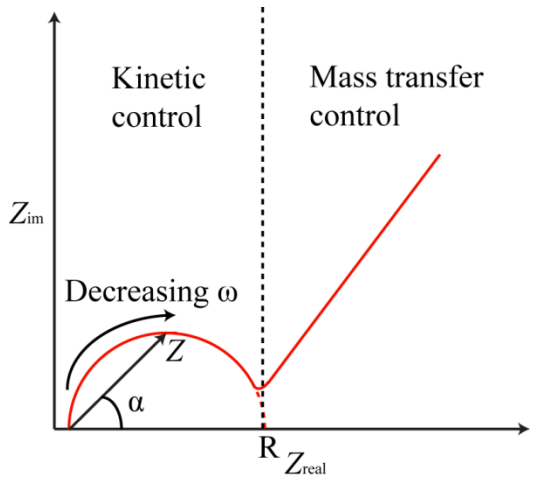

Figure 1.22 *Illustration of a typical Nyquist plot showing the relationship between applied frequency and type of control.*[49]

The greater the phase angle on the Nyquist plot the greater the imaginary impedance, therefore imaginary impedance is governed by the capacitance of the double layer. As double layer capacitance is very small at high frequencies, the solution resistance dominates and is therefore found at the highest frequency intercept of the curve with the real impedance. As the frequency decreases, double layer capacitance increases and the charge-transfer resistance begins to dominate total impedance, causing the imaginary impedance to drop off. The real impedance at this point will be a combination of the solution resistance and the charge-transfer resistance, meaning that the diameter of the semicircle corresponds with the charge-transfer resistance.[49]

Depending on the system being studied, very low frequencies can show a feature known as Warburg impedance. This is represented as a straight line with a phase angle of 45 ° and relates to semi-infinite linear diffusion to a large planar electrode. Therefore, we can assume that at high frequencies the system is under kinetic control whereas at low frequencies mass transport processes dominate.[49]

1.2.3.2 Circuit Diagrams

To effectively understand data collected during EIS, we can breakdown the system monitored into individual electrical components. This is achieved by building circuit diagrams; values are applied to each component in the circuit diagram until it can successfully simulate previously collected Bode and/or Nyquist plots. A simple Randles circuit, used to simulate an interfacial electrochemical reaction at a large planar electrode, is displayed in Figure 1.23.[58]

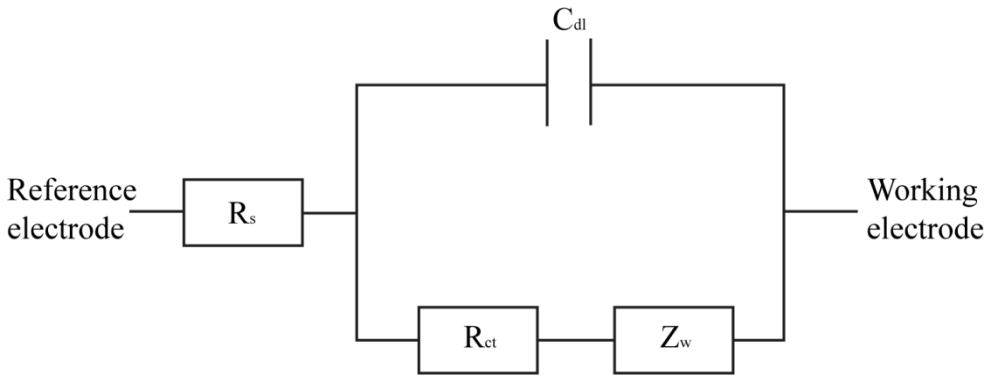

Figure 1.23 *The Randles Circuit.*

R_s represents the bulk solution resistance, R_{ct} is the resistance to charge-transfer at the electrode surface, C_{dl} is the capacitance of the double layer and Z_W is the Warburg impedance associated with the mass-transfer of the electrochemically active species.

For less ideal systems, we can replace the capacitor component with a constant phase element (CPE). This allows the circuit diagram to model the behaviour of imperfect dielectrics which are between being an ideal resistor and ideal capacitor.[55]

1.2.3.3 Previous Studies Using EIS

EIS has been used to investigate processes within the fields of biology,[59, 60] energy,[61, 62] electronics[63] and materials manufacturing.[64] In particular, EIS is most frequently used to examine corrosion processes.[65, 66] These studies commonly involve the evaluation of polymer coatings for metal corrosion protection.[67, 68]

1.3 Liquid/liquid Interfaces

Reactions that take place at an immiscible liquid/liquid interface are prevalent across a wide variety of systems, from the biological to the industrial [69, 70]. For example, phase transfer catalysis[71], metal extraction[72], nanoparticle synthesis[73], classes of electroanalytical sensors[74] and biomimetic systems[75] all rely on understanding physicochemical process at liquid/liquid interfaces. The interactions that take place at liquid/liquid interfaces have been studied using a variety of techniques, including electroanalytical methods.[76-81] These studies commonly involve but are not limited to the interface between two immiscible electrolyte solutions. In this section, the structure of liquid/liquid interfaces and the methodology behind some of the techniques used to analyse them will be reviewed.

1.3.1 Structure of the Liquid/liquid Interface

The structure of the liquid/liquid interface can be thought of as a more complex version of the double layer at the surface of a charged solid (see section 1.2.3.2 for details). The liquid/liquid interface will be comprised of two double layers, which unlike the solid-solution interface will both interact with each other and allow the passage of ions from one side of the interface to the other.

Defining the interaction at the interface between the two double layers has proved to be contentious, with several different theories on their arrangement being put forward (see Figure 1.24). Verwey and Niessen were the first to describe the interface between two immiscible electrolyte solutions (ITIES) as two non-interacting diffuse layers, one at each side of the interface.[82] This model was subsequently extended by Gavach *et al.*, who introduced an ion free transition layer of oriented solvent molecules at the ITIES analogous to the inner Helmholtz layer at a solid-liquid interface.[83] An alternative

model was postulated by Girault and Schiffrin, who proposed that the interface will be comprised of a mixed solvent layer.[84] Subsequent molecular dynamic simulations by Benjamin *et al.* have suggested that capillary waves will be present at the surface of the liquid/liquid interface, leading to an overall rough surface.[85] This theory was then generalised to take into account the non-linear polarization of the double layer, which has helped to explain the effect of potential difference and ionic strength on interfacial capacitance at the liquid/liquid interface.[86] Neutron reflectivity experiments carried out at the 1,2-dichloroethane/aqueous potassium hydroxide interface have since been performed which agree with theoretical predictions.[87]

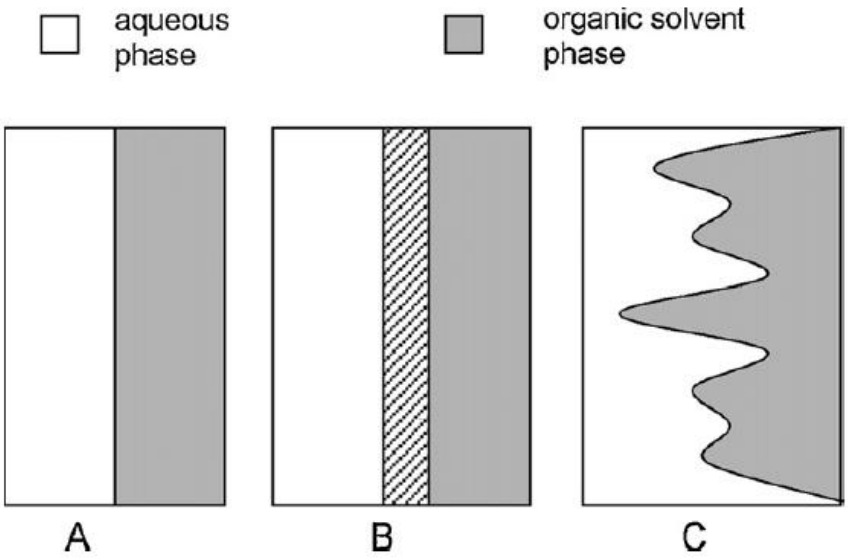

Figure 1.24 *Structure of the ITIES: (A) Verwey-Niessen model, (B) modified Verwey-Niessen model with an ion-free layer or mixed solvent layer and (C) capillary wave model.*[88]

1.3.2 Formation of Membranes at the Liquid/liquid Interface

Membranes at the liquid/liquid interface play important roles in cell biology, catalysis and interfacial polymerisation. These systems can be investigated using model liquid/liquid interfaces where membranes are either inserted at the interface or allowed to grow, thus utilising the defect-free interface to determine reaction kinetics.

The assembling of phospholipids at liquid/liquid interfaces can produce useful models for biomembranes. For example, Méndez *et al.* have used ion-transfer voltammetry (see section 1.3.3) to examine the disruption of phospholipid monolayers between an electrode supported water/1,2-dichlorethane interface by the antimicrobial peptide melittin.[89]

Catalysis at liquid/liquid interfaces has been explored in a wide range of studies.[90-92] For example, enhancement of ion transfer has been observed following the assembly of cobalt and cobalt-boron nanoparticle films at a liquid/liquid interface.[93] Due to the catalytic nature of certain metallic and semiconducting nanoparticle films, their electrodeposition at liquid/liquid interfaces has also been extensively investigated.[77, 94, 95] The most likely mechanism suggested for film formation is the nucleation of film growth from initial particles formed on the interface (aka progressive nucleation).[96]

Interfacial polymerisation at liquid/liquid interfaces has been studied using a number of electroanalytical methods. One approach is to use ion-transfer voltammetry (see section 1.3.3) to monitor the as a polymerisation reaction across an interface progresses.[97] Voltammetric techniques have also been used to measure the doping levels in electropolymerised terthiophene.[98] The electro-polymerisation of aniline and pyrrole composites at the ITIES incorporating carbon nanotubes has also been examined using cyclic voltammetry, impedance spectroscopy and Raman spectroscopy.[99, 100]

1.3.3 Micropipettes

Processes that take place at a liquid/liquid interface can be studied using electroanalytical techniques through the formation of a micro-interface at the tip of a micropipette.[101-105] Micropipettes (with a radius of between 1 and 50 μm) are typically fabricated by pulling glass capillaries to a fine point. The micropipette is then filled with either the organic or aqueous phase, which is subsequently immersed into the bulk

solution of the other phase to form a micro-interface at the tip of the pipette (see Figure 1.25). This interface can be transformed into a "working electrode" by inserting a silver wire into the pipette. Another electrode is then placed into bulk solution to act as the reference electrode, thus potential can be applied between the two electrodes to drive ion transfer or electron transfer across the interface.

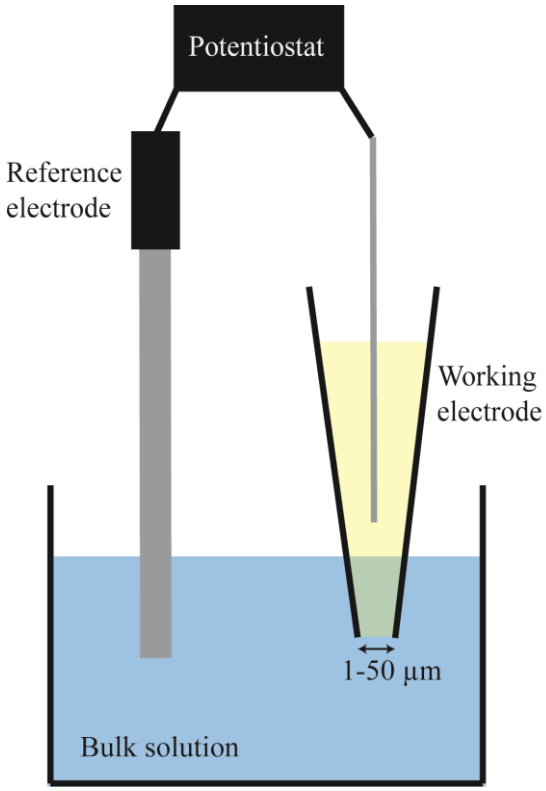

Figure 1.25 *General setup for electroanalysis across a liquid/liquid interface formed at the mouth of micropipette.*

There are a few extra considerations that must be taken into account for effective electroanalysis with liquid/liquid interfaces. Supporting electrolytes must be placed in each phase to ensure that resistance and migration effects do not impede ion transport from one phase to another.[106] These supporting electrolytes must also be carefully chosen to ensure that any ions of interest do not transfer outside the potential window. To achieve wide potential windows at liquid/liquid interfaces, the electrolyte in the organic phase should be a large, organic and highly hydrophobic. In parallel, the inorganic electrolyte for the aqueous phase should be small with highly localised charge

to maximise hydrophilicity.[107] Micropipettes must also be silanized to stop water leaking into the organic phase, thus ensuring that the area of the interface is remains well defined.[108] When the organic phase is inside the pipette the inside walls must be silanized, whereas when the organic phase is outside the pipette it is the outside walls that must be silanized.

One major characteristic observed when using micropipettes for electroanalysis is the change in the type of diffusion at the liquid/liquid interface depending on the direction of ion flow, as shown in Figure 1.26. When ions transfer from inside the pipette to bulk solution, their confinement within the shaft of the capillary will make the diffusion field towards the interface predominantly linear. In the reverse case where ions transfer from bulk solution to the interface, a hemispherical diffusion zone will form around the mouth of pipette.[109]

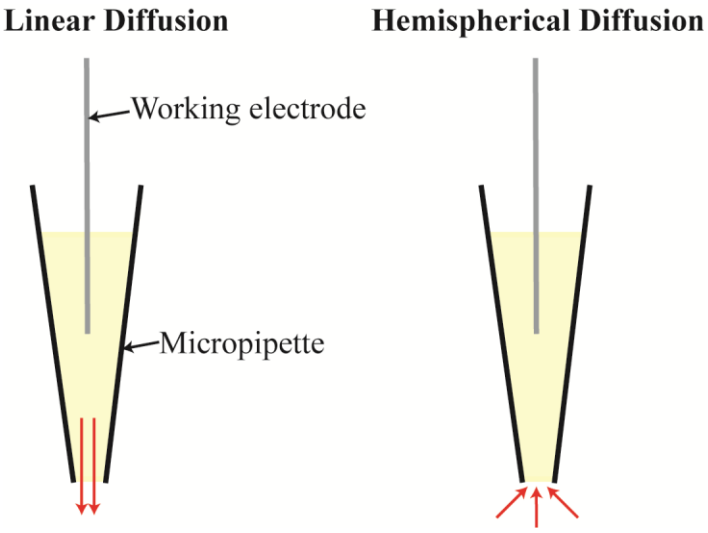

Figure 1.26 *Illustration showing the two types of diffusion at the tip of a micropipette.*

The direction of ion flow can be readily perceived during cyclic voltammetry experiments, with linear diffusion of ions out of the micropipette generating diffusion-limited current and hemispherical diffusion of ions into the micropipette generating steady-state current. The direction that ions will flow across the interface will be

dependent upon the potential applied to the working electrode. When a positive potential is applied to the working electrode, negative ions flow into the micropipette and positive ions are repelled out. Conversely, when a negative potential is applied positive ions will flow into the micropipette and negative ions will be repelled out. The magnitude of the current generated from ion transfer will be dependent on the area of the interface, with larger areas producing higher currents. Faster scan rates during cyclic voltammetry will also produce higher currents, as ions can diffuse to the interface more quickly due to the thinner diffusion field.

As mentioned previously, it is important to select suitable electrolytes for each phase to ensure that the potential window is wide enough to clearly assign the transfer of any other ions of interest. The width of the potential window will be constrained by the potentials at which the supporting electrolytes transfer across the interface. A typical cyclic voltammogram of a potential window at the liquid/liquid interface involving only supporting electrolytes is shown in Figure 1.27. The negative end of the potential window is controlled by the transfer of ions A^+ and/or D^- and the positive end of the potential window is controlled by the transfer of ions B^- and/or C^+.

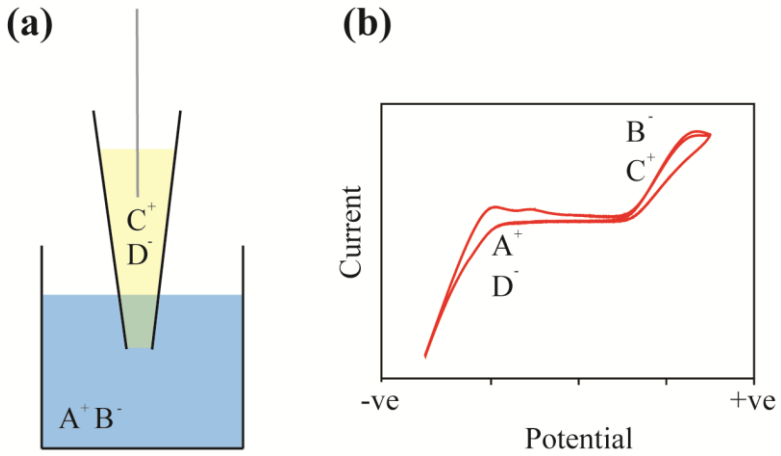

Figure 1.27 *(a) Diagram showing the location of ions in each liquid phase; (b) a cyclic voltammogram of the potential window showing ion transfer across the liquid/liquid interface at extreme potentials.*

1.3.4 Microelectrochemical Measurements at Expanding Droplets (MEMED)

Electrochemistry has previously been used to characterise the processes taking place at an oil droplet-water interface. Microelectrochemical measurements at expanding droplets (MEMED) has been shown to be a powerful technique when quantifying the chemical processes that take place at a liquid/liquid interface.[110-114] Figure 1.28 shows a general schematic of the MEMED setup.

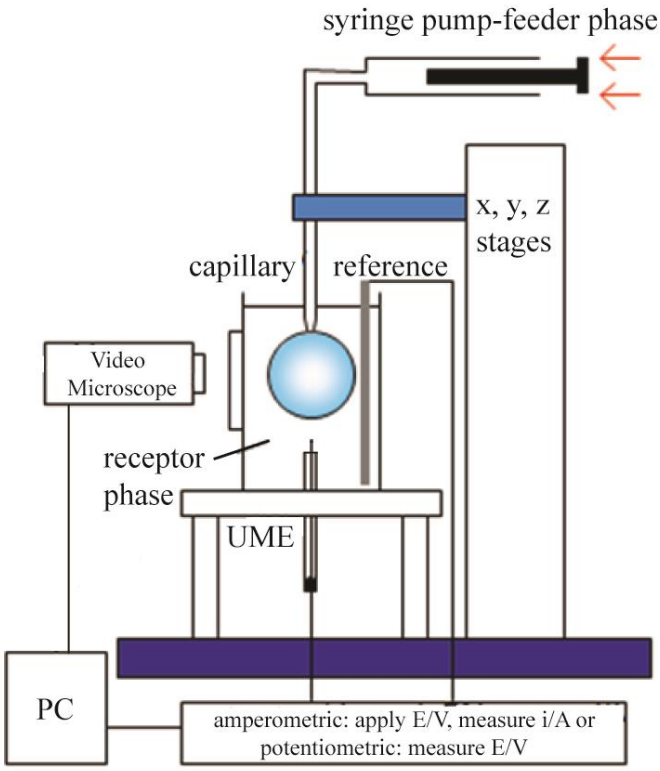

Figure 1.28 *Schematic of the general setup for MEMED, showing the scenario where the droplet phase is denser than the receptor phase.*

In brief, a glass capillary is connected to a syringe containing the feeder phase. This capillary is then positioned using manual x, y, z stages until it is directly opposite a UME in the receptor phase (note: if the feeder phase is less dense than the receptor phase the positions of the capillary and the UME must be reversed). Using a high-precision syringe pump, the feeder phase is passed out of the capillary into the receptor phase, forming a droplet that expands towards the UME. Any analyte of interest within

the feeder phase will be transported out of the droplet during expansion and eventually detected by the UME operating in either potentiometric or amperometric mode. By recording these current or voltage measurements alongside time-stamped photographs taken by a video microscope, analyte concentration can be coupled to electrode-droplet separation and thus the kinetics of interfacial transfer can be calculated.

1.4 Scanning Probe Microscopy (SPM)

Scanning probe microscopy (SPM) encompasses a collection of techniques capable of measuring surface topography and surface properties. SPM techniques commonly employ piezoelectric actuators to finely control the movement of a probe across a surface. The probe is typically moved in a raster scan, with the data collected at discrete points during the scan used to build images of topography and other surface features. The resolution of these images will depend not only on the number of data points collected during the scan but also on the sharpness of the probe (i.e. the sharper the probe the better the resolution).

The values recorded during SPM will also depend on the mode of operation, which will be based on either maintaining the probe at constant distance above the surface or using a feedback loop to maintain a constant interaction between the probe and the surface. Although constant distance mode will lack any potential feedback artefacts, more care must be taken to ensure that the probe does not crash into the sample surface. Therefore, so long as feedback artefacts are minimised it is often more desirable use constant interaction mode when using SPM techniques. The two SPM techniques used in this thesis both utilise feedback loops to ensure well-controlled interaction between the probe and the surface and are discussed below.

1.4.1 Atomic Force Microscopy (AFM)

Atomic force microscopy (AFM) is an SPM technique capable of tracing surface topography on the nanometre scale to form 3D profiles of a surface. It achieves this by measuring the force between a sharp probe (<10 nm) and surface. The probe is mounted on a flexible cantilever, which allows fine movement of the probe tip in the z-direction. As the AFM tip touches the surface, the small force between the probe and surface can be measured (ranging between *ca.* 10^{-12}–10^{-7} N).[115] This force is dependent on both the spring constant (stiffness) of the cantilever and the distance between the probe and sample surface, as described by Hooke's Law:

$$F = -k \bullet x \tag{1.14}$$

where F is force (N), k is the spring constant (N m^{-1}) and x is the cantilever deflection (m). The spring constant will depend on tip length, material (typically silicon or silicon nitride) and shape.

So long as the spring constant of the cantilever is less than that of the surface, contact with the surface should cause it to bend. AFM instrumentation uses a "beam bounce" method to monitor this deflection, as shown in Figure 1.29. As the cantilever is scanned over the sample, a laser beam is bounced off it onto a photodiode detector. The photodiode is split into sections, proving positional sensitivity to the movement of the laser across its surface. This positional information is relayed to the electronics of the AFM, which register the position and deflection of the tip on the sample to build a topographical image of the surface.

Positional information is also used to instigate the feedback mechanism to maintain a constant force between the tip and the sample. A set of piezoelectric positioners attached to the cantilever provide fine-tuned movement in the x, y and z direction. The piezoelectric element in the z-direction is used to continually adjust the position of the

cantilever to maintain constant tip deflection, thus ensuring constant interaction between the tip and the surface.

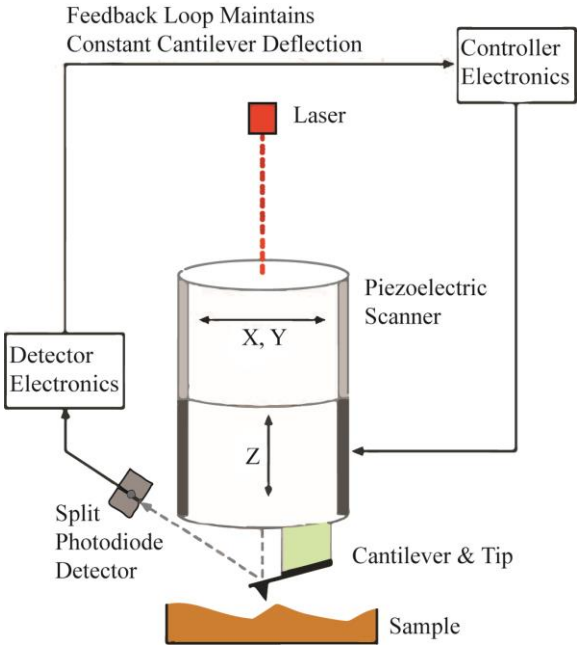

Figure 1.29 *Diagram of the general setup of an atomic force microscope. The displacement of the tip as it interacts with the sample will displace the position of the reflected laser beam onto the split photodiode detector, thus providing positional information and feedback.*

AFM can be used to measure long range interactions such as capillary forces,[116] chemical bonding,[117] electrostatic forces,[118] magnetic forces[119] and solvation forces.[120] However, more commonplace AFM techniques measure the Van der Waals (VdW) interactions experienced at shorter probe-sample distances. During contact with the sample, the probe primarily experiences repulsive VdW forces. This leads to the tip deflection described previously. As the tip is retracted away from the surface, attractive VdW forces become dominant. The type of VdW interaction experienced at the tip can be harnessed to yield different imaging modes during AFM, as shown in Figure 1.30.

There are three main types of imaging mode:

Contact Mode. The tip experiences repulsive VdW interactions, which cause tip deflection. This deflection is maintained using feedback loops to keep the force between

the tip and the sample constant. Constant mode AFM is beneficial for fast scanning of samples; however the higher forces can damage or deform softer samples.

Non-contact Mode. The tip oscillates above an adsorbed fluid layer on the surface (unless under vacuum or in an environmental chamber, in which case there is no fluid layer present). As it oscillates the tip experiences attractive VdW interactions, which will change the oscillation amplitude. This change in amplitude can be used within a feedback loop to maintain probe-sample force. Unlike contact mode, non-contact mode is suitable for delicate samples. However, surface contamination is likely to affect tip oscillation and images are generally lower quality resolution.

Intermittent (Tapping) Mode. This imaging mode is similar to contact mode, however in this mode the cantilever is oscillated at its resonant frequency. The probe will lightly "tap" the surface as it makes contact during the bottom swing of the oscillation. The oscillation amplitude is maintained to ensure that the deflection of the tip during each tap remains constant. Tapping mode allows for the high resolution imaging of samples that are delicate or loosely held to a surface. However, slower scan speeds are required and it is more difficult to image in liquids.

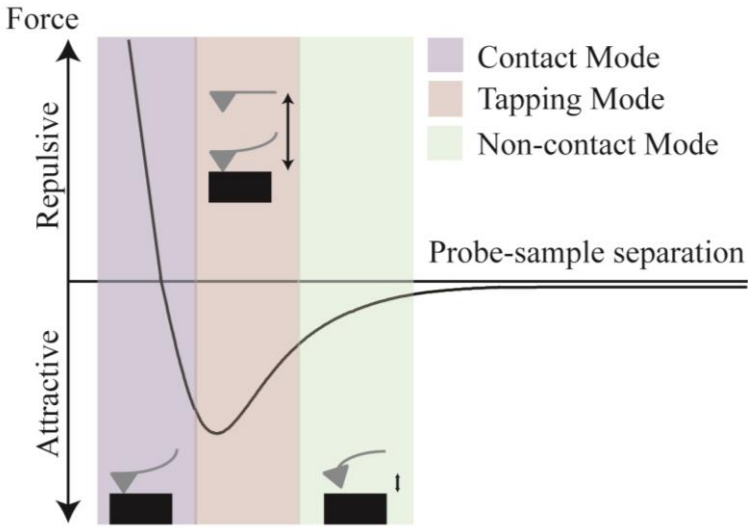

Figure 1.30 *Plot of force as a function of probe-sample separation.*

1.4.1.1 AFM for Polymer Imaging

AFM has been used to image polymer films formed on surfaces.[121-123] Due to their often delicate structure and predisposition to being dragged across the surface by a probe in contact mode, tapping mode AFM is the technique of choice when imaging surface-bound polymers.[124] AFM can be used to determine polymer film structure[125] and other characteristics such as suitable deposition parameters[126] and solvent-dependent phase-change.[127]

1.4.2 Scanning Electrochemical Cell Microscopy (SECCM)

Electrochemical SPMs (EC-SPM) have been developed to probe topography and other properties of surfaces. The simplest method of EC-SPM is scanning electrochemical microscopy (SECM),[128] which scans an electrode across a surface to study a particular electrochemical reaction. An alternative procedure for measuring electrochemical activity of a surface is through the formation of a defined droplet between a pipette and surface. This will define a "cell" area on the surface, thus removing the need to immerse the sample in bulk solution. Initial iterations of this approach include the scanning micropipette contact method (SMCM), which uses a micron sized micropipette to record localised electrochemical measurements within a droplet of equal geometry to the micropipette orifice.[129]

Although SMCM allows for meniscus-confined electrochemical measurements on a surface, it has no independent mode of feedback. Therefore, it is difficult to control tip-sample separation whilst measuring localised activity and as such can be prone to tip crash. By exchanging the single barrelled pipette for a dual barrelled "theta" pipette, as is the case in scanning electrochemical cell microscopy (SECCM, shown in Figure 1.31), the migratory current between barrels can be used for positional feedback on both conducting and non-conducting surfaces. When the electrolyte solution in the tip comes

into contact with a surface, the meniscus formed between them is deformed. This deformation will modulate solution resistance and thus DC current, giving rise to an AC current component that the tip does not experience when not in contact with the surface. Therefore, positional feedback is achieved by using an AC current set point to ensure that the electrochemical cell remains in contact with the surface. As well as depending on meniscus size and geometry, DC current will also be sensitive to the local conductance of a surface. Therefore, information on both sample topography and surface properties can be found from the measurement of *i*AC and *i*DC respectively.

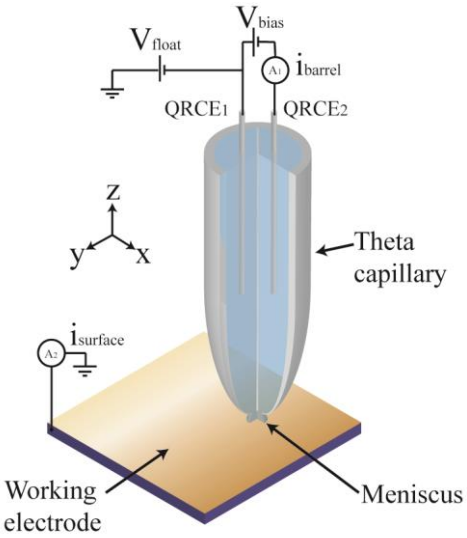

Figure 1.31 *Illustration of the SECCM setup. V_{bias} is applied between quasi-reference counter electrodes (QRCEs) in each barrel of the theta pipette, giving rise to barrel current (i_{barrel}). Positional feedback of the probe is based upon the alternating current component ($i_{barrel\ AC}$) generated as the probe meniscus is deformed during vertical oscillation. The surface of the working electrode is biased as the inverse of the average of the bias applied to each QCRE (-(V_2+V_1)/2). The surface current ($i_{surface}$) is measured with respect to the ground.*

Since it was first demonstrated by Ebejer *et al.*[130], the SECCM technique has been used to probe electron transfer on electrochemically-active surfaces such as basal plane graphite,[131, 132] carbon nanotubes,[133-136] gold nanoparticles[137, 138], platinum[139, 140] and boron doped diamond.[141] The technique has also been utilised to chemically pattern

surfaces[141, 142] and fabricate larger surface structures such as ZnO films[143] and conducting polymer wires.[144]

SECCM provides a number of advantages over other EC-SPM techniques such as SECM or its hybrids. As it is a non-contact technique, the range of surfaces that can be imaged is high. The fact that the probe comes into contact with the surface for only a short amount of time is favourable when working with samples that will passivate or corrode. In addition, as the probe only comes into contact with a small area of a sample, neighbouring areas will not influence the portion of the surface being investigated.

1.5 Aims of Thesis

The overall objective of this thesis is to investigate and gain new understanding of the underlying processes which take place during various interfacial polymerisation reactions. This chapter has discussed the methods of polymer synthesis examined, which can be split into polymerisation at liquid/liquid interfaces for microcapsule synthesis and polymerisation at the solid/liquid interface for biofunctional materials. The electroanalytical techniques used to probe these reactions were subsequently discussed, as well as the theory behind the structure of the liquid/liquid interface and how it can be studied using electrochemical methods. Scanning probe methods used for the synthesis (scanning electrochemical cell microscopy) and analysis (atomic force microscopy) of polymer films formed at the solid/liquid interface have also been explained. The experimental details for all of the techniques used in this thesis can be found in Chapter 2.

Chapter 3, the first results chapter, focuses on the interfacial processes that take place at the oil-water interface of an epoxy-amine emulsion polymerisation system. The temperature-dependent flux of epoxide into water or an amine solution was quantified

using time-lapse microscopy. A combination of MEMED followed by finite element modelling was subsequently used to measure the fast transfer of amine into the water phase out of an expanding epoxide-amine droplet. Transfer was characterised using an Au microelectrode coated with an electrodeposited iridium oxide film, which could sense the local pH change in the aqueous phase near the surface of the expanding droplet.

Chapter 4 describes the use of electrochemical impedance spectroscopy and scanning electron microscopy to investigate how different reaction conditions will affect the formation of a poly(urea) film at a micro-liquid/liquid interface. Impedance was measured as a function of time to investigate the influence of isocyanate concentration/ratio, amine concentration and temperature. Poly(urea) films formed during these experiments were then examined using scanning electron microscopy in an attempt to correlate impedance data with film morphology. Increasing isocyanate /amine concentration and temperature was found to both speed up the rate of initial film formation and influence film morphology.

Chapter 5 details the fabrication and analysis of biofunctional polymer films on gold substrates. A reducing potential applied during scanning electrochemical cell microscopy was used to polymerise acrylamide monomers at the interface between the surface and the probe meniscus. Atomic force microscopy and x-ray photoelectron spectroscopy were used to examine the effect of changing reaction conditions on the extent of film deposition.

1.6 References

1. J. O. Hollinger and G. C. Battistone, *Clinical orthopaedics and related research*, 1986, **207**, 290-306.
2. L. Billiet, D. Fournier and F. Du Prez, *Polymer*, 2009, **50**, 3877-3886.
3. T. Fukuda, T. Terauchi, A. Goto, K. Ohno, Y. Tsujii, T. Miyamoto, S. Kobatake and B. Yamada, *Macromolecules*, 1996, **29**, 6393-6398.
4. S. Aoshima and S. Kanaoka, *Chem. Rev.*, 2009, **109**, 5245-5287.
5. N. Hadjichristidis, M. Pitsikalis, S. Pispas and H. Iatrou, *Chem. Rev.*, 2001, **101**, 3747-3792.
6. M. Kamigaito, T. Ando and M. Sawamoto, *Chem. Rev.*, 2001, **101**, 3689-3746.
7. G. Tse, D. Blankschtein, A. Shefer and S. Shefer, *J. Controlled Release*, 1999, **60**, 77-100.
8. P. J. Dowding, R. Atkin, B. Vincent and P. Bouillot, *Langmuir*, 2004, **20**, 11374-11379.
9. S. Freiberg and X. Zhu, *Int. J. Pharm.*, 2004, **282**, 1-18.
10. K. Eggers, D. Szopinski and G. A. Luinstra, *Macromolecular Symposia*, 2014, **346**, 32-35.
11. S. Leclercq, K. R. Harlander and G. A. Reineccius, *Flavour and Fragrance Journal*, 2009, **24**, 17-24.
12. R. Arshady, *J. Microencapsulation*, 1989, **6**, 13-28.
13. S. K. Chung, J. Y. Seo, J. H. Lim, H. H. Park, M. J. Yea and H. J. Park, *J. Food Sci.*, 2013, **78**, E709-E714.
14. K. Kondo, T. Niwa and K. Danjo, *European Journal of Pharmaceutical Sciences*, 2014, **51**, 11-19.
15. J. J. Richardson, D. Teng, M. Björnmalm, S. T. Gunawan, J. Guo, J. Cui, G. V. Franks and F. Caruso, *Langmuir*, 2014, **30**, 10028-10034.

16. M. I Ré, *Drying Technol.*, 1998, **16**, 1195-1236.

17. E. Duquesne, P. Degee, J. Habimana and P. Dubois, *Chem. Commun.*, 2004, DOI: 10.1039/B316645G, 640-641.

18. C. Marestin, C. Noël, A. Guyot and J. Claverie, *Macromolecules*, 1998, **31**, 4041-4044.

19. E. Lobry, F. Jasinski, M. Penconi, A. Chemtob, C. Croutxe-Barghorn, E. Oliveros, A. M. Braun and A. Criqui, *RSC Advances*, 2014, **4**, 43756-43759.

20. T.-M. Don and J. P. Bell, *J. Appl. Polym. Sci.*, 1998, **69**, 2395-2407.

21. B. Radhakrishnan, E. Cloutet and H. Cramail, *Colloid. Polym. Sci.*, 2002, **280**, 1122-1130.

22. M. A. Abd El-Ghaffar, M. H. Sherif and A. Taher El-Habab, *Chem. Eng. J.*, 2016, **301**, 285-298.

23. L. Tian, X. Li, P. Zhao, X. Chen, Z. Ali, N. Ali, B. Zhang, H. Zhang and Q. Zhang, *Macromolecules*, 2015, **48**, 7592-7603.

24. L. Zhang, Y. Cao, L. Wang, L. Shao and Y. Bai, *J. Appl. Polym. Sci.*, 2016, **133**, n/a-n/a.

25. F. Nazzaro, P. Orlando, F. Fratianni and R. Coppola, *Curr. Opin. Biotechnol.*, 2012, **23**, 182-186.

26. I. M. Martins, M. F. Barreiro, M. Coelho and A. E. Rodrigues, *Chem. Eng. J.*, 2014, **245**, 191-200.

27. G. Wu, J. An, X.-Z. Tang, Y. Xiang and J. Yang, *Adv. Funct. Mater.*, 2014, **24**, 6751-6761.

28. B. Dong, Y. Wang, G. Fang, N. Han, F. Xing and Y. Lu, *Cem. Concr. Compos.*, 2015, **56**, 46-50.

29. M. Andersson Trojer, L. Nordstierna, J. Bergek, H. Blanck, K. Holmberg and M. Nydén, *Adv. Colloid Interface Sci.*, 2015, **222**, 18-43.

30. W. L. Lee, P. Wee, C. Nugraha and S. C. J. Loo, *Journal of Materials Chemistry B*, 2013, **1**, 1090-1095.

31. C. Zheng, Y. Ding, X. Liu, Y. Wu and L. Ge, *Int. J. Pharm.*, 2014, **475**, 17-24.

32. C. Wang, Q. Ge, D. Ting, D. Nguyen, H.-R. Shen, J. Chen, H. N. Eisen, J. Heller, R. Langer and D. Putnam, *Nat Mater*, 2004, **3**, 190-196.

33. G. Ma, *J. Controlled Release*, 2014, **193**, 324-340.

34. J. Wei, X.-J. Ju, X.-Y. Zou, R. Xie, W. Wang, Y.-M. Liu and L.-Y. Chu, *Adv. Funct. Mater.*, 2014, **24**, 3312-3323.

35. R. Grillo, A. H. Rosa and L. F. Fraceto, *International Journal of Environmental Science and Technology*, 2013, **11**, 1691-1700.

36. B. Hack, H. Egger, J. Uhlemann, M. Henriet, W. Wirth, A. W. P. Vermeer and D. G. Duff, *Chem. Ing. Tech.*, 2012, **84**, 223-234.

37. I. P. Rivas, M. E. Gil-Alegre and A. I. Torres-Suárez, *Anal. Chim. Acta*, 2006, **557**, 245-251.

38. H. B. Scher, M. Rodson and K.-S. Lee, *Pesticide Science*, 1998, **54**, 394-400.

39. B. P. Binks and M. Kirkland, *PCCP*, 2002, **4**, 3727-3733.

40. K. Matyjaszewski, *Macromolecules*, 2012, **45**, 4015-4039.

41. K. Min, H. Gao and K. Matyjaszewski, *Macromolecules*, 2007, **40**, 1789-1791.

42. S. Fleischmann, B. M. Rosen and V. Percec, *J. Polym. Sci., Part A: Polym. Chem.*, 2010, **48**, 1190-1196.

43. Y. Kwak, A. J. D. Magenau and K. Matyjaszewski, *Macromolecules*, 2011, **44**, 811-819.

44. K. Matyjaszewski, S. Coca, S. G. Gaynor, M. Wei and B. E. Woodworth, *Macromolecules*, 1997, **30**, 7348-7350.

45. A. J. D. Magenau, N. C. Strandwitz, A. Gennaro and K. Matyjaszewski, *Science*, 2011, **332**, 81-84.

46. S. Park, P. Chmielarz, A. Gennaro and K. Matyjaszewski, *Angew. Chem. Int. Ed.*, 2015, **54**, 2388-2392.

47. A. J. D. Magenau, N. Bortolamei, E. Frick, S. Park, A. Gennaro and K. Matyjaszewski, *Macromolecules*, 2013, **46**, 4346-4353.

48. W. Tang, Y. Kwak, W. Braunecker, N. V. Tsarevsky, M. L. Coote and K. Matyjaszewski, *J. Am. Chem. Soc.*, 2008, **130**, 10702-10713.

49. A. J. Bard and L. R. Faulkner, *Electrochemical Methods: Principles and Applications*, 2001, 386-428.

50. A. Brückman, *Thermochim. Acta*, 1994, **245**, 231-233.

51. E. Lindner and B. D. Pendley, *Anal. Chim. Acta*, 2013, **762**, 1-13.

52. E. Ayranci and O. Duman, *Food Chem.*, 2004, **84**, 539-543.

53. R. Naumann, C. Alexander-Weber, R. Eberhardt, J. Giera and P. Spitzer, *Analytical and Bioanalytical Chemistry*, 2002, **374**, 778-786.

54. E. J. F. Dickinson, J. G. Limon-Petersen, N. V. Rees and R. G. Compton, *The Journal of Physical Chemistry C*, 2009, **113**, 11157-11171.

55. A. Lasia, in *Modern aspects of electrochemistry*, Springer, 2002, pp. 143-248.

56. E. Barsoukov and J. R. Macdonald, *Impedance spectroscopy: theory, experiment, and applications*, John Wiley & Sons, 2005.

57. S.-M. Park and J.-S. Yoo, *Anal. Chem.*, 2003, **75**, 455 A-461 A.

58. J. E. B. Randles, *Discussions of the Faraday Society*, 1947, **1**, 11-19.

59. K. T. Rodolfa, A. Bruckbauer, D. Zhou, A. I. Schevchuk, Y. E. Korchev and D. Klenerman, *Nano Lett.*, 2006, **6**, 252-257.

60. E. P. Randviir and C. E. Banks, *Analytical Methods*, 2013, **5**, 1098-1115.

61. Q. Wang, J.-E. Moser and M. Grätzel, *The Journal of Physical Chemistry B*, 2005, **109**, 14945-14953.

62. Z. He and F. Mansfeld, *Energy & Environmental Science*, 2009, **2**, 215-219.

63. J. Guo, A. Sun, X. Chen, C. Wang and A. Manivannan, *Electrochim. Acta*, 2011, **56**, 3981-3987.

64. J. M. McIntyre and H. Q. Pham, *Prog. Org. Coat.*, 1996, **27**, 201-207.

65. M. Alvarez-Lopez, M. D. Pereda, J. A. del Valle, M. Fernandez-Lorenzo, M. C. Garcia-Alonso, O. A. Ruano and M. L. Escudero, *Acta Biomaterialia*, 2010, **6**, 1763-1771.

66. R. Oltra and M. Keddam, *Electrochim. Acta*, 1990, **35**, 1619-1629.

67. E. P. M. van Westing, G. M. Ferrari and J. H. W. De Wit, *Electrochim. Acta*, 1994, **39**, 899-910.

68. I. Sekine, *Prog. Org. Coat.*, 1997, **31**, 73-80.

69. A. G. Volkov, *Liquid interfaces in chemical, biological and pharmaceutical applications*, CRC Press, 2001.

70. K. Piradashvili, E. M. Alexandrino, F. R. Wurm and K. Landfester, *Chem. Rev.*, 2016, **116**, 2141-2169.

71. D. Li, J. Li, Z. Zhang, L. Yan, N. Liu, C. Li and W. Hou, *Catal. Commun.*, 2017, **89**, 9-13.

72. T. V. Hoogerstraete, B. Onghena and K. Binnemans, *The Journal of Physical Chemistry Letters*, 2013, **4**, 1659-1663.

73. H. Mehl, M. M. Oliveira and A. J. G. Zarbin, *J. Colloid Interface Sci.*, 2015, **438**, 29-38.

74. E. Alvarez de Eulate, J. Strutwolf, Y. Liu, K. O'Donnell and D. W. M. Arrigan, *Anal. Chem.*, 2016, **88**, 2596-2604.

75. T. J. Stockmann, J.-M. Noël, A. Abou-Hassan, C. Combellas and F. Kanoufi, *The Journal of Physical Chemistry C*, 2016, **120**, 11977-11983.

76. P. D. Beattie, A. Delay and H. H. Girault, *J. Electroanal. Chem.*, 1995, **380**, 167-175.

77. F. Li, M. Edwards, J. Guo and P. R. Unwin, *The Journal of Physical Chemistry C*, 2009, **113**, 3553-3565.

78. J. C. Newland, P. R. Unwin and J. V. Macpherson, *PCCP*, 2014, **16**, 10456-10463.

79. A. Molina, E. Laborda and R. G. Compton, *The Journal of Physical Chemistry C*, 2014, **118**, 18249-18256.

80. F. O. Laforge, T. Kakiuchi, F. Shigematsu and M. V. Mirkin, *Langmuir*, 2006, **22**, 10705-10710.

81. C. J. Slevin and P. R. Unwin, *Langmuir*, 1997, **13**, 4799-4803.

82. A. G. Volkov, D. W. Deamer, D. L. Tanelian and V. S. Markin, *Prog. Surf. Sci.*, 1996, **53**, 1-134.

83. C. Gavach, P. Seta and B. D'Epenoux, *Journal of Electroanalytical Chemistry and Interfacial Electrochemistry*, 1977, **83**, 225-235.

84. W. N. Hansen, D. M. Kolb, D. W. Lynch, H. H. Girault and D. J. Schiffrin, *Journal of Electroanalytical Chemistry and Interfacial Electrochemistry*, 1983, **150**, 43-49.

85. I. Benjamin, *The Journal of chemical physics*, 1992, **97**, 1432-1445.

86. L. Daikhin, A. Kornyshev and M. Urbakh, *J. Electroanal. Chem.*, 2000, **483**, 68-80.

87. J. Strutwolf, A. L. Barker, M. Gonsalves, D. J. Caruana, P. R. Unwin, D. E. Williams and J. R. Webster, *J. Electroanal. Chem.*, 2000, **483**, 163-173.

88. Z. Samec, *Electrochim. Acta*, 2012, **84**, 21-28.

89. M. A. Méndez, Z. Nazemi, I. Uyanik, Y. Lu and H. H. Girault, *Langmuir*, 2011, **27**, 13918-13924.

90. J. J. Nieminen, I. Hatay, P. Ge, M. A. Mendez, L. Murtomaki and H. H. Girault, *Chem. Commun.*, 2011, **47**, 5548-5550.

91. E. Smirnov, P. Peljo, M. D. Scanlon and H. H. Girault, *Electrochim. Acta*, 2016, **197**, 362-373.

92. E. Aslan, I. Akin and I. H. Patir, *ChemCatChem*, 2016, **8**, 719-723.

93. C. I. Cámara, L. M. A. Monzón, J. M. D. Coey and L. M. Yudi, *J. Electroanal. Chem.*, 2015, **756**, 77-83.

94. M. Platt, R. A. W. Dryfe and E. P. L. Roberts, *Electrochim. Acta*, 2004, **49**, 3937-3945.

95. R. Knake, A. W. Fahmi, S. A. M. Tofail, J. Clohessy, M. Mihov and V. J. Cunnane, *Langmuir*, 2005, **21**, 1001-1008.

96. M. Platt and R. A. W. Dryfe, *PCCP*, 2005, **7**, 1807-1814.

97. K. Maeda, H. Jänchenová, A. Lhotský, I. Stibor, J. Budka and V. r. Mareček, *J. Electroanal. Chem.*, 2001, **516**, 103-109.

98. M. Vignali, R. Edwards and V. J. Cunnane, *J. Electroanal. Chem.*, 2006, **592**, 37-45.

99. P. S. Toth, A. K. Rabiu and R. A. W. Dryfe, *Electrochem. Commun.*, 2015, **60**, 153-157.

100. V. H. R. de Souza, M. M. Oliveira and A. J. G. Zarbin, *J. Power Sources*, 2014, **260**, 34-42.

101. G. Taylor and H. H. J. Girault, *Journal of Electroanalytical Chemistry and Interfacial Electrochemistry*, 1986, **208**, 179-183.

102. Y. Shao, M. D. Osborne and H. H. Girault, *Journal of Electroanalytical Chemistry and Interfacial Electrochemistry*, 1991, **318**, 101-109.

103. A. A. Stewart, Y. Shao, C. M. Pereira and H. H. Girault, *Journal of Electroanalytical Chemistry and Interfacial Electrochemistry*, 1991, **305**, 135-139.

104. B. R. Horrocks and M. V. Mirkin, *Anal. Chem.*, 1998, **70**, 4653-4660.

105. Y. Yuan, L. Wang and S. Amemiya, *Anal. Chem.*, 2004, **76**, 5570-5578.

106. Y. Shao, A. A. Stewart and H. H. Girault, *J. Chem. Soc., Faraday Trans.*, 1991, **87**, 2593-2597.

107. N. E. A. Cousens and A. R. Kucernak, *Electrochem. Commun.*, 2011, **13**, 1539-1541.

108. Y. Shao and M. V. Mirkin, *Anal. Chem.*, 1998, **70**, 3155-3161.

109. J. A. Campbell and H. H. Girault, *Journal of Electroanalytical Chemistry and Interfacial Electrochemistry*, 1989, **266**, 465-469.

110. J. Zhang and P. R. Unwin, *The Journal of Physical Chemistry B*, 1999, **104**, 2341-2347.

111. J. Zhang and P. R. Unwin, *Phys. Chem. Chem. Phys.*, 2000, **2**, 1267-1271.

112. J. Zhang and P. R. Unwin, *Phys. Chem. Chem. Phys.*, 2002, **4**, 3820-3827.

113. J. Zhang and P. R. Unwin, *Langmuir*, 2002, **18**, 2313-2318.

114. J. Zhang, J. H. Atherton and P. R. Unwin, *Langmuir*, 2004, **20**, 1864-1870.

115. G. Binnig, C. F. Quate and C. Gerber, *Phys. Rev. Lett.*, 1986, **56**, 930-933.

116. J. Jang, G. C. Schatz and M. A. Ratner, *The Journal of Chemical Physics*, 2004, **120**, 1157-1160.

117. Aleksandr Noy, a. Dmitri V. Vezenov and C. M. Lieber, *Annu. Rev. Mater. Sci.*, 1997, **27**, 381-421.

118. N. S. Malvankar, S. E. Yalcin, M. T. Tuominen and D. R. Lovley, *Nat Nano*, 2014, **9**, 1012-1017.

119. J. J. Sáenz, N. García, P. Grütter, E. Meyer, H. Heinzelmann, R. Wiesendanger, L. Rosenthaler, H. R. Hidber and H. J. Güntherodt, *J. Appl. Phys.*, 1987, **62**, 4293-4295.

120. S. J. O'Shea, M. E. Welland and T. Rayment, *Appl. Phys. Lett.*, 1992, **60**, 2356-2358.

121. W. Ma, C. Yang, X. Gong, K. Lee and A. J. Heeger, *Adv. Funct. Mater.*, 2005, **15**, 1617-1622.

122. J. Pyun, T. Kowalewski and K. Matyjaszewski, *Macromol. Rapid Commun.*, 2003, **24**, 1043-1059.

123. X. Li, W. Guan, H. Yan and L. Huang, *Mater. Chem. Phys.*, 2004, **88**, 53-58.

124. G. Bar, Y. Thomann, R. Brandsch, H. J. Cantow and M. H. Whangbo, *Langmuir*, 1997, **13**, 3807-3812.

125. M. Boltau, S. Walheim, J. Mlynek, G. Krausch and U. Steiner, *Nature*, 1998, **391**, 877-879.

126. P. G. Hartley, H. Thissen, T. Vaithianathan and H. J. Griesser, *Plasmas Polym.*, 2000, **5**, 47-60.

127. D. M. Jones, J. R. Smith, W. T. S. Huck and C. Alexander, *Adv. Mater.*, 2002, **14**, 1130-1134.

128. A. J. Bard, F. R. F. Fan, J. Kwak and O. Lev, *Anal. Chem.*, 1989, **61**, 132-138.

129. C. G. Williams, M. A. Edwards, A. L. Colley, J. V. Macpherson and P. R. Unwin, *Anal. Chem.*, 2009, **81**, 2486-2495.

130. N. Ebejer, M. Schnippering, A. W. Colburn, M. A. Edwards and P. R. Unwin, *Anal. Chem.*, 2010, **82**, 9141-9145.

131. S. C. S. Lai, A. N. Patel, K. McKelvey and P. R. Unwin, *Angew. Chem.*, 2012, **124**, 5501-5504.

132. A. N. Patel, S.-y. Tan and P. R. Unwin, *Chem. Commun.*, 2013, **49**, 8776-8778.

133. A. G. Güell, N. Ebejer, M. E. Snowden, K. McKelvey, J. V. Macpherson and P. R. Unwin, *Proceedings of the National Academy of Sciences*, 2012, **109**, 11487-11492.

134. A. G. Güell, K. E. Meadows, P. V. Dudin, N. Ebejer, J. V. Macpherson and P. R. Unwin, *Nano Lett.*, 2013, **14**, 220-224.

135. J. C. Byers, A. G. Güell and P. R. Unwin, *J. Am. Chem. Soc.*, 2014, **136**, 11252-11255.

136. A. G. Guell, K. E. Meadows, P. V. Dudin, N. Ebejer, J. C. Byers, J. V. Macpherson and P. R. Unwin, *Faraday Discuss.*, 2014, **172**, 439-455.

137. S. C. S. Lai, P. V. Dudin, J. V. Macpherson and P. R. Unwin, *J. Am. Chem. Soc.*, 2011, **133**, 10744-10747.

138. S. E. F. Kleijn, S. C. S. Lai, T. S. Miller, A. I. Yanson, M. T. M. Koper and P. R. Unwin, *J. Am. Chem. Soc.*, 2012, **134**, 18558-18561.

139. C.-H. Chen, K. E. Meadows, A. Cuharuc, S. C. S. Lai and P. R. Unwin, *PCCP*, 2014, **16**, 18545-18552.

140. B. D. B. Aaronson, S. C. S. Lai and P. R. Unwin, *Langmuir*, 2014, **30**, 1915-1919.

141. H. V. Patten, L. A. Hutton, J. R. Webb, M. E. Newton, P. R. Unwin and J. V. Macpherson, *Chem. Commun.*, 2015, **51**, 164-167.

142. P. M. Kirkman, A. G. Güell, A. S. Cuharuc and P. R. Unwin, *J. Am. Chem. Soc.*, 2013, **136**, 36-39.

143. D. Zhan, D. Yang, Y. Zhu, X. Wu and Z.-Q. Tian, *Chem. Commun.*, 2012, **48**, 11449-11451.

144. K. McKelvey, M. A. O'Connell and P. R. Unwin, *Chem. Commun.*, 2013, **49**, 2986-2988.

Chapter 2

Experimental

2.1 Chemicals

All chemicals were used as received apart from where stated. All solutions were prepared using Milli-Q water (Millipore Corp), with compounds weighed out using a four figure analytical balance (Sartorius A2008). pH measurements were taken using a pH meter (S20 SevenEasy™ pH, Mettler Toldeo) which was calibrated using buffer solutions of pH 4, 7 and 10 (Fisher Scientific).

Table 2.1 *List of chemicals used in this thesis.*

Chemical	Supplier	Details
1,2-Dichloroethane (DCE)	Sigma-Aldrich	Anhydrous, 99.8%
2-Hydroxyethyl disulphide	Sigma-Aldrich	Technical grade
Acetonitrile, anhydrous (ACN)	Sigma-Aldrich	99.8%
Benzyltributylammonium chloride (BTBACl)	Alfa Aesar	98%
Bis[2-(2-bromoisobutyryloxy)ethyl] disulphide	Synthesised in house[1]	
Copper(II) chloride	Sigma-Aldrich	≥99.995% trace metals basis
Dimethyltrimethylsilylamine	Sigma-Aldrich	97%
Ferrocenylmethyltrimethylammonium	Synthesised in house[2]	

hexafluorophosphate ($FcTMA^+$)		
Hexamethylene-1,6-diamine (HMDA)	Merck	≥99%
Hydrogen Peroxide	Sigma-Aldrich	30 wt.%
Iridium(IV) chloride hydrate	Sigma-Aldrich	Technical grade
Jeffamine D230	Alfa Chemicals	
Lithium chloride	Sigma-Aldrich	≥99.99% trace metals basis
N-hydroxyethyl acrylamide (HEAA)	Sigma-Aldrich	97%
Oxalic acid dihydrate	Sigma-Aldrich	99.999% trace metals basis
Polyethylenimine, ethylenediamine branched (PEI)	Sigma-Aldrich	Averaged M_w ~ 800, average M_n ~ 600
Polymethylene polyphenylisocyanate (PMPPI)	Sigma-Aldrich	Average M_n ~ 340
Potassium carbonate	Fisher Scientific	≥99%
Potassium chloride	Sigma-Aldrich	≥99%
Potassium nitrate	Sigma-Aldrich	≥99%
Potassium tetrakis(4-chlorophenyl)borate	Sigma-Aldrich	Selectophore™, 98.0%
Propan-2-ol (IPA)	Sigma-Aldrich	Anhydrous, 99.5%
Resorcinol diglycidyl ether (RDGE)	Sigma-Aldrich	
Sodium perchlorate	Sigma-Aldrich	≥98%
Sulfuric acid	Fisher Chemical	95%

Tetrabutylammoniumchloride hydrate	Fisher Scientific	98%
Tetrabutylammonium tetrakis (4-chlorophenyl) borate (TBATPBCl)	Synthesised in house[3]	
Toluene 2,4-diisocyanate (TDI)	Sigma-Aldrich	Technical grade, ≥90%
Tris[2-(dimethylamino)ethyl]amine (Me_6TREN)	Synthesised in house[4]	

Table 2.2 *List of materials used in this thesis.*

Material	**Supplier**	**Details**
Ag wire	Goodfellow	0.125 mm diameter
Alumina slurry	Buehler	0.05 µm
Borosilicate capillaries	Harvard Apparatus	
Carbon conductive adhesive tape	Agar Scientific	
Conducting silver epoxy	Circuitworks, ITW Chemtronics	
Dri-Ref™	World Precision Instruments	2 mm diameter (short)
MicroFil	World Precision Instruments	
Non-conductive epoxy	Araldite	
Pt wire	Sigma-Aldrich	1 mm diameter, 99.99%
Saturated calomel electrode (SCE)	Cambria Scientific	

Silicon/silicon oxide wafer	IDB Technologies Ltd.	n-type, 525 µm thickness with 300 nm thermally grown silicon oxide on each side
Teflon tubing	VWR International Ltd.	0.5 mm inner diameter

2.2 Imaging Techniques

2.2.1 Field Emission-Scanning Electron Microscopy (FE-SEM)

Field-emission scanning electron microscopy (FE-SEM) is an imaging technique capable of providing high-resolution images of conductive and non-conductive surfaces. High energy electrons are produced under vacuum and accelerated (0.1 – 30 kV) towards a surface, with magnets used to adjust their trajectory (see Figure 2.1). The irradiation of surface atoms by the electron beam results in the emission of backscattered or secondary electrons, which are collected using a detector to construct an image of the surface.[5] Standard SEM experiments tend to collect secondary electrons, which are emitted following the inelastic reflection of the incident beam. Secondary electrons are particularly useful for studying surface topography as different elements and different structures will produce different amounts of secondary electrons. Backscattered electrons produced by an elastic reflection of the incident beam can be monitored using an in-lens detector, which will produce images showing the differences in conductivity on a surface. Conductive areas of a sample will adsorb more electrons, causing fewer electrons to be scattered and thus appearing darker in the final SEM image.

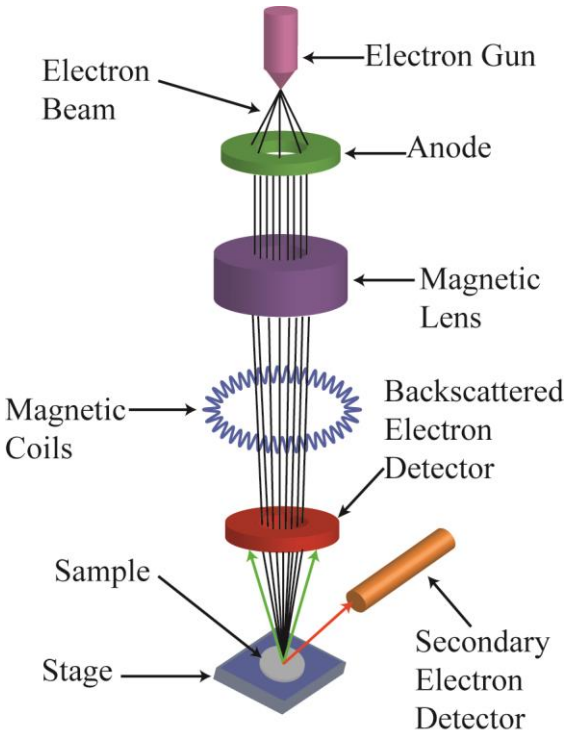

Figure 2.1 *Schematic of a scanning electron microscope.*

Poly(urea) films formed during electrochemical impedance experiments (see Chapter 4) and double-barrelled theta pipettes used for SECCM (see Chapter 5) were examined using SEM. To prepare the samples, glass capillaries were adhered onto SEM sample holders using carbon conductive adhesive tape. The sample was then coated with a thin layer of gold using a sputter coater (Moorfield, UK). The FE-SEM instrument (FE-SEM Zeiss SUPRA 55 VP) using an in-lens detector was set at an acceleration speed of 3.0 kV with a working distance of 10-12 mm.

2.2.2 Atomic Force Microscopy (AFM)

The surface morphology of poly(HEAA) films formed on Au substrates by scanning electrochemical cell microscopy (see Chapter 5) was characterised using a Bruker Innova AFM with Nanodrive version 8.02 software (Bruker, UK). Tapping mode imaging was carried out using AFM tips made from antimony (n) doped silicon with 3 µm long cantilevers and a nominal frequency of 75 kHz (Model RFESP, Bruker, UK).

Images were processed using scanning probe microscopy software SPIP 6.1 (Image Metrology, Denmark).

2.2.3 X-ray Photoelectron Spectroscopy (XPS)

X-ray photoelectron spectroscopy (XPS) is a spectroscopic technique capable of measuring the elemental composition of a surface.[6] Samples are placed inside the XPS under ultra-high vacuum (UHV) and irradiated with a focused beam of X-rays (see Figure 2.2). Irradiation will cause electrons to be emitted from the very top layer of the sample (~0.1 nm), which are subsequently analysed. XPS spectra are obtained by counting the number of electrons emitted and their specific kinetic energy (eV).

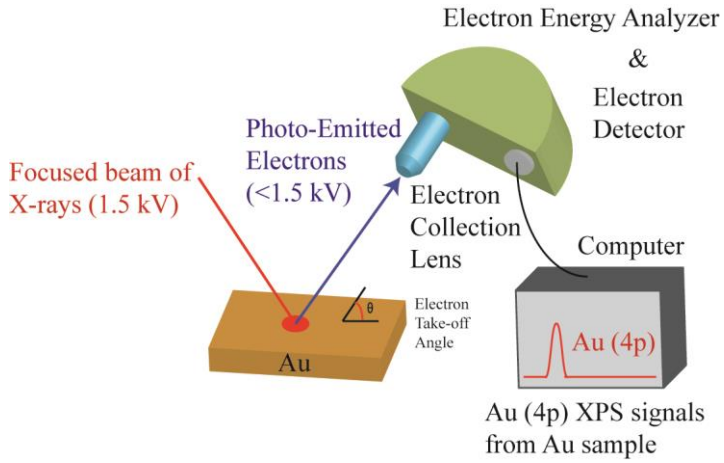

Figure 2.2 *Diagram of the basic components of an X-ray photoelectron spectroscopy system.*

XPS analysis (see Chapter 5) was conducted using a Kratos Axis Ultra DLD photoelectron spectrometer, with a monochromated Al kα X-ray source (1486.69 eV) operating at 150 W. All measurements were performed under ultra-high vacuum (UHV) conditions with a spectrometer base pressure of 2×10^{-10} mbar. Survey and core level spectra were collected with pass energies of 160 eV and 20 eV respectively with a 1 mm spot size, obtaining a resolution of ca. 0.4 eV for core level scans. All datas were collected was subject to Shirley background subtraction.

2.3 Electrochemistry

2.3.1 Fabrication of Ag|AgCl wire and Ag|AgTPBCl quasi reference electrodes

Silver wire (0.125 mm diameter, Goodfellow, UK) was immersed with a platinum counter electrode (1 mm diameter, Goodfellow, UK) in either a saturated aqueous solution of potassium chloride (for Ag|AgCl reference) or in a solution of 10 mM TBATPBCL in DCE (for Ag|AgTPBCl reference). The applied potential was then swept between 7 V and 10 V for 5 minutes to coat the silver wire in the appropriate counter anion. A black layer was shown to form on the silver wire following AgCl formation and a gold layer following AgTPBCl formation.

2.3.2 Fabrication of pH-sensitive UMEs (for MEMED)

Construction. A 2 mm diameter borosilicate glass tube (Harvard apparatus) was pulled using a home-built heating coil to form a 100-200 µm diameter tip at one end. A 15 mm long piece of 75 µm diameter Au wire (Goodfellow Ltd, Cambridge, UK) coated in PTFE was attached alongside the end of a 15 cm long, 250 µm diameter copper wire using conductive silver paint, with around half the length of the Au wire protruding past the tip of the copper wire. The wire was then carefully pushed through the glass tube until the Au wire was protruding from the narrow end of the tube. The end of the copper wire protruding from the glass tube was then wrapped around the end of the glass tube to keep the wire in place, leaving a straight section at the end for connections to be attached to. The ends of the glass tube were then sealed around the wire using epoxy adhesive (Araldite®). A photograph of one of the constructed Au wire microelectrodes is shown in Figure 2.3.

Figure 2.3 *Photograph of an Au wire microelectrode following electrodeposition of iridium oxide.*

Electrodes were tested against a standard calomel electrode (SCE) in a 500 µM Ferrocenylmethyltrimethylammonium hexafluorophosphate ($FcTMA^+PF_6^-$) solution containing 0.1 M KNO_3 using cyclic voltammetry (CV) (scan speed 10 mV/s). $FcTMA^+PF_6^-$ was synthesized in-house as described previously,[7] following the metathesis reaction between ferrocenylmethyltrimethylammonium iodide and silver hexafluorophosphate. The steady-state limiting current response for $FcTMA^+$ oxidation was then used to calculate electrode radius (see Chapter 1, equation 1.6), thus ensuring that they were fully sealed aside from the Au at the tip of the wire.

Iridium Oxide Film Electrodeposition. Iridium oxide film formation on the electrode surface is controlled by the reaction:[8, 9]

$$\left[Ir(COO)_2(OH)_4\right]^{2-}_{(aq)} + 2OH^- \rightarrow \left[IrO_2(OH)_2 \bullet 2H_2O\right]_{(s)} + 2CO_2 + 2e^- \quad (2.1)$$

The iridium oxide solution used for the electrodeposition was prepared as described in the literature[10] and stored at 4 °C between uses. A three electrode system consisting of a Ag|AgCl wire reference electrode, a platinum counter electrode and a fabricated Au wire working electrode (sensor to be functionalised) was assembled in the iridium solution. Anodic deposition was carried out using a potentiostat (CHI800B, CH Instruments Inc.) connected to a desktop computer, with a potential of 0.8 V *vs.* Ag|AgCl applied for 180 seconds. The electrodes were then left overnight in deionised

water to hydrate, as this has been shown to stabilise the pH response. [11] A current-time (*I-t*) curve for the anodic electrodeposition of iridium oxide is shown in Figure 2.4.

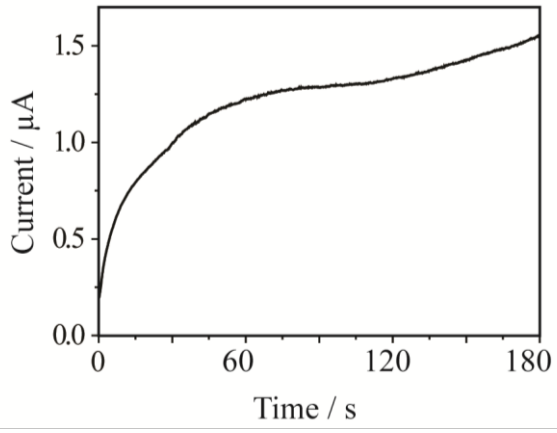

Figure 2.4 *A typical I-t curve for the anodic deposition of iridium oxide onto an Au wire microelectrode at 0.8 V vs. Ag|AgCl.*

2.3.3 Micro-capillary Electrochemical Method (MCEM)

Micro-capillary electrochemical cells have been utilised in a number of studies to investigate surface processes.[12, 13] Figure 2.5 shows the experimental setup used during preliminary polymer deposition experiments (see Chapter 5).

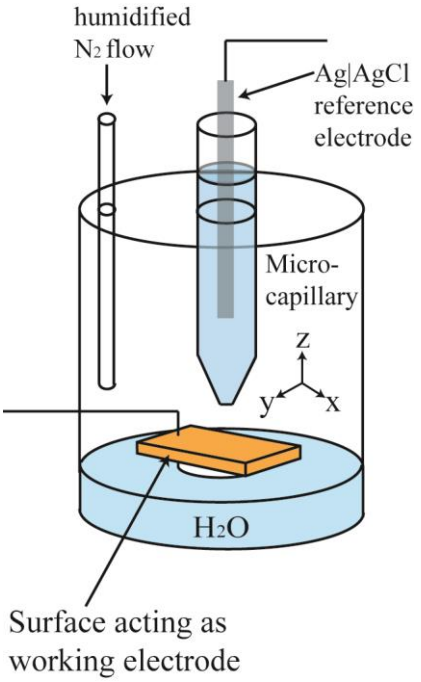

Figure 2.5 *General schematic of the setup used during micro-capillary electrochemical method experiments.*

A single barrel borosilicate capillary (1.2 mm outer diameter, 0.69 mm inner diameter) was pulled to a fine point (8-10 µm diameter) using a laser pipet puller (Model P-2000, Sutter Instruments). Pipet dimensions were characterised using optical microscopy. The capillary was filled with electrolyte solution (see Chapter 5), and a Ag|AgCl quasi-reference counter electrode (QRCE) inserted into the barrel. It was then mounted on a manual *x, y, z* stage and positioned above the sample. A *z*-micro positioner holding a platinum wire (1 mm diameter, Goodfellow, UK) was used to bring the platinum wire in contact with the sample, thus turning the surface into a working electrode. To eliminate evaporation effects and remove oxygen from the system, a humidity cell was used. A small amount of H_2O was placed at the bottom of the cell, with the sample raised above the water line. Parafilm® is placed over the glass cell and N_2 gas flown inwards to remove oxygen and keep the atmosphere within the cell humid.

2.3.4 Scanning Electrochemical Cell Microscopy (SECCM)

Probe Fabrication. Dual barrel borosilicate glass theta pipettes (o.d. 1.5 mm, i.d. 0.23 mm, Harvard Apparatus) were pulled using a laser puller (Model P-2000, Sutter instruments) to produce tapered pipets of either 1 µm diameter (for grid deposition), 200 nm diameter (for spiral deposition) or 1.5 µm diameter (for oxygen reduction experiments). Pipet dimensions were accurately measured using field emission-scanning electron microscopy (FE-SEM Zeiss SUPRA 55 VP), as shown in Figure 2.6.

Figure 2.6 *FE-SEM image of a pipet used for SECCM.*

SECCM Measurements. Deposition experiments were performed within a Faraday cage (see Figure 2.7). The procedure for SECCM has been described previously.[14, 15] The Au or Au/SAM working electrode was mounted on a high-precision 100 µm range *x,y*-piezoelectric stage (P-622.1CL or P-622.2CL PIHera, PhysikInstrumente, Germany) and connected to a custom built electrometer (built by Dr Alex Colburn) for surface current ($i_{surface}$) measurements. Probes were filled with the appropriate aqueous solution, and Ag/AgCl quasi reference counter electrodes (QRCEs) were inserted into each barrel. The probe was then mounted on a high-dynamic 38 µm range z-piezoelectric positioner (P-753CD LISA, PhysikInstrumente, Germany).

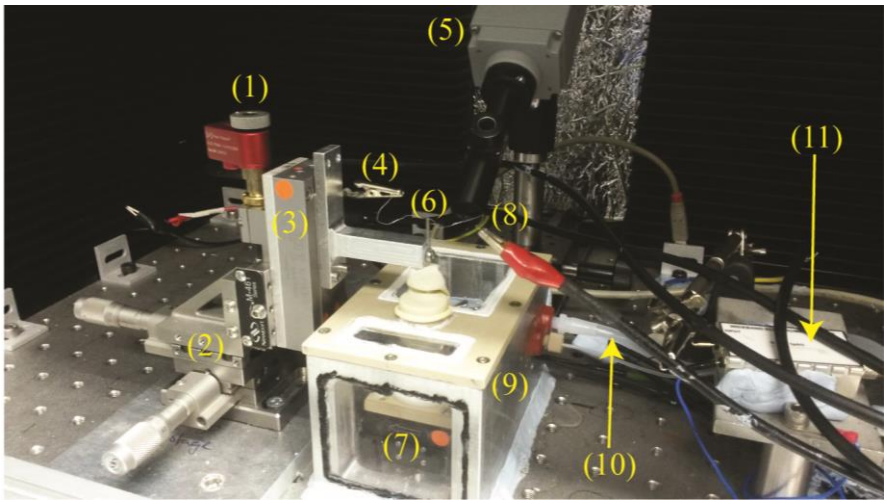

Figure 2.7 *Photograph showing the setup used during SECCM experiments detailing individual components: (1) z-picomotor, (2) x,y-manual stage, (3) z-piezoelectric positioner, (4) electrode 1, (5) PixelLink video camera, (6) SECCM tip, (7) x,y-piezoelectric positioner, (8) electrode 2, (9) environmental cell, (10) argon gas line and (11) electrometer head (100 pA – 100 fA sensitivity) for surface current measurements.*

The QRCEs were connected to a custom made bipotentiostat (see Figure 2.8), which was used to control the bias voltage between the QRCEs (V_2). Potential of the substrate ($V_{surface}$) was defined by applying a second voltage (V_1) to the bipotentiostat, which upon contact between the probe meniscus and the surface will apply potential in accordance to the equation $V_{surface} = -V_1 - V_2/2$. The probe was oscillated in the z direction to induce

tip height modulation (~10 % of the tip diameter) by applying a set frequency via a lock-in amplifier (SR830, Stanford Research Systems, USA). This oscillation induced an alternating current component ($i_{barrel\ AC}$) in the barrel current (i_{barrel}) due to the changing geometry and thus resistance of the meniscus upon contact with the surface, which was used for positional feedback to maintain a constant distance between the probe and surface. For SECCM experiments under argon, the set-up was encased in a sealed environmental cell which had been de-aerated for at least an hour. Data was acquired during SECCM experiments using a 40 MHz FPGA card (PCIe 7852R, National Instruments, USA), which allowed for fast data collection. Data was processed via a home-built interface capable of converting multiple BNC terminals to a single SCSI-type cable. Experiments were controlled through a LabVIEW interface (written by Dr Kim McKelvey, version 13.0, National Instruments, USA), which was used to control applied voltages to both piezos and electrodes.

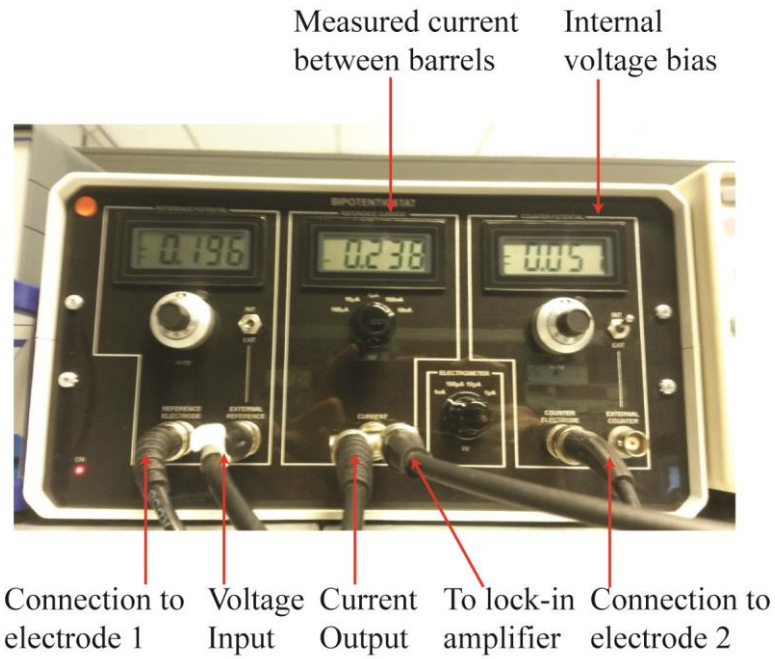

Figure 2.8 *Photograph of bipotentiostat used during SECCM experiments.*

2.4 Liquid/liquid Interfaces

2.4.1 Micropipette Fabrication

Construction of Micropipettes for Time-lapse Microscopy of RDGE Droplet Dissolution. A borosilicate glass capillary (2.0 mm outer diameter, Harvard Apparatus Limited) was heated at a point a third along its length in order to bend it by an angle of ca. 90 °. It was then heated further along the long end of the capillary to bend the capillary back on itself of (ca. 90 °), thus forming a U-shape. Another smaller borosilicate glass capillary (1.0 mm outer diameter, Harvard Apparatus Limited) was heat pulled to form a fine tip then shortened. This was then inserted and sealed into the shorter end of the U-shaped capillary using epoxy adhesive (Araldite®).

Construction of Micropipettes for MEMED. A borosilicate glass capillary (2.0 mm outer diameter, Harvard Apparatus Limited) was heat pulled to form a fine tip, then shortened. This was then polished flat (6 µm polishing pad, Buehler) to form an orifice of ca. 100 µm diameter.

Construction of Micropipettes for Cyclic Voltammetry and Electrochemical Impedance Spectroscopy at the Liquid/liquid Interface. A borosilicate capillary (1.2 mm outer diameter, 0.69 mm inner diameter) was heat pulled using a laser pipet puller (Model P-2000, Sutter Instruments) to form a tapered end. Pulled pipettes were screened using optical microscopy (Olympus BH2-UMA) to ensure that only those with short shafts and a diameter of between 8 and 10 µm at the end were used in experiments. The interiors of suitable micropipettes were then silanized via the injection of 5 mL dimethyltrimethylsilylamine vapour into the barrel. Silanized micropipettes were subsequently dried for 3 minutes using a home-built heat puller set to around 50 °C.

2.4.2 Cyclic Voltammetry

Silanized micropipettes were filled with the organic phase (1,2-dichloroethane) using a Microfil connected to a glass syringe. A Ag|AgTPBCl QRCE (see section 2.3.1 for fabrication) was then inserted into the micropipette barrel. The tip of the micropipette was immersed into a small glass petri dish containing the aqueous phase and Dri-Ref™ Ag|AgCl reference electrode, as shown in Figure 2.9. Cyclic voltammograms (FAS2 Femtostat, Gamry Instruments, Philadelphia, US) were then run with respect to the reference, with the electrified liquid/liquid interface acting as the working electrode.

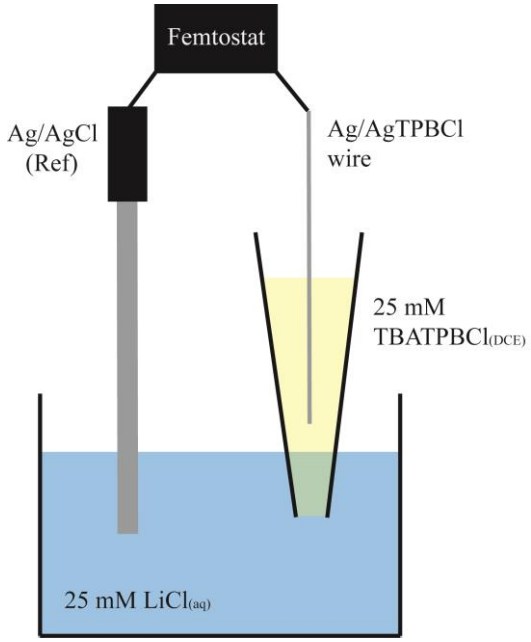

Figure 2.9 *Schematic of the setup used for cyclic voltammetry and electrochemical impedance spectroscopy experiments at the micro-interface between two immiscible electrolyte solutions.*

2.4.3 Electrochemical Impedance Spectroscopy (EIS)

The electrochemical setup for electrochemical impedance spectroscopy (EIS) across the liquid/liquid interface was similar to that used for cyclic voltammetry experiments. EIS was carried out using a Femtostat (FAS2 Femtostat, Gamry Instruments, Philadelphia, US). Isocyanate monomers were placed into the organic phase, and amine monomers in the aqueous phase (see Chapter 4 for details).

2.5 References

1. J. A. Syrett, M. W. Jones and D. M. Haddleton, *Chem. Commun.*, 2010, **46**, 7181-7183.
2. S. G. Lemay, D. M. van den Broek, A. J. Storm, D. Krapf, R. M. M. Smeets, H. A. Heering and C. Dekker, *Anal. Chem.*, 2005, **77**, 1911-1915.
3. Y. Shao and H. H. Girault, *Journal of Electroanalytical Chemistry and Interfacial Electrochemistry*, 1991, **282**, 59-72.
4. M. Ciampolini and N. Nardi, *Inorg. Chem.*, 1966, **5**, 41-44.
5. I. M. Watt, *The principles and practice of electron microscopy*, Cambridge University Press, 1997.
6. W. E. Swartz, *Anal. Chem.*, 1973, **45**, 788A-800a.
7. S. G. Lemay, D. M. van den Broek, A. J. Storm, D. Krapf, R. M. Smeets, H. A. Heering and C. Dekker, *Anal. Chem.*, 2005, **77**, 1911-1915.
8. B. P. Nadappuram, K. McKelvey, R. Al Botros, A. W. Colburn and P. R. Unwin, *Anal. Chem.*, 2013, **85**, 8070-8074.
9. E. Bitziou, D. O'Hare and B. A. Patel, *Anal. Chem.*, 2008, **80**, 8733-8740.
10. T. L. Read, E. Bitziou, M. B. Joseph and J. V. Macpherson, *Anal. Chem.*, 2013, **86**, 367-371.
11. L. D. Burke and D. P. Whelan, *Journal of Electroanalytical Chemistry and Interfacial Electrochemistry*, 1984, **162**, 121-141.
12. T. M. Day, P. R. Unwin and J. V. Macpherson, *Nano Lett.*, 2007, **7**, 51-57.
13. S. P. E, T. S. Miller, J. V. Macpherson and P. R. Unwin, *PCCP*, 2015, **17**, 26394-26402.
14. N. Ebejer, M. Schnippering, A. W. Colburn, M. A. Edwards and P. R. Unwin, *Anal. Chem.*, 2010, **82**, 9141-9145.

15. M. E. Snowden, A. G. Güell, S. C. S. Lai, K. McKelvey, N. Ebejer, M. A. O'Connell, A. W. Colburn and P. R. Unwin, *Anal. Chem.*, 2012, **84**, 2483-2491.

Chapter 3

Using Electrochemical and Optical Techniques to Understand the Formation of Polymeric Microparticles

This chapter focuses on the investigation of physicochemical processes that take place at the oil-water interface of an epoxy-amine emulsion polymerisation system. Electrochemical characterisation of PMP monomers has shown that both the resorcinol diglycidyl ether (RDGE) epoxide and jeffamine D230 amine used in the PMP synthesis process studied will foul electrode surfaces, thus leaving voltammetric and amperometric techniques unsuitable for quantifying flux of monomers from an epoxide-amine droplet into the aqueous phase. Temperature-dependent dissolution of epoxide in deionised water and an aqueous amine solution has been quantified using time-lapse microscopy. A combination of MEMED and finite element method (FEM) modelling has been used to measure the transfer of amine from an organic phase comprised of RDGE and jeffamine D230 into an aqueous phase. Transfer was characterised using an Au microelectrode coated with an electrodeposited iridium oxide film, which could sense the local pH change in the aqueous phase near the surface of the expanding droplet.

3.1 Introduction

Chapter 1 described the preparation of capsules for agrichemical encapsulation based on emulsion polymerisation reaction between an epoxide (RDGE) and an amine (Jeffamine D230). Figure 3.1 shows a conceptual model of an epoxy-amine droplet within the aqueous phase, with particles of kaolin clay at the liquid-liquid interface. Whilst the curing reaction is expected to take place in the organic phase, monomer transfer into the aqueous phase will lead to enhanced curing at the liquid-liquid interface or in the aqueous phase itself. Therefore, to fully understand epoxy-amine PMP formation, cure kinetics in both phases and the extent of monomer transfer need to be quantified. Implementation of analytical techniques capable of describing these processes is highly desirable to ensure effective industrial scale up of epoxy-amine emulsion polymerisation technology.

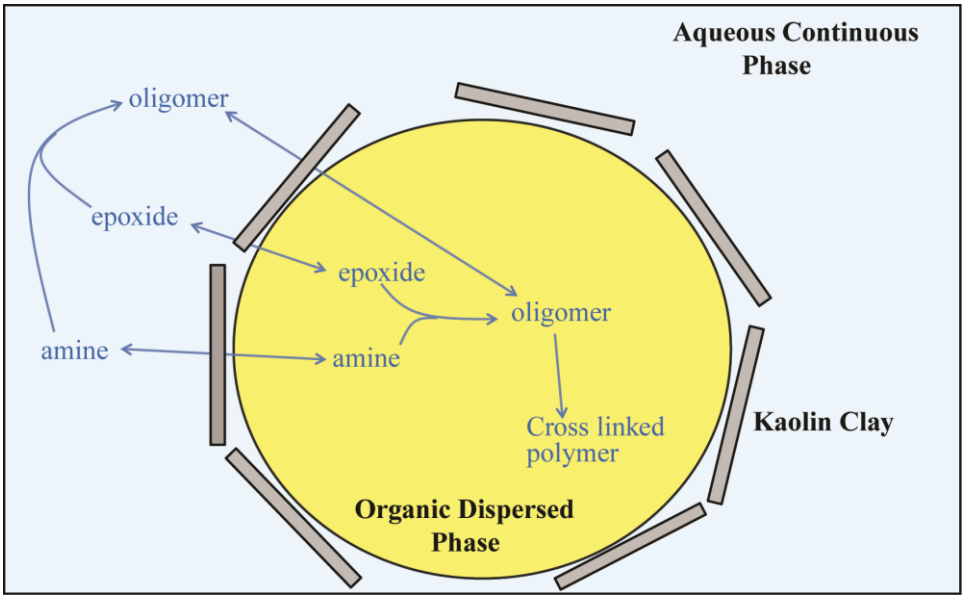

Figure 3.1 *A conceptual model of the polymeric microparticle (PMP) curing process which shows amine and epoxide transfer across the oil-water interface and the location of the epoxy-amine curing reaction.*

3.1.1 Commonly Used Analytical Techniques for the Quantification of Epoxy-Amine Cure Kinetics

Cure kinetics in the organic phase have relied on bulk or *ex-situ* analytical techniques. Fourier transform infra-red (FT-IR) spectroscopy and isothermal differential scanning calorimetry (DSC) have been used to measure cure kinetics of epoxy-amine mixtures at different temperatures, with higher temperatures causing faster curing kinetics.[1, 2] Activation energies for epoxy-amine cure systems have been extracted using the Kamal equation from DSC kinetic data.[3] High-performance liquid chromatography (HPLC) has also been used to study how changing the amine-to-epoxide ratio can affect the progress of a curing reaction.[4] This particular study, using a model system of phenyl glycidyl ether, the curing agent *p*-chloroaniline and the accelerator Monuron, showed that catalysed amine curing of epoxy resins is controlled by a competition between epoxy homopolymerisation and amine addition to the epoxy. This competition is influenced by the ratio of epoxy-to-amine, catalyst concentration and temperature.

Studies into epoxy-amine cure kinetics in the presence of water are less widespread, however there are examples in the literature. Initial studies into the effect of absorbed water on undercured epoxy-amine thermosets indicated that additional curing would take place in the presence of hot water.[5, 6] This is due to a reaction between unreacted epoxide and water. More recently, Choi *et al.* have used FTIR to quantify the cure kinetics of an epoxy-amine thermoset in the presence of different amounts of water.[7]

The aforementioned analytical techniques cannot sufficiently describe monomer transfer or curing taking place at the liquid-liquid interface. This chapter examines these physicochemical processes, with the aim of both characterising the RDGE epoxide and jeffamine D230 used in PMP formation and using analytical techniques to examine the

position of the curing reaction (i.e. does it take place in the organic phase or the aqueous phase?), which will influence the overall microcapsule morphology.

3.1.2 Electrochemical Characterisation of Epoxides and Amines

Prior to the characterisation of an epoxide-amine curing process using different electrochemical methods, it is important to review any previous electrochemical studies that have taken place using one or a combination of the chemicals (or related chemicals). Both the oxidation and reduction of epoxides has been achieved electrochemically. Safavi and Iranpoor have studied the electrochemical hydrolyses of epoxides using an acid catalyst electrogenerated around 1.5 V.[8] Mercury cathodes set at -2 V have been used to reduce epoxides by cleaving activated C-O bonds.[9]

Different types of amines (primary, secondary and tertiary) have also been studied electrochemically. Masui *et al*. have reported that aliphatic amines can be irreversibly oxidised using cyclic voltammetry, with waves seen for secondary and tertiary amines.[10] C. K. Mann has explored the relationship between aliphatic amine substitution and the peak potential required to oxidise each compound.[11] More recently, Gallardo *et al.* have investigated the oxidation mechanism and subsequent attachment of aliphatic amines to electrode surfaces during cyclic voltammetry.[12] Primary amines have also been detected using calix[6]arene ionophore based ion sensitive electrodes capable of exhibiting a Nernstian response.[13]

3.1.3 Microelectrochemical Measurements at Expanding Droplets (MEMED)

Microelectrochemical measurements at expanding droplets (MEMED) is a technique that has been shown to be powerful for quantifying the chemical processes that take place at a liquid/liquid interface.[14] It employs either amperometric or potentiometric detection to measure local changes in concentration as a droplet expands towards a stationary microelectrode placed in an immiscible receptor liquid phase. MEMED has previously been used to investigate stripping kinetics and electron transfer at oil-water interfaces, as well as the characterisation of mass-transport in both the oil and aqueous phases.[15, 16] Mass-transport models can be generated which use the convective-diffusion equation and appropriate boundary conditions to generate theoretical concentration profiles which can be used to quantify chemical fluxes at the liquid/liquid interface.[15, 17] MEMED has been used in this chapter to quantify flux of amine for an epoxy resin carrier into the aqueous phase using pH-sensitive microelectrodes.

3.1.4 Time-lapse Microscopy of Liquid Droplet Dissolution

The dissolution of a liquid droplet into a receptor liquid can also be characterised using optical techniques. Needham *et al.* have used a calibrated video micrograph to measure the dissolution of aniline droplets into water and vice-versa as a function of solution saturation.[18] The dissolution of liquid micro droplets into a receptor liquid has also been quantified by Poesio *et al*., by recording images of a hexadecane droplet in an acetone receptor phase, and measuring droplet radius over time using software written in MATLAB© which was capable of fitting circles to the droplet images.[19] A similar technique is used in this chapter to quantify temperature-dependent initial flux of RDGE epoxide into water or jeffamine D230 aqueous solution.

3.2 Experimental

3.2.1 CV and DPV of RDGE and Jeffamine D230

All solutions were prepared with deionised water (Milli-Q, Millipore, 18.2 MΩ cm resistivity at 25°C). Voltammetric measurements were carried out using Electrochemical Analyzer (CH Instruments Inc., USA) potentiostats. Electrodes were polished using an alumina micro polish (0.05 µm, MasterPrep, Buehler, Germany) before electrochemical measurements were taken.

All CV and DPV experiments were carried out using a three electrode set-up including a standard calomel reference electrode (SCE) and a Pt wire counter electrode. The 2 mm diameter Pt disc working electrode was commercially obtained from CH Instruments Inc. The 1 mm diameter pBDD disc working electrode was produced in-house using diamond grown by Element 6^{TM}.

3.2.2 RDGE Droplet Dissolution

A schematic of the experimental setup is shown in Figure 3.2a. A circulating water jacket was filled with either deionised water or an aqueous solution of 5 mM jeffamine D230 and heated to 40, 50 or 70 °C. RDGE droplets of ca. 800 µm diameter were formed at the tip of a fine glass capillary (internal diameter ca. 40 µm) immersed in the aqueous phase. The capillary was connected via a Luer syringe needle attached to PTFE tubing (Cole-Palmer) to a 10 mL syringe (BD Plastipak) containing 5 mL of RDGE. A syringe pump (KD Scientific) using a flow rate of 400 µL/h was used to push RDGE from the syringe to the tip of the glass capillary. A PixeLINK© B700 camera positioned downwards was then used to take photographs of the droplet every 20 seconds for 2000

seconds as dissolution took place (see Figure 3.2b). These photographs were analysed in MATLAB© (see Appendix) to calculate the change in droplet diameter over time and thus the dissolution flux of RDGE moving from droplet into the aqueous phase.

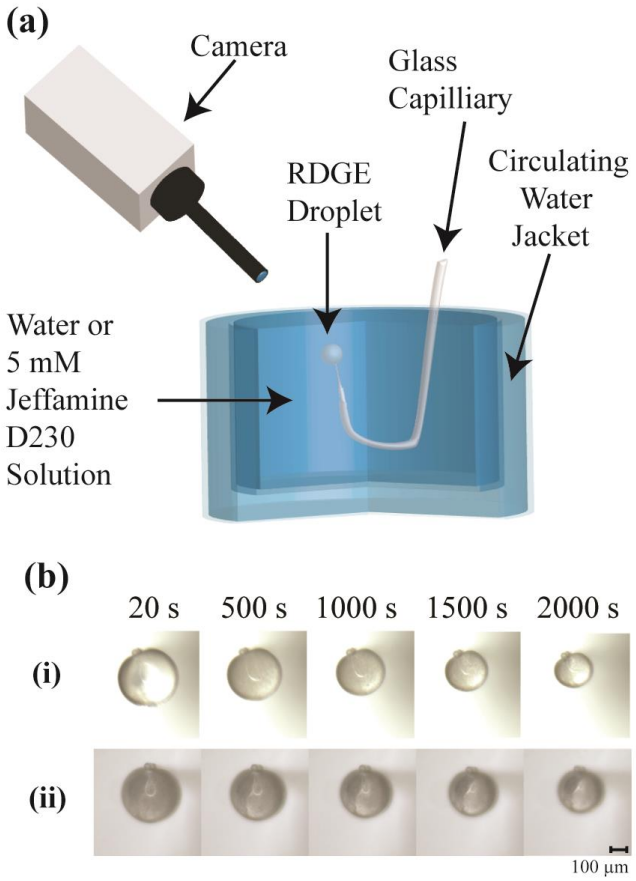

Figure 3.2 *(a) Experimental setup for time lapse microscopy of an RDGE droplet held in water or a 5 mM jeffamine D230 solution heated to different temperatures using a circulating water jacket. (b) Photographs of an RDGE droplet in (i) water or (ii) jeffamine D230 heated to 50 °.*

3.2.3 MEMED

3.2.3.1 Apparatus and Procedure

A schematic of the experimental setup used is shown in Figure 3.3. The set up for MEMED has been described previously.[17] In this study, droplets of RDGE containing jeffamine D230 (in a 2:1 molar ratio) were grown from a tapered glass capillary (internal diameter ca. 100 µm, see experimental for information on construction)[17] into a receptor phase of deionised water. A pH-sensitive microelectrode (see experimental

for information on construction and calibration) was placed in the receptor phase opposite the tapered glass capillary, held in the PTFE base using wax. The flow of the RDGE/jeffamine D230 organic phase was controlled by a high precision syringe pump (KD Scientific), with a flow rate of 800 µL/h to ensure fast refreshment of the interface. Potentiometric detection was used to measure the transfer of jeffamine D230 into the aqueous phase as the droplet expanded. Time stamped photographs were taken at intervals in the range of 20-300 ms of the expanding droplet using a PixeLINK© B700 camera. These were related the response of the pH sensitive probe to its distance from the droplet, from which the time dependent concentration profiles were obtained. All measurements were made at ambient temperature (21 °C ± 1 °C).

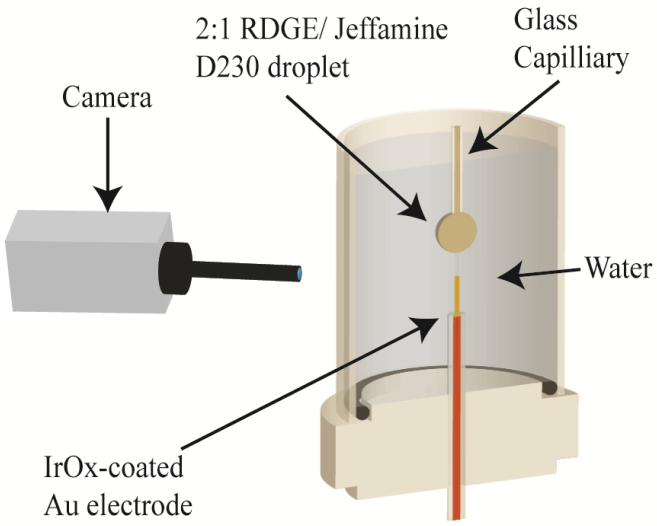

Figure 3.3 *Schematic of the experimental setup used for MEMED of a 2:1 RDGE/ jeffamine D230 droplet expanding towards a pH-sensitive IrOx-coated Au microelectrode in water.*

3.2.3.2 Electrochemical and Optical Measurements

Potentiometric measurements were carried out using a two electrode set up, consisting of the previously calibrated pH-sensitive microelectrode and a saturated calomel electrode (SCE). The potential was measured using a purpose-built voltage follower. An

external data acquisition card (NI USB-6211, National Instruments, Austin, TX) connected to a desktop PC was used to record open circuit potential (OCP)-time data.

Software written in LabVIEW© (National Instruments) recorded the OCP every 35-40 ms and ensured that photographs were taken during the same time period. Photographs were later analysed in MATLAB© (see Appendix) to measure the electrode-droplet separation as a function of time and thus directly relate the OCP to the distance between the droplet and the electrode. Previous electrode calibration data was then used to convert OCP measurements to pH and hence the concentration of jeffamine D230 in the aqueous phase.

3.3 Results and Discussion

3.3.1 Electrochemical Characterisation of RDGE and Jeffamine D230

Prior to the electrochemical monitoring of RDGE dissolution from aqueous droplets, it is important to first characterise the response when an electrode is placed into an RDGE solution. This will provide information on the electrochemical response of RDGE in different solvents, at different concentrations, using different electrode materials and at different scan speeds. Most importantly however, it will provide information on the exact electrochemical potential required to oxidise or reduce the molecule. This knowledge can then be used to develop a system capable of monitoring RDGE dissolution via the measurement of current generated from the application of a specific oxidising or reducing voltage.

3.3.1.1 Cyclic voltammetry of RDGE in aqueous acetonitrile (ACN)

As mentioned previously, CVs of RDGE in ACN using polycrystalline boron doped diamond (pBDD) and platinum (Pt) macroelectrodes were performed to identify the

electrochemical parameters of this system. Figure 3.4 shows background subtracted cyclic voltammograms for different concentrations of RDGE in a 0.1 M $NaClO_4$ solution made up of a 1.5:1 ratio of ACN and water. A pBDD macroelectrode was determined to be the most suitable electrode for this initial test due to the unique properties of diamond electrodes. These include wide potential windows, low background currents and high resistance to deactivation via fouling.[20]

The voltammograms show a linear relationship between the concentration of RDGE in solution and peak current generated, as well as confirming that RDGE can be successfully oxidised on a pBDD electrode surface. It is however interesting to note that the peak current (seen around 1.5 V) seems to shift to more positive potentials the higher the RDGE concentration. Also, the absence of a reverse reduction peak indicates that the oxidation of RDGE is irreversible.

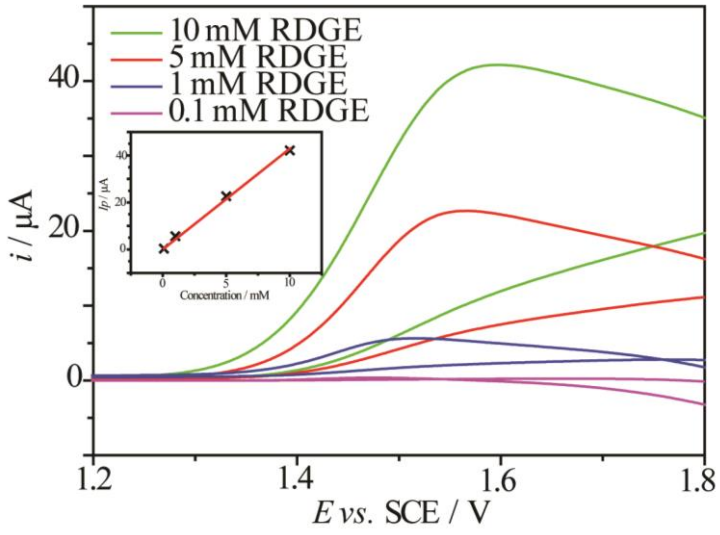

Figure 3.4 *Background subtracted cyclic voltammograms (CVs) of 10, 1, 5 and 0.1 mM RDGE in 0.1 M $NaClO_4$ (in a 1.5:1 ACN: H_2O solution) recorded using a 1 mm pBDD electrode using a scan speed of 100 mV/s. Inset plot shows linear relationship between peak current and concentration of RDGE in solution (R^2 = 0.99).*

The experiment was then repeated using a Pt macroelectrode instead of a pBDD macroelectrode. pBDD UMEs are currently difficult to fabricate, so it was deemed

necessary to explore if RDGE could be oxidised on electrode materials that can be used in UME fabrication (as UMEs are required for SECM). Figure 3.5 shows background subtracted cyclic voltammograms for different concentrations of RDGE recorded using a 2 mm diameter platinum macroelectrode.

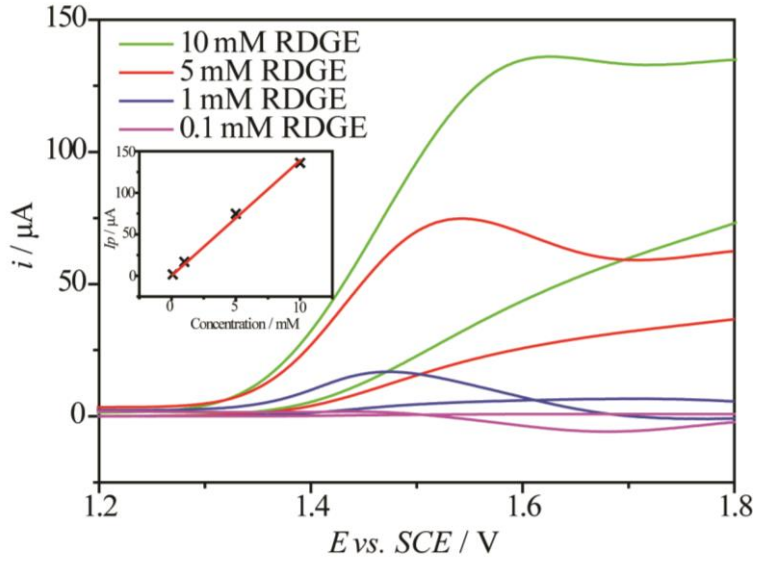

Figure 3.5 *Background subtracted CVs of 10, 1, 5 and 0.1 mM RDGE in 0.1 M $NaClO_4$ (in a 1.5:1 ACN: H_2O solution) recorded using a 2 mm diameter platinum electrode using a scan speed of 100 mV/s. Inset plot shows linear relationship between peak current and concentration of RDGE in solution (R^2 = 0.99).*

The CVs recorded on the platinum macroelectrode were similar to those recorded using the pBDD electrode, although peaks were less defined due to water electrolysis at higher potentials. Similar to Figure 3.4, a linear relationship between peak current and RDGE concentration was observed, as was the peak current shift towards higher potentials with increasing concentration.

3.3.1.2 Differential Pulse Voltammetry (DPV) and Cyclic Voltammetry of RDGE in water

As stated in the previous section, RDGE was dissolved in an ACN/water solution as it is almost immiscible in water. However, as the RDGE/Jeffamine D230 emulsion

polymerisation takes place in a water-only solvent system it will be more useful for mechanistic studies to electrochemically monitor epoxide dissolution in water alone.

As the experiments in section 3.3.1.1 had shown a shifting of the peak current with concentration, it was difficult to determine the exact potential at which RDGE oxidation was at its peak. Figure 3.6 shows the results of a DPV experiment carried out in order to determine the oxidation potential of RDGE. The background subtracted voltammograms for each RDGE concentration show peak current at around 1.3 V, which is lower than what was suggested in previous cyclic voltammetry studies (in both ACN:water and water systems). This is unsurprising, as DPV uses small potential steps to eliminate charging current contributions from changing the potential. The inset plot shows a non-linear relationship between RDGE concentration and peak current at 1.3 V, which suggests that the electrode surface is fouling during epoxide oxidation.

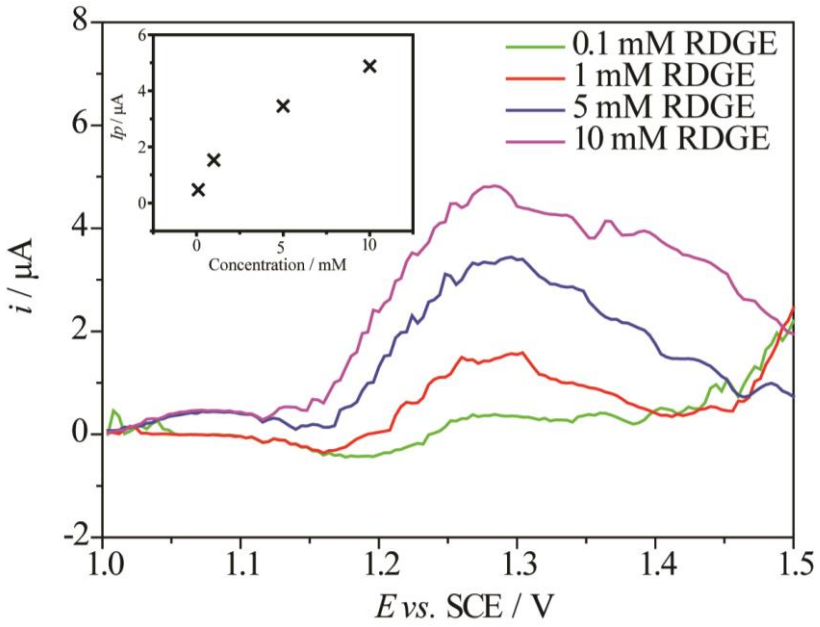

Figure 3.6 *Background subtracted DPVs of 10, 1, 5 and 0.1 mM RDGE in 0.1 M* $NaClO_{4\,(aq)}$ *recorded using a 1 mm diameter pBDD electrode using a scan speed of 100 mV/s. Inset plot shows relationship between peak current and concentration of RDGE in solution.*

As well as monitoring the current response when changing the concentration of a substance, changing the scan speed during a cyclic voltammogram can also provide insights into the processes taking place at an electrode surface. Figure 3.7 shows background subtracted CVs of 10 mM RDGE recorded using different scan speeds. A clear relationship can be seen between scan speed and peak current, with peak current shifting to higher potentials at faster scan rates.

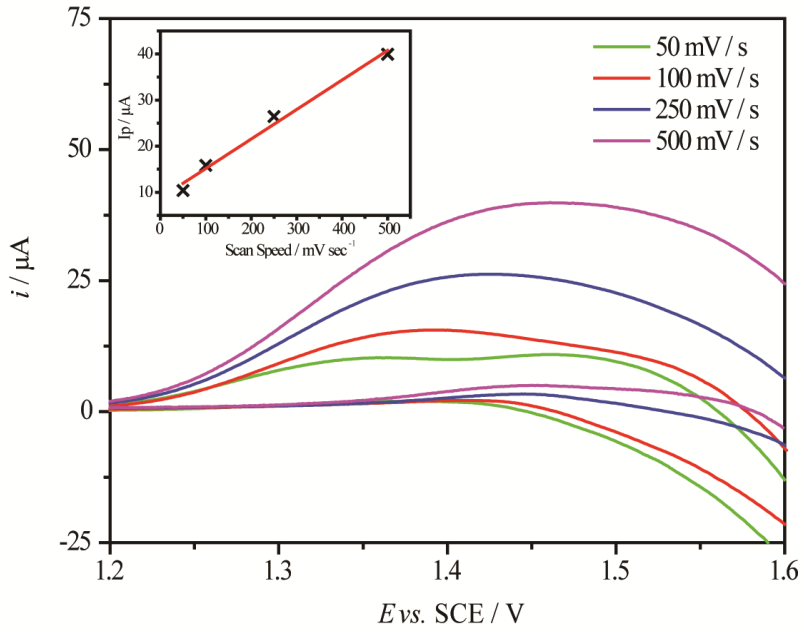

Figure 3.7 *Background subtracted CVs of 10 mM RDGE in 0.1 M $NaClO_{4\ (aq)}$ recorded using a 1 mm diameter pBDD electrode at scan speeds of 50, 100, 250 and 500 mV/s. Inset plot shows relationship between peak current and scan speed (R^2 = 0.98).*

It is interesting to note that at the lower scan speeds (50 and 100 mV / s) there seems to be two peaks visible, one around 1.35 V and the other around 1.5 V. It is possible that the second peak at 1.5 V is the oxidation of previously oxidised RDGE, made more prominent by the fact that a lower scan speed will cause the electrode to oxidise RDGE over a longer period of time.

The observations that peak current shifts to more positive potentials with concentration, that two peaks are observed at lower scan speeds, and that for DPV there is a non-linear relationship between current and concentration have led to the conclusion that electrode

surface fouling is taking place during RDGE oxidation. Repeated cycling also showed peak reduction over time. Although cleaning the electrode between each measurement provided reproducible data, it did not solve the problem of fouling during measurements. This will become an issue when using SECM on RDGE droplets, as it can be assumed that the closer to the RDGE droplet the electrode is placed the more fouled it will become. Therefore, attempts were made to find a method of cleaning the electrode *in situ*. Figure 3.8 is an example of this, showing CVs of different concentrations of RDGE on a previously clean electrode and after a 10 second -5 V pulse. The pulse was intended to clean the electrode after previous fouling; however as Figure 3.8b shows peak current remains both reduced and shifted to positive potentials which suggested that the electrode surface remained blocked.

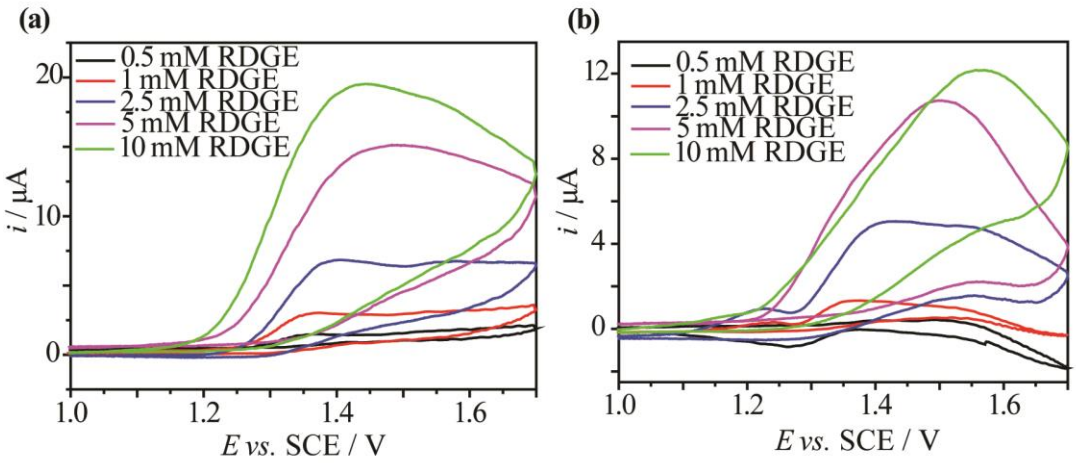

Figure 3.8 *(a) Background subtracted CVs of 0.5, 1, 2.5, 5 and 10 mM RDGE in 0.1 M* $NaClO_{4\,(aq)}$ *recorded using a clean 1 mm diameter pBDD electrode at a scan speed of 100 mV/s. (b) CVs taken after a 10 second pulse of -5 V, which was applied after the CVs in (a) were recorded.*

Other cleaning strategies were attempted with the aim of clearing the electrode surface of fouled product. Holding the potential at -6 V for 60 seconds produced CVs with higher currents that decreased with subsequent pulsing, which suggested that the electrode surface was not being completely cleaned. Scanning from 1 V to 4 V, with the

aim of cleaning the electrode surface using bubbles/H^+ ions produced during water electrolysis, also did not significantly improve the observed signal.

3.3.1.3 Cyclic Voltammetry of Jeffamine D230

In tandem with the electrochemical characterisation of RDGE, similar experiments were carried out using different concentrations of the amine monomer Jeffamine D230. Figure 3.9 shows cyclic voltammograms of different concentrations of Jeffamine D230 recorded using a 1 mm diameter pBDD electrode.

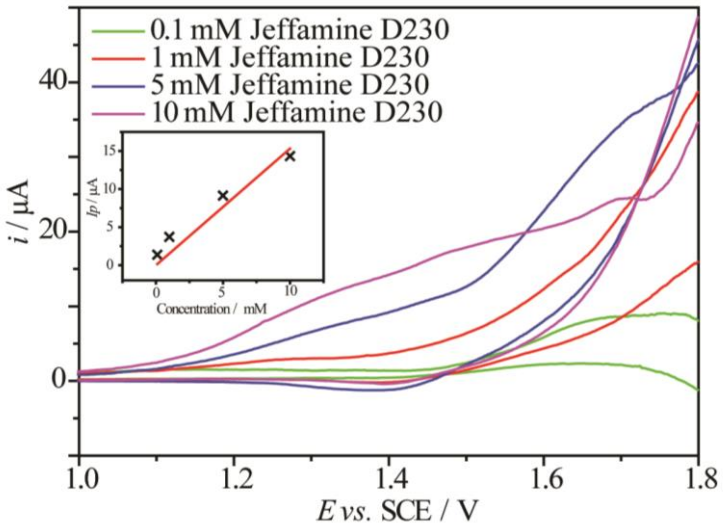

Figure 3.9 *Background subtracted CVs of 0.1, 1, 5 and 10 mM Jeffamine D230 in 0.1 M $NaClO_{4\,(aq)}$ recorded using a 1 mm diameter pBDD electrode at a scan speed of 100 mV/s. Inset plot shows relationship between peak current and concentration of Jeffamine D230 (R^2 = 0.96).*

The CVs show a clear relationship between the concentrations of Jeffamine D230 in solution and current around 1.4 V. However repeated cycling showed reduced peaks over time, indicating that Jeffamine D230 also fouls the surface of the electrode during oxidation. As the current peaks were unclear (most likely due to fouling) and the potential of oxidation was close to that of RDGE, it was decided that measuring the concentration of Jeffamine D230 as it moves out of RDGE carrier droplets into the aqueous phase by applying a potential would be unsuitable. Therefore, other techniques

were devised to monitor RDGE and jeffamine D230 transfer across the liquid/liquid interface that did not utilise the application of overpotential.

3.3.2 Characterisation of RDGE Droplet Dissolution

3.3.2.1 Time-lapse Microscopy of RDGE Droplet Dissolution in Water and 5 mM Jeffamine D230

As shown in Figure 3.10, RDGE droplet dissolution was characterised by forming similar sized RDGE droplets (c.a. 800 μm diameter) in a vessel containing either water or aqueous jeffamine D230 solution immersed in a controlled temperature cell and using time-lapse microscopy to monitor the change in size. Image analysis of droplet size by time-lapse microscopy was then used to determine the radius of the RDGE droplet as a function of time.

Typical results of this analysis can be seen in Figure 3.10, which clearly shows how varying the temperature of the aqueous solution will affect the rate of RDGE droplet dissolution. It appears that higher temperatures lead to a faster initial droplet dissolution rate. However, it is apparent that over time the rate decreases dramatically, indicating a shutting off of the dissolution reaction. Moreover, the cessation of dissolution occurs earlier the higher the aqueous receptor solution temperature. An explanation is that as RDGE dissolves, it may react with water and homopolymerise. As the epoxide polymerises at the liquid-liquid interface, or near the interface, it adsorbs to the droplet surface, resulting in a barrier layer that impedes dissolution. This hypothesis is supported by the work of Qu *et al.*, who have shown that water at higher temperatures can promote the ring-opening of epoxides by acting as a modest acid catalyst.[21] Ring-opening of epoxides will form alcohol groups, which have been shown to react with adjacent epoxide groups under hot water conditions to form polyethers.[22]

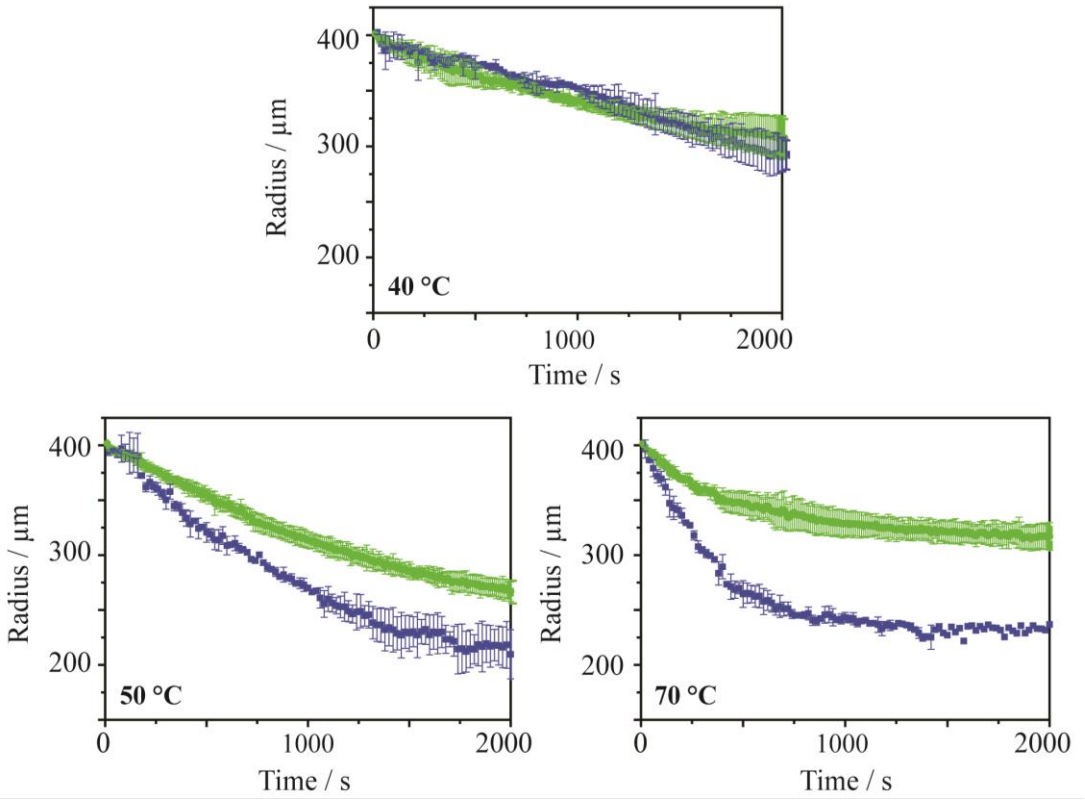

Figure 3.10 *Averaged radius versus time profiles (3-5 runs) for an RDGE droplet held in water (■) or 5 mM jeffamine D230 aqueous solution (●) heated to 40, 50 and 70 ℃.*

RDGE droplet dissolution into aqueous jeffamine D230 solution (5 mM) is also influenced by temperature (see Figure 3.10). The initial rate of RDGE droplet dissolution (until droplet reaches 350 µm radius) appears to increase as the temperature is increased; however this rate decreases in a temperature-dependent manner, qualitatively consistent to the results for droplet dissolution in water. It is also clear that in the temperature range 50 °C – 70 °C, the jeffamine D230 has a significant impact on the dissolution rate. This is reasonable because hot water-promoted ring-opening of epoxides has been shown to be enhanced in the presence of amines in comparison to without.[21] The closely similar dissolution profiles for RDGE droplets in the presence of jeffamine D230 and water at 40° remain similar, indicating sluggish like curing or homopolymerisation on the timescale considered.

The overall shape of these profiles can be described as unusual, as you would expect droplet radius change to speed up over time as the surface area:volume ratio increases. It could be reasonable to suggest that when the dissolution profile is linear there is proportional relationship between droplet curing and droplet dissolution.

In an attempt to quantify droplet dissolution kinetics, the droplet radius calculated from image analysis of each frame in the time-lapse was used to calculated droplet volume and surface area. Given the molar volume of RDGE of 183.67 $cm^3 mol^{-1}$, this then ready allowed initial fluxes in the two media and at the range of temperatures to be calculated. These are shown in Table 3.1, which compares the average initial flux of RDGE out of RDGE droplets in water and aqueous jeffamine D230. Average initial dissolution flux values increase dramatically with increasing temperature for RDGE droplets in water, but at equivalent temperatures in aqueous jeffamine D230 they are comparatively lower. It can also be noted that as the temperature increases, the difference between the initial flux of RDGE from a droplet in water and the initial flux of RDGE from a droplet in an aqueous jeffamine D230 solution is much more significant. The higher the temperature, the more the RDGE-jeffamine D230 curing reaction rate is enhanced and thus the earlier the blocking of dissolution occurs.

Table 3.1 *Initial flux (with standard error) of RDGE into the aqueous phase from droplets held in either water or aqueous jeffamine D230 heated to different temperatures.*

	40 °C	**50 °C**	**70 °C**
Initial flux in water / nmol $cm^{-2} s^{-1}$	37.6±5.9	86.4±4.7	234.0±3.5
Initial flux in 5 mM jeffamine D230 / nmol $cm^{-2} s^{-1}$	35.1±0.9	52.5±3.9	68±6.2

3.3.3 Characterisation of the Jeffamine D230 Transfer across an Oil Droplet-Water Interface using Local pH Measurements

3.3.3.1 MEMED of an RDGE Droplet Containing Jeffamine D230

The concentration of jeffamine D230 adjacent to the moving droplet surface was calculated from pH (potentiometric) measurements taken during MEMED. The concentration of a weak base can be calculated from the pH of the solution so long as the pK_a is known. This is achieved using the Henderson-Hasselbalch equation:

$$pOH = pK_b + \log\frac{\left[BH^+\right]}{\left[B\right]} \tag{3.1}$$

where BH^+ denotes the conjugate acid of the corresponding base B. This equation can be rearranged into the form:

$$pK_b = pOH - \log\frac{\left[BH^+\right]}{\left[B\right]} \tag{3.2}$$

By taking the negative anti-log of each side, the equilibrium constant K_b can be derived:

$$K_b = \frac{\left[BH^+\right]\left[OH^-\right]}{\left[B\right]} \tag{3.3}$$

The pK_a of jeffamine D230 has been calculated to be ~9.4 (Ref: Syngenta Jealott's Hill International Research Centre, Bracknell), which can be converted to a K_a value of 3.98 x 10^{-10}. This value can then be used to calculate the K_b value using the relationship:

$$K_b = \frac{K_w}{K_a} \tag{3.4}$$

where K_w is self-ionization constant of water. The pH of a solution can be converted into a pOH value using the equation:

$$pOH = 14 - pH \tag{3.5}$$

from which the concentration of OH^- ions generated by the addition of the base can be derived:

$$\left[OH^-\right] = 10^{-pOH} \tag{3.6}$$

If the ratio between the concentration of the conjugate acid of the base and OH^- ions is assumed to be 1:1, equation 3.3 can be rearranged to find the concentration of base added that has not been protonated:

$$\left[B\right] = \frac{\left[BH^+\right]\left[OH^-\right]}{K_b} \tag{3.7}$$

The total concentration of base in the solution can then be calculated by adding [B] and $[BH^+]$ together. However, as each jeffamine D230 molecule contains two amine groups this value must halved to give the true concentration.

As detailed in chapter 2, pH-sensitive microelectrodes for jeffamine D230 detection were fabricated by the deposition of an iridium oxide (IrOx) film on to a 75 µm diameter Au wire electrode. Cyclic voltammetry of Au microelectrodes in 0.1 M H_2SO_4 (scan rate 0.1 V s^{-1}) was carried out before and after electrochemical deposition to confirm iridium oxide film formation, as shown in Figure 3.11 .

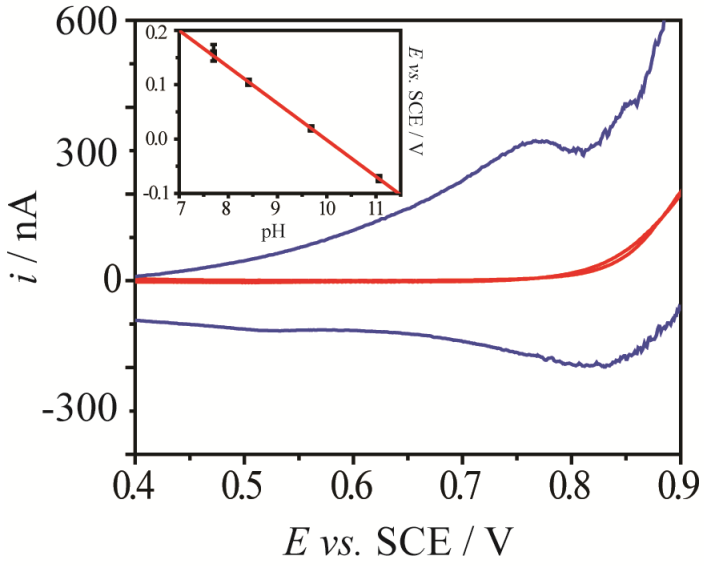

Figure 3.11 *Cyclic voltammograms at a 75 µm diameter Au wire electrode before (-) and after (-) electrodeposition of iridium oxide; 0.1 M H_2SO_4, scan rate 0.1 V s^{-1}. Inset shows potential-pH calibration of a typical IrOx-coated Au microelectrode.*

The anodic peak at 0.75 V corresponds to the oxidation of Ir(III) to Ir(IV) and the cathodic peak corresponds to the reduction of Ir(IV) back to Ir(III). Similar peak potentials for the oxidation of Ir(III) in H_2SO_4 have been reported in the literature.[23, 24]

The pH-sensitive potentiometric response of iridium oxide electrodes is governed by the redox process: [25, 26]

$$2\left[IrO_2(OH)_{2-x}\bullet(2+x)H_2O\right]^{(2-x)-}+(3-2_x)H^++2e^-\longleftrightarrow\left[Ir_2O_3(OH)_3\bullet 3H_2O\right]+3H_2O \quad (3.8)$$

This process means that iridium oxide electrodes often exhibit a super-Nernstian pH response, with calibration slopes reported ranging from -59 to -90 mV per pH unit.[27] A typical calibration plot for a pH-sensitive Au microelectrode is shown in Figure 3.11 inset. Calibration slopes of -68 mV/pH ± 2 mV were obtained over pH range 7.5-11. Previous pH probe calibrations in the literature have indicated that the pH response of iridium oxide films can be affected by the constituents of the solution in which they are placed.[28] Thus, to ensure that the potentiometric response of the electrode would adequately reflect the pH change of water as jeffamine D230 transfers into the aqueous phase, pH microelectrode probe calibration was carried out using aqueous solutions of jeffamine D230. The pH of the aqueous jeffamine D230 calibration solutions ranged between pH 7.75 to 11.06 (measured using a conventional glass pH electrode, S20 SevenEasy™ pH, Mettler Toldeo). The open circuit potential (OCP) of the pH-sensitive microelectrode versus an SCE was measured for 100 seconds in each solution in order of increasing basicity. This was then reversed and repeated to provide at least three measurements at each pH and to ensure that the pH probe was stable.

MEMED experiments were carried out using a 2:1 molar ratio of RDGE and jeffamine D230 as the organic phase and deionised water as the receptor phase. Raw experimental data for jeffamine D230 transport studied by potentiometric detection is shown in Figure 3.12a. Shown alongside are photographs taken a various times during the potentiometric-time transient. This indicates that the voltage measured remains essentially constant until the surface of the drop is very close to the probe electrode, between positions (iii) and (iv), when the potentiometric response changes rapidly with time in a manner indicating a rapid increase in pH. Note that a key feature of this type of pH electrode is its rapid response time[25] so that it can faithfully follow the pH gradient in the boundary layer near the droplet.

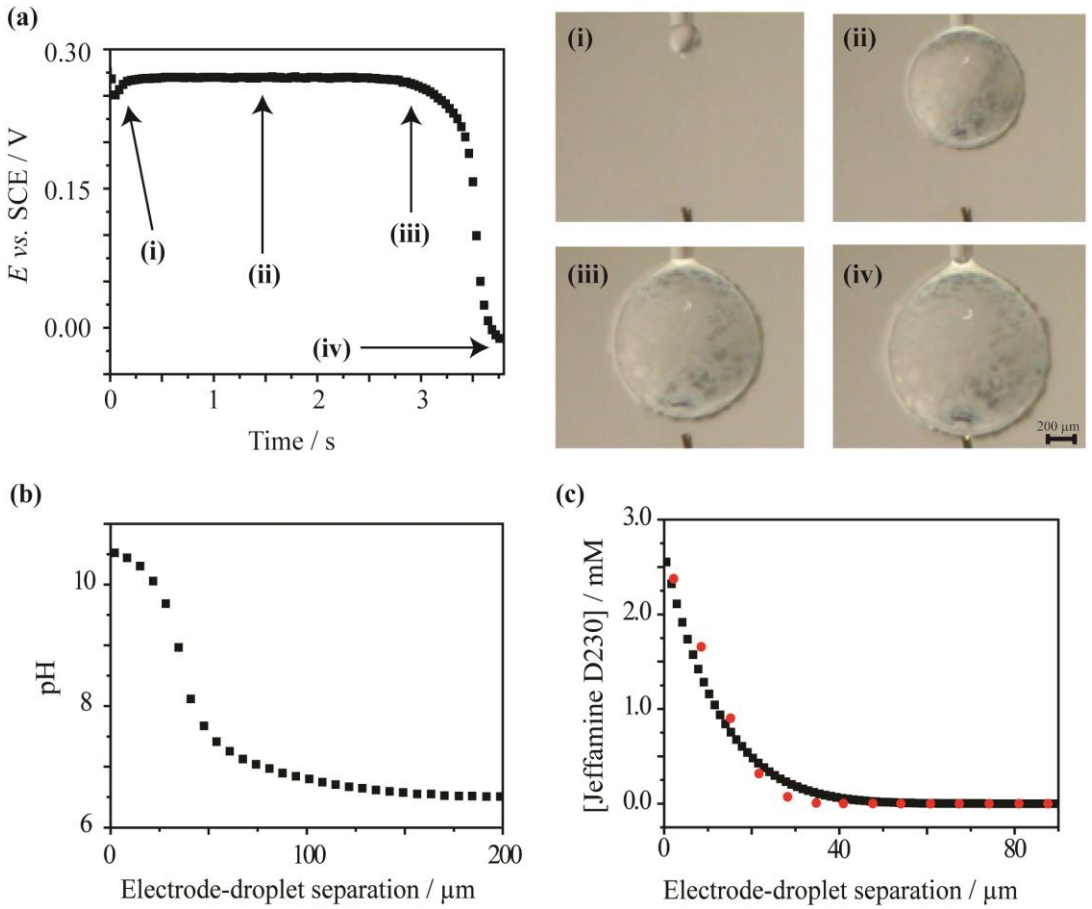

Figure 3.12 *(a) A typical potentiometric transient recorded at an IrOx-coated Au microelectrode during the transfer of jeffamine D230 into the aqueous phase from a growing 2:1 RDGE/jeffamine D230 drop surface. Images (i)-(iv) show the relative positions of the capillary, drop and IrOx-coated Au microelectrode and correspond to the points indicated on the transient. (b) Calculated pH versus electrode-droplet separation. (c) Calculated jeffamine D230 concentration versus electrode-droplet separation (•). Alongside is the theoretical concentration versus separation profile (■) generated using a moving plane model built in COMSOL software (explained in section 3.3.3.2).*

Analysis of time lapse photographs such as those in Figure 3.12a (i)-(iv) allowed the electrode-droplet separation to be deduced as a function of time. Potentiometric measurements were converted to corresponding pH values using a calibration curve such as that shown in Figure 3.11. Figure 3.12b shows a typical resulting pH versus electrode-droplet separation profile. As the droplet interface approached within a sufficiently close distance to the probe electrode (electrode-droplet separation ≤ 100 µm), the pH increase corresponds to a local jeffamine D230 concentration increase. pH

measurements were then converted into concentration of jeffamine D230, with a typical profile shown in Figure 3.12c. FEM modelling, as described in section 3.3.3.2, generated theoretical concentration profiles that matched well with experimental data for an interfacial flux value of 17.5±5.1 nmol cm^{-2} s^{-1}. This highlights how MEMED provides new quantitative information on this initial liquid reactive interface system.

3.3.3.2 FEM Simulation of Jeffamine D230 Transfer from an Expanding Droplet

Previous MEMED studies have solved mass-transport problems for symmetrically expanding spheres[14, 16, 29], however as the droplets in this study do not expand in a symmetrical manner it was instead assumed that treating the drop surface approaching the electrode as a moving plane would be a more accurate approximation. The convective-diffusion equation which describes this case and is used as the basis of this model is:[17]

$$\frac{\partial c_i}{\partial t} = D_x \frac{\partial^2 c_x}{\partial r^2} - 2v_r \frac{\partial c_x}{\partial r} \tag{3.9}$$

where D_x is the diffusion coefficient (m^2 s^{-1}), c_x is the concentration of jeffamine D230 (mol m^{-3}), t is time (s) and r is the spherical coordinate measured from the centre of the drop (m). The variable v_r is the convective velocity (m s^{-1}) of the moving surface of the expanding drop and is given by:

$$v_r = \frac{q}{4\pi}\left(\frac{1}{r^2} - \frac{1}{r_0^2}\right) \tag{3.10}$$

where q is the volume flow rate ($m^3\ s^{-1}$), which was modified in the model to ensure that the total drop time, $t_{d,}$ correlated with the total drop time recorded experimentally. The (time-dependent) drop radius, $r_{0,}$ was calculated using the equation:

$$r_0 = \left(\frac{3q}{4\pi}\right)^{1/3} t^{1/3} \tag{3.11}$$

where t is any time less than $t_{d.}$ The mass-transport of a species described by equation 3.9 was solved for the domain within the model where $r > r_0$, which describes the aqueous phase outside the droplet. Mass-transport within the droplet was not considered, as depletion and hence diffusional effects within the droplet are negligible under these experimental conditions. The boundary condition placed on this domain can be described as:

$$r \longrightarrow \infty : c = 0 \tag{3.12}$$

The surface of the drop during MEMED can be described by Fick's first law of diffusion which is:

$$j = -D_x \frac{\partial c_x}{\partial r} \tag{3.13}$$

where j is the interfacial flux of the species of interest (mol $m^{-2}\ s^{-1}$), c_x is the concentration of the species of interest (mol m^{-3}) and D_x is the diffusion coefficient ($m^2\ s^{-1}$). Diffusion coefficient, $D_{x,}$ was calculated using the Wilke-Chang formula :[30]

$$D = \frac{7.4\times10^{-8}\left(\phi\times M_B\right)^{\frac{1}{2}} T}{\mu\times V_A^{\,0.6}} \tag{3.14}$$

where D is the diffusion coefficient ($cm^2\ s^{-1}$), $\emptyset$ is the association parameter for the solvent, M_B is the molecular weight of the solvent ($g\ mol^{-1}$), μ is the viscosity of the solvent (cP), V_A is the molecular volume of the molecule ($cm^3\ mol^{-1}$) calculated by the LeBas method[31] and T is temperature (K). This approach is appropriate in that it will give diffusion coefficient values for jeffamine D230 in water, however it should be noted that this formula is known to have an error of around 13%.[32]

The values used and calculated for jeffamine D230 using the Wilke-Chang estimation are shown in Table 3.2.

Table 3.2 *Parameters used and diffusion coefficient calculated for jeffamine D230 in water at 21 °C using the Wilke-Chang estimation.*

Parameter	$\emptyset$	M_B / **g mol^{-1}**	μ / **cP**	V_A / **cm^3 mol^{-1}**	T / **K**	D / **cm^2 s^{-1}**
Value at 21 °C	2.6	18	1.002	296.4	294.15	4.89×10^{-6}

To quantify the flux of jeffamine D230 partioning into the aqueous phase, a finite element method (FEM) model was built to simulate mass-transport from an expanding droplet as a function of time. The three domains simulated are shown in Figure 3.13. The uni-axis spatial geometry was built consisting of a line from 0 mm (P_a) to 5 mm (P_d), with a fixed point at 0.682 mm (P_c) to simulate the position of the electrode in terms of distance from the centre of the droplet. Another point at 1 nm (P_b) was built to simulate the surface of the droplet; during the simulation this was displaced in accordance with the droplet expansion equation 3.11. The flux value at P_b was fixed to achieve the best correlation between experimental data with the model.

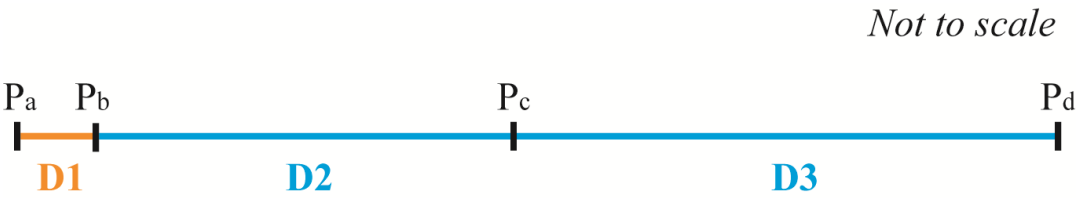

Figure 3.13 *Schematic of the 1D model built in COMSOL to simulate the local concentration change at a fixed point (the electrode; P_c) as a droplet ($P_a \rightarrow P_b$) expands towards it.*

The droplet (domain D1) was defined as the distance between P_a and P_b. The convective-diffusion equation 3.9 was solved only for domains D2 and D3, which represents the distance between the droplet surface and the electrode and the distance between the electrode and the edge of the simulation geometry, respectively. The diffusion coefficient of jeffamine D230 was set to 4.4 x 10^{-6} cm^2 s^{-1}. The initial concentration of jeffamine D230 in domains D2 and D3 was set as zero.

A mesh was built with an element length of 10^{-11} m at point P_b; the remaining domains were meshed continuously at a growth rate of 1.01x per element from this point until they reached a maximum size of 1 µm at the edge of the simulation domain. Free deformation of meshing within all domains allowed for mesh displacement of point P_b in accordance with equation 3.11. The mesh consisted of 24354 elements and was solved in a time-dependent manner for the duration of droplet experiments using the MUMPS solver within COMSOL.

3.4 Conclusions

The aim of this chapter was to investigate interfacial processes that take place during an epoxy-amine emulsion polymerisation reaction currently used in the agrichemical industry for active ingredient encapsulation. Initial investigations focused on electrochemical characterisation of the main chemical constituents used in the

polymerisation process (RDGE and Jeffamine D230), as it was hoped that this would pave the way for the development of voltammetric methods for the measurement of their transfer across a liquid-liquid interface. However, cyclic voltammetry and differential pulse voltammetry experiments have shown that both RDGE and Jeffamine D230 will block electrode surfaces following their electrochemical oxidation. This in turn will lead to concentration measurements that are not quantitative, meaning that voltammetric techniques were deemed unsuitable for the quantification of the interfacial processes taking place within this particular polymerisation system.

As a consequence of unsuitability of voltammetric methods, the interfacial processes that take place during an emulsion polymerisation reaction have been studied using a mixture of MEMED and time-lapse microscopy. Local pH measurements recorded during MEMED of 2:1 molar ratio droplets of RDGE and jeffamine D230 and subsequent FEM modelling have quantified jeffamine D230 transfer from the organic phase into the aqueous phase, giving a value of 17.5 ± 5.1 nmol cm^{-2} s^{-1}.

Time-lapse microscopy of RDGE droplets held in either deionised water or an aqueous solution of jeffamine D230, at different temperatures, has been used to monitor the effect of solution and temperature on RDGE dissolution into the aqueous phase and the interfacial curing reaction of the amine and the epoxide. Interestingly, without amine, RDGE appears to homopolymerise in water at higher temperatures, but the addition of jeffamine D230 promotes the interfacial curing reaction so that it becomes faster than the RDGE homopolymerisation reaction. With increasing resorcinol diglycidyl ether flux values at higher temperatures, we expect higher concentrations of resorcinol diglycidyl ether to be present in the aqueous phase adjacent to the oil phase droplet. Alongside the influence of thermal effects on the kinetics and the fast transfer of the jeffamine D230 into the aqueous phase, these effects have the potential to influence the

density of microcapsules produced by this technology. For example, with curing close to the liquid-liquid interface and in the aqueous phase, it can be postulated that oligomers formed from the curing reaction will cross-link at the interface, which could lead to PMPs with a heterogeneous density. This would influence the extent of AI inclusion and the rate of release upon PMP wall decomposition. The studies herein provide vital chemical insight on monomer transfer and reactivity that should be valuable for deeper understanding of the consequences for PMP morphology.

3.5 References

1. C. C. Riccardi, H. E. Adabbo and R. J. J. Williams, *J. Appl. Polym. Sci.*, 1984, **29**, 2481-2492.
2. A. Moroni, J. Mijovic, E. M. Pearce and C. C. Foun, *J. Appl. Polym. Sci.*, 1986, **32**, 3761-3773.
3. R. Mezzenga, L. Boogh and J. A. E. Månson, *J. Polym. Sci., Part B: Polym. Phys.*, 2000, **38**, 1893-1902.
4. C. Byrne, G. Hagnauer and N. Schneider, *Polym. Compos.*, 1983, **4**, 206-213.
5. A. N. Netravali, R. E. Fornes, R. D. Gilbert and J. D. Memory, *J. Appl. Polym. Sci.*, 1985, **30**, 1573-1578.
6. P. Johncock, *J. Appl. Polym. Sci.*, 1990, **41**, 613-618.
7. S. Choi, A. P. Janisse, C. Liu and E. P. Douglas, *J. Polym. Sci., Part A: Polym. Chem.*, 2011, **49**, 4650-4659.
8. A. Safavi, N. Iranpoor and L. Fotuhi, *Bull. Chem. Soc. Jpn.*, 1995, **68**, 2591-2594.
9. K. Boujlel and J. Simonet, *Electrochim. Acta*, 1979, **24**, 481-487.
10. M. Masui, H. Sayo and Y. Tsuda, *Journal of the Chemical Society B: Physical Organic*, 1968, DOI: 10.1039/J29680000973, 973-976.
11. C. K. Mann, *Anal. Chem.*, 1964, **36**, 2424-2426.
12. A. Adenier, M. M. Chehimi, I. Gallardo, J. Pinson and N. Vilà, *Langmuir*, 2004, **20**, 8243-8253.
13. W. H. Chan, K. K. Shiu and X. H. Gu, *Analyst*, 1993, **118**, 863-867.
14. C. J. Slevin and P. R. Unwin, *Langmuir*, 1997, **13**, 4799-4803.
15. J. Zhang and P. R. Unwin, *Phys. Chem. Chem. Phys.*, 2000, **2**, 1267-1271.
16. J. Zhang, J. H. Atherton and P. R. Unwin, *Langmuir*, 2004, **20**, 1864-1870.
17. C. J. Slevin and P. R. Unwin, *Langmuir*, 1999, **15**, 7361-7371.

18. P. B. Duncan and D. Needham, *Langmuir*, 2006, **22**, 4190-4197.

19. P. Poesio, G. P. Beretta and T. Thorsen, *Phys. Rev. Lett.*, 2009, **103**, 064501.

20. J. V. Macpherson, *PCCP*, 2015, **17**, 2935-2949.

21. Z. Wang, Y. Cui, Z. Xu and J. Qu, *J. Org. Chem.*, 2008, **73**, 2270-2274.

22. C. J. Morten, J. A. Byers, A. R. Van Dyke, I. Vilotijevic and T. F. Jamison, *Chem. Soc. Rev.*, 2009, **38**, 3175-3192.

23. D. O. Wipf and F. Ge, *Anal. Chem.*, 2000, **72**, 4921-4927.

24. J. E. Baur and T. W. Spaine, *J. Electroanal. Chem.*, 1998, **443**, 208-216.

25. B. P. Nadappuram, K. McKelvey, R. Al Botros, A. W. Colburn and P. R. Unwin, *Anal. Chem.*, 2013, **85**, 8070-8074.

26. E. Bitziou, D. O'Hare and B. A. Patel, *Anal. Chem.*, 2008, **80**, 8733-8740.

27. H. A. Elsen, C. F. Monson and M. Majda, *J. Electrochem. Soc.*, 2009, **156**, F1-F6.

28. P. Steegstra and E. Ahlberg, *Electrochim. Acta*, 2012, **76**, 26-33.

29. J. Zhang, C. J. Slevin, L. Murtomäki, K. Kontturi, D. E. Williams and P. R. Unwin, *Langmuir*, 2001, **17**, 821-827.

30. C. R. Wilke and P. Chang, *A. I. Ch. E. Journal*, 1955, 264-270.

31. J. S. Gulliver, *Introduction to chemical transport in the environment*, Cambridge University Press, 2007.

32. R. Sitaraman, S. H. Ibrahim and N. R. Kuloor, *Journal of Chemical & Engineering Data*, 1963, **8**, 198-201.

Chapter 4

Investigating Poly(Urea) Film Formation at a Micro-Liquid/Liquid Interface

This chapter describes the use of electrochemical impedance spectroscopy and scanning electron microscopy to investigate how different reaction conditions will affect the formation of a poly(urea) film at a micro-liquid/liquid interface. The reaction studied was between polymethylene polyphenylisocyanate (PMPPI) and toluene 1,6-diisocyanate (TDI) in the DCE phase and polyethylenimine (PEI) or hexamethylene-1,6-diamine (HMDA) in the aqueous phase, which was used as a model for the formation of a microcapsule wall. Initially, cyclic voltammetry was used to find a suitable DC potential for EIS experiments where poly(urea) film formation would not be disturbed by ion transfer across the liquid/liquid interface. Electrochemical impedance spectra were then recorded before and after films formed both with and without the addition of PEI or HMDA monomers to the aqueous phase. Circuit diagram modelling of the resulting impedance spectra found that film formation caused an increase in interfacial resistance and a decrease in interfacial capacitance. The tendency towards more ideal capacitive behaviour at the interface also suggested that the film formed was compact. Films formed in the absence of additional amine monomers had a lower interfacial resistance and less ideal interfacial capacitance. This observation, combined with SEM imaging, suggested that they were more porous compared to those formed in the presence of additional amine monomers. Impedance was measured as a

function of time to investigate the influence of monomer concentration on film formation. It was found that the rate of poly(urea) film formation will remain constant until the concentration of isocyanate monomers is reduced below a threshold, where it becomes concentration-dependent. The availability of amine monomers and their ability to insert into the liquid/liquid interface will also influence the rate of film formation. Film formation via isocyanate monomer hydrolysis was shown to be slow compared to when additional amine monomers were present. Film formation appeared to be stable at higher concentrations but became more unstable at lower concentrations. This was attributed to the mechanism of film growth, which was thought to progress via the deposition of poly(urea) at nucleation sites that grow and eventually merge to form a single film. Film formation using different molar ratios of isocyanate was also investigated. Both the rate of film formation and the appearance of films after SEM imaging seemed similar, suggesting that despite the change in molar ratio the more reactive TDI monomer remains the dominant reactant during film formation. Increasing the temperature at which poly(urea) films form has also been shown to increase the rate of reaction and thus affect the structure of the resulting film.

4.1 Introduction

Film formation at liquid–liquid interfaces plays an important role in many different biological and industrial processes. Interfacial polymerisation (IP) processes in particular have been utilised in industry for the synthesis of thin film composite membranes, gas separation membranes and microcapsules for controlled release of AIs such as agrichemicals. One method of microcapsule formation, which relies on the hydrolysis of an isocyanate at the interface between two immiscible liquids to form a poly(urea) shell, is conceptually shown in Figure 4.1.

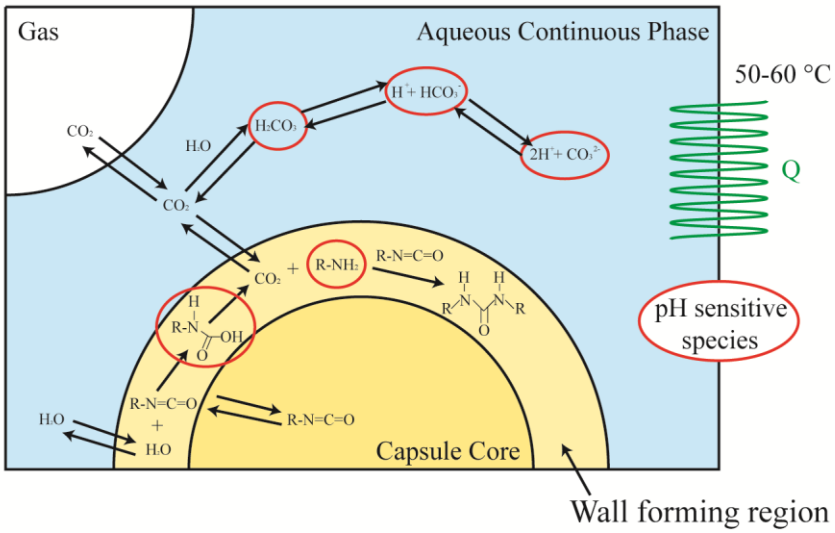

Figure 4.1 *A conceptual model of isocyanate hydrolysis at an immiscible liquid-liquid interface and the reactions that follow to form a poly(urea) capsule.*

The exact method used for the preparation of these poly(urea) capsules is mentioned in more detail in Chapter 1 under methods of microcapsule formation. Essentially, hydrophobic isocyanate monomers in an organic solvent are dispersed in a continuous aqueous phase as an emulsion, reacting with water at the liquid-liquid interface to eventually form a poly(urea) wall. Microcapsules can also be formed by the addition of a hydrophilic amine monomer to the aqueous phase, which will react with the isocyanate monomers alongside amine monomers generated following the isocyanate hydrolysis reaction to form poly(urea). Despite the widespread use of this process in industry, the mechanism of wall formation remains poorly understood. As the microstructure of the polymer wall will affect properties such as film density and thus release rates,[1, 2] the development of analytical methods that could bring new insight into the IP mechanism would be highly desirable. Subsequent improved understanding of the polymer precipitation mechanism may lead to enhanced safety and cost effectiveness during industrial scale up.

4.1.1 Experimental and Modelling Studies of Isocyanate IP

There have been a number of experimental and theoretical studies into the IP of isocyanates. Pearson *et al*. used infrared spectroscopy to follow the reduction in the concentration of isocyanate groups during the IP of an isocyanate with a diol.[3] A conceptual model based upon their results suggested that the interfacial reaction was controlled by a mixture of kinetic parameters and the mass transfer by diffusion of the diol into the organic phase. A similar model for the IP of hydrophobic monomer hexamethylene-1,6-diisocyanate (HMDI) and hydrophilic monomer HMDA was employed by Yadav *et al*.[4] This study combined mathematical modelling with experimental data collected by monitoring the pH of the continuous phase during the curing reaction to find time of encapsulation. The size of microcapsules was found to depend on the time of encapsulation, which was either a proportional relationship in the case of the kinetically-controlled formation (small microcapsules) or proportional to the square of size in the case of diffusion-controlled formation (large microcapsules). This work was then built upon to consider the effect of ionic equilibria in the aqueous phase, as $–NH_2$ functional groups will exist in different forms depending on the pH of the media.[1] This is an important factor to consider as it has been suggested that only the protonated form can partition into the site of the reaction.[5]

More recently, Wagh *et al*. have used on-line pH measurements during IP of HMDI and HMDA to determine that solvent polarity will influence the reaction rate to a much greater extent than the partioning coefficient of the hydrophilic monomer into the organic phase.[6] The experimental data collected during this study was used to test a model for IP built by Dhumal *et al.*,[7] which modified a similar model by Karode *et al.* to predict not only reaction kinetics but also evolution over time of film thickness, mass

crystallinity and MWD.[8] The model by Dhumal *et al.* has since been applied to both spherical and flat film geometries.[9]

Several studies have been carried out focusing more specifically on the mechanism of the isocyanate hydrolysis reaction. Raspoet *et al.* have used a combination of experimental and theoretical results to show that the hydrolysis reaction involves a chain of water molecules, with a second-order dependence on water during its nucleophilic addition across the N=C bond.[10] These finding were subsequently applied to computational studies by Ivanova *et al.*, who compared the effect of different substituents on the rate of isocyanate hydrolysis.[11]

4.1.2 Electrochemical Impedance Spectroscopy (EIS)

Electrochemical impedance spectroscopy has been shown to be a powerful technique for studying electrochemical processes.[12] For example, it has been used to characterise self-assembled monolayers on electrode surfaces,[13] electrochemical deposition of polymer layers[14], solvent effects on doped polymer[15] and mechanisms of ion transport within films.[16-18]

4.1.2.1 Studying the Liquid-Liquid Interface Using EIS

EIS has been used to study a wide range of liquid/liquid interfaces.[19, 20] For example, Samec *et al.* have explored the effect of interfacial capacitance and solvent viscosity on the kinetics of tetraethylammonium ion transfer across a water/*o*-nitrophenyl octyl ether interface.[21, 22] More recently, Silver *et al.* have used EIS to quantify tetraethylammonium ion transfer kinetics across the water/1,2-dichloroethane interface.[23]

The effect of polymer films on ion transport at a liquid/liquid interface has been examined using EIS.[24, 25] The formation of polymer films at liquid/liquid interfaces has

also been studied, however so far these investigations have been limited to electropolymerisation systems.[26-28] On the bulk scale, EIS has been used to characterise the emulsion polymerisation of styrene online.[29] However, although this study could provide information on particle size, polymerization rate and monomer conversion, it could not provide information on film formation kinetics.

This chapter aims to examine the interfacial processes that take place during the IP of isocyanates to form poly(urea). The formation of a poly(urea) film at a micro water/1,2-dichloroethane interface was probed using cyclic voltammetry and EIS in the prospect of improving understanding of IP mechanism at the liquid/liquid interface.

4.2 Experimental

Micropipettes were fabricated as described in chapter 2 of this thesis. Cyclic voltammetry and EIS experiments employed an electrochemical cell setup as shown in Figure 4.2.

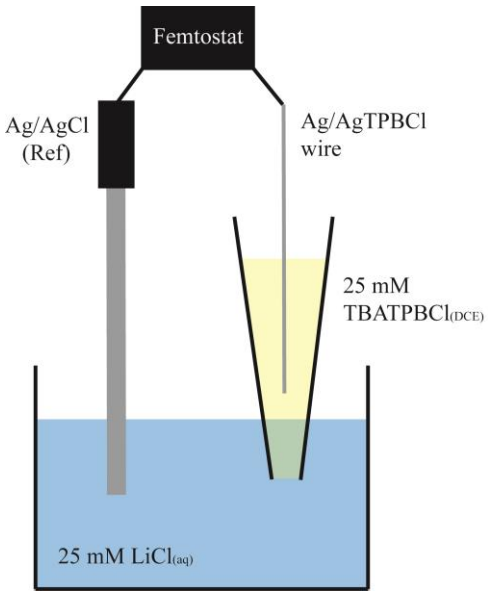

Figure 4.2 *Electrochemical cell set-up used in cyclic voltammetry and EIS experiments. Isocyanate monomers were placed in the micropipette containing 1,2-DCE and amine monomers were placed in the aqueous phase. Micropipette diameter was between 8 and 10 micrometres.*

A Ag/AgTPBCl wire was inserted into the micropipette as the working electrode and a Dri-Ref Ag/AgCl electrode was placed into the aqueous phase as the reference. The full electrochemical cell arrangement was as follows:

Cell 1: $Ag_{(s)}$ | $AgTPBCl_{(s)}$ | 25 mM TBATPBCl, 3.2 mM PMPPI, 6.9 mM $TDI_{(1,2\text{-DCE})}$ | 25 mM LiCl, 40 µM $PEI_{(aq)}$ or 11.8 mM HMDA (optional) | $AgCl_{(s)}$ | $Ag_{(s)}$

The isocyanates used to form a poly(urea) film at the liquid/liquid interface were polymethylene polyphenylisocyanate (PMPPI) and toluene 2,4-diisocyanate (TDI), which were both placed in the DCE phase. Polyethylenimine (PEI) and HMDA were placed in the aqueous phase, although as explained in Chapter 1 isocyanates can form poly(urea) in the presence of water without the addition of amine. For EIS experiments at elevated temperature, the set-up was placed inside a circulating water bath and the temperature was raised accordingly. Cyclic voltammetry and EIS experiments (FAS2 Femtostat, Gamry Instruments, Philadelphia, US) were performed on the liquid/liquid system during poly(urea) film formation. Impedance and Nyquist plots collected during EIS were analysed and equivalent circuit diagrams built using the Echem Analyst software (Version 6.04, Gamry Instruments, Philadelphia, US).

Poly(urea) films formed at the tip of the micropipette after cyclic voltammetry and initial EIS experiments were examined using an optical microscope (Olympus BH2-UMA light microscope, range x50 to x1000 magnification). Poly(urea) films formed under different reaction conditions were later examined using a scanning electron microscope (Zeiss SUPRA 55-VP FE-SEM).

4.3 Results and Discussion

4.3.1 Cyclic Voltammetry

Cyclic voltammetry was initially used to find a suitable DC potential for EIS experiments, as previous similar studies have shown that applying a DC potential where significant ion transfer across the liquid/liquid interface is taking place will perturb film formation.[30] Prior to the addition of isocyanate to the DCE phase and amine monomers to the aqueous phase a cyclic voltammogram of the potential window was performed, which is shown in Figure 4.3.

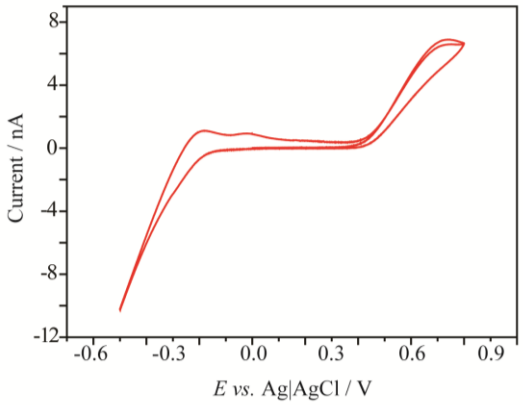

Figure 4.3 *Cyclic voltammogram of the potential window from -0.5 V to +0.8 V at the DCE/water interface with no isocyanate or amine monomers present in either phase. Scan rate 100 mV / s.*

The CV shows a wide potential window between -0.1 V and 0.5 V in which a DC potential could be fixed so as not perturb poly(urea) film formation. However, to ensure that the solvent window did not change with the addition of isocyanate and amine monomers, cyclic voltammograms were carried out in the presence of PMPPI, TDI, PEI and HMDA. The first of these is illustrated in Figure 4.4, which shows a CV of the potential window at the DCE/water interface when PMPPI and TDI are present in the oil phase and PEI is present in the aqueous phase.

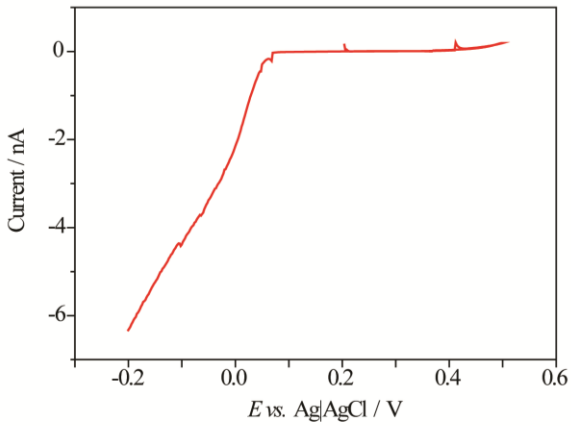

Figure 4.4 *Cyclic voltammogram of the potential window from -0.2 V to +0.5 V at the DCE/water interface with 3.2 mM PMPPI and 6.9 mM TDI in the DCE phase and 40 µM PEI in the aqueous phase. Scan rate 100 mV / s.*

No significant ion transport was observed between + 0.1 V and + 0.45 V, so it can be assumed that PMPPI, TDI and PEI do not transfer across the liquid/liquid interface at these potentials. It is, however, interesting to note that the solvent window appears to narrow in the presence of these chemicals. A solvent window measurement in the presence of 11.8 mM HMDA was also performed to ensure that it did not transfer at these potentials, which is shown in Figure 4.5.

The CV shows that HMDA transfer across the liquid/liquid interface will not be induced until a potential of + 0.75 V is reached. Therefore, following the characterisation of the DCE/water interface in the presence of isocyanate and amine monomers a DC potential of + 0.2 V was chosen for subsequent EIS experiments.

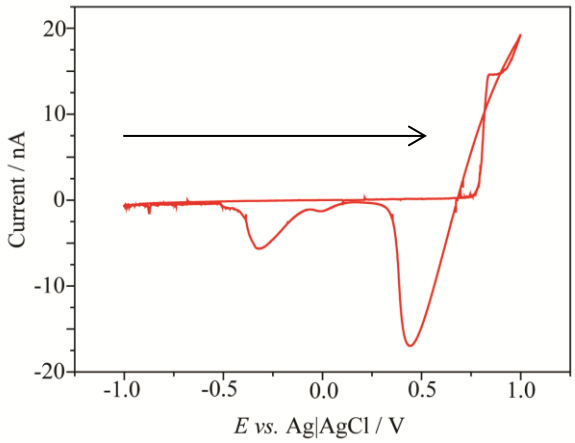

Figure 4.5 *Cyclic voltammogram of the potential window from – 1 V to + 1 V at the DCE/water interface with 11.8 mM HMDA in the aqueous phase. Scan rate 100 mV / s. Arrow denotes scan direction.*

4.3.2 Potentiostatic Electrochemical Impedance Spectroscopy of Poly(urea) Film Formation

4.3.2.1 Potentiostatic Electrochemical Impedance Spectroscopy of Poly(urea) Film Formation Using PMPPI, TDI and PEI

Prior to the implementation of single frequency measurements over time to measure change in impedance with film formation, a suitable frequency had to be found. To achieve this, electrochemical impedance spectra were collected during poly(urea) film formation. Figure 4.6 shows Impedance, Phase and Nyquist plots collected during poly(urea) film formation. Poly(urea) film formation was induced after bringing the DCE phase micropipette, which contained PMPPI and TDI isocyanates, into contact with the PEI aqueous solution. An optical image of the poly(urea) film formed is also shown.

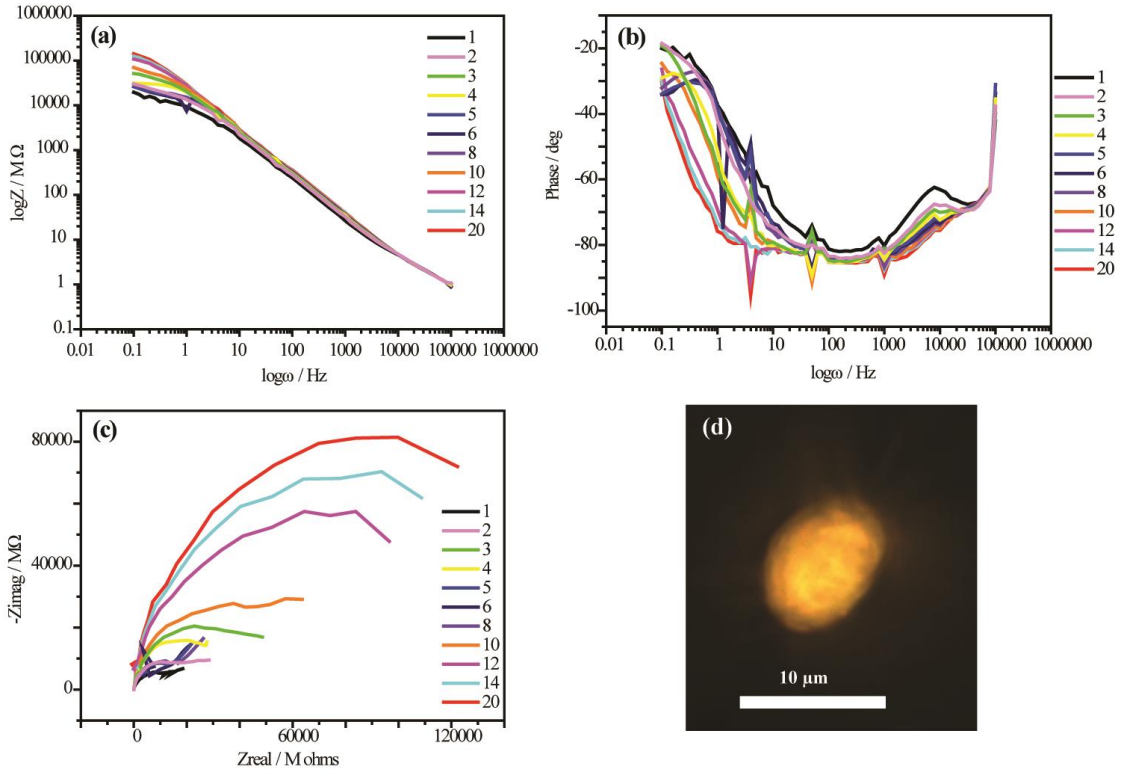

Figure 4.6 *(a) Impedance, (b) Phase and (c) Nyquist spectra recorded at the DCE/water interface over the course of poly(urea) film formation (~2 hours) using 320 µM PMPPI, 690 µM TDI and 40 µM PEI. Twenty spectra were recorded in succession, each taking seven minutes to record. Not all spectra are shown. Spectra were recorded using a DC voltage of + 0.2 V and an AC voltage of 10 mV. (d) Optical microscope image of the tip of a 10 µm diameter micropipette after poly(urea) film formation under EIS conditions.*

All of the spectra shown in Figure 4.6 indicate that at certain frequencies the formation of an interfacial poly(urea) film will have a large effect on the electrochemical impedance recorded. Figure 4.6a shows that between 0.1 Hz and 2000 Hz the formation of poly(urea) film will be represented as an increase in the electrochemical impedance. This increase in electrochemical impedance is more pronounced the lower the frequency, indicating that a lower frequency would be more sensitive to changes in impedance from film formation. Figure 4.6b shows that the change in phase is most distinct at frequencies below 10 Hz, again suggesting that a lower frequency would be more sensitive to poly(urea) film formation. The Nyquist plots shown in Figure 4.6c

indicate that there is large increase in the charge transfer resistance of the system, which can be associated with the formation of poly(urea) at the tip of the micropipette. Formation of the poly(urea) film was confirmed by optical microscopy, as shown in Figure 4.6d. Optical images confirmed that these EIS conditions will allow a flat, uniform, and therefore naturally representative poly(urea) film to form.

To gain a fuller picture of the effect of poly(urea) film formation on the impedance at the DCE/water interface, spectra recorded at the start and end of film formation have been placed alongside spectra recorded in the absence of any isocyanate and amine monomers. These comparisons are made in Figure 4.7.

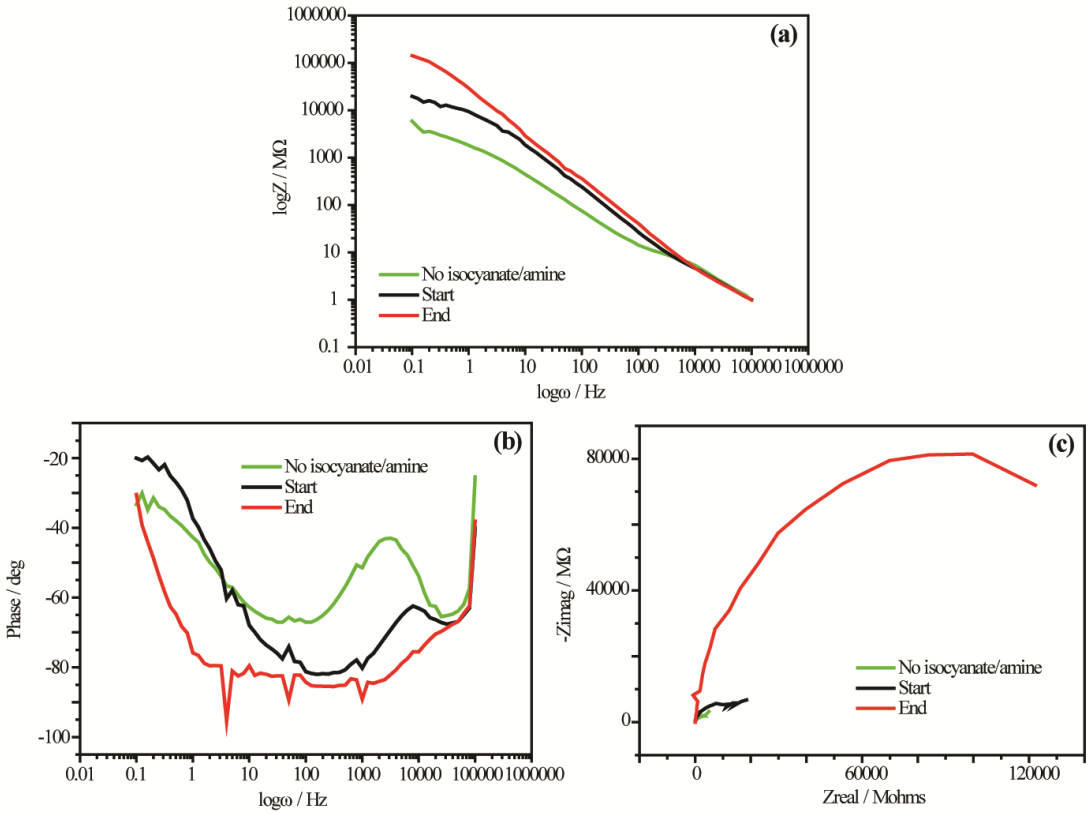

Figure 4.7 *(a) Impedance, (b) Phase and (c) Nyquist spectra recorded at the DCE/water interface in the absence of isocyanate and amine monomers and at the start and end of poly(urea) film formation (~2 hours) using 320 µM PMPPI/690 µM TDI in the DCE phase and 40 µM PEI in the aqueous phase. Spectra were recorded using a DC voltage of + 0.2 V and an AC voltage of 10 mV.*

The impedance spectra shown in Figure 4.7 all appear to suggest that film formation had already begun by the time the first impedance spectra for PMPPI/TDI/PEI had been recorded. Therefore, it was decided that any subsequent comparisons of impedance at the DCE/water interface should be between spectra recorded in the absence of isocyanate/amine monomers and spectra recorded once film formation had finished.

4.3.2.2 Potentiostatic Electrochemical Impedance Spectroscopy of Poly(urea) Film Formation Using PMPPI, TDI and HMDA

Following the observation that the impedance measured above 1000 Hz is unaffected by poly(urea) film formation, impedance spectra were henceforth collected between 0.1 and 1000 Hz. Figure 4.8 shows Impedance, Phase and Nyquist plots collected without any isocyanate and amine present in either the DCE or aqueous phase alongside spectra taken after poly(urea) film had formed using PMPPI and TDI in the DCE phase and HMDA in the aqueous phase.

Figure 4.8a and Figure 4.8b show that similarly to the previous electrochemical impedance spectra recorded for poly(urea) formation using PMPPI, TDI and PEI, lower frequencies appear to be more sensitive to changing impedance with poly(urea) film formation. The Nyquist plot shown in Figure 4.8c also shows a large increase in charge transfer resistance following poly(urea) film formation.

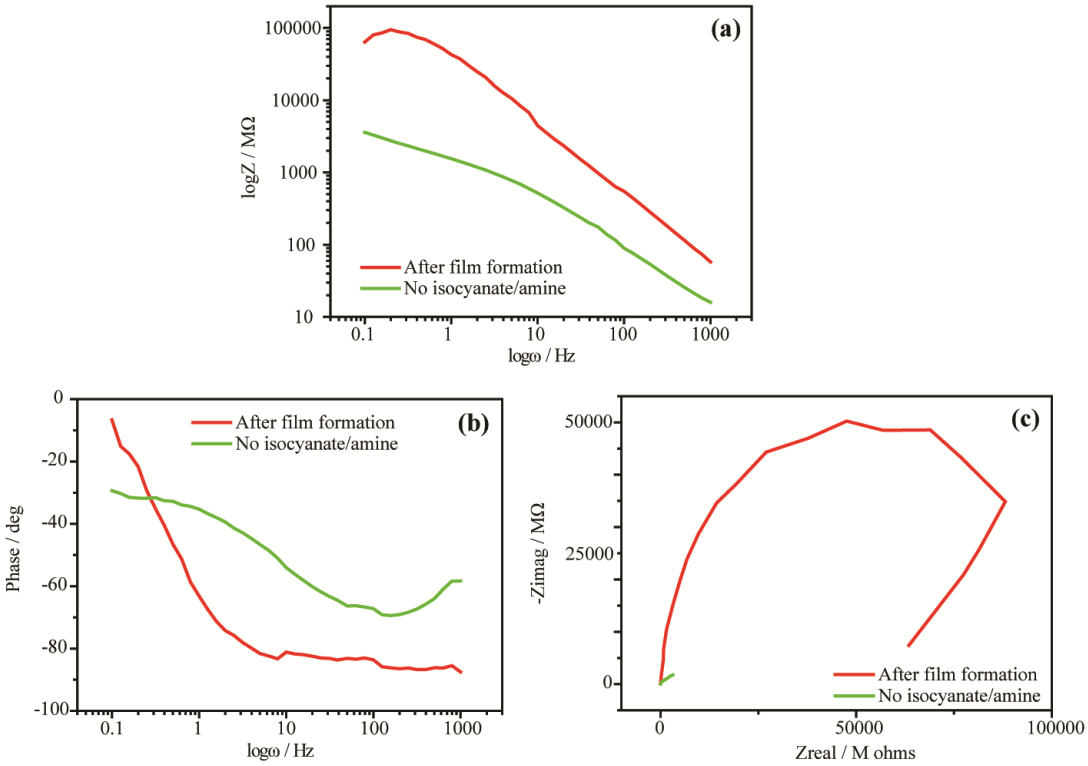

Figure 4.8 *(a) Impedance, (b) Phase and (c) Nyquist spectra recorded at the DCE/water interface with no PMPPI/TDI/PEI present and at the end of poly(urea) film formation (~2 hours) using 3.2 mM PMPPI/6.9 mM TDI in the DCE phase and 11.8 mM HMDA in the aqueous phase. Spectra were recorded using a DC voltage of + 0.2 V and an AC voltage of 10 mV.*

4.3.2.3 Potentiostatic Electrochemical Impedance Spectroscopy of Poly(urea) Film Formation Using PMPPI and TDI

As previously explained in chapter 1, poly(urea) films can form following isocyanate hydrolysis without adding additional amine monomers. Figure 4.9 shows Impedance, Phase and Nyquist plots collected without any isocyanate and amine present in either the DCE or aqueous phase alongside spectra taken after poly(urea) film had formed using PMPPI and TDI in the DCE phase.

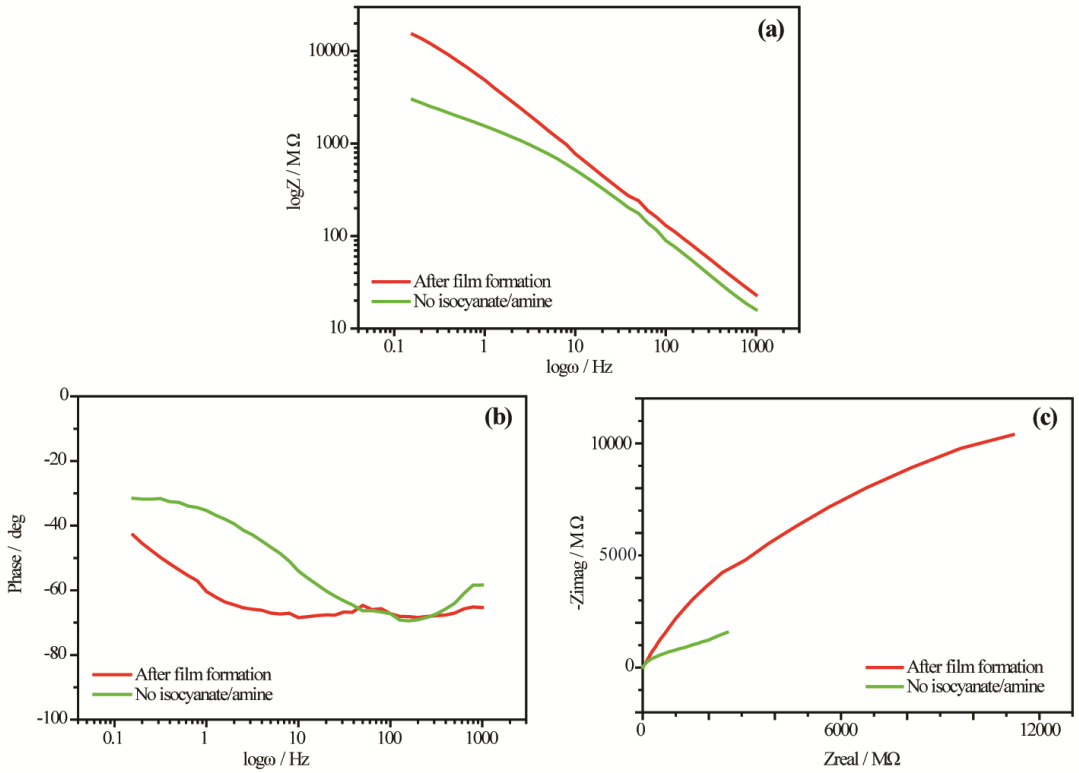

Figure 4.9 *(a) Impedance, (b) Phase and (c) Nyquist spectra recorded at the DCE/water interface with no PMPPI/TDI/PEI present and at the end of poly(urea) film formation (~2 hours) using 3.2 mM PMPPI/ 6.9 mM TDI in the DCE phase. Spectra were recorded using a DC voltage of + 0.2 V and an AC voltage of 10 mV.*

Similarly to the spectra recorded after poly(urea) film formation in the presence of amine monomers PEI and HMDA, the largest changes in impedance and phase can be observed at lower frequencies. Interestingly, the impedance and Nyquist plots after film formation suggest that the film is less resistive than those formed in the presence of HMDA or PEI. It may be that the film formed is less compact, or had not fully finished forming.

4.3.3 Circuit Diagram Modelling of Impedance Spectra Before and After Poly(urea) Film Formation

Following the collection of electrochemical impedance data spectra, it was necessary to use circuit diagram modelling to gain further insight into the processes influencing the

change in impedance with film formation. Figure 4.10 shows the simple circuit which was built; it was essentially comprised of a Randles system (see Chapter 1 for a full description of the Randles circuit) with a few extra modifications.

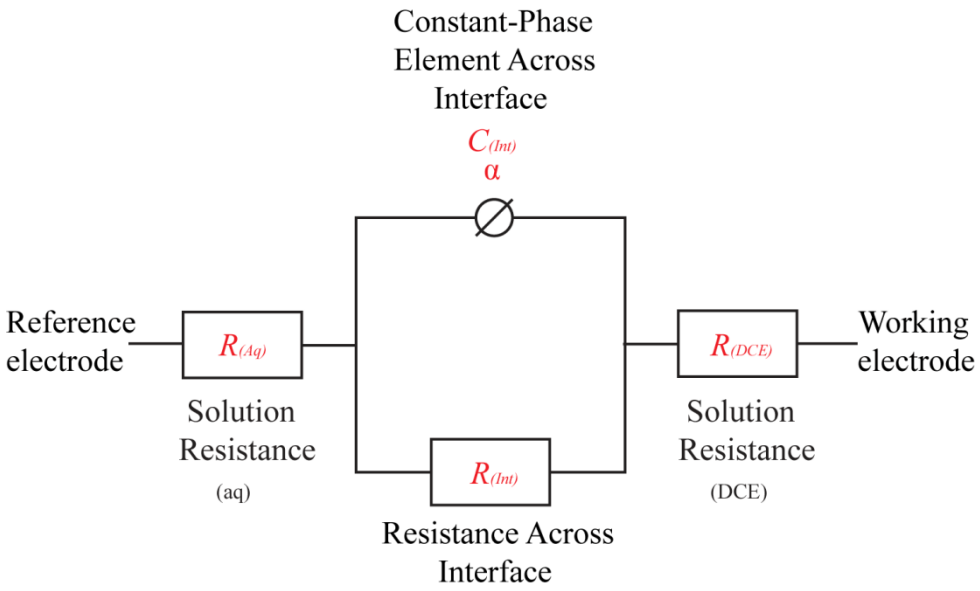

Figure 4.10 *Circuit diagram built to model poly(urea) film at water/DCE interface.*

$R_{(Aq)}$ and $R_{(DCE)}$ represent the solution resistances of the aqueous phase and the DCE phase, respectively. The combined charge-transfer resistance of supporting electrolyte to the double layer on either side of the interface and interfacial resistance is represented by $R_{(Int)}$. The behaviour of the double layer across the interface is modelled by a constant-phase element (CPE), $C_{(Int)}$. In other words, the model assumes that both before and after poly(urea) film formation the interface will perform like a non-ideal capacitor. The parameter α denotes whether CPE $C_{(Int)}$ is behaving more like a capacitor (α=1) or a resistor (α=0). A CPE has been used in place of an ideal capacitor in a number of previous studies to take into account to non-ideality of the liquid/liquid interface.[31, 32]

To simulate the impedance data collected (Figure 4.7, Figure 4.8 Figure 4.9) using the circuit diagram (Figure 4.10), the following equation was used:

$$Z_{equiv} = R_{(Aq)} + \frac{R_{(Int)} \times X_{C_{(Int)}}}{\sqrt{R_{(Int)} + X_{C_{(Int)}}^{2}}} + R_{(DCE)} \quad (4.1)$$

where Z_{equiv} is the equivalent impedance, $R_{(Aq)}$ is the solution resistance in the aqueous phase, $X_{C(Int)}$ is the capacitive reactance of the interface, $R_{(Int)}$ is the resistance at the interface and $R_{(DCE)}$ is the solution resistance in the DCE phase.

4.3.3.1 Modelling Poly(urea) Film Formation Using PMPPI, TDI and PEI

Table 4.1 shows the values for each circuit component (Figure 4.10) used to model previous EIS data (Figure 4.7), characterising the DCE/water interface before and after poly(urea) film formation in the presence of PEI.

Table 4.1 *Values for circuit components (Figure 4.10) used to model the impedance spectrum before and after the formation of a poly(urea) film at the DCE/water interface. Red font highlights the values changed to model the interface after poly(urea) film formation was complete.*

Circuit Component	Salt Solutions Only	After film formation	Units
$R_{(Aq)}$	3.90 x 10^{4}	3.9 x 10^{4}	ohm
$R_{(Int)}$	5.32 x 10^{9}	1.79 x 10^{11}	ohm
$R_{(DCE)}$	2.42 x 10^{9}	2.42 x 10^{9}	ohm
$C_{(Int)}$	1.62 x 10^{-10}	6.9 x 10^{-12}	Ω x s^{α}
α	0.67	0.93	n/a

The resistances of the water and DCE solutions, $R_{(Aq)}$ and $R_{(DCE)}$, were close to values found by cyclic voltammetry of each solution alone (3.33 x 10^{4} ohms for 25 mM $LiCl_{(aq)}$, 5.0 x 10^{9} ohms for 25 mM $TBATPBCl_{(DCE)}$). $R_{(Int)}$ and $C_{(Int)}$ were allowed to change, as it can be envisioned that interfacial resistance and capacitance will change

with the formation of a poly(urea) film. The decrease in the CPE value at the interface due to film formation, $C_{(Int)}$, can be contributed to the formation of a dense film which increases charge separation. However, the increase in value of the CPE exponent α from 0.67 to 0.93 indicates that, with film formation, the interface will act more like an ideal capacitor. The large increase in resistance at the interface due to film formation, $R_{(Int)}$, can be contributed to the blocking of charge transfer across the interface by the presence of the poly(urea) film.

Interfacial capacitance can be calculated using $C_{(Int)}$ and $R_{(Int)}$ using Equation 4.2:

$$C = \frac{(C_{(Int)} \times R_{(Int)})^{\left(\frac{1}{\alpha}\right)}}{R_{(Int)}} \tag{4.2}$$

where C is capacitance, $C_{(Int)}$ is the CPE value, α is the CPE exponent and $R_{(Int)}$ is the interfacial resistance in parallel to the CPE. Interfacial capacitance was found to be 1.51 x 10^{-10} F before film formation and 7.01 x 10^{-12} F after film formation, again suggesting that the film formed is dense.

Figure 4.11 shows the impedance spectrum simulations from the circuit diagram modelling alongside experimental data collected when no isocyanate/amine monomers are present in either phase and no poly(urea) film is present.

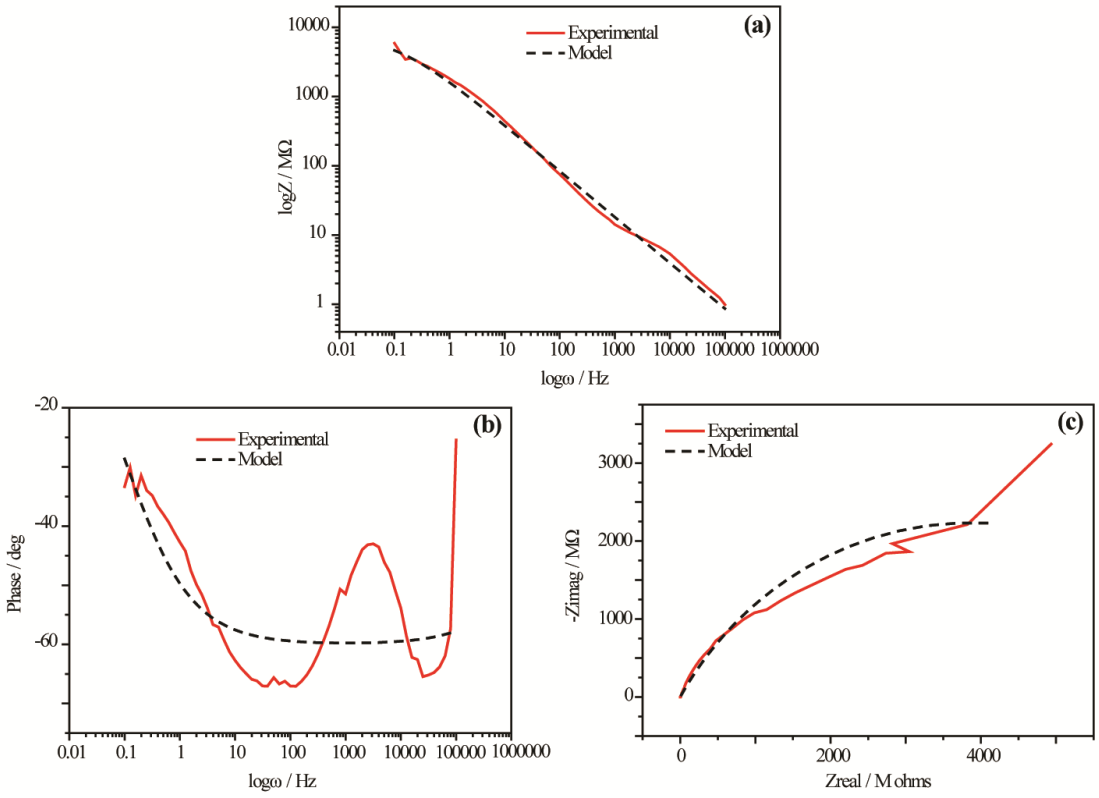

Figure 4.11 *(a) Impedance, (b) Phase and (c) Nyquist plots recorded at a DC potential of 0.2 V when no isocyanate/amine monomers were present in either phase and no interfacial poly(urea) film was present alongside simulations from circuit diagram modelling (Figure 4.10).*

The model was shown to be in fairly good agreement with the experimental data, therefore it was applied to the impedance spectrum data collected after poly(urea) film formation in the presence of PEI (data originally shown in Figure 4.7). The simulations are shown alongside the experimental data in Figure 4.12.

The circuit model shown in Figure 4.10 also appears to be in good agreement with the experimental data collected after poly(urea) formation using PMPPI, TDI and PEI. The implementation of values for circuit components, $R_{(Int)}$ and $C_{(Int),}$ has allowed for the quantification of the capacitance and resistance change due to film formation at the interface.

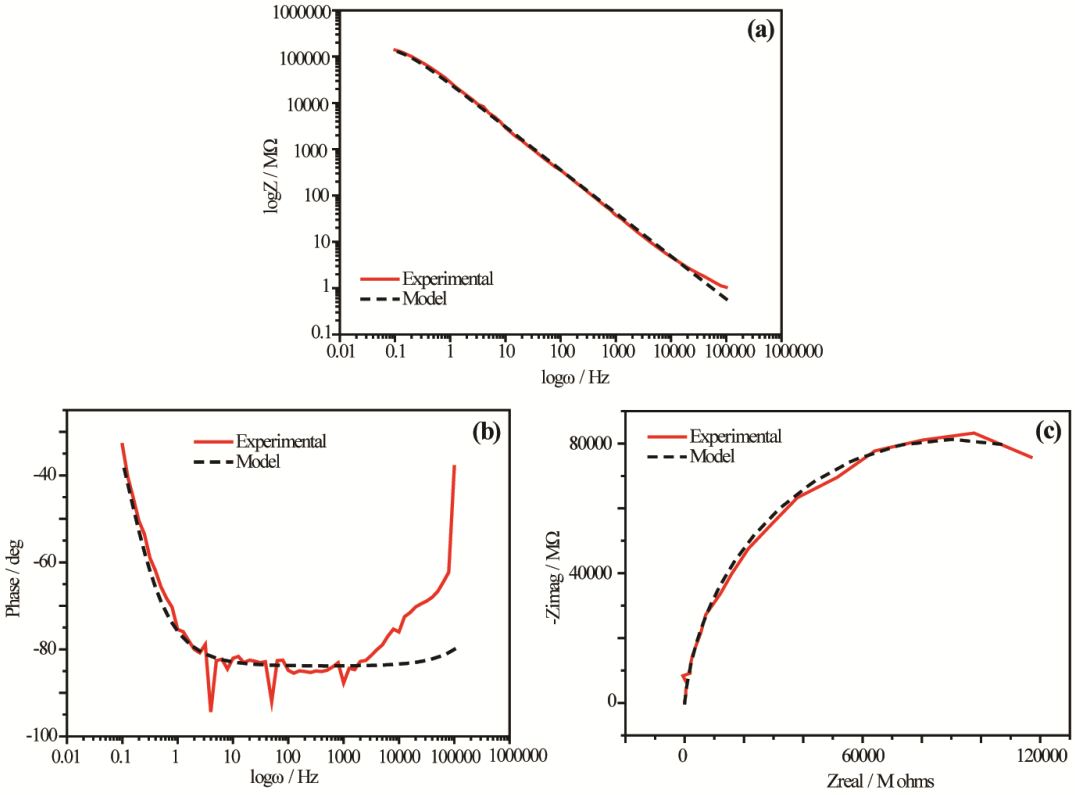

Figure 4.12 *(a) Impedance, (b) Phase and (c) Nyquist plots recorded at a DC potential of 0.2 V after poly(urea) film formation (using 320 µM PMPPI/690 µM TDI in the DCE phase and 40 µM PEI in the aqueous phase) alongside simulations from circuit diagram modelling (Figure 4.10).*

To further understand whether it was the increase in capacitance or increase in resistance that was the dominant process in changing the impedance spectrum following film formation, impedance plots where only one circuit element was changed were simulated. The first of these is shown in Figure 4.13, which shows the effect of changing the constant-phase element value at the interface ($C_{(Int)}$) on the impedance and phase spectrums.

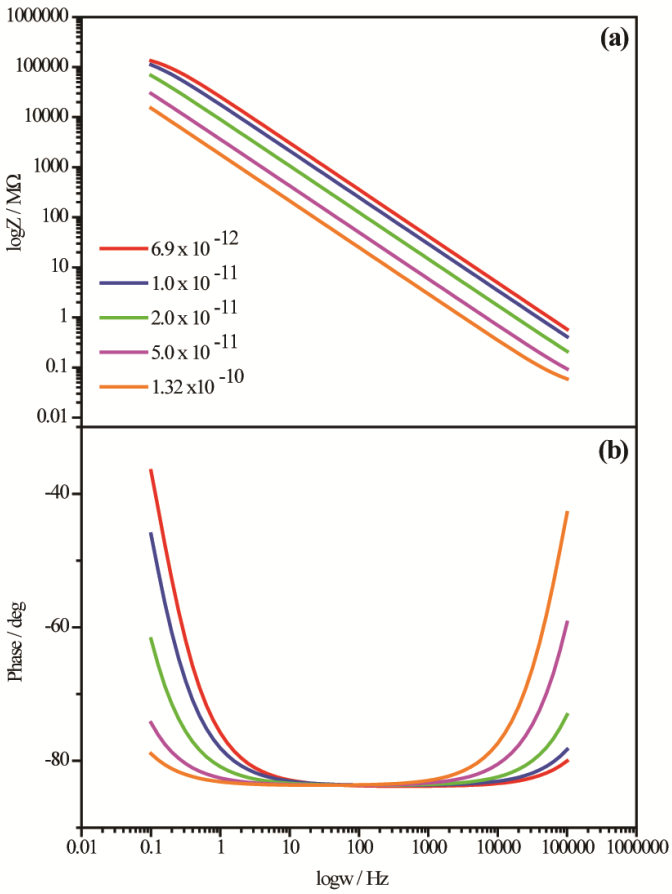

Figure 4.13 *(a) Impedance and (b) Phase plots simulated using circuit element values calculated for impedance spectrum after poly(urea) film formation (Table 4.1). The value of circuit element $C_{(Int)}$ was changed to assess the impact of film capacitance on the appearance of the impedance spectrum. The CPE exponent α was kept at a value of 0.93.*

The simulations shown in Figure 4.13 show that increasing the capacitance at the interface will decrease impedance measured at all frequencies. However, neither the impedance plot or phase plot simulated using the pre poly(urea) film CPE value (1.32 x 10^{10}) look like the pre-poly(urea) film experimental data. In particular, the phase plots are a bad fit to the experimental data at lower frequencies and the impedance plots are a bad fit at higher frequencies. Therefore, the next step was to change the resistance at the interface following film formation. The results of these simulations are shown in Figure 4.14.

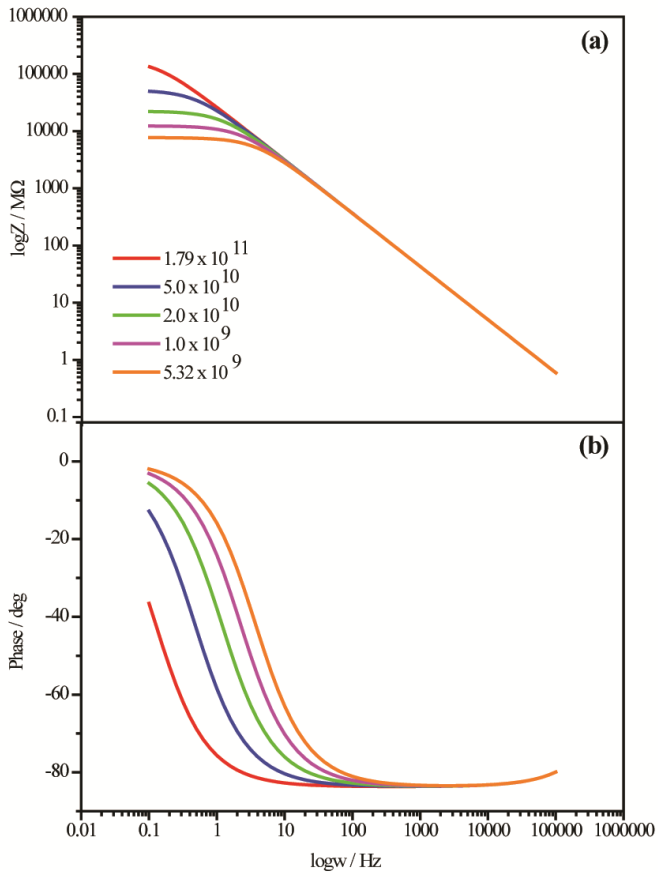

Figure 4.14 *(a) Impedance and (b) Phase plots simulated using circuit element values calculated for impedance spectrum after poly(urea) film formation (Table 4.1). The value of circuit element* $R_{(Int)}$ *(in ohms) was changed to assess the impact of film resistance on the appearance of the impedance spectrum.*

The simulations shown in Figure 4.14 suggest that changing the resistance at the interface will have a large effect on the appearance of the impedance and phase spectra at low frequencies (<10 Hz). Although increasing the interfacial resistance causes impedance and phase changes similar to those seen during film formation, simulations using resistance values which were closest to the before film formation interfacial resistance value were a bad fit to the experimental data.

Overall the change in impedance with film formation appears to be controlled by a mixture of changing interfacial resistance and capacitance, with neither element

dominating over the other. However, it must be kept in mind that these simulations were carried out using a CPE exponent value of 0.93, when it has been shown that before film formation the value is around 0.67. In other words, the simulations do not take into account the change in behaviour of the interfacial capacitance from less-ideal to more-ideal as the film forms.

4.3.3.2 Modelling Poly(urea) Film Formation Using PMPPI, TDI and HMDA

Circuit diagram modelling was applied to the experimental data originally shown in Figure 4.8. Figure 4.15 shows the impedance spectrum simulations from the circuit diagram modelling alongside experimental data collected after poly(urea) film formation in the presence of HMDA.

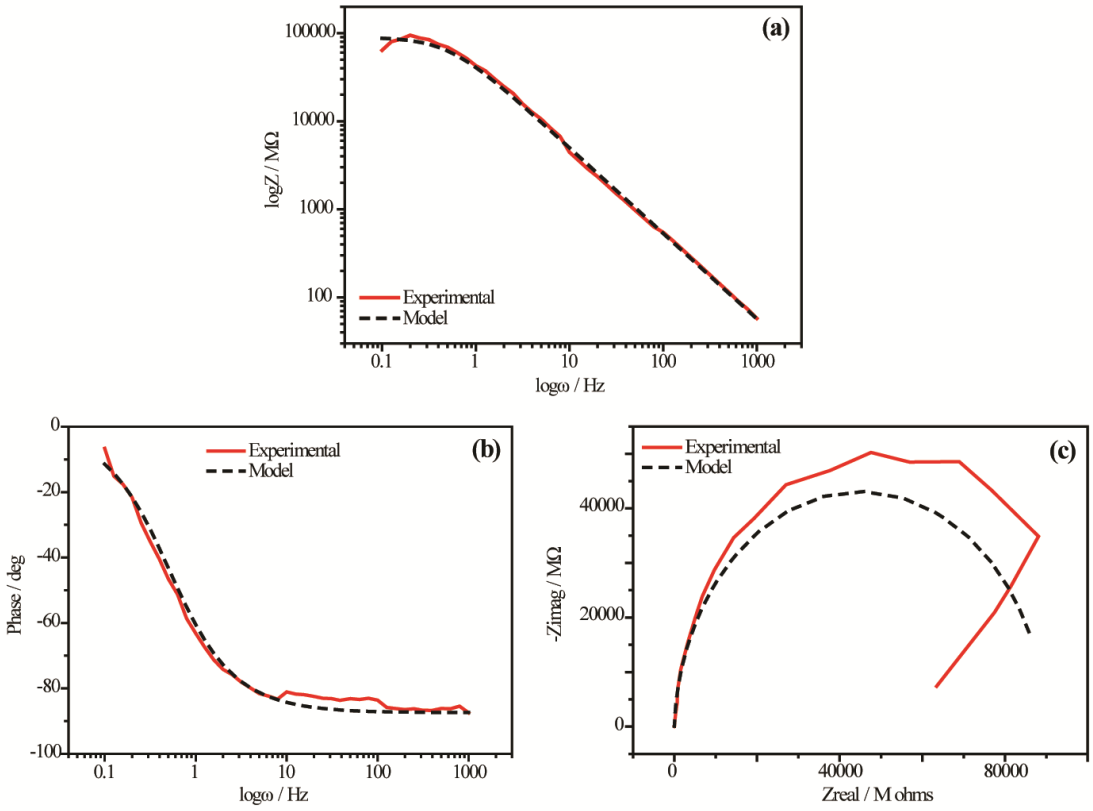

Figure 4.15 *(a) Impedance, (b) Phase and (c) Nyquist plots recorded at a DC potential of 0.2 V after poly(urea) film formation (using 3.2 mM PMPPI/6.9 mM TDI in the DCE phase and 11.8 mM HMDA in the aqueous phase) alongside simulations from circuit diagram modelling (Figure 4.9).*

Table 4.2 shows the values for each circuit component (Figure 4.10) used to model previous EIS data (Figure 4.8) characterising the DCE/water interface before and after poly(urea) film formation in the presence of amine HMDA.

Table 4.2 *Values for circuit components (Figure 4.10) used to model the impedance spectrums before and after the formation of a poly(urea) film at the DCE/water interface in the presence of HMDA. Red font highlights the values changed to model the interface after poly(urea) film formation was complete.*

Circuit Component	Salt Solutions Only	After film formation	Units
$R_{(Aq)}$	3.90×10^{4}	3.9×10^{4}	ohm
$R_{(Int)}$	5.32×10^{9}	8.77×10^{10}	ohm
$R_{(DCE)}$	2.42×10^{9}	2.42×10^{9}	ohm
$C_{(Int)}$	1.62×10^{-10}	3.58×10^{-12}	$\Omega \times s^{\alpha}$
α	0.67	0.97	n/a

Similarly to the circuit element values for interfacial resistance and capacitance seen in Table 4.1, poly(urea) film formation in the presence of amine HMDA leads to increased interfacial resistance and decreased interfacial capacitance. The CPE exponent also increases to a value of 0.97, indicating that the interface is almost behaving like an ideal capacitor. Overall, we can assume from the magnitude of the values calculated by circuit diagram modelling that the poly(urea) film formed in the presence of HMDA has the same characteristics as the film formed in the presence of PEI.

4.3.3.3 Modelling Poly(urea) Film Formation Using PMPPI and TDI

To fully understand the effect of film formation in the presence of additional amine versus film formation without additional amine, circuit diagram modelling was applied to the experimental data originally shown in Figure 4.9. Figure 4.16 shows the impedance spectrum simulations from the circuit diagram modelling alongside experimental data collected after poly(urea) film formation where no additional amine was present in the aqueous phase.

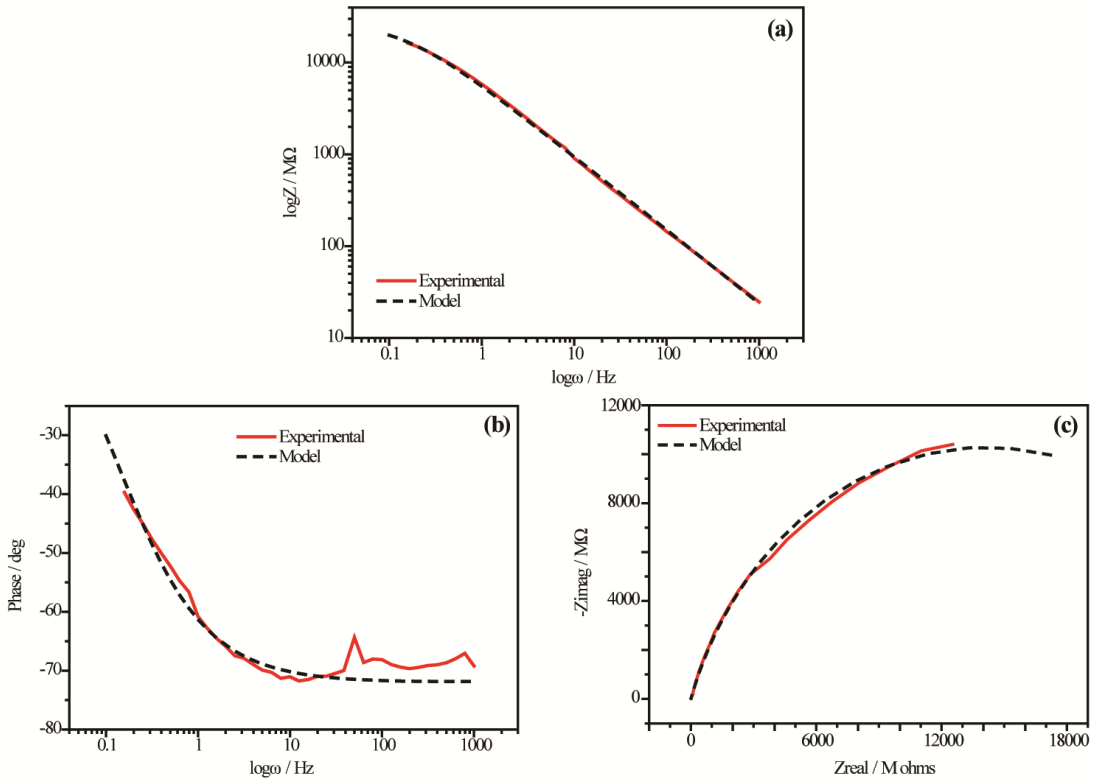

Figure 4.16 *(a) Impedance, (b) Phase and (c) Nyquist plots recorded at a DC potential of 0.2 V after poly(urea) film formation (using 3.2 mM PMPPI and 6.9 mM TDI in the DCE phase) alongside simulations from circuit diagram modelling (Figure 4.10).*

The simulations shown in Figure 4.16 are generally good fits to the experimental data. Table 4.3 shows the values for each circuit component (Figure 4.10) used to model previous EIS data (Figure 4.9) characterising the DCE/water interface before and after poly(urea) film formation without the addition of amine to the aqueous phase.

Table 4.3 *Values for circuit components (Figure 4.10) used to model the impedance spectrums before and after the formation of a poly(urea) film at the DCE/water interface following isocyanate hydrolysis. Red font highlights the values changed to model the interface after poly(urea) film formation was complete.*

Circuit Component	Salt Solutions Only	After film formation	Units
$R_{(Aq)}$	3.9×10^{4}	3.90×10^{4}	ohm
$R_{(Int)}$	5.32×10^{9}	2.60×10^{10}	ohm
$R_{(DCE)}$	2.42×10^{9}	2.42×10^{9}	ohm
$C_{(Int)}$	1.62×10^{-10}	3.84×10^{-12}	$\Omega \times s^{\alpha}$
α	0.67	0.80	n/a

Even without additional amine in the aqueous phase, the hydrolysis of isocyanate at the liquid/liquid interface leads to the formation of a poly(urea) film. The circuit values shown in Table 4.3 imply that the formation of a film leads to increased interfacial resistance and reduced interfacial capacitance, analogous to film formation in the presence of PEI or HMDA amine in the aqueous phase. However, it appears that the magnitude of the change in interfacial resistance does not reach the value seen for film formation in the presence of HMDA or PEI in the aqueous phase. The CPE exponent α also only reaches a value of 0.80 after film formation, suggesting that the film formed behaves as a less-ideal capacitor than those formed in the presence of HMDA or PEI. As such, it can be hypothesized that even after 2 hours film formation had not reached full completion. Therefore, we can expect the formation of poly(urea) films through the isocyanate hydrolysis reaction alone to be slower than in the presence of additional amine using equivalent concentrations of TDI/PMPPI in the DCE phase.

4.3.4 Monitoring the Time Course of Poly(urea) Film Formation Using Electrochemical Impedance Spectroscopy

Single-frequency EIS experiments were carried out to measure the rate of interfacial poly(urea) film formation at the tip of a micropipette using different concentrations of isocyanate and amine monomers. As mentioned previously, a DC potential of +0.2 V with an oscillation of 10 mV was applied to the Ag/AgTPBCL wire electrode to ensure that there would be no net transfer of ions across the interface capable of disturbing the natural film formation process. As the experimental data shown in Figure 4.7-Figure 4.9 has indicated, the major change in impedance with interfacial film formation is seen at lower frequencies (<1 Hz). Therefore, 0.5 Hz was chosen as the frequency for single-frequency EIS experiments as a compromise between the sensitivity of the lowest frequencies to the need for reasonable time-resolution of a few seconds.

4.3.4.1 Poly(urea) Film Formation Using Different Concentrations of PMPPI, TDI and PEI

Prior to the measurement of impedance over time during film formation, impedance was monitored over time with only PEI amine in the aqueous phase (no PMPPI/TDI isocyanate monomers in the DCE phase) to check the stability of the system. Results are shown in Figure 4.17. The impedance over time shown suggests that background impedance at this frequency remained stable, implying that any impedance change with the addition of isocyanate monomers would be due to interfacial film formation.

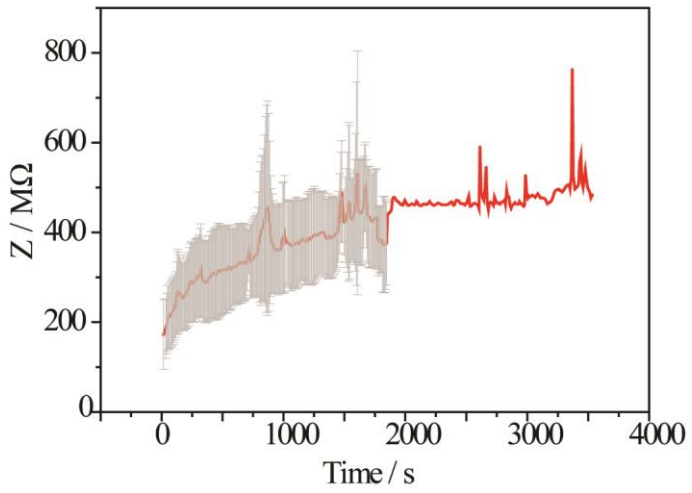

Figure 4.17 *Mean impedance over time recorded using the set-up shown in Figure 4.2 with 40 µM PEI (0.1 wt.% PEI) included in the aqueous phase. DC potential was +0.2 V with an oscillation of 10 mV, frequency was 0.5 Hz.*

Table 4.4 details the different concentrations of isocyanate used in the DCE phase in conjunction with 40 µM (0.1 wt.%) PEI in the aqueous phase for single-frequency impedance over time experiments.

Table 4.4 *Concentrations of PMPPI and TDI isocyanate monomers used in impedance versus time experiments (~2:1 molar ratio [TDI]:[PMPPI]).*

Wt. % in DCE	[TDI] / mM	[PMPPI] / mM
0.1	6.9	3.2
0.08	5.52	2.56
0.06	4.14	1.92
0.04	2.76	1.28
0.02	1.38	0.64
0.01	0.69	0.32
0.005	0.35	0.16
0.002	0.14	0.06
0.001	0.07	0.03

A number of repeat experiments (between 3 and 4) were carried out at each set of concentrations. As the background impedance shown in Figure 4.17 was negligible compared to the impedance recorded during film formation it was deemed unnecessary to subtract. The impedance versus time spectra for each concentration are shown in Figure 4.18.

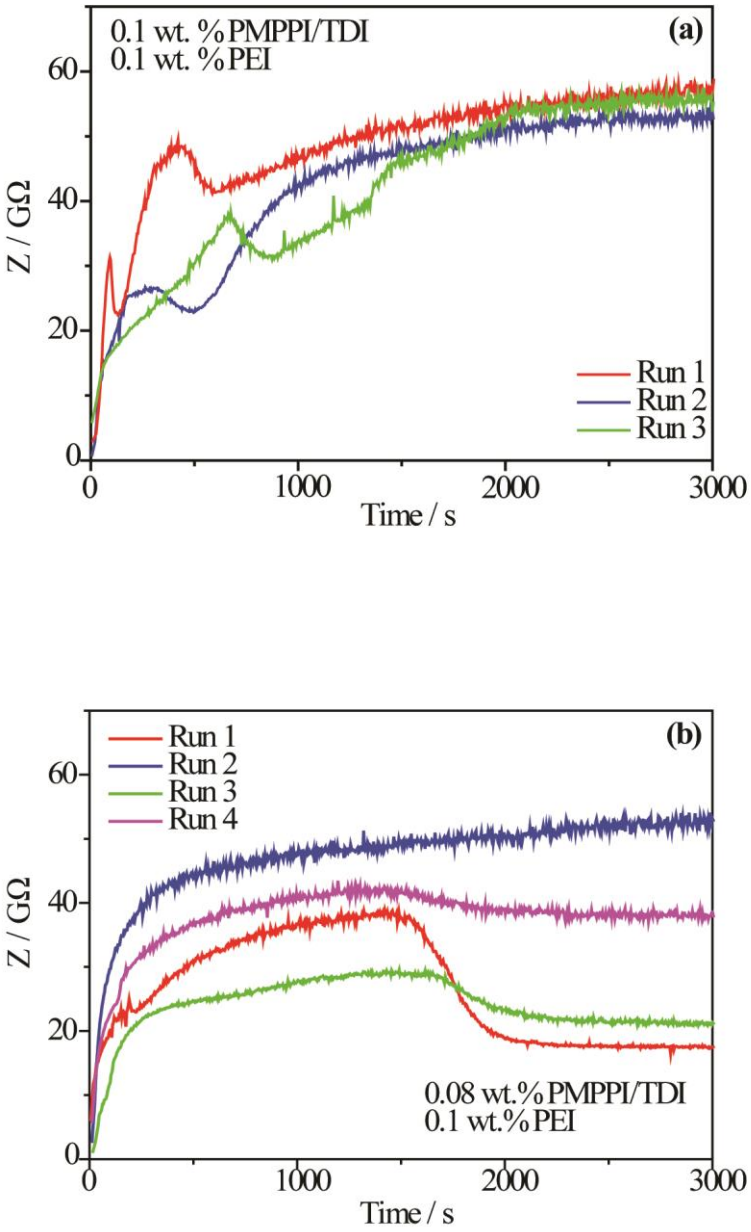

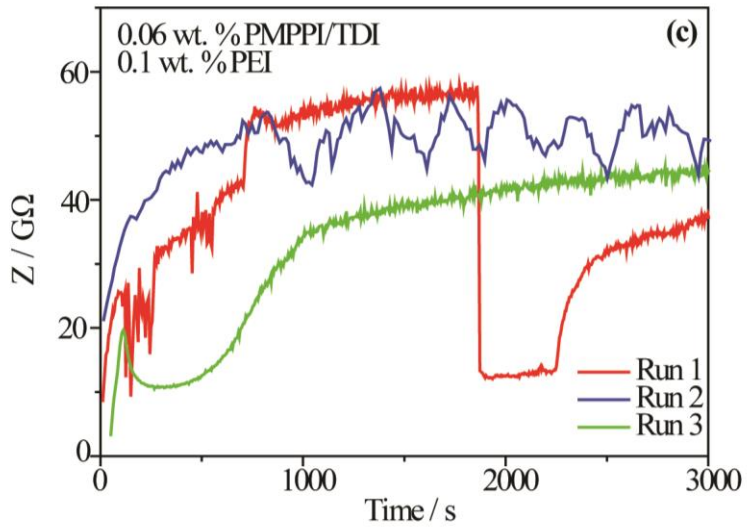
0.06 wt. % PMPPI/TDI
0.1 wt. % PEI
(c)
Z / GΩ
Time / s
Run 1
Run 2
Run 3

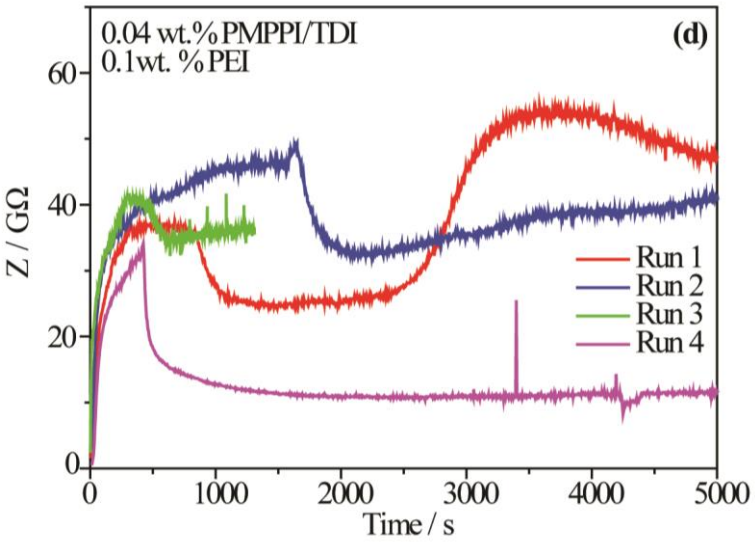
0.04 wt.% PMPPI/TDI
0.1wt. % PEI
(d)
Z / GΩ
Time / s
Run 1
Run 2
Run 3
Run 4

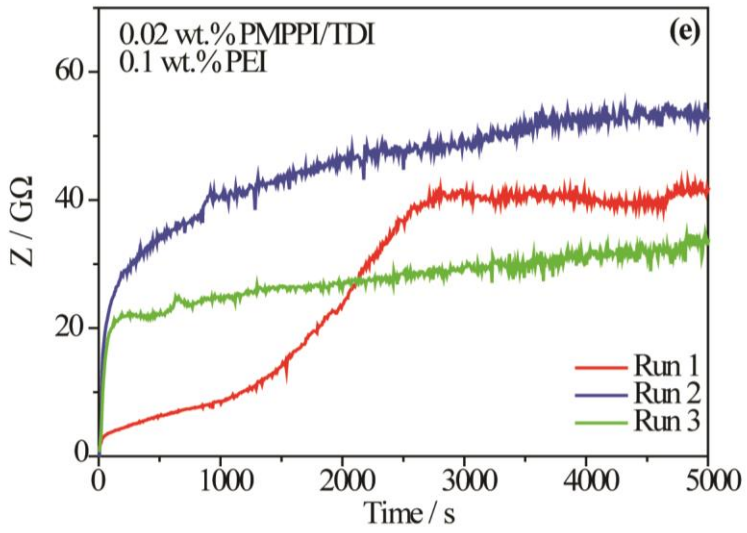
0.02 wt.% PMPPI/TDI
0.1 wt.% PEI
(e)
Z / GΩ
Time / s
Run 1
Run 2
Run 3

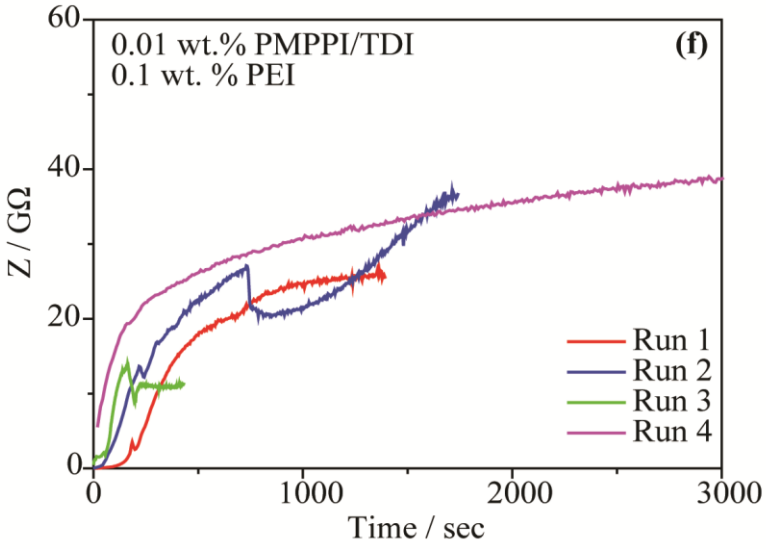
0.01 wt.% PMPPI/TDI
0.1 wt. % PEI
(f)
Z / GΩ
Time / sec
Run 1
Run 2
Run 3
Run 4

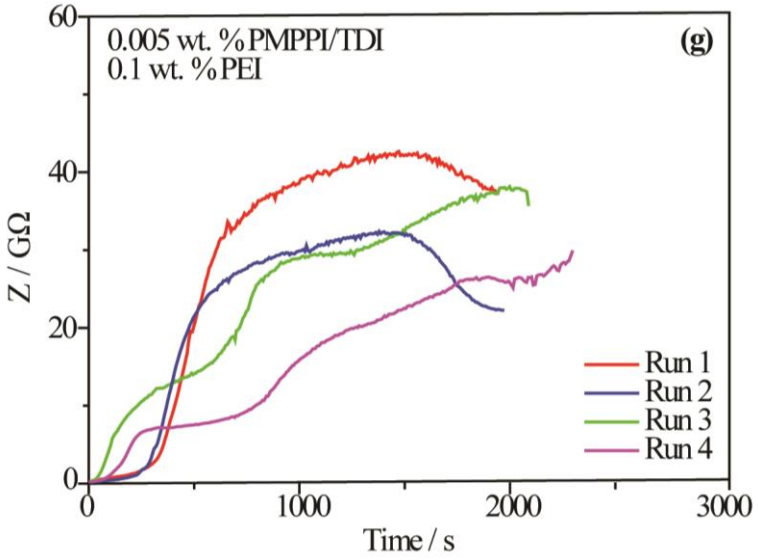
0.005 wt. % PMPPI/TDI
0.1 wt. % PEI
(g)
Z / GΩ
Time / s
Run 1
Run 2
Run 3
Run 4

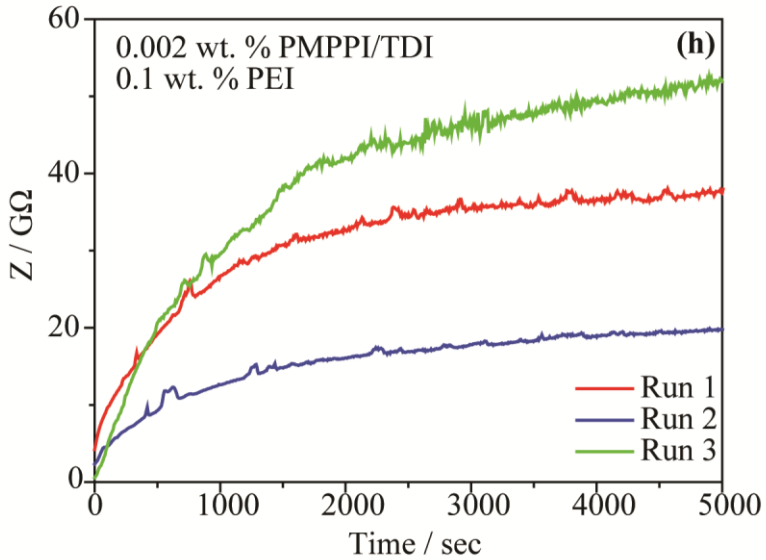
0.002 wt. % PMPPI/TDI
0.1 wt. % PEI
(h)
Z / GΩ
Time / sec
Run 1
Run 2
Run 3

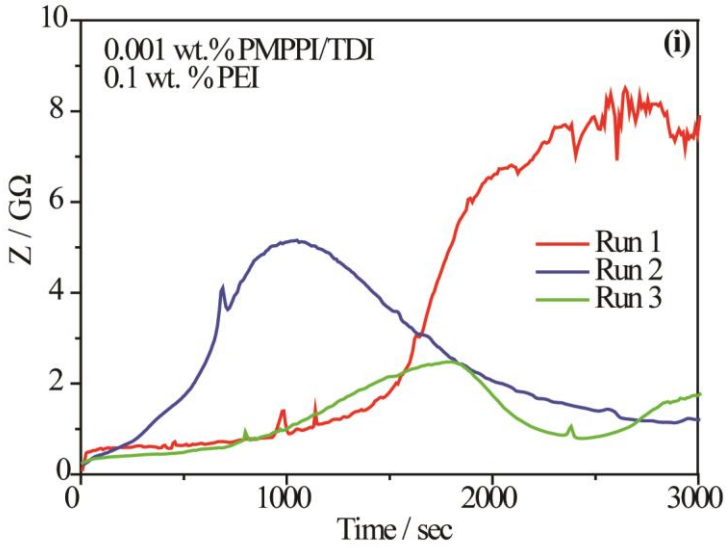

Figure 4.18 *Impedance versus time spectra recorded during poly(urea) film formation using (a) 6.9 mM TDI/ 3.2 mM PMPPI (0.1 wt.%), (b) 5.52 mM TDI/ 2.56 mM PMPPI (0.08 wt.%), (c) 4.14 mM TDI/ 1.92 mM PMPPI (0.06 wt. %), (d) 2.76 mM TDI/ 1.28 mM PMPPI (0.04 wt.%), (e) 1.38 mM TDI/ 0.64 mM PMPPI (0.02 wt.%), (f) 0.69 mM TDI/ 0.32 mM PMPPI (0.01 wt. %), (g) 0.35 mM TDI/ 0.16 mM PMPPI (0.005 wt. %), (h) 0.14 mM TDI/ 0.06 mM PMPPI (0.002 wt. %) and (i) 0.07 mM TDI/ 0.03 mM PMPPI (0.001 wt. %) in the DCE phase. 40 µM PEI (0.1 wt. %) was present in the aqueous phase for all experiments. DC potential was +0.2 V with an oscillation of 10 mV, frequency was 0.5 Hz.*

The impedance versus time data shown in Figure 4.18 appears to suggest that, in general, the rate poly(urea) film formation in the presence of PEI slows and become more varied within a set as the concentration of isocyanate monomers in the DCE phase is decreased. Decreasing the concentration of isocyanate also appears make it more likely that the impedance measured during film formation will suddenly drop. These sudden events mean the interface tends towards its initial state due to parts of the film falling off before complete film formation. This is caused by reduced availability of isocyanate monomers at the liquid/liquid interface.

In an attempt to compare the rate of film formation with isocyanate concentration, data collected during the first 1500 seconds for each concentration was averaged. This

timespan was chosen as it was short enough to be unaffected by film drop and could be used for all data sets. The average impedance versus time profile for each concentration is shown in Figure 4.19.

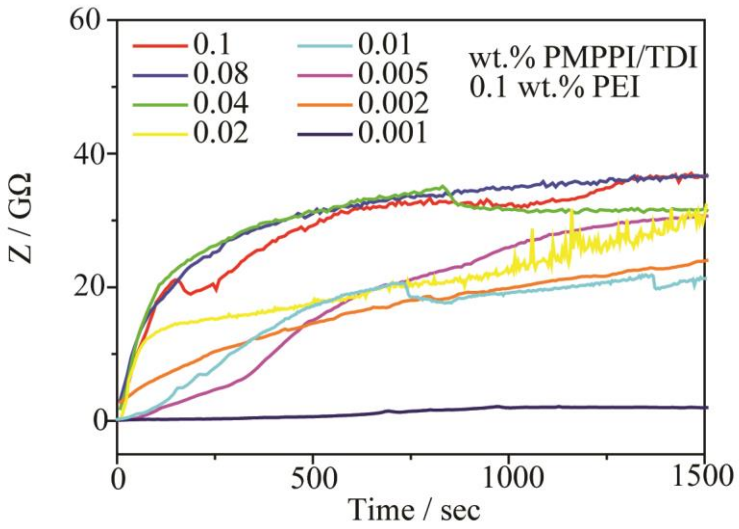

Figure 4.19 *Average impedance over time recorded during poly(urea) film formation using different concentrations of 2:1 molar ratio TDI: PMPPI (DCE phase) in the presence of 40 µM PEI (aqueous phase). Impedance was recorded at a frequency of 0.5 Hz using a DC potential of +0.2V with an oscillation of 10 mV.*

The averaged impedance versus time for each isocyanate monomer concentration shows that the rate of interfacial poly(urea) film formation increases with isocyanate monomer concentration until there is ~0.02 wt.% TDI/PMPPI in the DCE phase. There on, the rate of film formation remains the same no matter how high the concentration of isocyanate in the DCE phase, which suggests that the rate of reaction is limited by the concentration of isocyanate at the water/DCE interface. It can be hypothesized that once a concentration threshold is reached the isocyanate monomers will saturate the liquid/liquid interface, so that the rate of reaction becomes limited by the rate of diffusion of isocyanate monomers to the liquid/liquid interface.

To quantify the impact of isocyanate monomer concentration on the rate of poly(urea) film formation, Figure 4.20 shows the time for all impedance profiles recorded to reach half their final value was plotted versus the concentration of TDI/PMPPI in the DCE phase.

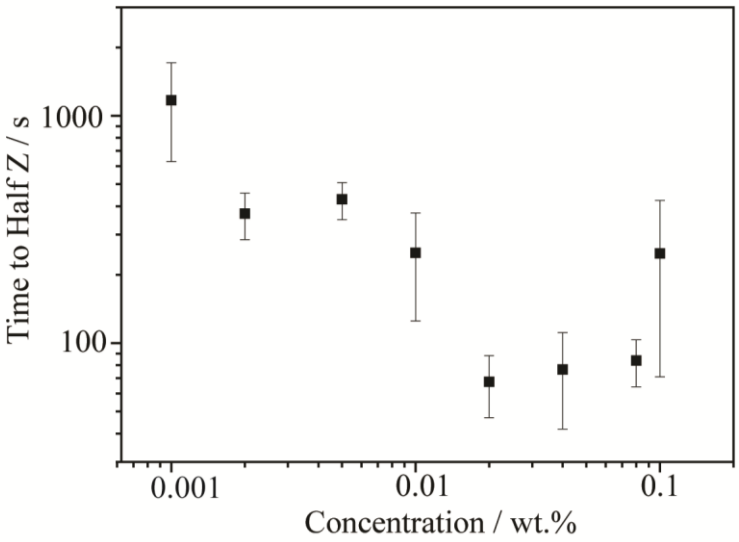

Figure 4.20 *Plot of time for impedance profiles to reach half their final value versus concentration of PMPPI/TDI used (wt.% in the DCE phase) with standard deviation. 40 µM of PEI was present in the aqueous phase.*

The plot shows that below 0.02 wt.% the time taken for film formation to complete is inversely proportional to isocyanate concentration. At concentrations above 0.02 wt.% isocyanate, the rate of the film formation is essentially the same. The rate of film formation at 0.1 wt.% appears slightly slower on average, which may be due to the larger amount of poly(urea) being formed disturbing the stability of the growing interfacial film. Thus, the appearance of the time versus concentration plot suggests that the interfacial reaction is concentration dependent until water/DCE interface is saturated with isocyanate monomers, at which point the rate of reaction becomes limited by the rate of diffusion of isocyanate monomers to the liquid/liquid interface and availability of water/PEI monomers.

4.3.4.2 Poly(urea) Film Formation Using Different Concentrations of PMPPI, TDI and HMDA

Similar to the previous study using PEI in the aqueous phase, impedance was monitored over time with only HMDA amine in the aqueous phase (no PMPPI/TDI isocyanate monomers in the DCE phase) to check the stability of the system. Unlike the previous study however, concentration of HMDA were changed in accordance with the concentration of isocyanate to mimic industrial practice.[1] Figure 4.21 shows impedance versus time collected using the set-up shown in Figure 4.2 with different concentrations of HMDA in the aqueous phase.

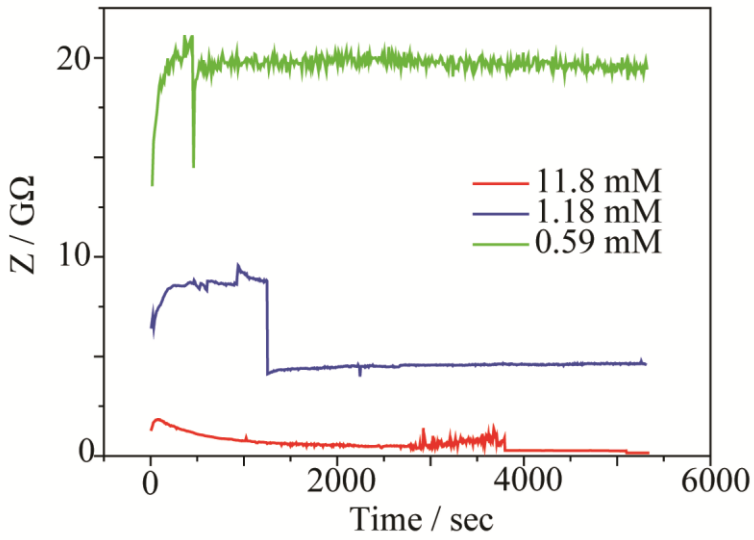

Figure 4.21 *Impedance over time recorded using the set-up shown in Figure 4.1 with 11.8 mM, 1.18 mM and 0.59 mM HMDA included in the aqueous phase. DC potential was +0.2 V with an oscillation of 10 mV, frequency was 0.5 Hz.*

Figure 4.21 shows that impedance remains stable over time but increases as the concentration of HMDA in the aqueous phase is reduced. It can be hypothesised that the charged amine molecules insert into the liquid/liquid interface, thus reducing the resistance to charge transfer. Therefore, the higher the concentration of amine in the aqueous phase the lower the interfacial resistance and thus impedance measured.

Table 4.5 lists the different concentrations of isocyanate used in the DCE phase in conjunction with different concentrations of HMDA in the aqueous phase for single-frequency impedance over time experiments. The concentration of HMDA is adjusted in line with the concentration of isocyanate to mimic the stoichiometry used in industry. The amount of HMDA added is in 5% excess to the number of isocyanate groups present, counting two reactive groups on each amine.

Table 4.5 *Concentrations used in impedance versus time experiments of PMPPI and TDI isocyanate monomers in the DCE phase (~2:1 molar ratio [TDI]:[PMPPI]) and HMDA monomers in the aqueous phase.*

Wt.% isocyanate in DCE phase	**[TDI] / mM**	**[PMPPI] / mM**	**[HMDA] / mM**
0.1	6.9	3.2	11.8
0.05	3.45	1.6	5.9
0.04	2.76	1.28	4.72
0.02	1.38	0.64	2.36
0.01	0.69	0.32	1.18
0.005	0.35	0.16	0.59

A number of repeat experiments were carried out using each concentration. The impedance versus time spectra for each concentration are shown in Figure 4.22.

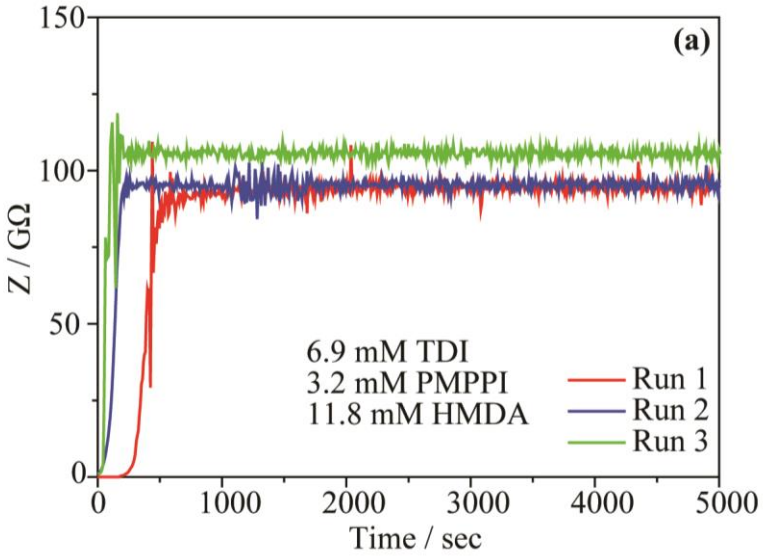
(a)
Z / GΩ
Time / sec
6.9 mM TDI
3.2 mM PMPPI
11.8 mM HMDA
Run 1
Run 2
Run 3

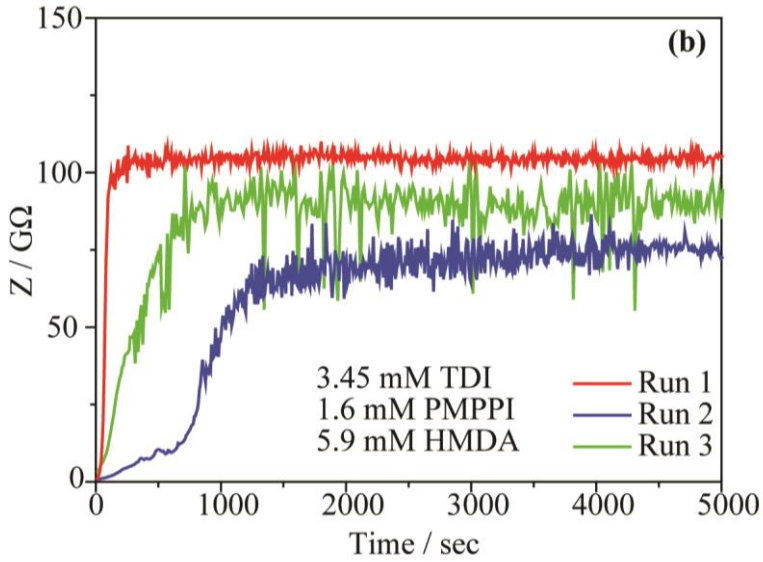
(b)
Z / GΩ
Time / sec
3.45 mM TDI
1.6 mM PMPPI
5.9 mM HMDA
Run 1
Run 2
Run 3

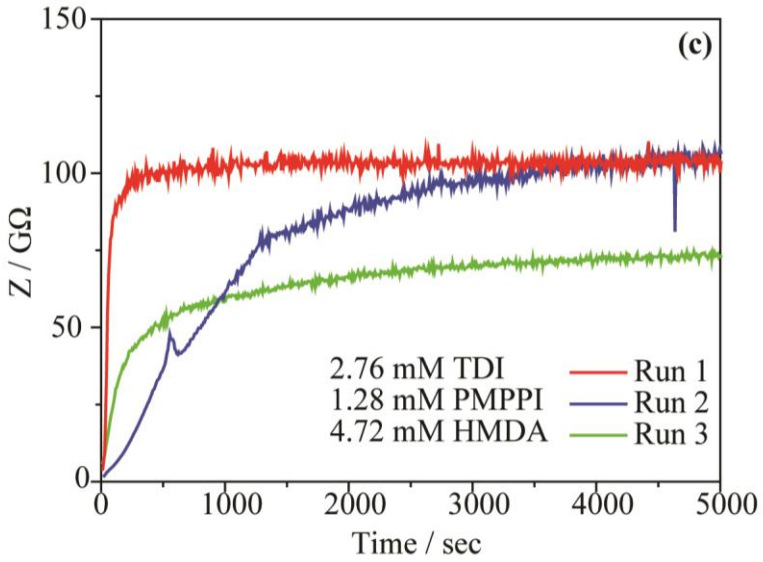
(c)
Z / GΩ
Time / sec
2.76 mM TDI
1.28 mM PMPPI
4.72 mM HMDA
Run 1
Run 2
Run 3

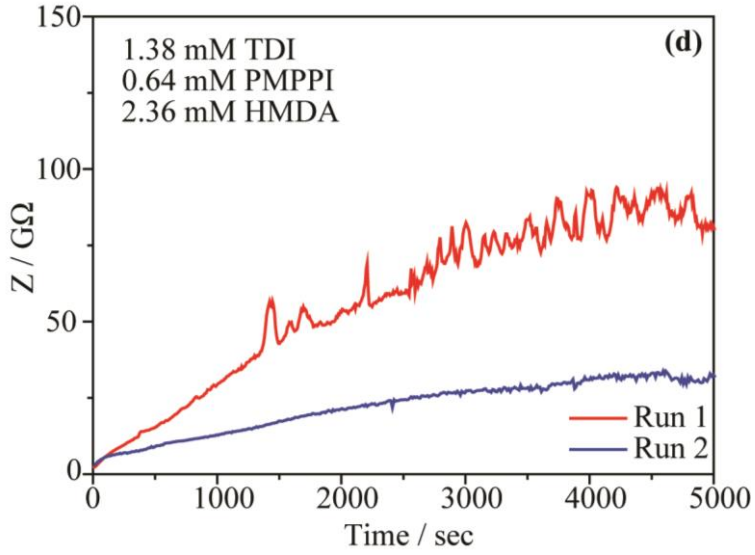
(d)
1.38 mM TDI
0.64 mM PMPPI
2.36 mM HMDA
Z / GΩ
Time / sec
Run 1
Run 2
0
50
100
150
0
1000
2000
3000
4000
5000

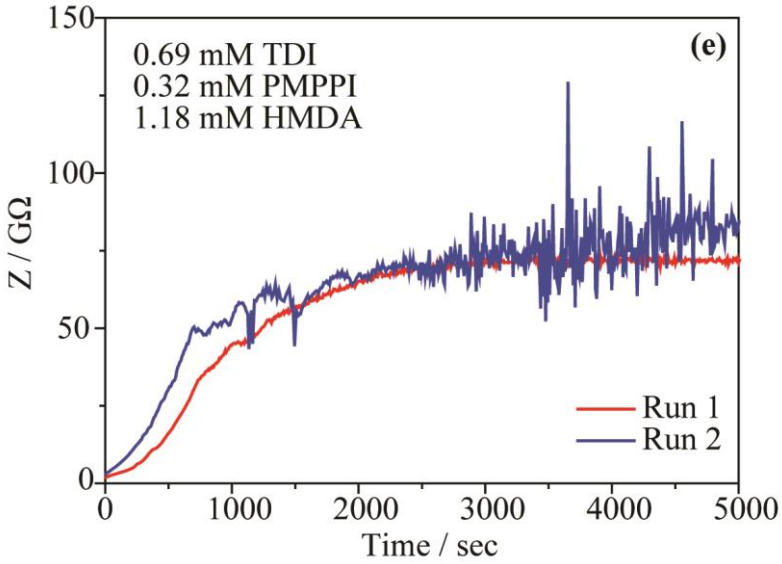
(e)
0.69 mM TDI
0.32 mM PMPPI
1.18 mM HMDA
Z / GΩ
Time / sec
Run 1
Run 2
0
50
100
150
0
1000
2000
3000
4000
5000

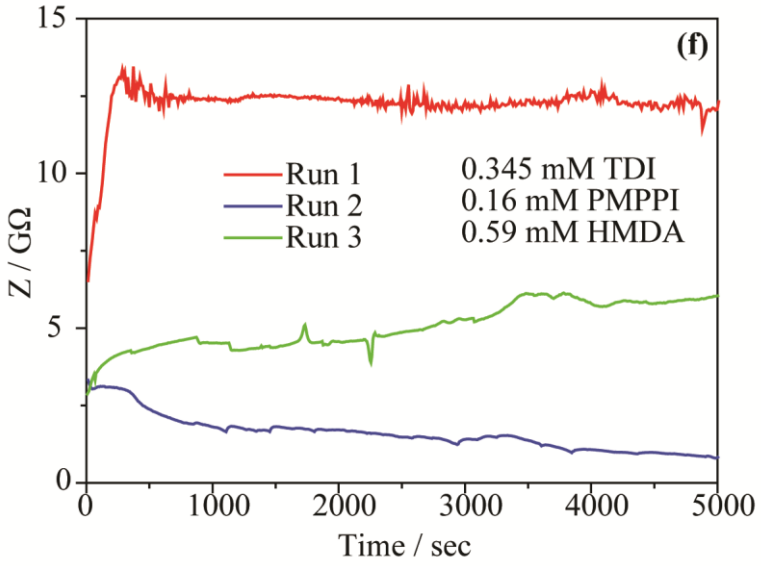

Figure 4.22 *Impedance versus time spectra recorded during poly(urea) film formation using (a) 6.9 mM $TDI_{(DCE)}$/ 3.2 mM $PMPPI_{(DCE)}$/ 11.8 mM $HMDA_{(aq)}$, (b) 3.45 mM $TDI_{(DCE)}$/ 1.6 mM $PMPPI_{(DCE)}$/ 5.9 mM $HMDA_{(aq)}$, (c) 2.76 mM $TDI_{(DCE)}$/ 1.28 mM $PMPPI_{(DCE)}$/ 4.72 mM $HMDA_{(aq)}$, (d) 1.38 mM $TDI_{(DCE)}$/ 0.64 mM $PMPPI_{(DCE)}$/ 2.36 mM $HMDA_{(aq)}$ (e) 0.69 mM $TDI_{(DCE)}$/ 0.32 mM $PMPPI_{(DCE)}$/ 1.18 mM $HMDA_{(aq)}$ and (f) 0.35 mM $TDI_{(DCE)}$/ 0.16 mM $PMPPI_{(DCE)}$/ 0.59 mM $HMDA_{(aq)}$. Impedance was recorded at a frequency of 0.5 Hz using a DC potential of +0.2V with an oscillation of 10 mV.*

The impedance spectra shown in Figure 4.22 appear to mimic the trends seen in Figure 4.18 in that reducing isocyanate concentration slows down the rate of poly(urea) film formation. Changing the concentration of HMDA in the aqueous phase also appears to have an effect on the impedance value recorded once the spectra plateau. Poly(urea) films formed using higher concentrations of isocyanate and HMDA not only form faster but also plateau at higher impedance values than those formed using lower concentrations of isocyanate and HMDA. The impedance spectra collected using 0.005 wt.% PMPPI/TDI was deemed to be unreliable due to the comparatively high impedance seen in Figure 4.21 when using such a low concentration of HMDA in the aqueous phase.

In an attempt to compare the rate of film formation with isocyanate concentration, data collected at each concentration was background subtracted to take into account the influence of changing the HMDA concentration and then averaged. The average impedance versus time profile for each concentration is shown in Figure 4.23.

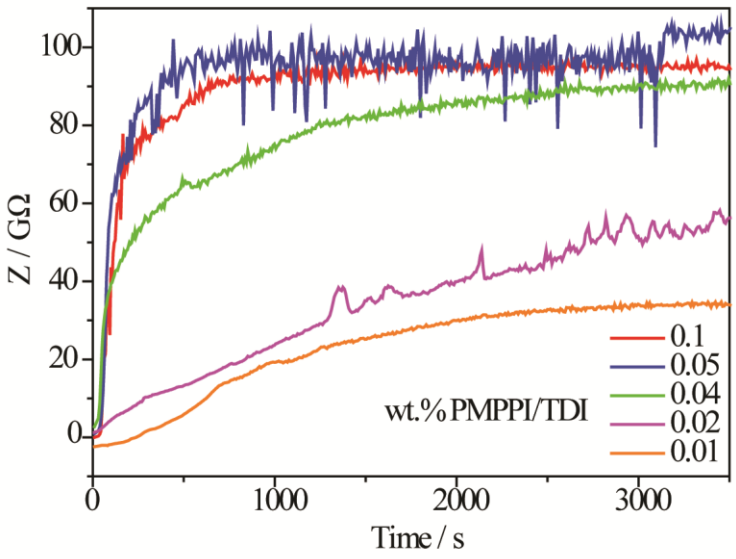

Figure 4.23 *Average impedance over time recorded during poly(urea) film formation using different concentrations of 2:1 molar ratio TDI: PMPPI (DCE phase) in the presence of different concentrations of HMDA (aqueous phase). Impedance was recorded at a frequency of 0.5 Hz using a DC potential of +0.2V with an oscillation of 10 mV.*

Like the previous impedance versus time profiles using PEI, the rate of poly(urea) film formation appears to be dependent on the concentration of isocyanate in the DCE phase. However, the availability of amine will also play a role in the reaction rate. Interestingly, it appears that the rate of reaction for 0.04, 0.02 and 0.01 wt.% PMPPI/TDI is slower than the equivalent isocyanate concentrations in the presence of 40 µM PEI. Although the concentration of HMDA is reduced with isocyanate concentration, it remains much higher than the amount of PEI used. Therefore, it could be that despite the low concentration of PEI compared to HMDA the rate of reaction at the interface is faster. This could be due to either the increased molar amount of amine groups per molecule for PEI or potentially its improved ability to insert into the

liquid/liquid interface compared to HMDA. Structural differences between HMDA and PEI could also explain why the overall impedance after film formation is generally lower for films formed in the presence of PEI compared to HMDA. The branched structure of PEI and its increased surface functionality which may interfere with reactions at the liquid/liquid interface would likely lead to more porous and thus unstable poly(urea) films. Henceforth, these characteristics may explain why impedance decreases attributed to film drop off are observed during poly(urea) formation in the presence of PEI and not HMDA.

To quantify the impact of isocyanate and HMDA monomer concentration on the rate of poly(urea) film formation, Figure 4.24 shows the time for all impedance profiles recorded to reach half their final value was plotted versus the concentration of TDI/PMPPI in the DCE phase. Unlike the equivalent half Z versus time plot for film formation in the presence of PEI, no discernible trends can be seen between concentration and time taken for film to form. It may be that at higher concentrations, isocyanate monomers saturate the liquid/liquid interface, and as there are enough amine monomers available the rate of reaction between these higher concentrations remains similar. However, once the concentration of isocyanate is lowered to the point at which the interface is no longer saturated, the low concentration of amine at the interface causes the reaction to slow down steeply.

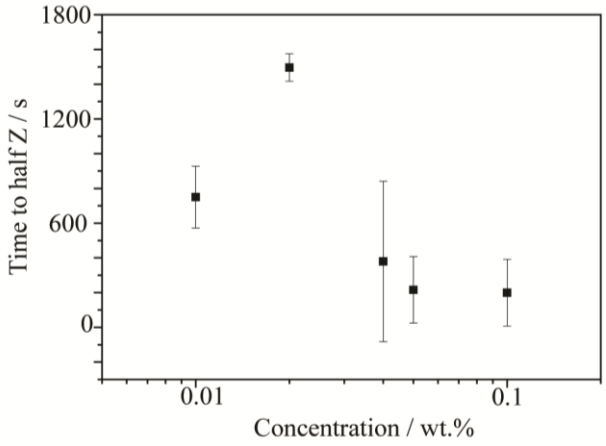

Figure 4.24 *Plot of time for impedance profiles to reach half their final value versus concentration of PMPPI/TDI used (wt.% in the DCE phase) with standard deviation. Stoichiometric proportions of HMDA were present in the aqueous phase (see Table 4.5).*

4.3.4.3 Poly(urea) Film Formation Using Different Concentrations of PMPPI and TDI

Experiments were carried out to probe poly(urea) film formation via isocyanate hydrolysis without additional amine in the aqueous phase. Initially, impedance over time without either isocyanate monomers in the DCE phase or amine monomers in the aqueous phase was measured to check the stability of the system. The mean of these readings is shown in Figure 4.25.

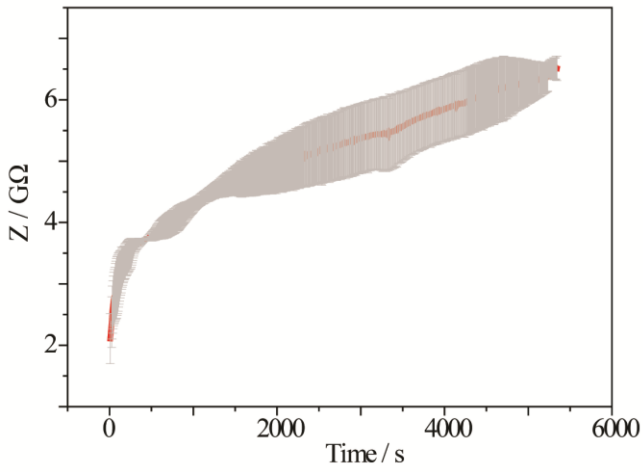

Figure 4.25 *Mean impedance over time with standard deviation recorded using the set-up shown in Figure 4.1. DC potential was +0.2 V with an oscillation of 10 mV, frequency was 0.5 Hz.*

The impedance over time shown in Figure 4.25 suggests that background impedance at this frequency will remain stable, implying that any impedance change with the addition of isocyanate monomers will be due to interfacial film formation alone. However, it appears that the background impedance without amine present in the aqueous phase will be higher than with amine present. Table 4.6 details the different concentrations of isocyanate used in the DCE phase for impedance measurements during poly(urea) film formation.

Table 4.6 *Concentrations used in impedance versus time experiments of PMPPI and TDI isocyanate monomers in the DCE phase (~2:1 molar ratio [TDI]:[PMPPI]).*

Wt.% in DCE	[TDI] / mM	[PMPPI] / mM
0.5	34.5	16
0.1	6.9	3.2
0.05	3.45	1.6
0.01	0.69	0.32
0.001	0.07	0.03

Although a number of repeat experiments were carried out at each concentration, it was found that the impedance profiles for each concentration could vary widely from run to run. The impedance profiles recorded using different concentrations of isocyanate are shown in Figure 4.26.

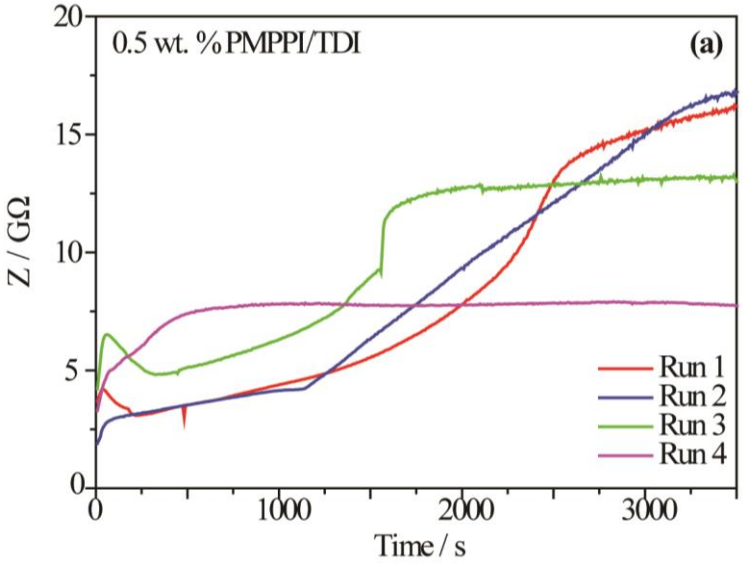
0.5 wt. % PMPPI/TDI
(a)
Z / GΩ
Time / s
Run 1
Run 2
Run 3
Run 4

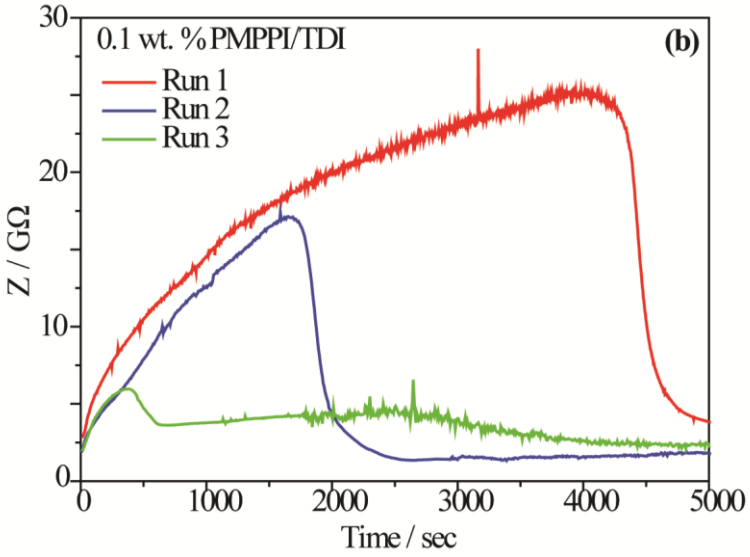
0.1 wt. % PMPPI/TDI
(b)
Z / GΩ
Time / sec
Run 1
Run 2
Run 3

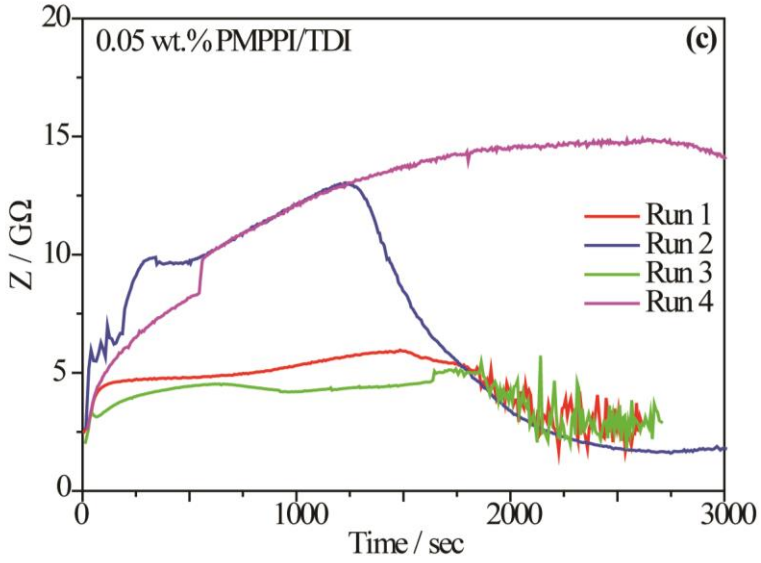
0.05 wt.% PMPPI/TDI
(c)
Z / GΩ
Time / sec
Run 1
Run 2
Run 3
Run 4

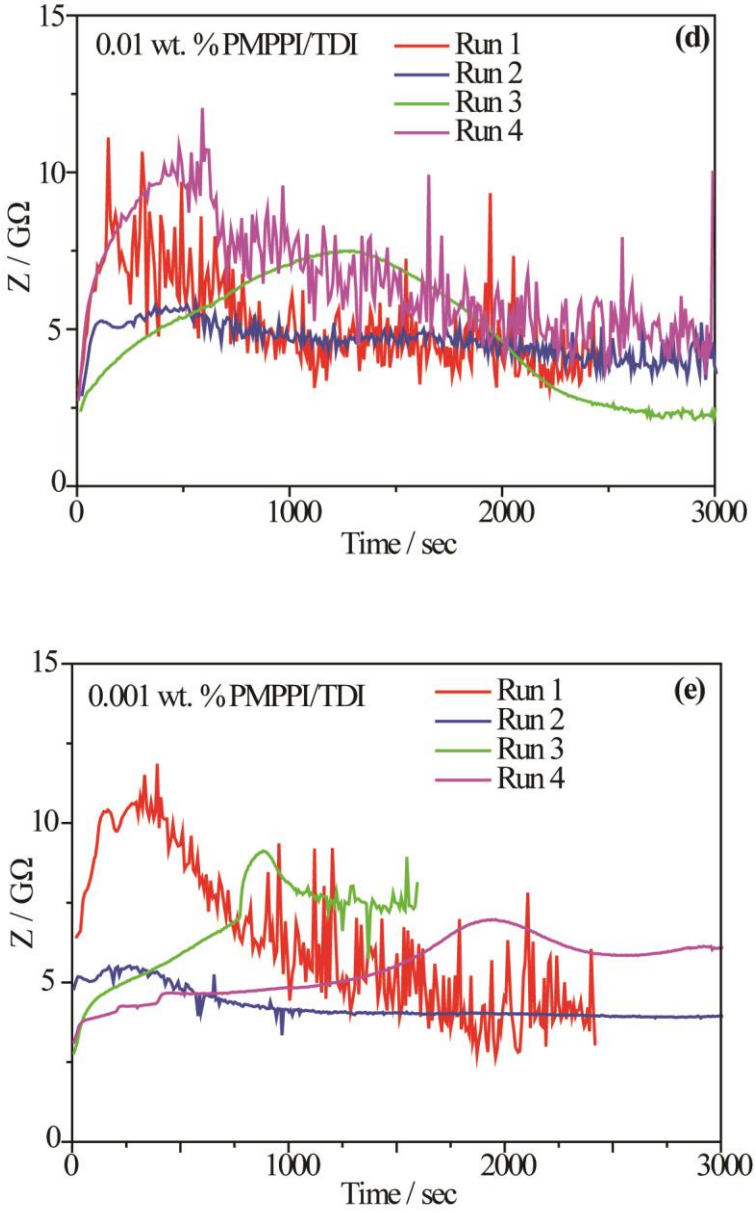

Figure 4.26 *Impedance versus time profiles recorded during poly(urea) film formation using (a) 34.5 mM TDI/ 16 mM PMPPI (0.5 wt.%), (b) 6.9 mM TDI/ 3.2 mM PMPPI (0.1 wt.%), (c) 3.45 mM TDI/ 1.6 mM PMPPI (0.05 wt.%), (d) 0.69 mM TDI/ 0.32 mM PMPPI (0.01 wt.%) and (e) 0.069 mM TDI/ 0.032 mM PMPPI (0.001 wt.%) in the DCE phase. DC potential was +0.2 V with an oscillation of 10 mV, frequency was 0.5 Hz.*

The data shown in Figure 4.26 suggests that film formation via isocyanate hydrolysis at the liquid/liquid interface will proceed slower than in the presence of additional amine monomers in the aqueous phase. It can also be observed that the total impedance after film formation is much lower in the absence of amine than impedance recorded during

film formation using equivalent isocyanate concentrations in the presence of HMDA or PEI. This could suggest that films formed in the absence of amine in the aqueous phase will be thinner or more porous. It must also be kept in mind that the background impedance in the absence of film is between 2000 and 7000 MΩ, which is a significant proportion of the overall impedance after film formation in the absence of amine. Film formation using 0.5 wt.% isocyanate appears to eventually form a stable film, after an initial lag time of around 1500 seconds. However, film formation using lower concentrations of isocyanate appears to cause unstable film formation. Impedance profiles showing unstable film formation appear to rise and then fall, where it can be assumed that the growing poly(urea) film has fallen off the micropipette tip. Impedance profiles collected at lower concentrations are also more likely to be noisy, which could be attributed to smaller poly(urea) growth and drop-off events at the liquid/liquid interface.

From these observations, it can be hypothesised that the mechanism of interfacial polymerisation at the liquid/liquid interface is analogous to metal nanoparticle film formation at liquid/liquid interfaces.[33-35] This process is shown in more detail in Figure 4.27a. Poly(urea) oligomers formed at the liquid/liquid interface act as attachment sites for other poly(urea) oligomers, causing poly(urea) to deposit as clumps that eventually join to form a film. If this process is too slow due to lack of available isocyanate monomers, the clumps of poly(urea) may fall off the interface and thus the process will begin again.

Another potential mechanism for film growth is shown in Figure 4.27b. In this process, a poly(urea) oligomers merge to form a "skin" which progressively thickens. This mechanism may explain the appearance of a few of the impedance versus time spectra shown previously, where impedance will rise slowly, stall, then continues to rise.

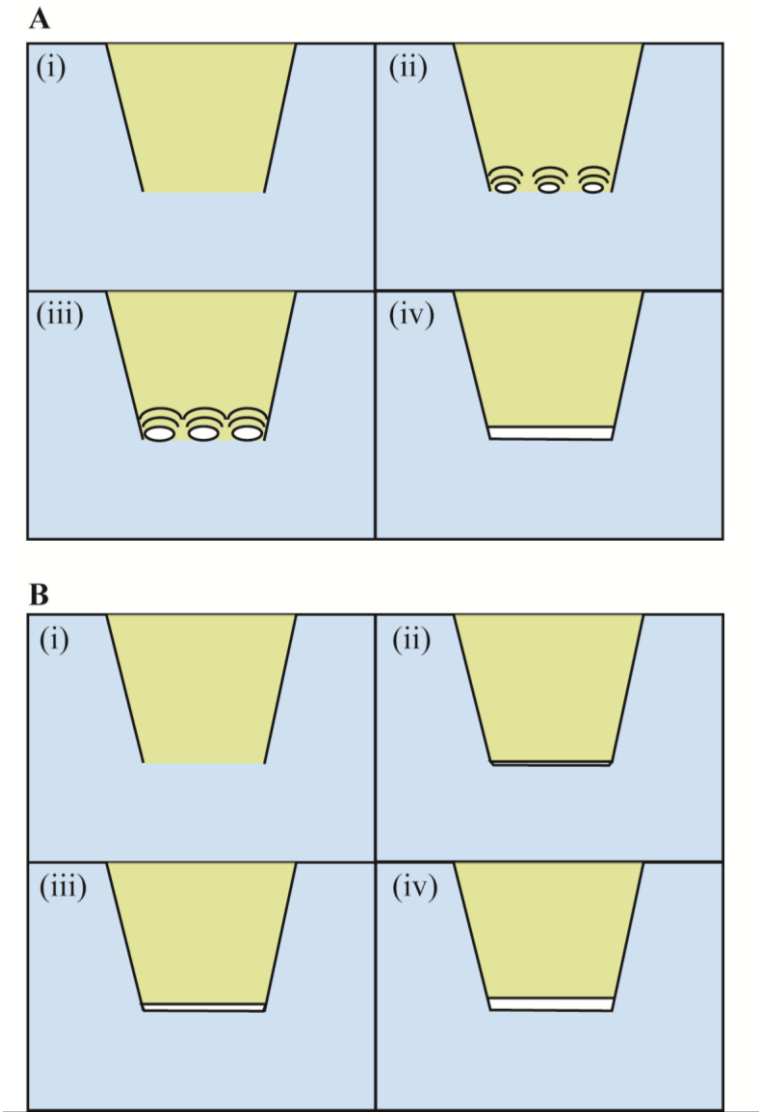

Figure 4.27 *Diagram showing the proposed mechanisms for poly(urea) film formation at the liquid/liquid interface. Mechanism A proceeds as follows: (i) Tip containing isocyanate monomers immersed into aqueous phase where they react with either water or amine monomers to form poly(urea) oligomers, (ii) islands of poly(urea) form at the interface, (iii) poly(urea) islands grow larger by acting as attachment sites for poly(urea) oligomers, (iv) poly(urea) islands eventually merge to form a film across the interface. Mechanism B proceeds as follows: (i) Tip containing isocyanate monomers immersed into aqueous phase where they react with either water or amine monomers to form poly(urea) oligomers, (ii) oligomers merge to form very thin film at the interface, (iii) interfacial film thickens, (iv) interfacial film stops thickening.*

4.3.4.4 Poly(urea) Formation Using Different Ratios of TDI: PMPPI Monomer

To explore the effect of each separate isocyanate monomer on poly(urea) film formation, impedance versus time experiments were carried out using ratios of TDI:PMPPI other than the usual 2:1 molar ratio. The first sets of experiments carried out were designed to explore the effect of an excess of TDI isocyanate to PMPPI on the impedance recorded during film formation. The impedance spectra recorded during poly(urea) formation using a 10:1 molar ratio of TDI:PMPPI isocyanate are shown in Figure 4.28.

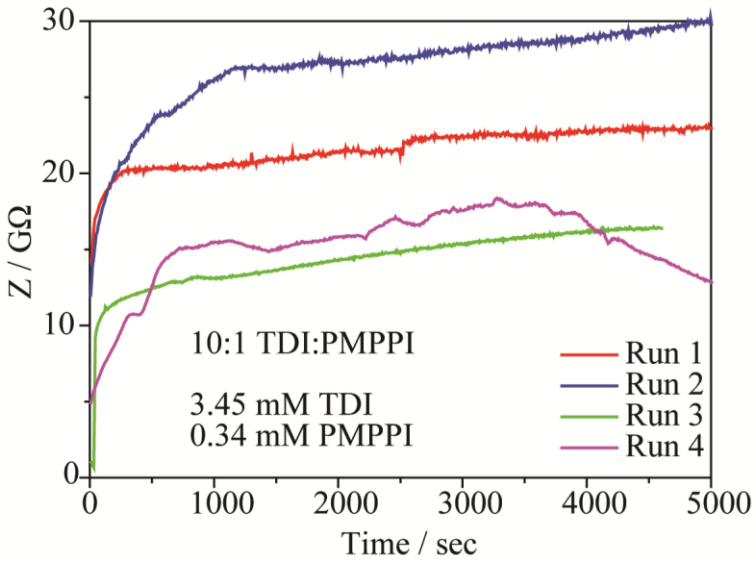

Figure 4.28 *Impedance versus time profiles recorded during poly(urea) film formation using a 10:1 molar ratio of TDI:PMPPI (3.45 mM TDI and 0.34 mM PMPPI in the DCE phase). DC potential was +0.2 V with an oscillation of 10 mV, frequency was 0.5 Hz.*

The impedance profiles shown in Figure 4.28 indicate that an excess of TDI to PMMPI will lead to impedance profiles that plateau between 10000 and 30000 MΩ. Surprisingly, three out of the four profiles show no drop in impedance over time even though previous experiments using either 3.45 mM TDI or 0.34 mM PMPPI in the 2:1 ratio showed drop in impedance over time. It is possible that films formed using an

excess of TDI are not only stable over these time periods but also compact, hence the higher on average final impedance values reached compared to data collected using a 2:1 molar ratio.

For completeness, experiments were carried out to assess the effect of an excess of PMPPI to TDI on the impedance recorded during poly(urea) film formation. The results of these experiments are shown in Figure 4.29.

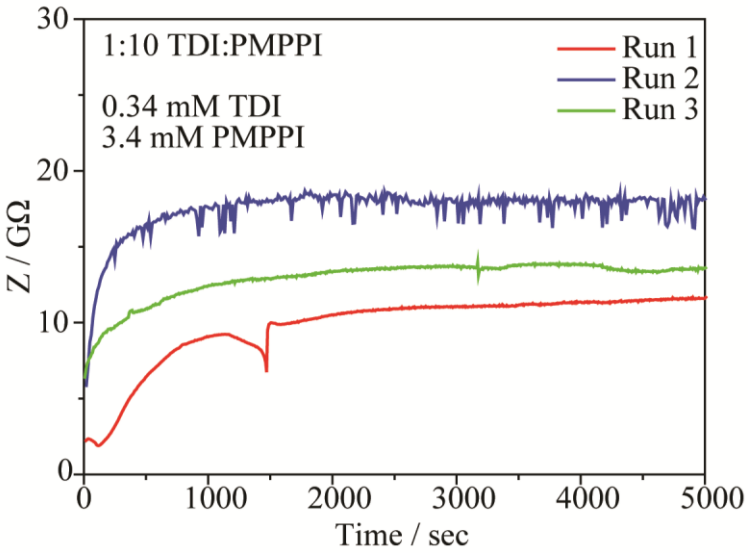

Figure 4.29 *Impedance versus time profiles recorded during poly(urea) film formation using a 1:10 molar ratio of TDI:PMPPI (0.34 mM TDI and 3.4 mM PMPPI in the DCE phase). DC potential was +0.2 V with an oscillation of 10 mV, frequency was 0.5 Hz.*

Interestingly, other than the impedance profiles plateauing at lower values (between 10000 to 20000 MΩ) they are similar to those collected using a 10:1 TDI:PMPPI ratio in that they show no drop over time. It may be that even though the concentration of TDI is reduced it is still high enough to form a film on a similar timescale to the 10:1 TDI:PMPPI experiments. However, like the previous study using different concentrations of isocyanate with no amine in the aqueous phase, it must be kept in mind that the background impedance will be a significant proportion of the total impedance recorded during film formation. Therefore, for both TDI:PMPPI ratios it can

be assumed that the impedance change from film formation is fairly small. This could suggest that the film formed is relatively thin or porous.

4.3.4.5 Poly(urea) Formation Using TDI and PMPPI at Different Temperatures

As previously mentioned, poly(urea) is typically formed under raised temperature to increase the reaction rate of the isocyanate monomers. To explore the effect of raising the temperature on the rate of film formation and characteristics of the poly(urea) film, impedance versus time experiments were carried out using a fixed concentration of isocyanate monomers heated to different temperatures. The results of these experiments are shown in Figure 4.30.

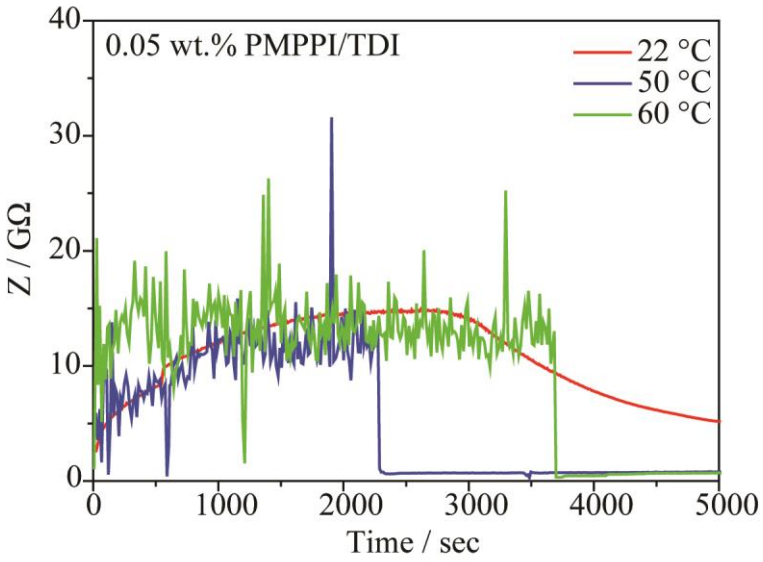

Figure 4.30 *Impedance versus time profiles recorded during poly(urea) film formation using 0.05 wt. % TDI/PMPPI in the DCE phase (3.45 mM TDI, 1.60 mM PMPPI) at different temperatures. DC potential was +0.2 V with an oscillation of 10 mV, frequency was 0.5 Hz.*

The impedance profiles shown in Figure 4.30 appear to show that the rate of poly(urea) film formation will be similar between room temperature and 50 °C. However, the film formation rate appears to be faster at 60 °C. Raising the temperature of the aqueous phase also appears to introduce noise to the measured impedance, which could be

attributed to more poly(urea) nucleation events at the liquid/liquid interface due to the increased rate of reaction. All three impedance profiles plateau at similar impedance values, suggesting that the films formed are of similar thickness and/or porosity. It also appears as though impedance will drop over time regardless of whether the temperature has been raised, although this drop off is more dramatic when the temperature is raised. It may be that if raising the temperature leads to an increased amount of nucleation sites there will be more natural faults in the poly(urea) film, potentially leading to film breakage and thus causing a sudden drop in the measured impedance.

4.3.5 Scanning Electron Microscopy of Poly(Urea) Films Formed During EIS Experiments

In order to correlate impedance data observations with poly(urea) film characteristics, SEM measurements were made of the films formed at the end of the glass capillary tips after EIS experiments.

4.3.5.1 Comparison of Poly(urea) Films Formed In The Presence or Absence of Additional Amine Monomers in the Aqueous Phase

SEM images were taken of poly(urea) films formed using a 2:1 molar ratio of TDI:PMPPI isocyanate in the presence or absence of amine monomers PEI or HMDA in the aqueous phase. The first of these was a poly(urea) film formed with PEI in the aqueous and is shown in Figure 4.31. The SEM image shows that poly(urea) films formed under these conditions appears flat at the resolution attainable. The white mesh-like structure was thought to be leftover salt and not part of the film.

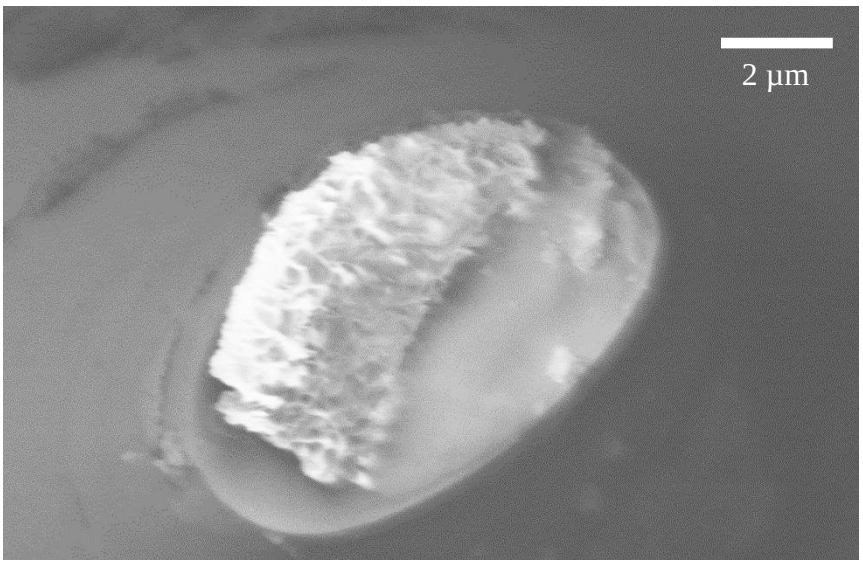

Figure 4.31 *SEM image of a poly(urea) film formed using 6.9 mM TDI and 3.2 mM PMPPI in the DCE phase and 40 µM PEI in the aqueous phase during an EIS experiment.*

To compare the structure of poly(urea) films formed using different amine monomers, SEM was carried out on a poly(urea) film formed using a 2:1 molar ratio of TDI:PMPPI isocyanate monomers in the presence of amine monomer HMDA in the aqueous phase. This is shown in Figure 4.32.

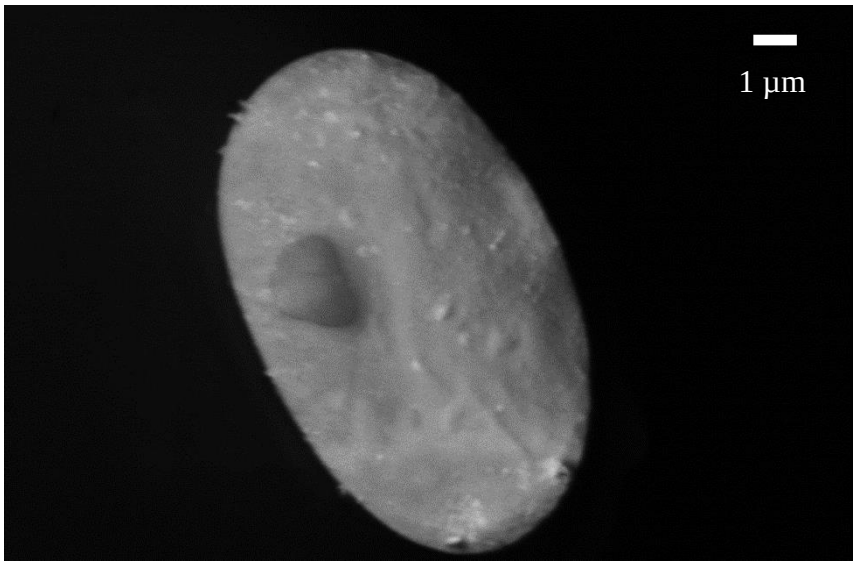

Figure 4.32 *SEM image of a poly(urea) film formed using 0.69 mM TDI and 0.32 mM PMPPI in the DCE phase and 1.18 mM PEI in the aqueous phase during an EIS experiment.*

Like the previous film formed using PEI in the aqueous phase, the SEM image shows that a relatively flat film will form when HMDA is present in the aqueous phase.

SEM was then carried out on a poly(urea) film formed in the absence of additional amine monomers in the aqueous phase. The SEM image of this film is shown in Figure 4.33

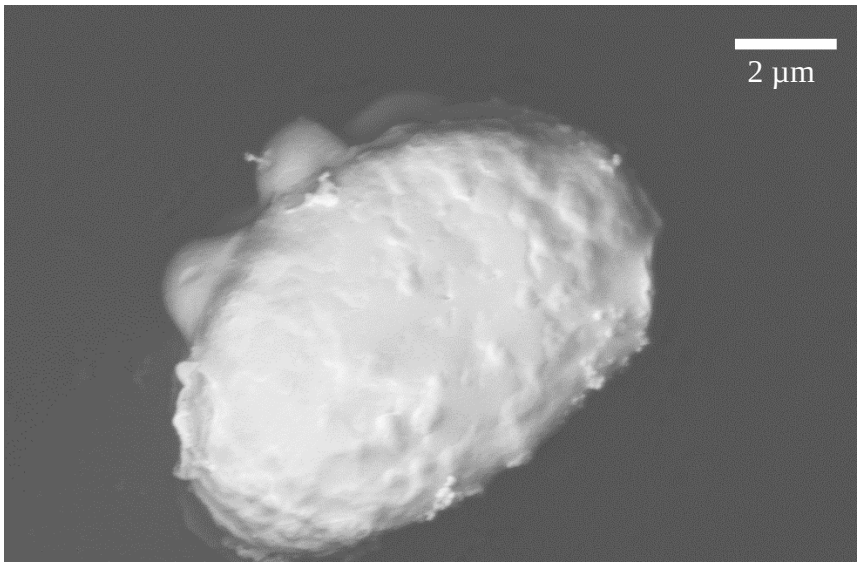

Figure 4.33 *SEM image of a poly(urea) film formed using 6.9 mM TDI and 3.2 mM PMPPI in the DCE phase and no additional amine monomers in the aqueous phase during an EIS experiment.*

Unlike the previous poly(urea) films formed in the presence of additional amine monomers, the film shown in Figure 4.33 has a bumpy exterior. The film also appears to extend over the edges of the glass capillary unlike those formed in the presence of PEI or HMDA. This could suggest some isocyanate monomers diffuse into and then hydrolyse in the aqueous phase rather than only at the liquid/liquid interface. Poly(urea) oligomers that form in the aqueous phase then attach themselves to either the glass wall or the growing polymer film. For films formed in the presence of PEI or HMDA, the faster reaction rate between isocyanates and amine monomers opposed to the rate of isocyanate hydrolysis means that isocyanate monomers have less time to diffuse into the aqueous phase before oligomerising. Henceforth, so long as an excess of amine

monomers are available at the liquid/liquid interface the film formed should be flat and compact.

Alternatively, the bumpy appearance of the film shown in Figure 4.33 may be due to foaming caused by the production of CO_2 following isocyanate hydrolysis (as shown in Figure 4.1). Films formed using lower concentrations of isocyanate or in the presence of amine will produce much lower levels of CO_2, thus foaming will be reduced and flatter films will be observed.

Overall, it appears that films formed in the presence of additional amine monomers appear flatter and more compact whereas films formed without are rougher and perhaps more porous. These observations are consistent with the trends seen in the previously collected impedance data, which showed that films formed in the presence of amine monomers would reach much higher final impedance values compared to those formed without.

4.3.5.2 Comparison of Poly(urea) Films Formed Using Different Ratios of TDI to PMPPI Isocyanate

SEM images were taken of poly(urea) films formed using a 10:1 and a 1:10 molar ratio of TDI:PMPPI in the absence of any additional amine monomers in the aqueous phase. Figure 4.34 shows a poly(urea) film formed using a 10:1 molar ratio of TDI:PMPPI isocyanate monomers. The clearly visible edges of the glass capillary suggest that the film formed under these conditions is relatively thin. The film also appears mostly flat, although a few poly(urea) "peaks" are visible.

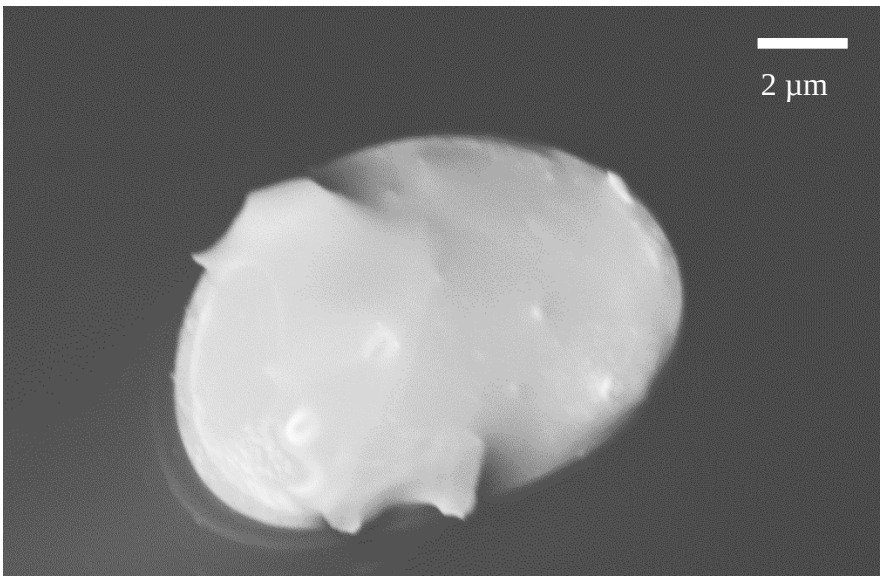

Figure 4.34 *SEM image of a poly(urea) film formed using a 10:1 molar ratio of TDI:PMPPI (3.4 mM TDI and 0.34 mM PMPPI) in the DCE phase and no additional amine monomers in the aqueous phase during an EIS experiment.*

SEM was then carried out on a poly(urea) film formed using a 1:10 molar ratio of TDI:PMPPI, which is shown in Figure 4.35.

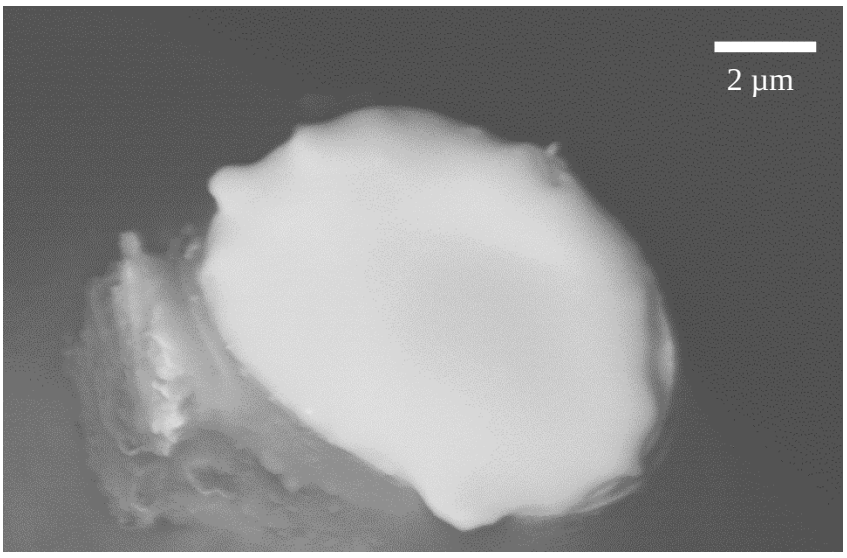

Figure 4.35 *SEM image of a poly(urea) film formed using a 1:10 molar ratio of TDI:PMPPI (0.34 mM TDI and 3.4 mM PMPPI) in the DCE phase and no additional amine monomers in the aqueous phase during an EIS experiment.*

The SEM image shows a flat film that appears to have grown over the edge of the glass capillary. Layers of film can also be observed on the side of the capillary.

Overall, it appears that changing the ratio of isocyanate monomers in this manner has a limited effect on the appearance of the poly(urea) film. It is surprising that both of the films appear flat, as without additional amine monomers present a bumpier appearance similar to that seen in Figure 4.33 was expected. The flatness of the film may be due to a lack of available isocyanate monomers leading to a reduced film thickness.

Coupling the SEM images shown in Figure 4.34 and Figure 4.35 with observations from previously collected impedance versus time data, it can now be hypothesised that an initial film forms which then builds up as the reaction progresses. It can also now be assumed that the change in impedance from film formation is mainly due to initial film formation and not subsequent film build-up, which would explain why similar peak impedance values (10000-30000 M ohms) are recorded in the absence of amine regardless of molar ratio or concentration of isocyanate used.

4.3.5.3 Comparison of Poly(urea) Films Formed At Different Temperatures

SEM images were taken of poly(urea) films formed under different temperature using a fixed concentration of isocyanate monomers. Figure 4.36 shows the first of these, which was a film formed at room temperature (22 °C). The SEM image shows a film of mixed roughness, with some parts that appear smooth and some that appear uneven. The smoothness of the film compared to the film shown in Figure 4.33 indicates that the lower concentration of isocyanate used has led to reduced film build up past the initial film formation stage.

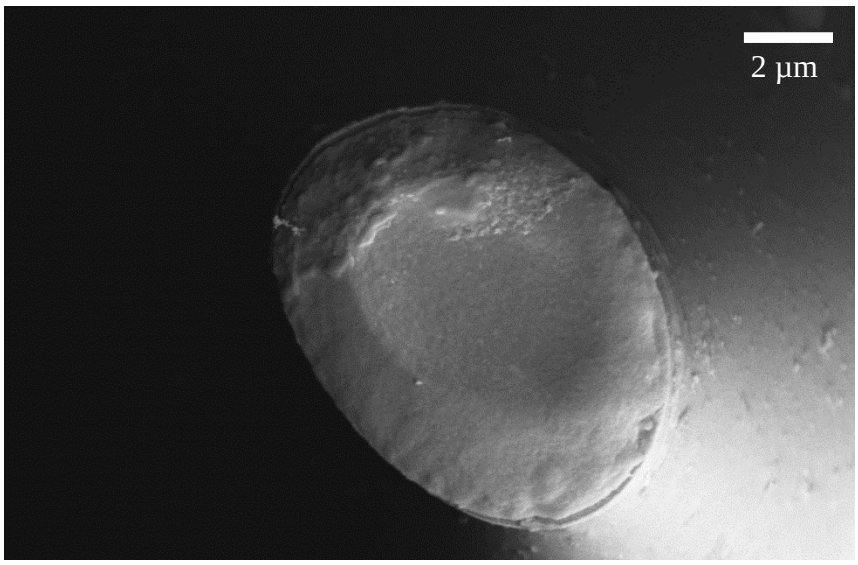

Figure 4.36 *SEM image of a poly(urea) film formed at room temperature (22 °C) using 3.45 mM TDI and 1.6 mM PMPPI in the DCE phase and no additional amine monomers in the aqueous phase during an EIS experiment.*

SEM images were then taken of poly(urea) films formed at raised temperature. Figure 4.37 shows a poly(urea) film formed at 50 °C.

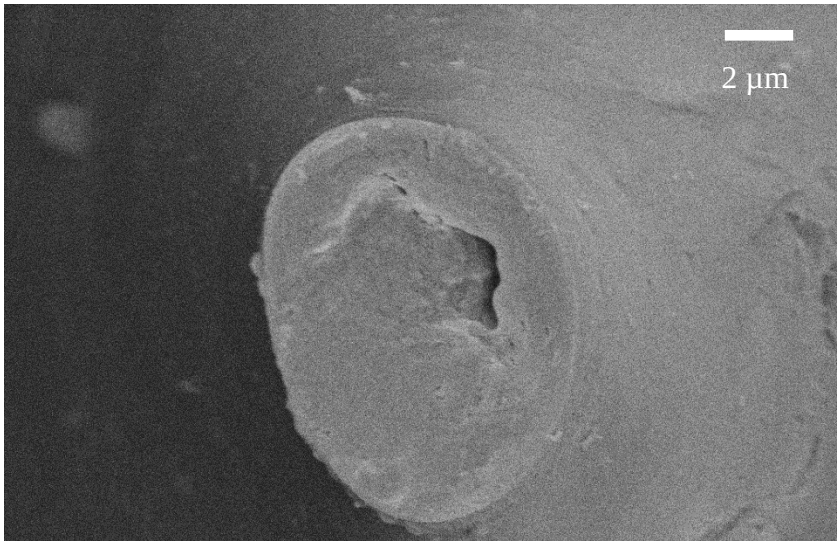

Figure 4.37 *SEM image of a poly(urea) film formed at 50 °C using 3.45 mM TDI and 1.6 mM PMPPI in the DCE phase and no additional amine monomers in the aqueous phase during an EIS experiment.*

The SEM image shows that a flat film will form when the temperature is raised to 50 °C. The image also shows that the middle part of the film has broken inwards; confirming that the film formed is relatively thin.

To see the effect of raising the temperature even higher, EIS experiments were also carried out at 60 °C. SEM images were then taken of films formed during these experiments, one of which is shown in Figure 4.38. The SEM image demonstrates that a flat film will also form at 60 °C. Overall, it appears that raising the temperature during poly(urea) film formation will lead to more even film surface. This could be due to the increased rate of isocyanate hydrolysis leading to a faster rate of initial film formation. As the isocyanate monomers have had less time to diffuse into the aqueous phase before the initial film forms across the interface, there are fewer isocyanate monomers/ poly(urea) oligomers available for subsequent film build up on the aqueous side and henceforth the films remain smooth.

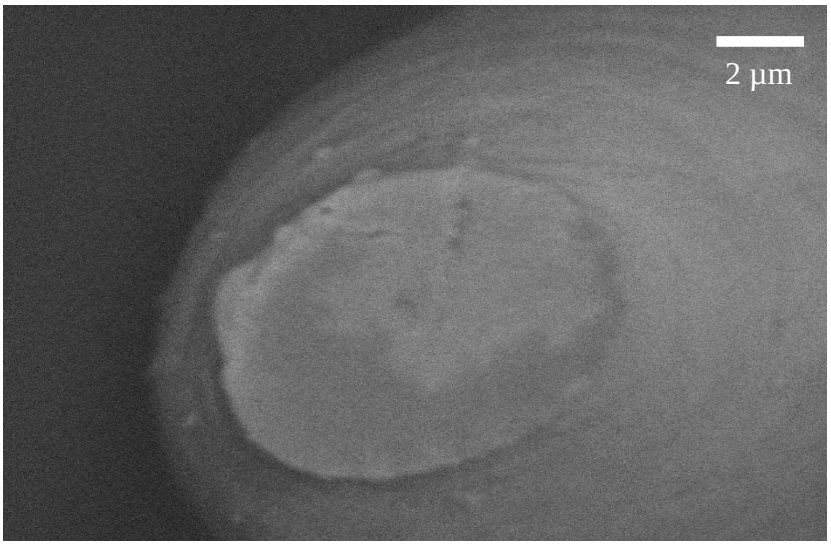

Figure 4.38 *SEM image of a poly(urea) film formed at 60 °C using 3.45 mM TDI and 1.6 mM PMPPI in the DCE phase and no additional amine monomers in the aqueous phase during an EIS experiment.*

4.4 Conclusions

The aim of the work presented in this chapter was to investigate the formation of a poly(urea) film at an immiscible liquid/liquid interface. Cyclic voltammetry was initially used to find a suitable DC potential where neither isocyanate nor amine monomers transferred across the liquid/liquid interface, allowing interfacial films to form in their natural state. EIS spectra taken before and after film formation both with and without amine monomers in the aqueous phase showed an increase in impedance which could be attributed to interfacial film formation.

A simple circuit diagram was used to model the impedance spectra, which showed that the increase in impedance with film formation could be attributed to a mixture of increased interfacial resistance and reduced interfacial capacitance. The tendency towards more ideal capacitive behaviour at the interface also suggested that the film formed was compact. However, the lower interfacial resistance and less-ideal capacitive behaviour for films formed in the absence of additional amine monomers suggest that these films may be more porous than those formed in the presence of additional amine monomers. SEM images collected afterwards appear to confirm that films formed in the presence of additional PEI or HMDA amine monomers will be more compact than those formed without.

The rate of interfacial poly(urea) film formation was monitored by measuring the change in impedance over time at a frequency of 0.5 Hz, as lower frequencies had previously been shown to be most sensitive to changing impedance with film formation. Poly(urea) formation under a range of different reaction conditions was investigated.

In the presence of 40 μM PEI, it was found that the rate of poly(urea) film formation will remain constant until the concentration of isocyanate monomers is reduced below a

particular threshold. Below this threshold, the rate of film formation becomes dependent on the concentration of isocyanate. It was therefore hypothesised that the interfacial reaction will be diffusion-controlled, until the interface is no longer saturated with isocyanate monomers and it thus switches to a concentration dependent regime.

In the presence of proportional amounts of HMDA to PMPPI/TDI, the rate of poly(urea) film formation appears to rapidly reduce below a certain monomer concentration threshold. At higher concentrations the rates of film formation appears similar, suggesting that the monomers saturate the liquid/liquid interface. However, as monomer concentrations are reduced the liquid/liquid interface is no longer saturated with isocyanate monomers but there are also fewer adjacent HMDA monomers available for the condensation reaction. Henceforth, the rate of film formation reduces steeply.

Poly(urea) film formation via isocyanate hydrolysis at the liquid/liquid interface was shown to proceed slower than in the presence of additional PEI/HMDA monomers in the aqueous phase. Film formation appeared to be stable at higher concentrations but became more unstable at lower concentrations. This was attributed to a postulated mechanism of film growth, which was thought to progress via the deposition of poly(urea) at nucleation sites that grow and eventually merge to form a single film.

The effect of changing the molar ratio of isocyanate monomers in the DCE phase was also explored. EIS measurements over time showed that changing the molar ratio from 10:1 to 1:10 TDI:PMPPI monomers had a limited effect on the rate of poly(urea) film formation. This was attributed to the much higher reactivity of the TDI monomer in comparison with the PMPPI monomer. SEM images of films formed using both monomer ratios showed flat, thin films.

Finally, poly(urea) film formation under different temperatures was investigated. EIS over time experiments showed that the rate of film formation will increase as the temperature is increased. SEM images taken after film formation indicated that increasing the temperature will increase the likelihood that the film formed will be smooth. Both of these observations were attributed to a faster rate of isocyanate hydrolysis at raised temperature leading to a faster rate of film formation.

4.5 References

1. S. K. Yadav, K. C. Khilar and A. K. Suresh, *AlChE J.*, 1996, **42**, 2616-2626.
2. S. K. Yadav, K. C. Khilar and A. K. Suresh, *Journal of Membrane Science*, 1997, **125**, 213-218.
3. R. G. Pearson and E. L. Williams, *Journal of Polymer Science: Polymer Chemistry Edition*, 1985, **23**, 9-18.
4. S. K. Yadav, A. K. Suresh and K. C. Khilar, *AlChE J.*, 1990, **36**, 431-438.
5. J. H. Bradbury, P. J. Crawford and A. N. Hambly, *Transactions of the Faraday Society*, 1968, **64**, 1337-1347.
6. S. J. Wagh, S. S. Dhumal and A. K. Suresh, *Journal of Membrane Science*, 2009, **328**, 246-256.
7. S. S. Dhumal, S. J. Wagh and A. K. Suresh, *Journal of Membrane Science*, 2008, **325**, 758-771.
8. S. K. Karode, S. S. Kulkarni, A. K. Suresh and R. A. Mashelkar, *Chem. Eng. Sci.*, 1998, **53**, 2649-2663.
9. S. S. Dhumal and A. K. Suresh, *Polymer*, 2010, **51**, 1176-1190.
10. G. Raspoet, M. T. Nguyen, M. McGarraghy and A. F. Hegarty, *The Journal of Organic Chemistry*, 1998, **63**, 6867-6877.
11. E. V. Ivanova and H. M. Muchall, *The Journal of Physical Chemistry A*, 2007, **111**, 10824-10833.
12. B.-Y. Chang and S.-M. Park, *Annual Review of Analytical Chemistry*, 2010, **3**, 207-229.
13. E. Boubour and R. B. Lennox, *Langmuir*, 2000, **16**, 4222-4228.

14. A. Galal, S. Darwish and R. Ahmed, *J. Solid State Electrochem.*, 2007, **11**, 531-542.

15. M. D. Levi, Y. Gofer, D. Aurbach and A. Berlin, *Electrochim. Acta*, 2004, **49**, 433-444.

16. V. Freger and S. Bason, *Journal of Membrane Science*, 2007, **302**, 1-9.

17. S. Bason, Y. Oren and V. Freger, *Journal of Membrane Science*, 2007, **302**, 10-19.

18. C. Deslouis, M. M. Musiani and B. Tribollet, *The Journal of Physical Chemistry*, 1994, **98**, 2936-2940.

19. H. G. L. Coster, T. C. Chilcott and A. C. F. Coster, *Bioelectrochem. Bioenerg.*, 1996, **40**, 79-98.

20. A. Lhotský, K. Holub, P. Neužil and V. Mareček, *J. Chem. Soc., Faraday Trans.*, 1996, **92**, 3851-3857.

21. Z. Samec, A. Lhotský and V. R. Mareček, *Electrochim. Acta*, 1999, **45**, 583-590.

22. Z. Samec, J. Langmaier and A. Trojánek, *J. Electroanal. Chem.*, 1997, **426**, 37-45.

23. B. R. Silver, K. Holub and V. Mareček, *J. Electroanal. Chem.*, 2014, **731**, 107-111.

24. Z. Samec, J. Langmaier and A. n. Trojánek, *J. Electroanal. Chem.*, 1999, **463**, 232-241.

25. R. Fortunato, L. C. Branco, C. A. M. Afonso, J. Benavente and J. G. Crespo, *Journal of Membrane Science*, 2006, **270**, 42-49.

26. K. Gorgy, F. Fusalba, U. Evans, K. Kontturi and V. J. Cunnane, *Synth. Met.*, 2001, **125**, 365-373.

27. L. Zheng and J. Li, *J. Electroanal. Chem.*, 2005, **577**, 137-144.

28. M. Vignali, R. A. H. Edwards, M. Serantoni and V. J. Cunnane, *J. Electroanal. Chem.*, 2006, **591**, 59-68.

29. S. Ghasemi, M. T. Darestani, Z. Abdollahi and V. G. Gomes, *Polym. Int.*, 2014, DOI: 10.1002/pi.4810, n/a-n/a.

30. S. E. C. Dale, PhD Thesis, University of Warwick, 2008.

31. N. E. A. Cousens and A. R. Kucernak, *Electrochem. Commun.*, 2013, **31**, 63-66.

32. C. I. Camara, L. M. A. Monzon, J. M. D. Coey and L. M. Yudi, *Phys. Chem. Chem. Phys.*, 2015, **17**, 414-421.

33. M. Platt, R. A. W. Dryfe and E. P. L. Roberts, *Electrochim. Acta*, 2004, **49**, 3937-3945.

34. R. Knake, A. W. Fahmi, S. A. M. Tofail, J. Clohessy, M. Mihov and V. J. Cunnane, *Langmuir*, 2005, **21**, 1001-1008.

35. F. Li, M. Edwards, J. Guo and P. R. Unwin, *The Journal of Physical Chemistry C*, 2009, **113**, 3553-3565.

Chapter 5

Surface Patterning of Polyacrylamide Gel on Gold Surfaces Using Scanning Electrochemical Cell Microscopy (SECCM)

This chapter describes the use of scanning electrochemical cell microscopy (SECCM) for the synthesis and deposition of vinyl polymer structures on initiator-functionalised Au surfaces. This work aimed to carry out polymer synthesis within the SECCM probe meniscus using a method of surface-initiated electrochemical atom transfer radical polymerisation (SI-eATRP). Au surfaces functionalised with *a*-bromoester thiol ATRP initiator (Au/Br_{SAM}) were characterised using cyclic voltammetry and X-ray photoelectron spectroscopy (XPS) to assess their suitability for subsequent SI-eATRP experiments. Initial polymer deposition experiments carried out using the micro-capillary electrochemical method (MCEM) indicated that poly(*N*-hydroxyethyl acrylamide, HEAA) films can be formed on Au/Br_{SAM} surfaces following the application of a negative overpotential to the surface. Similar reaction conditions were applied for subsequent polymer deposition on Au/Br_{SAM} surfaces using SECCM. XPS of Au/Br_{SAM} surfaces after polymer deposition showed a well-defined N 1s peak associated with the N-C bond in poly(HEAA). AFM imaging of surfaces showed a clear correlation between deposition time and film height, however the replication of this relationship on control thiol (Au/OH_{SAM}) surfaces and optical images of an SECCM tip after deposition confirmed that the polymerisation reaction took place within the tip and

was not surface-initiated. Therefore, the focus of the study subsequently shifted to deducing the mechanism of polymerisation reaction. AFM imaging showed that polymerisation of HEAA will take place in the absence of $CuCl_2$ and Me_6TREN, suggesting a standard free radical polymerisation mechanism. This was hypothesised to take place through the *in situ* production of free radicals from trace amounts of oxygen when a reducing potential is applied. Deposition of HEAA using different surface potentials and cyclic voltammetry of KCl aqueous solution in the SECCM setup under aerated and deaerated conditions confirmed both the polymerisation mechanism and the presence of trace amounts of oxygen in the environmental cell. Interestingly no polymer deposition took place when the SECCM setup was fully aerated, suggesting that polymerisation will only take place if there is a small flux of reactive oxygen species. An eATRP-like mechanism was also suggested for the enhancement of film deposition following the electrochemical generation of CuCl/Me_6TREN.

5.1 Introduction

The functionalization of surfaces with patterned polymer structures is currently of high interest in both electronic[1, 2] and biological fields.[3, 4] In particular, the grafting of polymer brushes onto surfaces can provide coatings which are not only functional but also stable and well-defined.

5.1.1 Polymer Brushes

Polymer brushes are layers of polymer chains tethered at one end to a surface, as illustrated in Figure 5.1. Polymer brush density on the surface is typically high, leading to repulsion between chains and thus their elongation away from the surface. The covalent attachment of the polymer chain to the surface provides a much stronger interaction than that experienced by bulk polymer thin films, hence their improved

stability. Polymer brushes have been used to bestow a wide range of functionality to surfaces, such as pH-sensitivity,[5] thermoresponsiveness,[6] biofunctionality,[7] capacity for energy storage,[8] tuneable wettability[9] and catalysis.[10]

5.1.1.1 Synthesis Methods

There are a number of different strategies when grafting polymer chains onto surfaces. These methods can be broadly split into two different approaches: *grafting to* and *grafting from*[11, 12], as demonstrated in Figure 5.1.

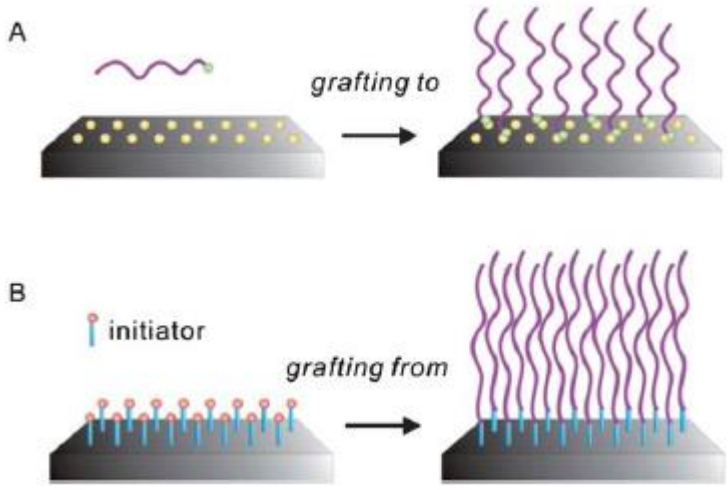

Figure 5.1 *Schematic of the two strategies used for polymer brush synthesis. (A) The "grafting" to approach whereby pre-formed end-functionalised polymer chains attach to complimentary groups immobilised on the surface. (B) The "grafting from" approach whereby polymer brushes will grow from surfaces modified with suitable polymerisation initiators.*[11]

The *grafting to* approach (Figure 5.1A) involves the attachment of pre-made end-functionalised polymer chains onto a surface modified with complementary attachment groups. The main advantage of this approach is the relative ease of surface functionalisation and polymer chain characterisation. However, this technique will often result in low grafting densities due to steric repulsion between polymer chains as they approach grafting sites, particularly when using high molecular weight polymer chains.

The *grafting from* approach (Figure 5.1B) involves the growth of polymer chains from an initiator-functionalised surface (surface-initiated polymerisation, SIP). Although more technically difficult than the *grafting to* approach, the *grafting from* approach provides greater control over the density, composition and architecture of polymer brush structures.

There are a number different of SIP methods, including surface-initiated reversible addition-fragmentation chain transfer (SI-RAFT)[13] and surface-initiated nitroxide-mediated polymerisation (SI-NMP).[14] Another common method is surface-initiated atom transfer radical polymerisation (SI-ATRP), based upon the atom transfer radical polymerisation (ATRP) method previously discussed in Chapter 1. By functionalising surfaces with ATRP initiators, polymer chains grow outwards from the site of the initiator molecule by periodic monomer addition. ATRP is commonly initiated using either bromoesters or bromoamides. Surfaces can be functionalised with these molecules (or their precursors) using a number of different functionalization techniques e.g. esterification of graphene oxide with acid bromide,[15] silanization on silica,[16] self-assembly of thiols on gold,[17] electrografting of aryldiazonium salts on conductive surfaces.[18] Additionally, by directing the position of initiator molecules on a surface, polymer brushes can be assembled into patterned domains capable of providing additional functionality to a surface e.g. polymer brushes as matrices for directed calcite thin film growth,[19] switchable bioactive interfaces.[20] SI-ATRP has been used to produce polymer brushes with well controlled molecular weight and density on a multitude of surfaces such as gold,[21] iron,[22] carbon nanotubes,[23] ultrananocrystalline diamond,[24] glassy carbon[25] and carbon fibre.[26]

SI-ATRP can also be induced electrochemically using the electrochemical atom transfer radical polymerisation (eATRP) technique previously described in Chapter 1. SI-eATRP has been used to form polymer brushes on conducting gold surfaces patterned

with Br-C15-thiol SAMs through micro contact printing.[27] Polymer brushes have also been grown on non-conducting gold surfaces placed opposite a tilted electrode, with the polymer brushes growing to different lengths due to distance-dependent diffusion of active catalyst from the electrode to the gold surface.[28] More recently, gradient polymer brushes have been grown on non-conducting glass plates using a bipolar electrode to generate a concentration gradient of active Cu(I) catalyst (as shown in Figure 5.2).[29]

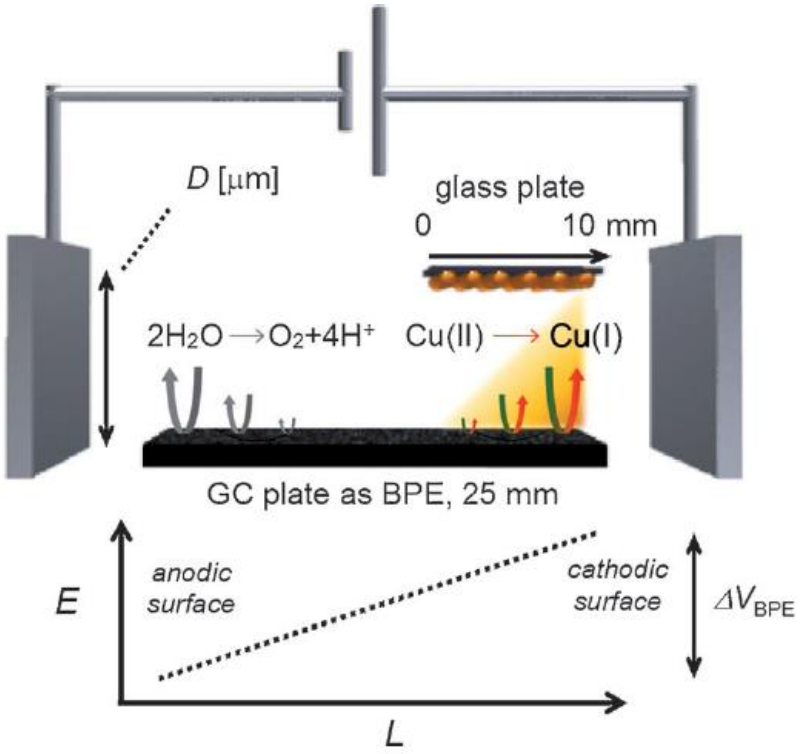

Figure 5.2 *An illustration of the electrochemical setup used to grow poly(NIPAM)brushes on initiator-modified glass plates using diffusion control eATRP. A glassy carbon bipolar electrode (set between two Pt driving electrode, 55 mm separation) held opposite was used to generate a concentration gradient of Cu(1) catalyst, thus producing polymer brushes of position-dependent thickness.*[29]

5.1.2 Polymer Patterning Techniques

Patterning of polymer structures on surfaces is commonly achieved using methods such as photolithography,[30] block copolymer self-assembly[31] and induction of chemical instability.[32] Although these techniques are useful for mass-production of materials, probe-based techniques can offer distinct design

capability when fabricating unique, intricate structures. Examples of probe-based methods include ink-jet printing,[33] dip-pen lithography,[34] polymer pen lithography,[35] electrospinning[36] and scanning electrochemical microscopy.[21] Techniques have also been developed to fabricate structures on a substrate through controlled contact between a surface and a probe-meniscus.[37] Meniscus-based methods tend to employ single-barrelled pipette probes for structure fabrication; however, the resulting lack of a feedback protocol for probe positioning can be restrictive in terms of the number of points of contact that can be made with the surface and potential tip crash. In light of these drawbacks, dual-barrel meniscus-based pipette probes have been developed to provide positional feedback between the probe meniscus and surface.[38, 39] The dual-barrel approach employed in scanning electrochemical cell microscopy (SECCM) offers a combination of well-controlled lateral movement and positional feedback of the probe that has been exploited in recent studies for microscale and nanoscale electrochemical patterning of surfaces.[40-42] Figure 5.3 shows a false-colour image of the result of one of these studies, which used SECCM to deposit conducting polyaniline (PANI) nanostructures on a surface.

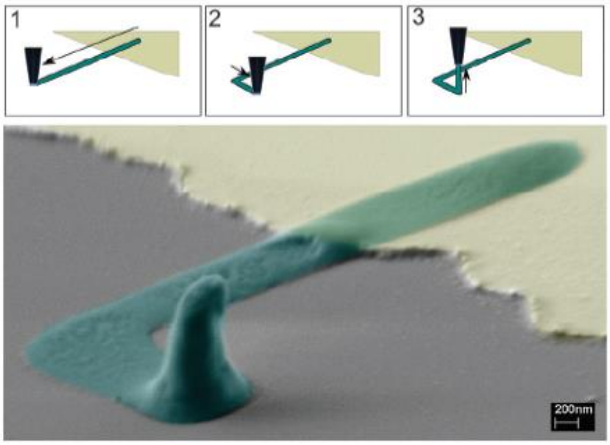

Figure 5.3 *A false colour SEM image of a PANI nanostructure formed using SECCM on a conducting (gold) and non-conducting (grey) surface. Stages of probe movement from the conducting to non-conducting parts of the surface during deposition are shown in boxes 1-3.*[41]

This chapter aims to use SECCM as a tool to carry out local polymer synthesis in the meniscus to pattern functional vinyl polymer structures on a surface. To some extent, the work takes the idea of electrochemically mediated atom transfer radical polymerisation (eATRP)[43] on a local scale with a moveable probe for the preparation of discretely functional surfaces. Electrochemically mediated surface initiated ATRP (SI-eATRP) has been explored in bulk reactions[29, 44-47] however prior to the following work it had never been attempted using a meniscus-based method like SECCM. Polymer deposition experiments were carried out with the aim of forming poly(HEAA) brushes through SI-eATRP, upon contact of the meniscus from the probe with the surface, via the electrochemical generation of activating Cu(I)Cl/Me_6TREN from Cu(II)Cl_2/Me_6TREN precatalyst within the tip.

5.2 Experimental

5.2.1 Macroscopic Cyclic Voltammetry (CV)

Solutions. A deaerated aqueous solution of 10 mM potassium ferricyanide redox mediator and 100 mM potassium chloride salt was for Au/Br_{SAM} macroelectrode characterisation.

An aqueous solution of 2 mM Me_6TREN, 1 M HEAA and 100 mM BTBACl was used to characterise Me_6TREN and HEAA reduction under aerated and deaerated conditions.

Setup. A CHI-730A potentiostat (CH Instruments, Inc., USA) was used to record macroscopic CVs in a standard three-electrode set-up. An AgCl-coated Ag wire and a Pt wire were used as a quasi-reference electrode and counter electrode, respectively. Prior to experiments, the Au working electrode (2 mm diameter) was immersed overnight in

an IPA solution containing 20 mM Bis[2-(2-bromoisobutyryloxy)ethyl] disulphide to ensure full coverage of the self-assembled monolayer (SAM).

5.2.2 Preparation of Au and SAM/Au Electrodes

Au substrates were prepared on silicon/silicon oxide wafers (n-type, 525 µm thickness with 300 nm of thermally grown SiO_2 on both sides, IDB Technologies Ltd., U.K.) using a Moorfield MiniLab deposition system (Moorfield Nanotechnology, U.K.) to thermally evaporate a 60.0 nm Au film on top of a 2.5 nm Cr adhesion layer. Two alkanethiols with different terminal groups were employed to form self-assembled monolayers (SAMs). 2-hydroxyethyl disulphide ($HO\text{-}C_2H_4\text{-}S_2\text{-}C_2H_4\text{-}OH$, Sigma-Aldrich) was used as received and bis[2-(2-bromoisobutyryloxy)ethyl] disulphide ($Br(CH_3)_2C\text{-}COO\text{-}C_2H_4\text{-}S_2\text{-}C_2H_4\text{-}OOC\text{-}C(CH_3)_2Br$) was synthesised according to literature procedures.[48] SAMs were formed by placing the Au substrates into a propan-2-ol (IPA) solution containing 20 mM of the required alkanethiol for at least 24 hours (see Figure 5.4). Subsequently, they were rinsed with water to remove any excess alkanethiol followed by a further rinse with IPA before drying under nitrogen. For SECCM experiments, the SAM/Au substrate was then placed on to a 3 x 3 cm glass slide and the edge connected to insulated copper wire using conductive silver epoxy. It was then left to dry overnight before use the next day.

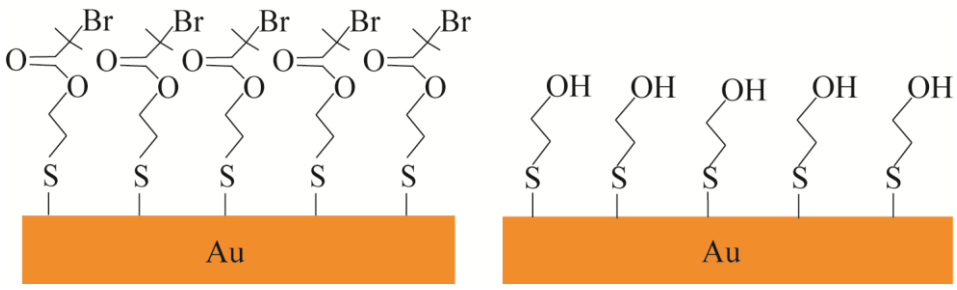

Figure 5.4 *Illustration of bis[2-(2-bromoisobutyryloxy)ethyl] disulphide (left) and 2-hydroxyethyl disulphide (right) assembly on Au surfaces.*

5.2.3 Micro-capillary Electrochemical Method (MCEM)

MCEM experiments were setup as described in Chapter 2 section 2.3.3. A CHI-730A potentiostat (CH Instruments, Inc., USA) was used to carry out both cyclic voltammetry and apply voltage over time. Single-barrel 10 µm diameter borosilicate pipettes were filled with a deaerated aqueous solution of 2 mM $CuCl_2$/Me_6TREN, 1 M n-hydroxyethyl acrylamide (HEAA) and 0.1 M benzyltributylammonium chloride (BTBACl). The tip was positioned above an Au substrate which had been immersed in bis[2-(2-bromoisobutyryloxy)ethyl] disulphide (Au/Br_{SAM}) to a point where it was almost touching the surface. A gentle tapping motion was used to bring the pipette meniscus into contact with the surface, following which a potential of -0.55 V was applied for a set time period.

5.2.4 Scanning Electrochemical Cell Microscopy (SECCM)

Solutions. 2 mM $CuCl_2$, 2 mM Me_6TREN and 1 M N-Hydroxyethyl acrylamide (HEAA) in Milli-Q water (Millipore Corp) were used for SECCM polymer deposition experiments, with $CuCl_2$ and/or Me_6TREN not included where stated for control experiments. 20 mM potassium chloride in Milli-Q water was used for SECCM oxygen reduction experiments. Solutions were also deaerated for all experiments performed under argon or nitrogen.

Probes. Dual barrel borosilicate glass theta pipettes (o.d. 1.5 mm, i.d. 0.23 mm, Harvard Apparatus) were pulled using a laser puller (Model P-2000, Sutter Instruments) to produce tapered pipets of either 1 µm diameter (for grid deposition), 200 nm diameter (for spiral deposition) or 1.5 µm diameter (for oxygen reduction experiments). Pipette dimensions were accurately measured using field emission-scanning electron microscopy (FE-SEM Zeiss SUPRA 55 VP).

SECCM Measurements. See section 2.3.4 for details on SECCM setup and associated measurements. Ag|AgCl quasi reference counter electrodes (QRCEs) were inserted into each theta pipette barrel, with a potential difference, V_{bias} of -100 mV applied between them. The probe was oscillated in the z direction to induce tip height modulation (~10 % of the tip diameter) by applying a frequency of 259.7 Hz via a lock-in amplifier. SECCM experiments were controlled through a LabVIEW interface written in house (version 13.0, National Instruments, USA) using a 40 MHz FPGA card (PCIe 7852R, National Instruments, USA). A voltage of -0.55 V *vs.* Ag|AgCl was applied at the surface when the probe meniscus was in contact with the surface to induce electrochemical polymerisation. Au and Au/SAM substrates within the SECCM setup were connected to a custom-built electrometer head (100 pA – 100 fA sensitivity) for surface current measurements.

5.3 Results and Discussion

5.3.1 Macroscopic Cyclic Voltammetry on an Au/Br_{SAM} Macroelectrode

As mentioned previously, ATRP can be initiated on surfaces functionalised with bromoester moieties. The self-assembly of bromoester alkanethiols on gold was the surface-functionalisation method selected for both ease of substrate preparation and substrate robustness. The alkanethiol bis[2-(2-bromoisobutyryloxy)ethyl] disulphide was chosen as the ATRP initiator due to its short chain length, which was hoped would provide functionality without impeding electron transfer between the surface electrode and ATRP catalyst. Cyclic voltammetry was used to characterise initiator self-assembly and suitability for eATRP, as shown in Figure 5.5. A 2 mm diameter Au macroelectrode was immersed overnight in a 20 mM solution of bis[2-(2-bromoisobutyryloxy)ethyl] disulphide so that sufficient alkanethiol self-assembly had taken place on the electrode surface. Cyclic voltammetry was then carried out on the macroelectrode before and after

the removal of the SAM through polishing. Potassium ferricyanide was chosen as the redox mediator probe as the electron transfer mechanism is thought to be inner sphere and therefore will be more affected by the presence of the SAM.[49]

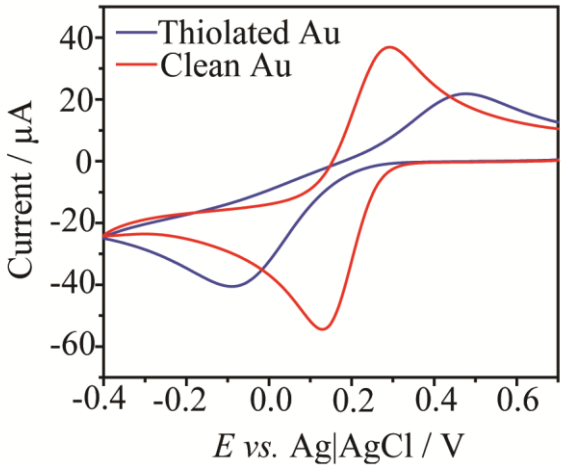

Figure 5.5 *CVs recorded at 100 mV s^{-1} for the reduction of $Fe(CN)_6^{3+}$ in 0.1 M KCl on a 2 mm Au macroelectrode either coated (thiolated) or uncoated (clean) with α-bromoester thiol SAM.*

Cyclic voltammetry of potassium ferricyanide on the SAM-covered macroelectrode showed a larger peak-to-peak separation than on the clean electrode, suggesting that electron transfer will be slowed by the presence of the SAM. Although the redox reaction is now quasi-reversible, the visible presence of both the oxidation and reduction peaks suggests that the SAM will not completely hinder electron transfer. Therefore, it was assumed that this particular alkanethiol would be suitable for use in polymer patterning experiments.

5.3.2 Polyacrylamide Gel Deposition on Au/SAM Surfaces Using MCEM

Proof-of-concept polymer patterning experiments were carried out on Au substrates modified with a self-assembled layer of bis[2-(2-bromoisobutyryloxy)ethyl] disulphide. X-ray photoelectron spectroscopy (XPS) was carried prior to patterning experiments for full characterisation of the Au/Br_{SAM} surface, as shown in Figure 5.6.

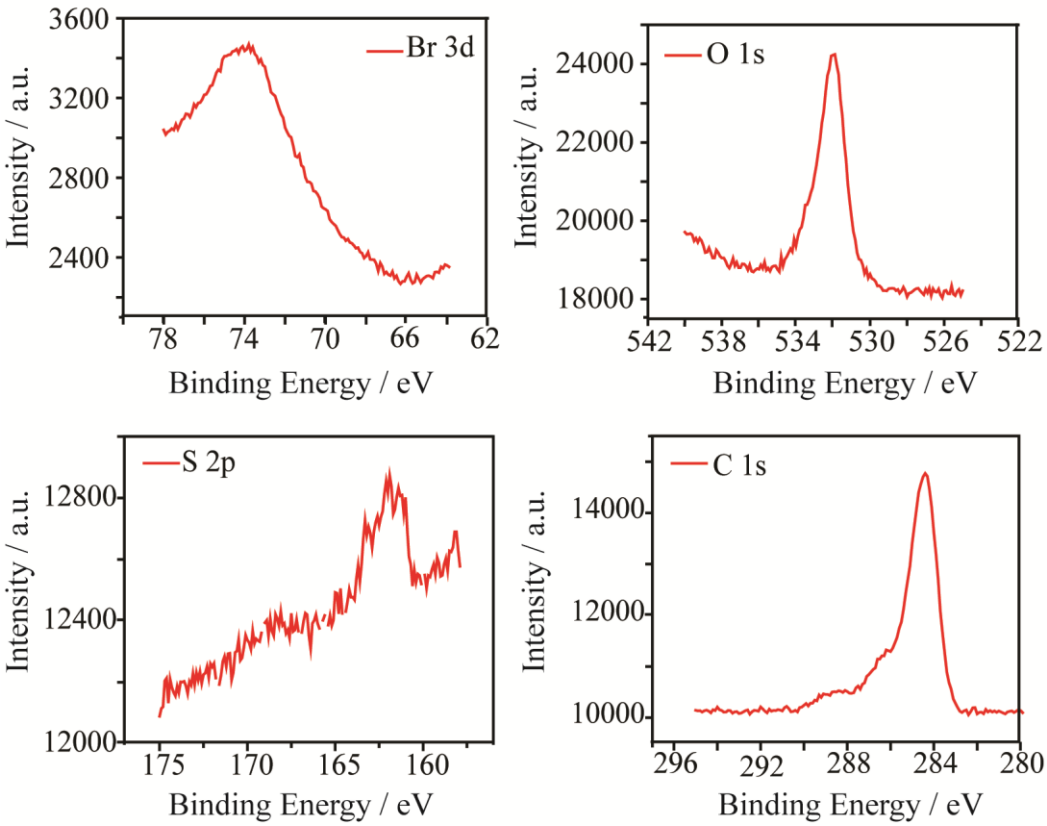

Figure 5.6 *XPS spectra of the Au/Br$_{SAM}$ surface showing core level scams for Br 3d, O 1s, S 2p and C 1s.*

The XPS data collected showed that bromine, oxygen, sulphur and carbon were present on the gold surface, which was consistent with the successful self-assembly of the alkanethiol to the gold surface. Following XPS characterisation, an Au/Br$_{SAM}$ substrate was placed into a glass cell for patterned polymer deposition using the micro-capillary electrochemical method (MCEM, see Chapter 2 for further details). The vinyl monomer *N*-hydroxyethyl acrylamide (HEAA) was chosen for polymer synthesis, as surfaces functionalised with polyacrylamide brushes have a wide range of applications in the field of biotechnology such as inhibition of non-specific fouling, protein separation, cell adsorption and drug encapsulation.[7] SI-eATRP in bulk solution has already been used to form polyacrylamide brushes on gold electrodes for Pb^{2+} sensing, however this was at elevated temperature and over a timescale of 1.5 hours.[50] Recent advances in reaction

conditions that allow the rapid polymerisation of acrylamides in aqueous solution were drawn upon to ensure that polymerisation took place within a suitable timescale.[51, 52]

A 10 µm diameter single-barrel pipette was filled with a deaerated aqueous solution of $CuCl_2$ catalyst, Tris[2-(dimethylamino)ethyl]amine (Me_6TREN) ligand, HEAA monomer and BTBACl salt for MCEM experiments. The pipette was then positioned above and moved down towards the Au/Br_{SAM} surface until there was contact between the pipette meniscus and the surface. Cyclic voltammetry was then carried out to find the applied potential at which the current associated with $CuCl_2/Me_6$TREN reduction reaches steady state, as shown in Figure 5.7a.

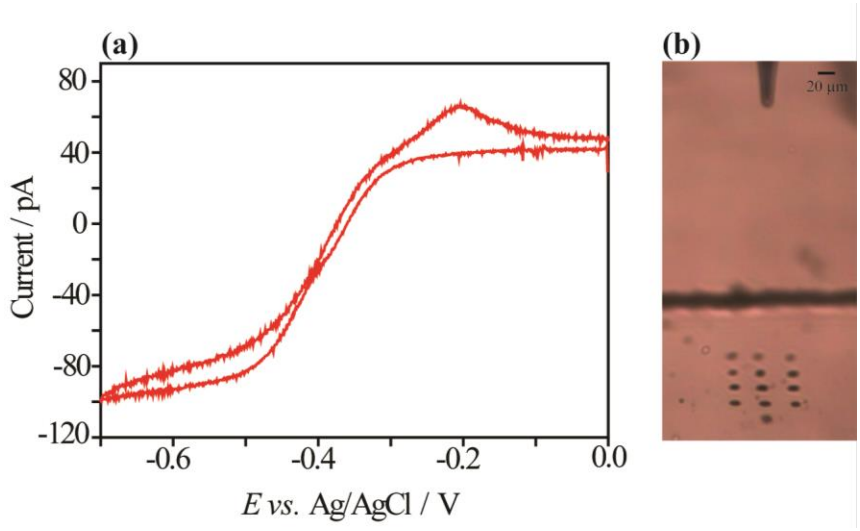

Figure 5.7*(a) CV recorded at 10 mV s^{-1} on an Au/Br_{SAM} surface for the reduction of 2 mM $CuCl_2/Me_6$TREN in the presence of 1 M HEAA and 0.1 M BTBACl. (b) Photograph taken following contact between the pipette meniscus and surface during time-dependent deposition experiments.*

Cyclic voltammetry on the Au/Br_{SAM} surface showed that the current associated with reduction of $CuCl_2/Me_6$TREN to $CuCl/Me_6$TREN reaches steady state below -0.5 V. Therefore, a reduction potential of -0.55 V was chosen for surface polymerisation experiments.

The probe meniscus was brought into contact at different points on the surface to form a grid, as shown in Figure 5.7b. At each point, a potential of -0.55 V was applied for a set time period (1-5, 10 or 15 minutes) to investigate the relationship between applied voltage length and polymer growth. A schematic of the eATRP reaction proposed to take place at the interface between the within the pipette meniscus and Au/Br_{SAM} surface is shown in Figure 5.8. The sample was then removed from the MCEM setup and rinsed with water and IPA prior to AFM imaging.

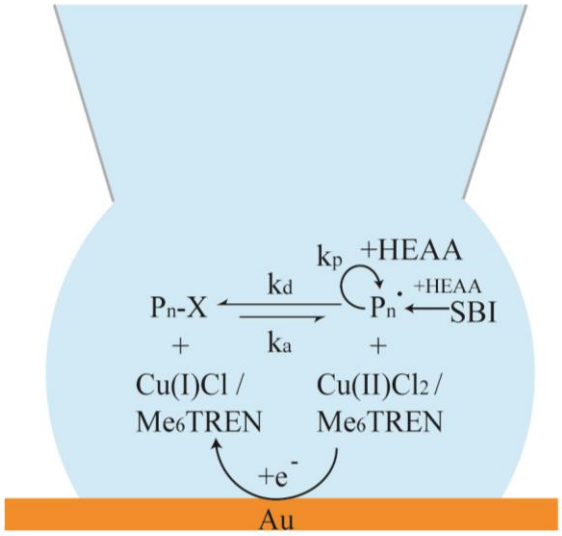

Figure 5.8 *Schematic of the proposed eATRP reaction at the Au/Br_{SAM} surface during MCEM experiments. SBI is surface-bound initiator.*

Imaging of the surface following MCEM showed that no polymer film growth took place when potential was applied for less than 15 minutes. Figure 5.9a shows a typical AFM image of a spot where no polymer deposition has taken place, alongside the associated current response Figure 5.9b. The features observed in the AFM image were thought to be salt crystals rather than polymer film. Figure 5.9c and Figure 5.9d show very little height change across the spot in comparison to the untouched surface.

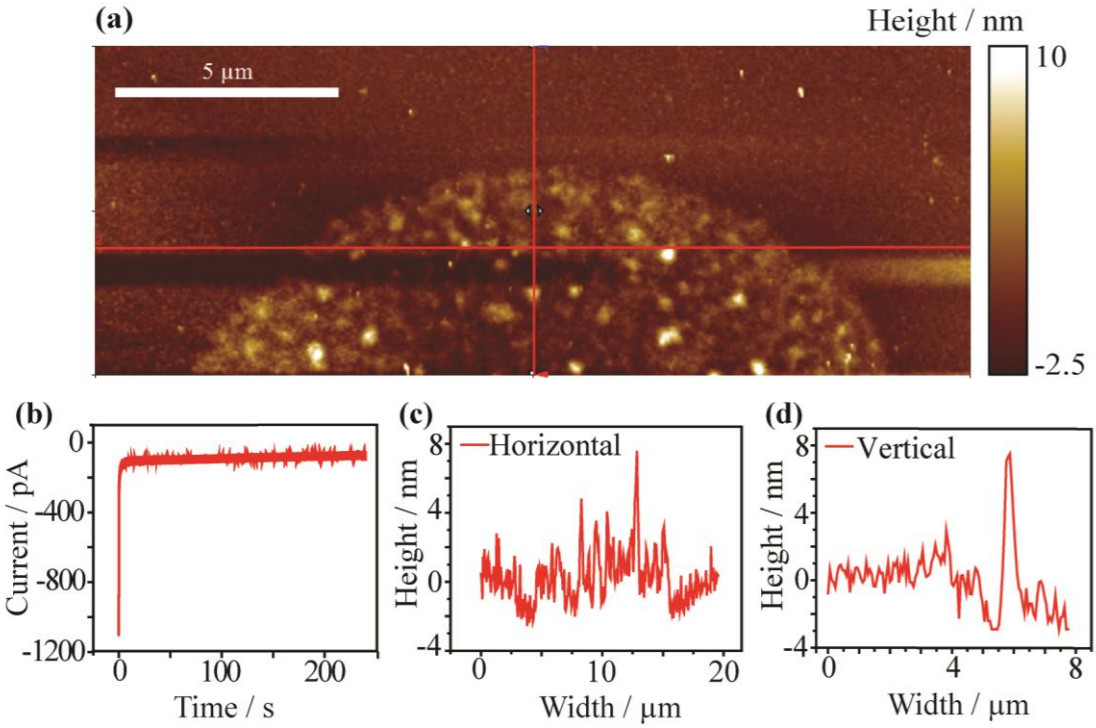

Figure 5.9 *(a) AFM image following the application of -0.55 V for 240 seconds on an Au/Br$_{SAM}$ surface using MCEM. (b) Associated current-time response. (c) Horizontal cross-section of AFM image. (d) Vertical cross-section of AFM image.*

However, appreciable polymer film growth could only be observed following a 900 second application of reducing potential, as shown in Figure 5.10. The AFM image shows the top of a circular film (see Figure 5.10a). The current-time response over this longer period of time shows a noticeable drop in current as time progresses (see Figure 5.10b), suggesting that polymer formation will gradually impede electron transfer at the surface. Film thickness was shown to be between 8-16 nm (see Figure 5.10c and Figure 5.10d).

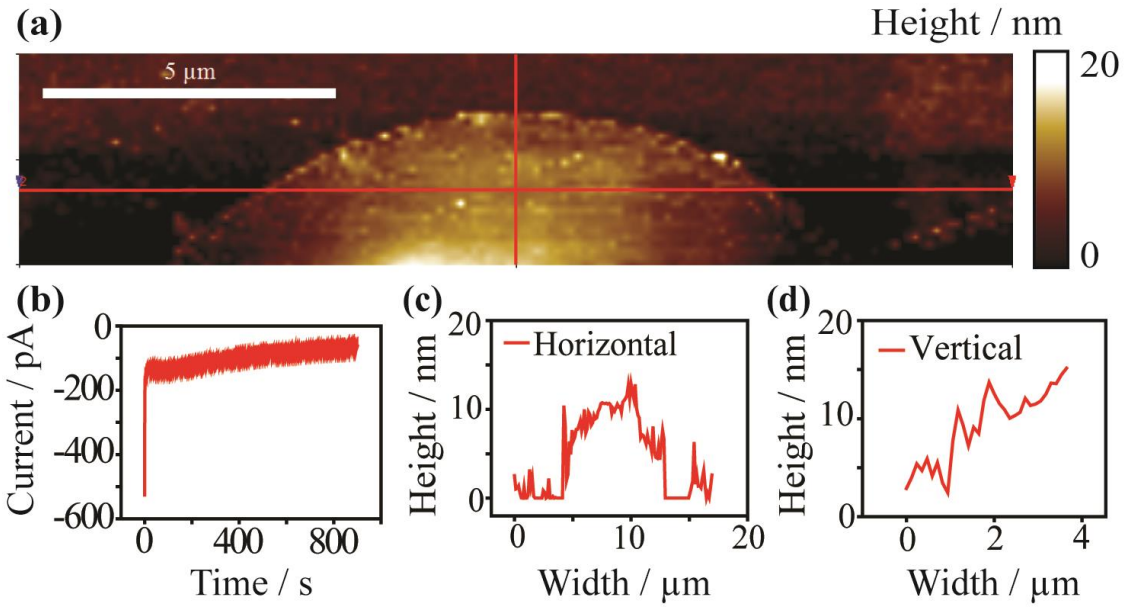

Figure 5.10 *(a) AFM image following the application of -0.55 V for 900 seconds on an Au/Br$_{SAM}$ surface using MCEM. (b) Associated current-time response. (c) Horizontal cross-section of AFM image and (d) Vertical cross-section of AFM image.*

5.3.3 Polyacrylamide Gel Deposition on Au/SAM Surfaces Using SECCM

Following initial experiments using MCEM, the focus of this study was turned towards using SECCM to carry out local polymer synthesis on an automated and much smaller scale. Successful film deposition during previous MCEM experiments led to the use of similar reaction conditions during initial SECCM experiments. General experimental procedures for SECCM experiments can be found in section 2.3.4.

5.3.3.1 Deposition of poly(HEAA) on Au/BrSAM and Au/OHSAM

Initial polymer deposition experiments using SECCM took place on gold substrates were functionalised with bis[2-(2-bromoisobutyryloxy)ethyl] disulfide (Br$_{SAM}$) to present the required *a*-bromoester initiating groups. Experiments were also attempted under argon, in a sealed environmental cell, to prevent inhibition by detrimental side reactions taking place between the growing polymer chains and excessive levels of molecular oxygen. Dual barrel borosilicate glass theta pipettes were filled with a deaerated aqueous solution containing HEAA

monomer, $CuCl_2$ and Me_6TREN (see Chapter 2 experimental) and positioned above an Au/Br_{SAM} substrate within the SECCM setup, as shown in Figure 5.11a. Polymerisation of HEAA at the interface between the meniscus and surface was initiated through the conversion of $Cu(II)Cl_2/Me_6TREN$ to $Cu(I)Cl/Me_6TREN$ via the application of a reducing potential to the substrate (see Figure 5.11b). Prior to patterning experiments, cyclic voltammetry (CV) was used to check the reducing potential (see Figure 5.11c). A $V_{surface}$ potential of -0.55 V was applied during all poly(HEAA) patterning experiments to ensure efficient turnover of the inactive Cu^{2+} species to the active Cu^{+} species.

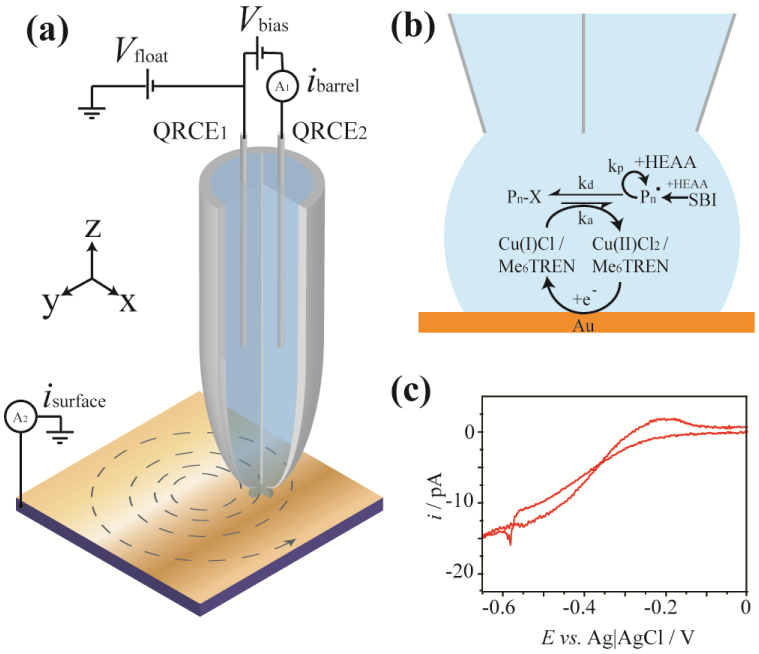

Figure 5.11 *(a) Illustration of the SECCM setup used for polymer deposition. The surface electrode was held at a potential of -0.55 V to induce polymerisation of HEAA at the interface between the surface and tip meniscus. (b) Proposed mechanism for SI-eATRP at the electrode surface. (c) CV (100 mV s^{-1}) using the SECCM setup under argon (1 µm diameter pipette) on Au/Br_{SAM} using 2 mM $CuCl_2/Me_6TREN$ and 1 M HEAA.*

To pattern poly(HEAA) using SECCM, the position and time that the meniscus was in contact with the surface was closely controlled. The pipette was brought down to the surface at a speed of 250 nm s^{-1} until the meniscus just contacted the surface, inducing an increase in AC barrel current magnitude ($i_{barrel\ AC}$) which was

used as a set point to keep the meniscus in contact with the surface for a set time period. Whilst the pipette was kept in contact with the surface, the probe position, surface current ($i_{surface}$), barrel ion-conductance current (i_{barrel}) and $i_{barrel\ AC}$ were all monitored and recorded (see Figure 5.12a (i)-(iv)) giving exquisite control over the reaction.

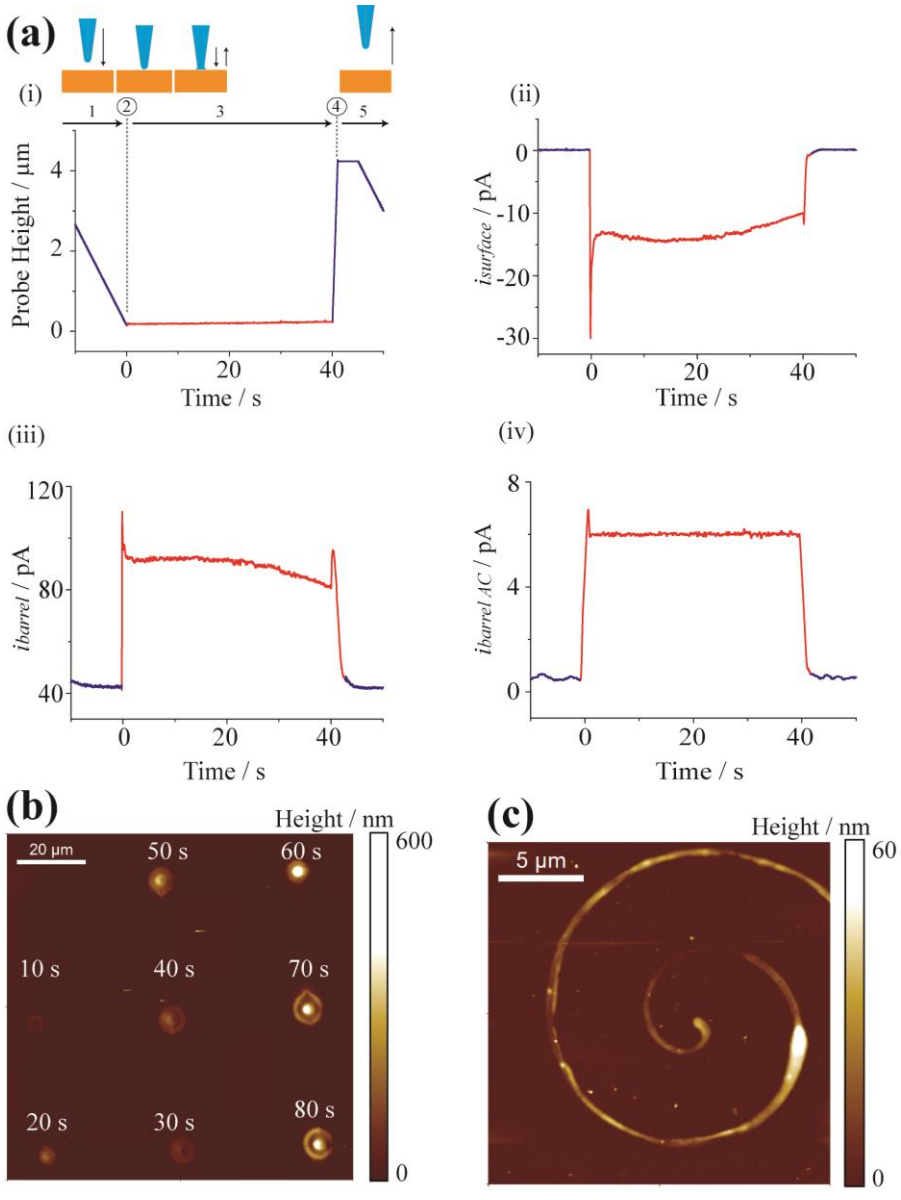

Figure 5.12 *(a) Typical SECCM responses during a 40 second deposition of poly(HEAA) including (i) probe height, (ii) surface current, (iii) barrel ion-conductance current and (iv) AC barrel current magnitude. Diagrams have been placed above to show the relationship between probe movement and the various current responses. (b) AFM image of an array of poly(HEAA) deposits on a Au/Br$_{SAM}$ surface formed by SECCM denoting deposition time above each feature. (c) AFM image of a poly(HEAA) spiral formed using fast-scanning SECCM.*

The scheme of the probe in Figure 5.12a shows the relationship between pipette positioned movement and the corresponding SECCM response during poly(HEAA) deposition. During region 1, the pipette meniscus is not in contact with the surface and only a small barrel ion-conductance current is observed (Figure 5.12a(iii)). At point 2, the meniscus comes into contact with the surface and both the AC and DC barrel currents (Figure 5.12a(iii) and Figure 5.12a(iv)) significantly increase due to the change in meniscus geometry.[39]

Current begins to flow through the surface (Figure 5.12a(ii)) due to the reduction of $Cu(II)Cl_2/Me_6TREN$ to $Cu(I)Cl/Me_6TREN$. During region 3, the pipette meniscus is held on the surface for the desired duration of poly(HEAA) deposition. The slight decrease in both surface and barrel ion conductance currents suggests that HEAA polymerisation will reduce current flow. This can be partially attributed to an increase in solution viscosity. As polymers have been shown to adsorb at surface-solution interfaces,[53] the passivation of the surface by poly(HEAA) adsorption is also envisioned to contribute to the drop in current. At point 4, the pipette is retracted a distance of 4 μm before being laterally moved during region 5 at a speed of 10 μm s^{-1} to the next deposition spot.

Initial patterning experiments involved using a 1 μm diameter pipette to form grid structures by depositing poly(HEAA) at evenly spaced points over incrementally increasing timescales (Figure 5.12b). Poly(HEAA) deposits increased in height with increasing deposition time, indicating increasing monomer conversion with length of applied activation potential. Control experiments using an applied $V_{surface}$ of -0.15 V showed no deposition, ascertaining that poly(HEAA), as opposed to monomer HEAA, was being deposited. To explore the capability of SECCM for deposition of more complex structures, a LabVIEW program previously developed for high-speed

electrochemical imaging[54] was utilised to deposit poly(HEAA) in spiral shapes using a 200 nm diameter pipette (Figure 5.12c).

Polymer deposition was confirmed using XPS following deposition experiments (see Figure 5.13). XPS survey spectra (Figure 5.13a) were collected for both the patterned (black) and unpatterned (red) surfaces in order to identify peaks of interest and ensure there was no contamination of the Au surface during sample preparation and loading. In both spectra the expected Au (4p, 4d and 4f) peaks are present as well as O 1s, with no obvious contamination for other elements observed.

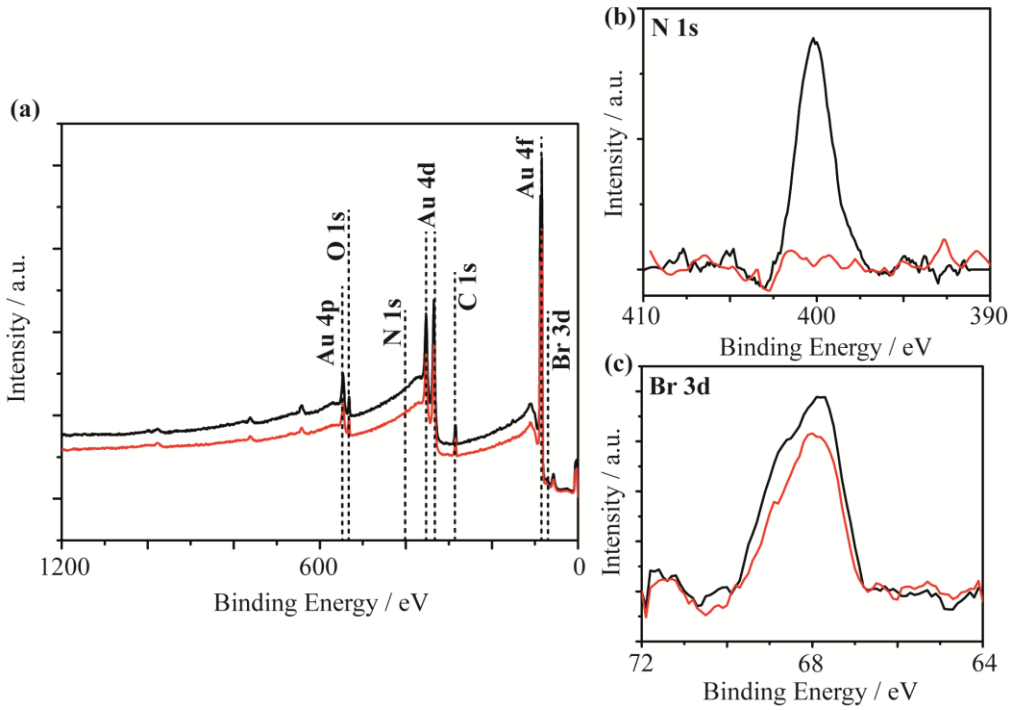

Figure 5.13 *XPS spectra of the patterned (-) and unpatterned (-) surface including: (a) survey scan and core level scans for N 1s (b) and Br 3d (c).*

In order to resolve the N 1s (400.1 eV) and Br 3d peaks (67.7 eV), core level XPS spectra were collected, shown in Figure 5.13b and Figure 5.13c respectively. No detectable nitrogen is present on the unpatterned surface (Figure 5.13B), whilst a clear N 1s peak is observed after patterning. This is attributed to the N-C bond in poly(HEAA).[55] Furthermore, a Br 3d is observed (Figure 5.13C) on both the patterned

and unpatterned surfaces due the presence of the Br_{SAM} on both samples,[56] but a smaller Br 3d signal intensity is observed after patterning, which is consistent with a layer of poly(HEAA) deposited on the surface.

Optical images of an SECCM tip after deposition experiments revealed a gel-like protrusion from the tip (Figure 5.14), indicating that some polymerisation takes place in solution rather than being completely bound to the surface.

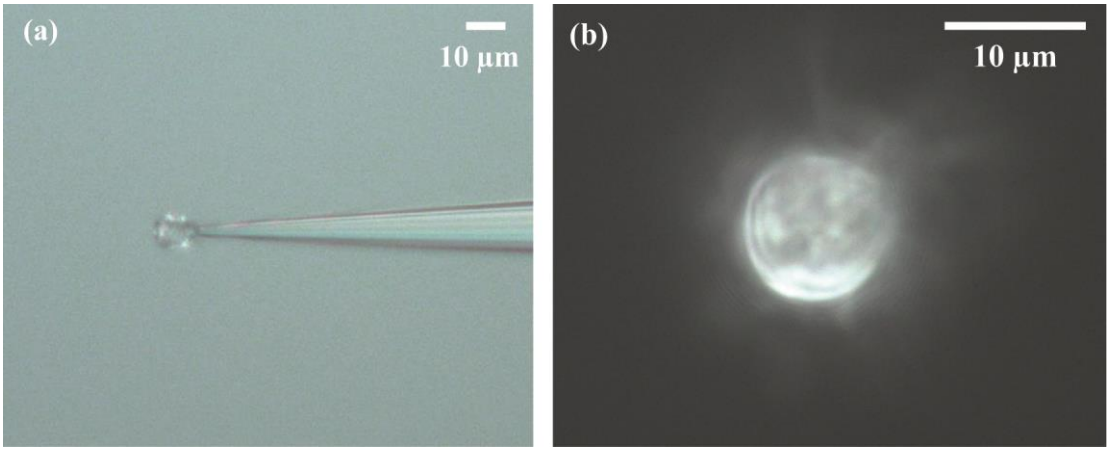

Figure 5.14 *Side-view (a) and top-view (b) optical images of a 1 µm diameter SECCM tip following poly(HEAA) deposition on an Au/Br_{SAM} surface.*

To test this hypothesis, grid deposition was carried out on a gold substrate functionalised with a non-initiating OH- terminated thiol 2-hydroxyethyl disulphide (OH_{SAM}). Polymer deposition could be seen on the Au/OH_{SAM} surface, which confirmed that polymerisation of HEAA was not surface-initiated (Figure 5.15a). Interestingly, the appearance of these deposits was somewhat different to those seen on the Au/Br_{SAM} surface, suggesting that hydrophobicity of the surface may influence deposition. However, comparison of average peak deposition height versus deposition time for equivalent spots on Au/Br_{SAM} and Au/OH_{SAM} surfaces was similar (see Figure 5.15b).

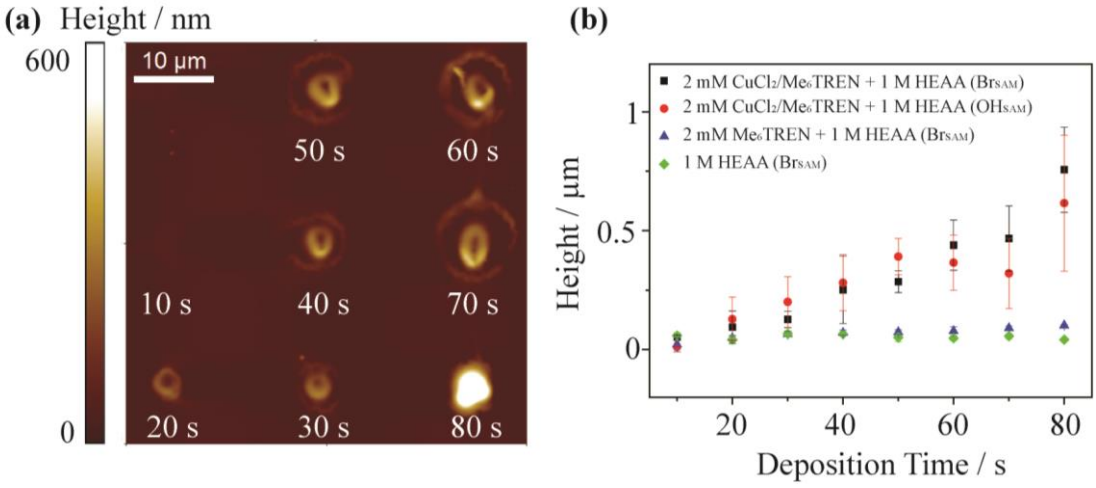

Figure 5.15 *(a) AFM image of an array of poly(HEAA) deposits on a Au/OH_{SAM} surface formed by SECCM denoting deposition time below each feature. (b) Average peak height of poly(HEAA) deposits formed on Au/Br_{SAM} or Au/OH_{SAM} surfaces during SECCM using a 1 µm diameter pipette containing aqueous solutions of 1 M HEAA with or without Me_6TREN ligand and $CuCl_2$ catalyst.*

5.3.3.2 Understanding the Polymerisation of poly(HEAA) During SECCM

Having established that HEAA polymerisation took place within the SECCM tip, the focus of the study shifted to deducing the mechanism of polymerisation initiation. Grid depositions were carried out on Au/Br_{SAM} surfaces using a 1 µm diameter pipette containing aqueous solutions of 1 M HEAA, with or without Me_6TREN, to determine if deposition occurred. Subsequent AFM images of the surfaces verified HEAA polymerisation in the absence of $CuCl_2$ and Me_6TREN (see Figure 5.16). However, average peak height of each poly(HEAA) deposit at different times was compared with deposits formed in the presence of $CuCl_2$/Me_6TREN, highlighting that there was an enhanced rate of HEAA polymerisation with the electrochemical generation of Cu(I)Cl/Me_6TREN (shown in Figure 5.15b). Average peak deposition height was similar for deposits formed using aqueous solutions of HEAA, with and without Me_6TREN, suggesting that Me_6TREN alone did not affect the polymerisation rate.

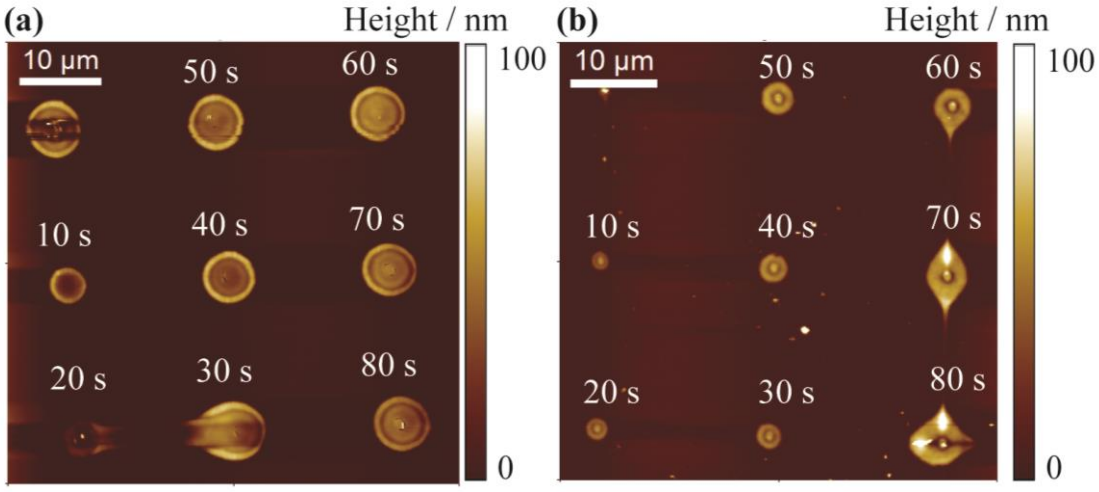

Figure 5.16 *AFM images of poly(HEAA) deposited for different times using SECCM on an Au/Br$_{SAM}$ surface at -0.55 V vs. Ag|AgCl. Experiments were carried out using a deaerated aqueous solution of 1 M HEAA (a) and 1 M HEAA/ 2 mM Me$_6$TREN (b).*

That polymerisation of HEAA occurred in the absence of $CuCl_2$/Me_6TREN suggested a standard free radical polymerisation mechanism. It was reasoned that there must be *in situ* production of free radicals capable of initiating polymerisation during SECCM when $V_{surface}$ -0.55 V is applied. Polymerisation of HEAA through HEAA reduction alone was discounted by cyclic voltammetry on a 2mm Au/Br$_{SAM}$ macroelectrode, which showed no discernible reduction peak for HEAA and Me_6TREN under deaerated solution conditions (see Figure 5.17). It was thus hypothesised that the source of free radical initiator could derive from traces of oxygen persisting even after deaeration.

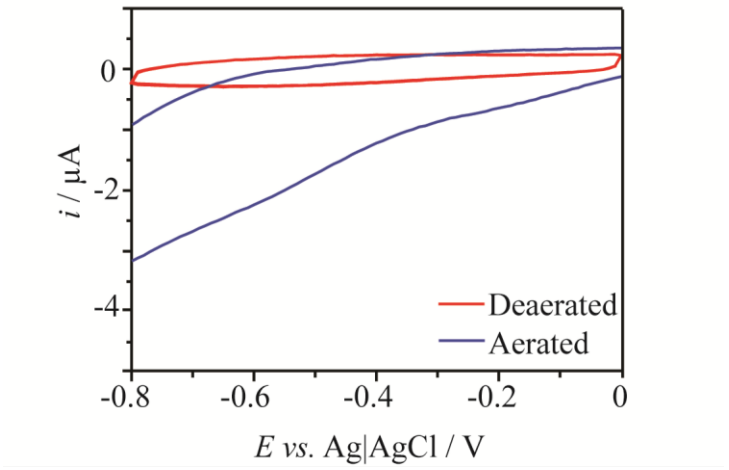

Figure 5.17 *Macroscopic CVs recorded in a deaerated or aerated aqueous solution of 2 mM Me$_6$TREN, 1 M HEAA and 100 mM BTBACl. Scan speed was 100 mV s^{-1}.*

To test this idea, initial experiments were carried out whereby the poly(HEAA) deposition experiments on Au/Br_{SAM} surfaces using $CuCl_2$, Me_6TREN and HEAA (described earlier) were repeated, but without deaeration. Interestingly, for solutions considered (2 mM $CuCl_2$/Me_6TREN + 1 M HEAA; 2 mM Me_6TREN + 1M HEAA, 1 M HEAA) no polymer deposition was observed, indicating inhibition of polymerisation. High concentrations of molecular oxygen can inhibit polymerisation via radical addition to propagating polymer chains forming less reactive peroxide radicals.[57]

To establish whether either trace molecular oxygen or a product of trace oxygen reduction initiated HEAA polymerisation, SECCM grid deposition on Au/Br_{SAM} surfaces was carried out under argon using a deaerated 1 M HEAA aqueous solution (see Figure 5.18). A different $V_{surface}$ was applied for each grid deposition, from -0.1 V to -0.4 V.

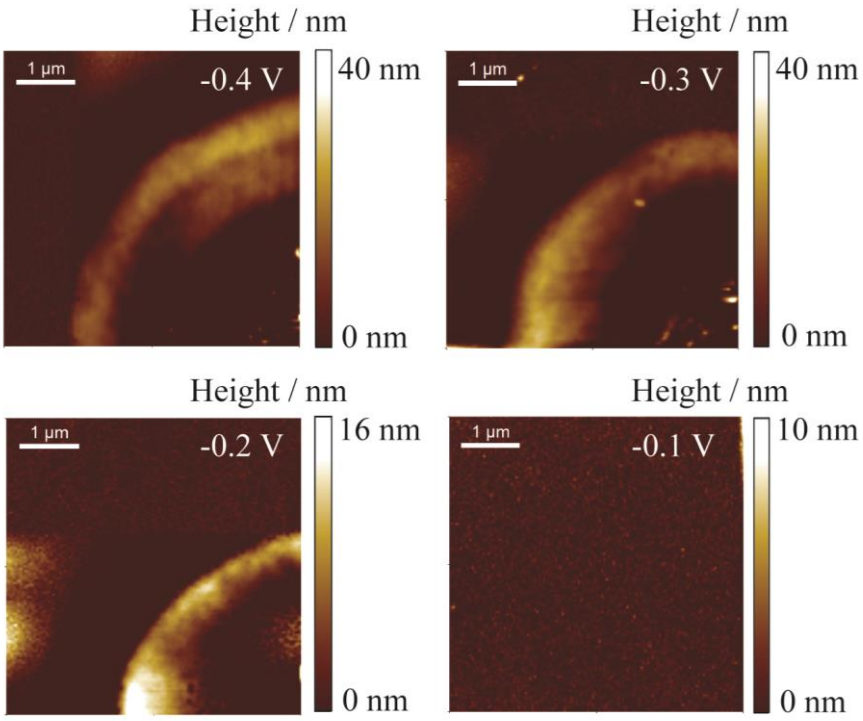

Figure 5.18 *AFM images of poly(HEAA) deposited for 80 seconds during SECCM patterning using a probe containing a aqueous solution of 1 M HEAA. Each image corresponds to a different applied* $V_{surface}$.

There was no detected deposit at -0.1 V and an increase in the amount deposited with increasing cathodic potential, which implies that the extent of deposition is related to the reduction potential and therefore the nature of oxygen species present. Reactive oxygen species (ROS) such as hydrogen peroxide have been shown to be produced during electrochemical reduction of molecular oxygen in aqueous solutions on gold electrodes.[58, 59] Thus, the extent of oxygen reduction is increased with increasing cathodic potential resulting in a decrease in the trace amount of inhibiting molecular oxygen and an increase in hydrogen peroxide, a well-known initiator of free radical polymerisation.[60] Ring shapes are thought to be due to sluggish polymerisation rate without $CuCl_2$/Me_6TREN, causing less material to be left behind after deposition.

To confirm that trace amounts of oxygen were present in the environmental cell used during SECCM, CVs were collected using the setup under aerated and deaerated conditions (Figure 5.19).

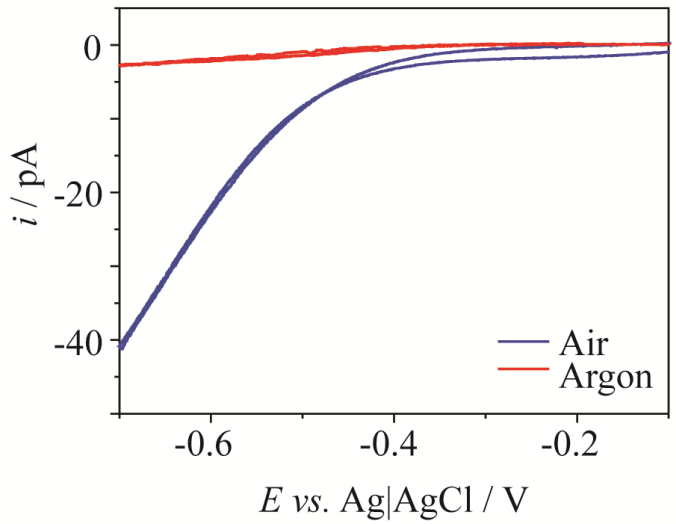

Figure 5.19 *CVs (50 mV s^{-1}) recorded using the SECCM setup (1.5 µm diameter pipette) under air or argon using an aqueous solution of 20 mM KCl.*

Cyclic voltammetry on a clean Au surface using a deaerated KCl solution showed oxygen reduction taking place whilst the SECCM system was under argon. However, the magnitude of the oxygen reduction current was more than ten times lower than when using an aerated KCl solution in an aerated SECCM setup. This indicated that effective initiation of HEAA polymerisation within the SECCM meniscus relies on the formation of only a small flux of ROS, as too much will inhibit polymerisation completely. Henceforth, a new mechanism for surface-initiated HEAA polymerisation during SECCM was proposed (Figure 5.20). The small amount of ROS generated by electrochemical reduction of molecular oxygen initiates HEAA polymerisation. The simultaneous electrochemical reduction of Cu(II)Cl_2/Me_6TREN (when present) to Cu(I)Cl/Me_6TREN ensures that polymer chains continue to propagate, thus enhancing the rate of HEAA polymerisation.

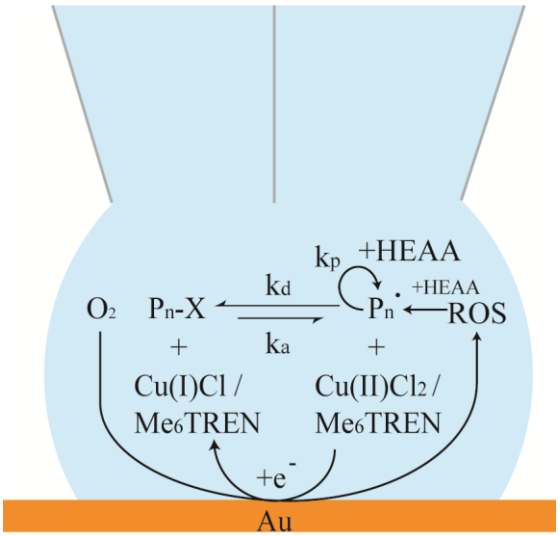

Figure 5.20 *Proposed mechanism for surface-initiated polymerisation of HEAA following the electrochemical reduction of molecular oxygen to a reactive oxygen species (ROS) initiator.*

5.4 Conclusions

In summary, the dual-barrel SECCM-based meniscus method can be used to pattern poly(HEAA) films on SAM-functionalised gold surfaces. Although the initial aim was to form poly(HEAA) brushes through SI-eATRP, the presence of trace amounts of oxygen in the setup led to the *in situ* production of reactive oxygen species capable of initiating free radical polymerisation within the tip. However, the enhancement of film deposition following the electrochemical generation of CuCl/Me_6TREN also suggests that an eATRP-like mechanism takes place concurrently within the pipette. Furthermore, it has been demonstrated that electrochemical control over polymerisation is possible for initiation by oxygen reduction. It is envisioned that with refinement of the catalytic system, the SECCM setup will be capable of meniscus-confined SI-eATRP for polymer brush patterning. Reduction of polymer feature size to the nanoscale should also be achievable by using hydrophobic surfaces to reduce wetting, speeding up lateral movement of the probe (in the case of spiral deposition) and by using smaller diameter SECCM tips.[61]

5.5 References

1. Z. Nie and E. Kumacheva, *Nat Mater*, 2008, **7**, 277-290.
2. H. G. Yoo, M. Byun, C. K. Jeong and K. J. Lee, *Adv. Mater.*, 2015, **27**, 3982-3998.
3. J. F. Fennell, S. F. Liu, J. M. Azzarelli, J. G. Weis, S. Rochat, K. A. Mirica, J. B. Ravnsbæk and T. M. Swager, *Angew. Chem. Int. Ed.*, 2016, **55**, 1266-1281.
4. M. Verhulsel, M. Vignes, S. Descroix, L. Malaquin, D. M. Vignjevic and J.-L. Viovy, *Biomaterials*, 2014, **35**, 1816-1832.
5. G. W. de Groot, M. G. Santonicola, K. Sugihara, T. Zambelli, E. Reimhult, J. Vörös and G. J. Vancso, *ACS Applied Materials & Interfaces*, 2013, **5**, 1400-1407.
6. C. Comminges, S. Frasca, M. Sutterlin, E. Wischerhoff, A. Laschewsky and U. Wollenberger, *RSC Advances*, 2014, **4**, 43092-43097.
7. C. J. Fristrup, K. Jankova and S. Hvilsted, *Soft Matter*, 2009, **5**, 4623-4634.
8. C.-H. Lin, W.-J. Chou and J.-T. Lee, *Macromol. Rapid Commun.*, 2012, **33**, 107-113.
9. A. A. Brown, O. Azzaroni, L. M. Fidalgo and W. T. S. Huck, *Soft Matter*, 2009, **5**, 2738-2745.
10. A. R. Kiasat and S. Nazari, *J. Mol. Catal. A: Chem.*, 2012, **365**, 80-86.
11. X. Zhou, X. Liu, Z. Xie and Z. Zheng, *Nanoscale*, 2011, **3**, 4929-4939.
12. O. Azzaroni, *J. Polym. Sci., Part A: Polym. Chem.*, 2012, **50**, 3225-3258.
13. N. Gurbuz, S. Demirci, S. Yavuz and T. Caykara, *J. Polym. Sci., Part A: Polym. Chem.*, 2011, **49**, 423-431.
14. T. N. T. Phan, J. Jestin and D. Gigmes, in *Controlled Radical Polymerization at and from Solid Surfaces*, ed. P. Vana, Springer International Publishing, Cham, 2016, DOI: 10.1007/12_2015_317, pp. 1-27.

15. S. H. Lee, D. R. Dreyer, J. An, A. Velamakanni, R. D. Piner, S. Park, Y. Zhu, S. O. Kim, C. W. Bielawski and R. S. Ruoff, *Macromol. Rapid Commun.*, 2010, **31**, 281-288.

16. H. Ma, D. Li, X. Sheng, B. Zhao and A. Chilkoti, *Langmuir*, 2006, **22**, 3751-3756.

17. H. Ma, J. Hyun, P. Stiller and A. Chilkoti, *Adv. Mater.*, 2004, **16**, 338-341.

18. S. Mahouche-Chergui, S. Gam-Derouich, C. Mangeney and M. M. Chehimi, *Chem. Soc. Rev.*, 2011, **40**, 4143-4166.

19. S. Tugulu, M. Harms, M. Fricke, D. Volkmer and H.-A. Klok, *Angew. Chem. Int. Ed.*, 2006, **45**, 7458-7461.

20. Q. Yu, P. Shivapooja, L. M. Johnson, G. Tizazu, G. J. Leggett and G. P. Lopez, *Nanoscale*, 2013, **5**, 3632-3637.

21. F. Hauquier, T. Matrab, F. Kanoufi and C. Combellas, *Electrochim. Acta*, 2009, **54**, 5127-5136.

22. T. Matrab, M. M. Chehimi, C. Perruchot, A. Adenier, A. Guillez, M. Save, B. Charleux, E. Cabet-Deliry and J. Pinson, *Langmuir*, 2005, **21**, 4686-4694.

23. T. Matrab, J. Chancolon, M. M. L'hermite, J.-N. Rouzaud, G. Deniau, J.-P. Boudou, M. M. Chehimi and M. Delamar, *Colloids and Surfaces A: Physicochemical and Engineering Aspects*, 2006, **287**, 217-221.

24. T. Matrab, M. M. Chehimi, J. P. Boudou, F. Benedic, J. Wang, N. N. Naguib and J. A. Carlisle, *Diamond Relat. Mater.*, 2006, **15**, 639-644.

25. T. Matrab, M. M. Chehimi, J. Pinson, S. Slomkowski and T. Basinska, *Surf. Interface Anal.*, 2006, **38**, 565-568.

26. T. Matrab, M. N. Nguyen, S. Mahouche, P. Lang, C. Badre, M. Turmine, G. Girard, J. Bai and M. M. Chehimi, *The Journal of Adhesion*, 2008, **84**, 684-701.

27. B. Li, B. Yu, W. T. Huck, F. Zhou and W. Liu, *Angew. Chem. Int. Ed. Engl.*, 2012, **51**, 5092-5095.

28. B. Li, B. Yu, W. T. S. Huck, W. Liu and F. Zhou, *J. Am. Chem. Soc.*, 2013, **135**, 1708-1710.

29. N. Shida, Y. Koizumi, H. Nishiyama, I. Tomita and S. Inagi, *Angew. Chem. Int. Ed.*, 2015, **54**, 3922-3926.

30. B. Li, M. He, L. Ramirez, J. George and J. Wang, *ACS Applied Materials & Interfaces*, 2016, **8**, 4158-4164.

31. L. Shen, C. He, J. Qiu, S.-M. Lee, A. Kalita, S. B. Cronin, M. P. Stoykovich and J. Yoon, *ACS Applied Materials & Interfaces*, 2015, **7**, 26043-26049.

32. J. J. S. Rickard, I. Farrer and P. Goldberg Oppenheimer, *ACS Nano*, 2016, **10**, 3865-3870.

33. A. Garcia, N. Hanifi, B. Jousselme, P. Jégou, S. Palacin, P. Viel and T. Berthelot, *Adv. Funct. Mater.*, 2013, **23**, 3668-3674.

34. M. Guardingo, P. González-Monje, F. Novio, E. Bellido, F. Busqué, G. Molnár, A. Bousseksou and D. Ruiz-Molina, *ACS Nano*, 2016, **10**, 3206-3213.

35. F. Huo, Z. Zheng, G. Zheng, L. R. Giam, H. Zhang and C. A. Mirkin, *Science*, 2008, **321**, 1658-1660.

36. J. Lee, S. Y. Lee, J. Jang, Y. H. Jeong and D.-W. Cho, *Langmuir*, 2012, **28**, 7267-7275.

37. J. T. Kim, S. K. Seol, J. Pyo, J. S. Lee, J. H. Je and G. Margaritondo, *Adv. Mater.*, 2011, **23**, 1968-1970.

38. K. T. Rodolfa, A. Bruckbauer, D. Zhou, A. I. Schevchuk, Y. E. Korchev and D. Klenerman, *Nano Lett.*, 2006, **6**, 252-257.

39. N. Ebejer, M. Schnippering, A. W. Colburn, M. A. Edwards and P. R. Unwin, *Anal. Chem.*, 2010, **82**, 9141-9145.

40. P. M. Kirkman, A. G. Güell, A. S. Cuharuc and P. R. Unwin, *J. Am. Chem. Soc.*, 2013, **136**, 36-39.

41. K. McKelvey, M. A. O'Connell and P. R. Unwin, *Chem. Commun.*, 2013, **49**, 2986-2988.

42. H. V. Patten, L. A. Hutton, J. R. Webb, M. E. Newton, P. R. Unwin and J. V. Macpherson, *Chem. Commun.*, 2015, **51**, 164-167.

43. A. J. D. Magenau, N. C. Strandwitz, A. Gennaro and K. Matyjaszewski, *Science*, 2011, **332**, 81-84.

44. B. Li, B. Yu, W. T. S. Huck, F. Zhou and W. Liu, *Angew. Chem.*, 2012, **124**, 5182-5185.

45. Y. Hu, G. Yang, B. Liang, L. Fang, G. Ma, Q. Zhu, S. Chen and X. Ye, *Acta Biomaterialia*, 2015, **13**, 142-149.

46. J. Yan, B. Li, B. Yu, W. T. S. Huck, W. Liu and F. Zhou, *Angew. Chem. Int. Ed.*, 2013, **52**, 9125-9129.

47. L. T. Strover, J. Malmström, L. A. Stubbing, M. A. Brimble and J. Travas-Sejdic, *Electrochim. Acta*, 2016, **188**, 57-70.

48. J. A. Syrett, M. W. Jones and D. M. Haddleton, *Chem. Commun.*, 2010, **46**, 7181-7183.

49. D. A. C. Brownson and C. E. Banks, *PCCP*, 2011, **13**, 15825-15828.

50. Y. Sun, H. Du, Y. Deng, Y. Lan and C. Feng, *J. Solid State Electrochem.*, 2016, **20**, 105-113.

51. P. Chmielarz, S. Park, A. Simakova and K. Matyjaszewski, *Polymer*, 2015, **60**, 302-307.

52. G. R. Jones, Z. Li, A. Anastasaki, D. J. Lloyd, P. Wilson, Q. Zhang and D. M. Haddleton, *Macromolecules*, 2016, **49**, 483-489.

53. M. A. O'Connell, A. de Cuendias, F. Gayet, I. M. Shirley, S. R. Mackenzie, D. M. Haddleton and P. R. Unwin, *Langmuir*, 2012, **28**, 6902-6910.

54. D. Momotenko, J. C. Byers, K. McKelvey, M. Kang and P. R. Unwin, *ACS Nano*, 2015, **9**, 8942-8952.

55. J. Zhang, S. Xiao, M. Shen, L. Sun, F. Chen, P. Fan, M. Zhong and J. Yang, *RSC Advances*, 2016, **6**, 21961-21968.

56. C. S. Park, H. J. Lee, A. C. Jamison and T. R. Lee, *ACS Applied Materials & Interfaces*, 2016, **8**, 5586-5594.

57. V. A. Bhanu and K. Kishore, *Chem. Rev.*, 1991, **91**, 99-117.

58. J. C. Byers, A. G. Güell and P. R. Unwin, *J. Am. Chem. Soc.*, 2014, **136**, 11252-11255.

59. G. Gotti, K. Fajerwerg, D. Evrard and P. Gros, *Electrochim. Acta*, 2014, **128**, 412-419.

60. J. L. Pradel, B. Boutevin and B. Ameduri, *J. Polym. Sci., Part A: Polym. Chem.*, 2000, **38**, 3293-3302.

61. A. G. Güell, A. S. Cuharuc, Y.-R. Kim, G. Zhang, S.-y. Tan, N. Ebejer and P. R. Unwin, *ACS Nano*, 2015, **9**, 3558-3571.

Chapter 6

Conclusions & Future Work

This thesis has focused on understanding the processes that take place during interfacial polymerisation reactions. The reactions studied were primarily those currently used in agrichemical industry for the synthesis of microcapsules for active ingredient (AI) encapsulation; however polymerisation reactions for surface functionalisation have also been investigated.

An investigation into the interfacial processes that take place during an epoxy-amine emulsion polymerisation used a combination of techniques capable of studying the liquid/liquid interface. Time-lapse microscopy has been used to monitor the effect of solution and temperature on resorcinol diglycidyl ether dissolution into an aqueous phase and interfacial curing reactions. It was found that without amine, resorcinol diglycidyl ether appears to homopolymerise in water at higher temperatures, but the addition of jeffamine D230 promotes the interfacial curing reaction so that it becomes faster than the resorcinol diglycidyl ether homopolymerisation reaction. Alongside the influence of thermal effects on the kinetics and the fast transfer of the jeffamine D230 into the aqueous phase, these new aspects to emulsion polymerisation are important for understanding microcapsule wall formation and the resulting properties of the polymer microcapsules. Ultimately, the wall properties determine the extent of active ingredient inclusion and the rate of release upon polymeric microparticle wall decomposition.

It is envisioned that the techniques applied in this study could be utilised to examine a wide range of interfacial processes at liquid/liquid interfaces, which are of general importance, from synthesis[1] and phase transfer kinetics[2] to studies of biomimetic systems.[3] In particular, simple optical microscopy methods coupled with FEM modelling have the potential to reveal detailed kinetic information. Indeed, dissolution/growth processes are widespread and optical techniques could find much more quantitative application.[4, 5] As has been discussed herein, interfacial processes in condensed phase systems involve mass transport and chemical reactions, leading to concentration gradients at interfaces. The ability to probe such gradients, as demonstrated in the MEMED studies, is a very powerful means of determining interfacial kinetics, taking full account of mass transport. The technique should find wider application.

A different approach was taken to try and understand the formation of poly(urea) at liquid/liquid interfaces, which is another process used for microcapsule synthesis. Electrochemical impedance spectroscopy was used to monitor a growing poly(urea) film formed at a model liquid/liquid interface at the tip of a micropipette. Electrochemical impedance spectra taken before and after film formation and subsequent circuit diagram modelling showed an increase in impedance from film formation associated with increased resistance and decreased capacitance at the liquid/liquid interface. Poly(urea) formation under a range of different reaction conditions was investigated by measuring the change in impedance over time. The rate of poly(urea) film formation appeared to be enhanced by both the presence of additional amine monomers in the water phase and temperature and depressed when the concentration of isocyanate was lowered below a certain threshold. Film formation appeared to be stable at higher concentrations but became more unstable at lower concentrations. This was attributed to a suggested mechanism of film growth thought to

progress via the deposition of poly(urea) at nucleation sites that grow and eventually merge to form a single film. More insight into this reaction could be gained by conducting experiments whereby a laser beam is shone down the capillary during film formation. Decreasing amounts of light will be collected on the other side of the film as it forms, thus the light signal could be used to measure the film formation rate.

Scanning electron microscopy (SEM) was used to inspect poly(urea) films formed following electrochemical impedance spectroscopy experiments. SEM taken of poly(urea) films formed in the presence of additional amine monomers were shown to be flatter and more compact than those formed without, correlating with previous impedance measurements which suggested that films formed without additional amine monomers were more porous. The porous nature of the film was thought to be due to either the slower rate of the isocyanate hydrolysis reaction in comparison to its reaction with amine monomers or due to a "foaming effect" caused by the generation of carbon dioxide following isocyanate hydrolysis.

Finally, the polymerisation of acrylamide monomers at the solid/liquid interface for discrete surface functionalisation was investigated using a combination of scanning electrochemical cell microscopy (SECCM) and atomic force microscopy (AFM). The aim of the study was to use SECCM as a tool to carry out local polymer synthesis using a mechanism called surface-initiated electrochemical atom transfer radical polymerisation. However, it was shown that the presence of oxygen in the setup led to the *in situ* production of hydroxyl radicals capable of initiating standard free radical polymerisation within the tip. Nevertheless, the enhancement of film deposition following the electrochemical generation of CuCl/Me_6TREN suggested that an eATRP-like mechanism will take place within the SECCM probe.

As briefly mentioned at the end of Chapter 5, it is envisioned that with refinement of the catalytic system, the SECCM setup will be capable of meniscus-confined SI-eATRP for polymer brush patterning. ATRP catalysts/ligands such as CuBr/2,2-bipyridine and CuBr/*N*,*N*,*N*′,*N*″,*N*″-pentamethyldiethylenetriamine will be reduced at more positive potentials[6], where oxygen reduction will not take place. Therefore, it should be possible to use SECCM to achieve polymer brush growth unaffected by the generation of radical initiators. Further study into the role of oxygen in the polymerisation reaction would also be desirable. Raman spectroscopy of polymer features formed during SECCM may provide information on the distribution of deposited polymer, potentially providing insight into this mechanism.

Overall, this thesis has achieved its objective in using a combination of different analytical techniques to study interfacial polymer formation. Polymer formation at liquid/liquid interfaces for microcapsule synthesis has been studied using a mixture of optical and electrochemical techniques. These methods have proved invaluable in understanding how the rate of species transfer across the liquid/liquid interface and reaction condition variation will affect interfacial polymerisation processes. Even though the mechanism turned out to be not entirely as expected, polymer synthesis at solid/liquid interfaces using SECCM has been achieved to discretely functionalise surfaces. These studies have shown that electrochemical control over polymerisation is possible for initiation by oxygen reduction, opening potential new avenues for polymer synthesis. It is also envisioned that with refinement of the catalytic system, the SECCM setup will be capable of meniscus-confined SI-eATRP for polymer brush patterning.

6.1 References

1. R. V. Salvatierra, C. E. Cava, L. S. Roman, M. M. Oliveira and A. J. G. Zarbin, *Chem. Commun.*, 2016, **52**, 1629-1632.
2. Q. Duong, Y. Tan, J. Corey, S. Anz and P. Sun, *The Journal of Physical Chemistry C*, 2015, **119**, 10365-10369.
3. P. Peljo, L. Murtomäki, T. Kallio, H.-J. Xu, M. Meyer, C. P. Gros, J.-M. Barbe, H. H. Girault, K. Laasonen and K. Kontturi, *J. Am. Chem. Soc.*, 2012, **134**, 5974-5984.
4. A. R. Perry, M. Peruffo and P. R. Unwin, *Crystal Growth & Design*, 2013, **13**, 614-622.
5. M. Adobes-Vidal, F. M. Maddar, D. Momotenko, L. P. Hughes, S. A. C. Wren, L. N. Poloni, M. D. Ward and P. R. Unwin, *Crystal Growth & Design*, 2016, DOI: 10.1021/acs.cgd.6b00543.
6. J. Qiu, K. Matyjaszewski, L. Thouin and C. Amatore, *Macromol. Chem. Phys.*, 2000, **201**, 1625-1631.

Appendix

Appendix 1- Code Written in MATLAB to Measure Changing Droplet Size during Time-Lapse Microscopy

```
% open file
Dir = uigetdir('C:\');
% create variable for directory using only tif files
A  = dir([Dir,'\*.tif']);
% calculate number of tif files in folder
L = length(A);
% open each file from A and carry out these tasks for each
for i = 1:L;
% create variable for file i from A (aka creates filename)
c = A(i).name;
% creates variable to open file i from directory
a = strcat(Dir,'\',c);

    %determine the name of the file
    %build a full filename

%read file
I = imread(a);
%change file to black and white
I3 = im2bw(I,0.2);
% crop file
I2 = I3(:,1:590,:);


% write program to find dark circles on light background

 [centers, radii] = imfindcircles(I2,[100
140],'ObjectPolarity','dark','sensitivity',0.975,'edgethreshold',0.9);

RadiusReal = radii*2.872;
Volume = 4/3*pi*RadiusReal^3;
Volume_mm3 = Volume*1e-9;
Surface_area = 4*pi*RadiusReal^2;

% output

%Build index by converting filename string to number
Index = str2num(c(8:end-4));
Results(i,1) = Index;
Results(i,2) = RadiusReal;
Results(i,3) = Volume_mm3;
Results(i,4) = Surface_area;

%make next filenumber i so that it is opened in next for loop
i = i+1;
end
```

Appendix 2- Code Written in MATLAB to Measure Electrode-Droplet Separation during MEMED

```
% open file
Dir = uigetdir('C:\Users\chemist\My Documents\Liz\MEMS');
%Dir = uigetdir('C:\Users/chemist/Documents/MATLAB');
% create variable for directory using only tif files
A  = dir([Dir,'\*.jpg']);
% calculate number of tif files in folder
L = length(A);
%%
% open each file from A and carry out these tasks for each
for i = 1:L;
% create variable for file i from A (aka creates filename)
c = A(i).name;
% creates variable to open file i from direc
tory
a = strcat(Dir,'\',c);

    %determine the name of the file
    %build a full filename

%read file
I = imread(a);
%change file to grayscale
I2 = rgb2gray(I);
% Sharpens image

G = imsharpen(I2);
% Adjusts colour in image to improve contrast
J = imadjust(G,[0.4 0.7],[]);
%change file to black and white
I3 = im2bw(J, 0.9);
%Reverses black and white
K=imcomplement(I3);
%Cuts image so electrode not included
I4 = K(86:600,:,:);

%Flips image so it turns the other way and becomes slice at point 400
along x axis in y axis direction
%I5=flipud(I4(:,424));
I5=I4(:,415);
I6=imfill(I5,'holes');
% Counts black pixels from top of image down
counter=0;
z=1;
pixel=I6(z);
while pixel==0
    pixel=I6(z);
    z=z+1;
    if z==593
        break
    end
end
```

```
%Build index by converting filename string to number
Index = str2num(c(13:end-11));
Results(i,1) = Index;
Results(i,2) = z;

%make next filenumber i so that it is opened in next for loop
i = i+1;
end
```